

**IONIC DIFFUSION AND ANOMALOUS LATTICE BEHAVIOR
IN FRAMEWORK COMPOUNDS: INELASTIC NEUTRON
SCATTERING AND FIRST-PRINCIPLES CALCULATIONS**

By

Baltej Singh

Enrolment No. PHYS01201504018

Bhabha Atomic Research Centre, Mumbai, India

*A thesis submitted to the
Board of Studies in Physical Sciences*

*In partial fulfilment of requirements
for the Degree of*

DOCTOR OF PHILOSOPHY

Of

HOMI BHABHA NATIONAL INSTITUTE



February 2019

STATEMENT BY AUTHOR

This dissertation has been submitted in partial fulfilment of requirements for an advanced degree at Homi Bhabha National Institute (HBNI) and is deposited in the Library to be made available to borrowers under rules of the HBNI.

Brief quotations from this dissertation are allowable without special permission, provided that accurate acknowledgement of source is made. Requests for permission for extended quotation from or reproduction of this manuscript in whole or in part may be granted by the Competent Authority of HBNI when in his or her judgment the proposed use of the material is in the interests of scholarship. In all other instances, however, permission must be obtained from the author.

Baltej Singh

DECLARATION

I, hereby declare that the investigation presented in the thesis has been carried out by me.

The work is original and has not been submitted earlier as a whole or in part for a degree / diploma at this or any other Institution/University.

Baltej Singh

List of Publications

In Refereed Journal:

Related to Thesis

1. *Role of phonons in negative thermal expansion and high pressure phase transitions in β - eucryptite: An ab-initio lattice dynamics and inelastic neutron scattering study.*

Baltej Singh, M K Gupta, R Mittal, M Zbiri, S Rols, S J Patwe, S N Achary, H Schober, A K Tyagi, and S L Chaplot.

J. Appl. Phys., **121**, 085106 (2017)

2. *Superionic Conduction in β -eucryptite: Inelastic neutron scattering and computational studies.*

Baltej Singh, M. K. Gupta, R. Mittal, M. Zbiri, S. Rols, S. J. Patwe, S. N. Achary, H. Schober, A.K. Tyagi, and S. L. Chaplot.

Phys. Chem. Chem. Phys., **19**, 15512-15520 (2017)

3. *Anomalous lattice behavior of vanadium pentoxide (V_2O_5): X- ray diffraction, inelastic neutron scattering and ab-initio lattice dynamics.*

Baltej Singh, M. K. Gupta, S. K. Mishra, R. Mittal, P. U. Sastry, S. Rols and S.L. Chaplot.

Phys. Chem. Chem. Phys., **19**, 17967-17984 (2017)

4. *Anomalous Thermal Expansion, Negative Linear Compressibility and High-Pressure Phase Transition in $ZnAu_2(CN)_4$: Neutron Inelastic Scattering and Lattice Dynamics Studies.*

M. K. Gupta, **Baltej Singh**, R. Mittal, M. Zbiri, A. B. Cairns, A. L. Goodwin, H. Schober, S. L. Chaplot

Phys. Rev. B, **96**, 214303 (2017)

5. *Ab-initio Molecular Dynamics study of 1-D Superionic Conduction and Phase Transition in β - Eucryptite.*
Baltej Singh, M. K. Gupta, R. Mittal and S. L. Chaplot.
J. Mater. Chem. A, **6**, 5052-5064 (2018)
6. *Phonons, Phase Transitions and Thermal Expansion in LiAlO_2 : An ab- initio Density Functional Study.*
Baltej Singh, M. K. Gupta, R. Mittal and S. L. Chaplot.
Phys. Chem. Chem. Phys., **20**, 12248-12259 (2018)
7. *Negative thermal expansion behaviour in MZrF_6 ($M=\text{Ca, Mg, Sr}$): Ab-initio Lattice dynamical studies.*
M. K. Gupta, **Baltej Singh**, R. Mittal and S.L. Chaplot.
Phys. Rev. B, **98**, 014301 (2018)
8. *Density Functional Studies Revealing Anomalous Lattice Behavior in Metal Cyanide, AgC_8N_5 .*
Baltej Singh, M. K. Gupta, R. Mittal and S.L. Chaplot.
J. Phys. Chem. C, **122**, 27, 15575–15581 (2018)
9. *Phonons and Anomalous Thermal Expansion Behaviour of H_2O and D_2O ice Ih.*
M. K. Gupta, R. Mittal, **Baltej Singh**, S. K. Mishra, D. T. Adroja, A. D. Fortes and S. L. Chaplot.
Phys. Rev. B, **98**, 104301 (2018)
10. Dynamics of alkali ions (Li, Na) in the layered structure of V_2O_5 .
Baltej Singh, M. K. Gupta, R. Mittal and S.L. Chaplot.
(Manuscript under preparation).

11. Phonons and Lithium diffusion in LiAlO_2 : Inelastic neutron scattering and *ab-initio* Molecular Dynamics studies

Baltej Singh, M. K. Gupta, R. Mittal, S. Rols, S. N. Achary, A. K. Tyagi and S. L. Chaplot.

(Manuscript under preparation).

In Other Areas:

1. Lattice dynamics and thermal expansion behavior in the metal cyanides MCN (M=Cu, Ag, Au): Neutron inelastic scattering and first-principles calculations.

M. K. Gupta, **Baltej Singh**, R. Mittal, S. Rols, and S. L. Chaplot,

Phys. Rev. B, **93**, 134307 (2016)

2. *Anomalous Lattice Dynamics in AgC_4N_3 : Insights from Inelastic Neutron Scattering and Density Functional Calculations.*

Baltej Singh, M. K. Gupta, R. Mittal, M. Zbiri, S. A. Hodgson, A. L. Goodwin, H. Schober and S. L. Chaplot.

Frontiers in Chemistry, **6**, 544 (2018)

3. *Phonons and Thermal Expansion Behaviour of NiSi and NiGe .*

P. Goel, M. K. Gupta, S. K. Mishra, **Baltej Singh**, R. Mittal, S. L. Chaplot.

Frontiers in Chemistry, **6**, 331 (2018)

4. *Understanding Thermal Expansion Behaviour and Phase Stability of LaPO_4 by Neutron Diffraction and Ab-initio Calculations.*

S. K. Mishra, M. K. Gupta, R. S. Ningthoujam, **Baltej Singh**, R. Mittal, R. K. Vatsa, M. Zbiri, T. Hansen, H. Schober and S. L. Chaplot.

Phys. Rev. Materials, **2**, 126003 (2018)

In Conferences:

Oral Presentations:

1. “Phonon Dispersion measurement for Cu using Triple Axis Spectrometer” at 6th AONSA Neutron School, 12th-17th October, 2014, BATAN, Indonesia.
2. A short Oral presentation and involved in “science communication discussion” in Hermes Summer School 2016 - Materials Modeling and Science Communication held at Imperial College London, UK from 27-31 July, 2016
3. “Li Diffusion in One-Dimensional Superionic Conductor, β - Eucryptite (LiAlSiO_4)” in 61st DAE-SSPS 2016 at KIIT, Bhubaneswar from 25-30 December 2016.
4. “ β - Eucryptite, LiAlSiO_4 : A unique solid electrolyte with negative thermal expansion” at 12th International Conference on Ceramic Materials and Components for Energy and Environmental Applications (CMCEE 2018), held in Singapore, 22-27 July 2018.
5. PhD thesis Presentation at 63rd DAE-Solid State Physics Symposium held at Guru Jambheshwar University of Science and Technology (GJUS&T), Hisar, Haryana during December 18-22, 2018, awarded with “**BEST PhD THESIS AWARD**”.

Poster Presentations:

1. “Thermal Expansion in LiAlSiO_4 as Studied by Inelastic Neutron Scattering and Lattice Dynamics” at 6th AONSA Neutron School, 12th-17th October, 2014, BATAN, Indonesia.
2. “Phonons and their Relation to Negative Thermal Expansion in LiAlSiO_4 : An Inelastic Neutron Scattering and Lattice Dynamics Simulation Study” 59th DAE-Solid State Physics Symposium, 16th -20th December, 2014, VIT, Vellore, Tamilnadu.

3. “High Temperature and High Pressure Study of Vanadium Pentaoxide (V_2O_5)” at 60th DAE-Solid State Physics Symposium, 21st -25th December, 2015, Amity University Noida, India, awarded with **“BEST POSTER AWARD”**.
4. “Phonons, Thermal Expansion and High Pressure Phase Transition in $LiAlO_2$ ” at 60th DAE-Solid State Physics Symposium, 21st-25th December, 2015, Amity University Noida, India.
5. “Superionic behavior in $LiAlSiO_4$: Inelastic neutron scattering and dynamical studies”, at 6th Conference on Neutron Scattering, November 21 - 23, 2016, Bhabha Atomic Research Centre, Mumbai
6. “An *ab-initio* Molecular Dynamics Study of Superionic Phase Transition in β -Eucryptite”, during 62nd DAE-Solid State Physics Symposium from 26th -30th December, 2017 at Bhabha Atomic Research Centre, Anushaktinagar, Mumbai, India.

Baltej Singh

Dedicated

To

My Dear Parents & Brother

ACKNOWLEDGEMENTS

At the foremost, I would like to acknowledge my supervisor, Dr. R. Mittal, Solid State Physics Division, BARC, for his guidance and constant support throughout the tenure of my degree. I am deeply grateful and indebted for his supervision and support, which were indispensable. I wish to express my special and sincere thanks to Dr. S. L. Chaplot, Raja Ramanna Fellow, BARC for his guidance, never-ending enthusiasm, excellent suggestions and constant support over the years. I would like to express my heartiest acknowledgement to Dr. M K Gupta, SSPD for his help at every stage during the tenure and his all time availability for research discussions. His way of describing and approaching research challenge has greatly influenced my way of thinking. I would also like to thank my doctoral committee members Dr. S. Basu, Dr. T. R. Ravindran, Dr. Ashok Arya, Dr. Nandini Garg and Dr. B K Nayak whose useful suggestions have been very helpful. Special thanks to Dr. Ashok Arya, Material Science Division, BARC, for his all time support and encouragement. I am very thankful to Dr. S. M. Yusuf, Head SSPD, BARC, for his constant support during my PhD research.

I thank Dr. Prabhatasree Goel, Dr. S. K. Mishra, Dr. Mala. N. Rao for always helping me in various research experiments and for fruitful discussions. I am also thankful to Dr. Surendra Singh, Dr. Amit Kumar and Dr. Keka Chakraborty and Dr. V. K. Sharma for their constant support during the period of my thesis work. I thank to my collaborators Dr. Stephane Rols and Dr. Mohamed Zbiri from ILL Grenoble, France, for their scientific collaboration in various experiments. I would also like to thank Dr. S. N. Achary for providing various samples for the measurements. In addition, I would like to acknowledge Mr. Vaibhav Shukla and Mrs. Vibhuti, Supercomputer Division, BARC for their help in computing accessibility of ANUPAM and PRITHVI supercomputers. My sincere thanks

are due to all my colleagues in Solid State Physics Division, Bhabha Atomic Research Centre, for helping me in different ways. The administrative staff of Solid State Physics Division are deeply acknowledged for their timely help.

I extend my thanks to my friends, Harwinder, Rajwinder, Pardeep, Sumit, Sukhdeep, Sarita, Indresh, Srikant, Mrinal, Purushottam, Pulkit, Dyaneshwar, Dipayan, Harish, Madhu, Anil, Abhishek, Naini, Priyanka, Usha, Nidhi, Swayam and Ashok for providing exciting and fun filled environment during my research years. I extend my thanks to all friends, well-wishers who made my stay pleasant and memorable in BARC. I thank all of them, whose name I might have missed, but whose assistance has helped in the progress of my research work.

I am very grateful to my simple and hardworking parents and my elder brother who have always taught me to do hard work with positive attitude. Their sacrifice for little and big things have made me achieve my dreams of higher education and research. Their pure and humble personality, unconditional love and all time support have always kept me motivated to achieve my PhD. Last but not the least, I greatly acknowledge my dearest friend, Channprit, for providing moral support and encouragement. She has always trusted and stood by me in difficult times.

Baltej Singh

CONTENTS

	Page No.
Synopsis	xxi
List of Figures	xxxiii
List of Tables	xlv
Aberrations	xlix
Chapter 1 Materials, Physical Properties and Techniques	1
1.1 Introduction	1
1.2 Materials of Interest	3
1.2.1 Battery Materials	3
1.2.2 Low Density Framework Structures	6
1.3 Experimental Techniques	8
1.3.1 X-ray Diffraction	8
1.3.2 Inelastic Neutron Scattering	9
1.4 Theoretical Methods	13
1.4.1 Lattice Dynamics	14
1.4.2 Density Functional Theory	18
1.4.2.1 Hohenberg-Kohn Theorems	21
1.4.2.2 Kohn-Sham Approach	22
1.4.2.3 Exchange Correlation Approximations	23
1.4.3 Thermodynamic and Elastic Properties	26
1.4.4 Transition State Theory	30
1.4.5 Molecular Dynamics Simulations	33
1.4.6- Ionic Diffusion in Solids	37
1.5 Objectives of Research	40
1.6 Summary	40
References	42
Chapter 2 β-Eucryptite LiAlSiO₄: A Potential Solid Electrolyte for Li-ion Battery	47
2.1 Introduction	47
2.1.1 Structural Details	48
2.1.2 Motivations and Objectives of Research	50

2.2 Experimental and Computational Details	52
2.3 Results and Discussions	54
2.3.1 Inelastic Neutron Scattering Measurements	54
2.3.2 Classical Molecular Dynamical Simulations	55
2.3.2.1 Phonon Spectra	55
2.3.2.2 Lithium Diffusion and Thermal Expansion	57
2.3.3 First-Principles Calculations	61
2.3.3.1 Mechanism of Negative Thermal Expansion	62
2.3.3.2 Activation Energy Barrier for Li Diffusion	68
2.3.4 <i>Ab-initio</i> Molecular Dynamics Simulations	70
2.3.4.1 High Temperature Phase Transition	71
2.3.4.2 Superionic Conductivity in HT Phase	76
2.3.4.3 Calculated Pair Distribution Functions	78
2.3.4.4 Role of NTE in Superionic Conduction	81
2.3.4.5 Role of Defects in Superionic Conduction	83
2.4 Conclusions	86
References	88

Chapter 3 Thermodynamic Properties and Li diffusion in Cathode Material, LiAlO₂

91

3.1 Introduction	91
3.1.1 Structural Details	91
3.1.2 Motivations and Objectives of Research	92
3.2 Experimental and Computational Details	94
3.3 Results and Discussions	95
3.3.1 Electronic Structure	96
3.3.2 Enthalpy and Phase Transitions	99
3.3.3 Phonon Spectra of Various Phases of LiAlO ₂	100
3.3.4 Pressure-Temperature Phase Diagram of LiAlO ₂	103
3.3.5 Structural Changes during Phase Transitions	105
3.3.6 Energy Barrier for γ to β Phase Transition	107
3.3.7 Phonons and High Temperature Phase Transitions	108
3.3.8 Thermal Expansion Behavior of γ - LiAlO ₂	110

3.3.9 Li Diffusion in γ -LiAlO ₂	112
3.4 Conclusions	117
References	118
Chapter 4 Phonons, Anomalous Lattice Behaviour and Li-ion Diffusion in a Potential Battery Cathode, V₂O₅	121
4.1 Introduction	121
4.1.1 Structural Details	122
4.1.2 Motivations and Objectives of Research	123
4.2 Experimental and Computational Details	125
4.3 Results and Discussions	126
4.3.1 X-ray Diffraction Study	126
4.3.2 Role of Van der Waals and Hubbard Interaction	129
4.3.3 Phonon Spectra of α -V ₂ O ₅	133
4.3.4 Elastic and Thermal Expansion Behavior of α -V ₂ O ₅	136
4.3.5 High Pressure Study of α -V ₂ O ₅	141
4.3.6 Dynamics of Li-ion in V ₂ O ₅ Layers	147
4.4 Conclusions	150
References	152
Chapter 5 Phonon Spectra and Anomalous Lattice Behaviour of ZnAu₂(CN)₄	155
5.1 Introduction	155
5.1.1 Structural Details	156
5.1.2- Motivations and Objectives of Research	157
5.2 Experimental and Computational Details	158
5.3 Results and Discussions	159
5.3.1 Experimental and Calculated Phonon Spectra	159
5.3.2 Anisotropic Thermal Expansion Behaviour	161
5.3.3 High Pressure Phase Transition	166
5.3.4 Negative Linear Compressibility	173
5.4 Conclusions	174
References	176

Chapter 6 Computational Discovery of Anomalous Lattice Behaviour in Metal

Cyanide Framework, AgC₈N₅	179
6.1 Introduction	179
6.1.1 Structural Details	180
6.1.2 Motivations and Objectives of Research	180
6.2 Computational Details	182
6.3 Results and Discussions	183
6.3.1 Elastic Properties and Born Stability Criteria	184
6.3.2 High Pressure Behavior	185
6.3.3 Total and Partial Phonon Density of States	189
6.3.4 Anisotropic Thermal Expansion Behaviour	192
6.3.5 Mechanism of Negative Thermal Expansion	193
6.4 Conclusions	196
References	198

Chapter 7 Negative Thermal Expansion in Polyhedral Framework Connected via

Terminal Atoms	201
7.1 Introduction	201
7.2 Metal Fluorides, MZrF ₆ (M=Mg, Ca, Sr)	202
7.2.1 Computational Details	204
7.2.2 Phonon Spectra	206
7.2.3 Thermal Expansion Behaviour	207
7.2.4 Anharmonicity of Phonon Modes	214
7.3 H ₂ O and D ₂ O Ice <i>Ih</i>	217
7.3.1 Computational Details	219
7.3.2 Total and Partial Phonon Density of States	220
7.3.3 Gruniesen Parameters and Thermal Expansion	221
7.3.4 Mechanism of Negative Thermal Expansion	227
7.3.5 High Pressure Stability of <i>Ih</i> Phase of Ice	229
7.4 Conclusions	230
References	231

Chapter 8 Summary and Future Research Plans	235
8.1 Summary	235
8.2 Future research Plans	239

SYNOPSIS

The research work presented in this thesis involves the study of role of phonon (lattice vibration) in giving rise to various thermodynamic and transport properties like thermal expansion, compressibility, ionic diffusion and phase transitions in crystalline solids. These properties are studied with focus especially on the Li ion battery materials and low-density framework compounds. The understanding of the atomic level mechanisms¹⁻⁴ responsible for above functionalities of the materials is important to improve their performance in order to use them in various applications.

Phonons are the quanta of collective atomic vibrations in a crystal and possess a typical energy of meV. The phonons give rise to propagation of sound waves, elastic properties, lattice specific heat, thermal expansion, ionic diffusion, thermal conductivity, superconductivity and many more properties of the materials⁵. The application of pressure or temperature on a material affects the anharmonic phonons and may be responsible for interesting thermodynamic behavior and phase transitions in the solids². The inclusion of vibrational entropy of a system enables us to accurately calculate the free energy of the system^{3, 6} which is very important to calculate the phase stability and temperature-pressure phase diagram of crystalline solids.

Li ion batteries are the most popular devices in portable energy storage technology⁷. The improvement in the existing battery materials is required for the efficient storage of energy and for making the batteries lighter, quickly chargeable, safer, long lived, stable and cost effective. The stability, safety and performance of these materials can be controlled by controlling their thermal expansion and elastic properties, enhancing ionic diffusion inside the solid material and avoiding the phase transitions in temperature and pressure range of battery operations. For example (i) the efficient

electrode for battery should not undergo large changes in the structure during the battery operation (intercalation/deintercalation of ions) or accidental high pressure/temperature conditions. This requires study of atomistic level mechanism responsible for phase transitions in the electrode materials in order to control their efficiency and stability⁸⁻¹⁰.

(ii) Moreover, a replacement of the present organic polymer salt-based electrolyte by some solid superionic conductor^{11, 12} could resolve the issue of leakage, chemical stability, vaporization, flammability and dendrites formation to a great extent and may wider temperature and pressure ranges of battery operation. It will also enable the use of metallic Li as anode material which will enhance the current charge capacities of the battery^{11, 13}. This requires solid ionic conductors which possess liquid like ionic conductivity and are highly stable under the diffusion. Therefore, the battery material research focuses on the discovery of highly suitable electrodes and solid electrolytes to make advanced batteries for electric vehicle applications.

The low-density metal organic framework compounds are very important for temperature pressure sensing and armor applications¹⁴⁻¹⁶. These compounds are very sensitive to applied pressure and temperature and give rise to negative thermal expansion (NTE), negative linear compressibility (NLC) and phase transitions^{14, 17-20}. The highly anisotropic nature of bonding and atomic vibrations gives rise to interesting mechanism of NTE and NLC behavior in these compounds^{14, 17, 20, 21}. The metal organic framework (MOF) materials are chosen to understand the role of phonon to their anomalous lattice behavior. This understanding can be further utilized to design better functional materials.

The present research work aims to extensively study the phonon spectra of battery materials and low density metal organic/inorganic framework compounds. The phonon studies in these compounds are used to understand the mechanisms responsible for ionic conduction, NTE, NLC and high temperature-pressure phase transitions. The various

factors affecting the ionic diffusion in these materials are also studied. Moreover, the accurate calculations of vibrational free energy (considering contributions only from vibrational entropy) is used to calculate temperature pressure phase diagrams and specific phonon modes responsible for these phase transitions are identified.

For this purpose, a combination of experimental tools like inelastic neutron scattering and X-ray diffraction and state of art computational methodologies like density functional theory (DFT), lattice dynamics (LD), classical molecular dynamics (MD) as well as *ab-initio* MD are used to study the battery materials and low-density framework compounds. Although, the pathways for atomic diffusion can be obtained from the temperature dependent X-ray²² and neutron diffraction techniques²³, however, Li atom, due to its small atomic number ($Z=3$), is known to be a poor scatterer of X-ray. Even for neutron, Li has low scattering cross section (= 1.37 barns) and high absorption cross section (= 70.5 barns), which makes it difficult to study the behaviour of Li using neutron scattering. Computational tools, like DFT and MD simulations, provide a very good alternative to study the atomic scale behaviour of Li atom²⁴⁻²⁶.

The thesis is arranged in eight chapters. The motivation for the study, details of the work done and the significance of the results obtained are given below in the brief description of various chapters.

Chapter 1 describes the basic introduction, motivation and objectives of work along with experimental and theoretical tools used to study the thermodynamical properties of interest. The inelastic neutron scattering (INS) technique to study dynamics, and X-ray diffraction for structural study of materials has been explained briefly. Thermal neutrons have a wavelength and energy of the order of atomic spacing and lattice vibrations, respectively and thus are suitable to study the phonons in the materials. The phonon dispersion and phonon density of states^{2, 3} can be measured using

the single crystal and polycrystalline samples, respectively. The measurements of temperature dependence of phonon density of states using the polycrystalline samples are performed using the IN4 and IN6 time-of-flight spectrometer at high flux reactor of Institut Laue-Langevin, Grenoble, France as described in this Chapter.

The theoretical techniques like quantum-mechanical *ab-initio* density functional theory (DFT), lattice dynamics, molecular dynamics (*ab-initio* as well as empirical potential based), density functional perturbation theory and transition state theory are discussed. These techniques have been used to calculate the phonon spectra, diffusion coefficients, diffusion pathways and activation energy for these pathways in the compounds of interest. The equilibrium structures, total energy and force constants in any given atomic configuration of the system are calculated. The basic formalism for the calculation of elastic properties and anisotropic linear thermal expansion coefficients of a crystalline system is given in detail.

Chapter 2 describes the extensive studies on potential solid electrolyte β -Eucryptite, LiAlSiO_4 . These studies include the origin of negative thermal expansion (NTE)²⁷, high temperature phase transition^{28, 29}, one-dimensional Li diffusion and their mutual connection²⁹ using *ab-initio* DFT, classical MD as well as *ab-initio* MD calculations along with experimental INS measurements. The interpretation of temperature dependence (300-900 K) of various peaks in measured (INS) phonon density of states is performed by classical force field molecular dynamical calculations. The large broadening in the partial phonon density of states shows that the melting of Li sub-lattice happens above 1200 K. The calculated diffusion coefficient for Li shows a superionic conduction above this temperature. The calculated trajectory of Li atoms at higher temperature shows nearly isotropic diffusion pathways due to the isotropic nature of the Columbic and Buckingham type interatomic potentials used in this

calculation. The experimentally observed anisotropy in Li diffusion and linear thermal expansion behavior is not obtained. This motivated us to perform *ab-initio* calculations.

The anisotropic stress dependence of the phonon spectrum is calculated using *ab-initio* lattice dynamics (LD) in order to obtain the thermal expansion behavior along various axes. The analysis of the polarization vectors of the phonon modes sheds light on the mechanism of the anisotropic negative thermal expansion and overall very low volume thermal expansion behavior. The *ab-initio* molecular dynamics simulations of β -Eucryptite provide the microscopic understanding of the one-dimensional superionicity that occurs along the hexagonal *c*-axis and is associated with the order-disorder nature of the phase transition. The inter- and intra-channel correlated motion of Li along the hexagonal *c*-axis gives the minimum energy pathway for Li ion conduction in LiAlSiO₄. The Li ionic conductivity is found to enhance due to the anisotropic negative thermal expansion along hexagonal *c*-axis. The introduction of defects in the crystal, e.g., excess Li in interstitial sites, Li vacancy and O vacancy are found to significantly increase the ionic conductivity and hence might reduce the temperature of the superionic phase transition in this material. These properties make this compound a potential solid electrolyte for Li ion batteries.

Chapter 3 describes the role of phonon in various temperature/pressure dependent phase transitions³⁰ and mechanism of Li diffusion in battery cathode material, LiAlO₂, using the *ab-initio* calculations and temperature dependent inelastic neutron scattering measurements. The electronic band structure as well as phonon spectra are calculated for various phases as a function of pressure. The vibrational entropy used for the calculations of Gibbs free energy is found to play an important role in the phase stability and phase transitions among various phases. A sudden increase in the polyhedral bond lengths (Li/Al-O) signifies the change from the tetrahedral to octahedral

geometry at high-pressure phase transitions. The activation energy barrier for the high-pressure phase transitions is calculated. The phonon modes responsible for the phase transition (upon heating) from high pressure phases to ambient pressure phases are identified. The *ab-initio* lattice dynamics calculations in the framework of quasi-harmonic approximations are used to calculate the anisotropic thermal expansion behavior of γ -LiAlO₂. The experimentally measured temperature dependent phonon spectra are interpreted by the molecular dynamics calculations to understand the role of phonon in Li diffusion. Moreover, Li diffusion coefficients and pathways for Li diffusion in this compound are calculated using the *ab-initio* molecular dynamical calculations. The calculations show that the diffusion in the crystal starts around 1600 K and the presence of defects in the crystal reduce the temperature of diffusion to 1200 K. The diffusion in *a-b* plane is more pronounced as compared to that along the *c*-axis.

Chapter 4 involves the structural, dynamical, elastic, diffusional and high-pressure phase transition studies in battery cathode material vanadium penta-oxide, V₂O₅ using temperature dependent X-ray diffraction, inelastic neutron scattering and *ab-initio* calculations³¹. The temperature dependent X-ray diffraction measurements reveal highly anisotropic and anomalous thermal expansion from 12K to 853K. The results do not show any evidence of structural phase transition or decomposition of α -V₂O₅, contrary to the previous transmission electron microscopy (TEM) and electron energy loss spectroscopy (EELS) experiments^{32, 33}. The inelastic neutron scattering measurements performed up to 673 K corroborate the result of our X-ray diffraction measurements. The analysis of the experimental data is carried out using *ab-initio* lattice dynamics calculation. The important role of van der Waals dispersion and Hubbard interactions on the structure and dynamics is revealed through the *ab-initio* calculations. The calculated anisotropic thermal expansion behavior agrees well with temperature

dependent X-ray diffraction. The mechanism of anisotropic thermal expansion and anisotropic linear compressibility is discussed in terms of calculated anisotropy in Grüneisen parameters and elastic coefficients. The calculated Gibbs free energy in various phases of V_2O_5 is used to understand the high pressure and temperature phase diagram of the compound. Moreover, the intercalation of alkali ions among the V_2O_5 layers³⁴ and dynamics of these ions at high temperature has been studied by performing *ab-initio* molecular dynamical simulations. The diffusion pathways of these ions from the MD simulations are predicted to follow the eigenvectors of soft phonon modes obtained in the intercalated structure. The diffusion happens in the *a-b* plane of the structure.

Chapter 5 describes temperature-dependent inelastic-neutron-scattering measurements, accompanied by *ab-initio* calculations of the phonon spectra and pressure dependent elastic properties to quantitatively explain an unusual combination of negative thermal expansion and negative linear compressibility (NLC) behaviour of $ZnAu_2(CN)_4$ ^{18, 20, 35}. The inelastic neutron scattering experiments and *ab-initio* calculations have been used to gain deeper insights into the structure and dynamics of $ZnAu_2(CN)_4$ as a function of temperature and pressure. The calculations of the structure, phonon spectrum, anisotropic thermal expansion and anisotropic compressibility are compared with experimental results. The mechanism of the negative thermal expansion is identified in terms of specific anharmonic phonon modes that involve bending of the -Zn-NC-Au-CN-Zn- linkage that correlate very well with the anomalous thermal expansion and compressibility exhibited by $ZnAu_2(CN)_4$. The large anisotropy in the elastic compliance matrix, which is attributed to the flexible network and Au bridging, are responsible for the NLC behaviour. It has been shown that NLC could be another factor in materials which leads to NTE. The large negative shear elastic compliance (s_{13} and s_{12}) and small tensile elastic compliance (s_{33}) are indeed the major

factors controlling the NTE behaviour in this compound. The known high-pressure transition at about 2 GPa is found to occur due to softening of an L-point phonon mode and its coupling with a zone-centre phonon and an M-point phonon. Further, the ambient pressure phase is found to be close to an elastic instability as revealed from violation of the Born stability criteria, which results in the phase transition being of a weakly first order nature.

Chapter 6 describes power of *ab-initio* computational tools to predict the negative linear compressibility and negative thermal expansion in metal cyanide³⁶, AgC_8N_5 . These studies involve the investigation of anomalous lattice behavior of metal organic framework compound AgC_8N_5 on application of pressure and temperature using *ab-initio* density functional theory and molecular dynamics simulations. The van der Waals dispersion interactions are found to play an important role in structural optimization and stabilization of this compound. Our *ab-initio* calculations show negative linear compressibility (NLC) along the *c*-axis of the unit cell. The *ab-initio* lattice dynamics as well as the molecular dynamics simulations show large negative thermal expansion (NTE) along the *c*-axis. The NLC and NTE along *c*-axis of the structure are governed by the dominant dynamics of Ag atoms in *a-b* plane which give rise to hinge-like mechanism. The NLC along the *c*-axis drives the NTE along that direction.

Chapter 7 describes the mechanism of negative thermal expansion in terminally connected polyhedral framework, i.e., metal fluorides MZrF_6 (M=Mg, Ca, Zr)³⁷ and *Ih* phase of H_2O and D_2O ice³⁸. The thermal expansion behavior of metal fluorides can be tuned by choosing appropriate metal cation. The *ab-initio* lattice dynamical studies on the metal fluorides (CaZrF_6 , MgZrF_6 and SrZrF_6) are performed and the anharmonic phonon modes responsible for the negative thermal expansion in these materials are identified. These phonons involve ZrF_6 polyhedral rotational motion, which

leads to large transverse amplitude of the vibrations of the fluorine atom in the Zr-F-Zr bond. The compounds with larger anisotropy in the thermal amplitude of the fluorine atoms show larger NTE behaviour. This has enabled to understand the large variation in thermal expansion behaviour of these compounds at high temperature.

In order to identify and quantitatively analyze the anharmonicity of phonons relevant to the anomalous thermal expansion in the *I_h* phase of ice, the *ab-initio* lattice dynamics calculations are performed³⁸. The anomalous expansion is quantitatively reproduced from the analysis of the neutron data as well as from the *ab-initio* calculations. Further, the *ab-initio* calculations are used to visualize the nature of anharmonic phonons across a large part of the Brillouin zone. The negative thermal expansion below 60 K in the hexagonal plane (*a-b* plane) is due to anharmonic librational motion of the hexagonal rings of the ice molecules, and that along the hexagonal axis originates from the transverse vibrations of the hexagonal layers.

Chapter 8 summarizes the results of the research work, their usefulness and contributions to the current field of material research followed by possible future directions. The thesis describes the study of thermodynamic properties of Li ion battery materials and low-density framework compounds using the experimental techniques like inelastic neutron scattering X-ray diffraction and state of art *ab-initio* and classical computational (DFT, LD and MD) techniques. An extensive study on the role of phonons in leading to anisotropic thermal expansion, anisotropic linear compressibility, ionic diffusion, and mechanism of various temperature/pressure driven phase transitions in these materials has been performed. The atomic motion, structural geometry and nature of bonding are found to govern the anomalous thermal expansion and compressibility behavior. The temperature dependence of diffusion, minimum energy pathways for the ionic diffusion and their relation with the thermal expansion behavior of the materials are

investigated. The complete pressure temperature phase diagrams are calculated considering the contribution from vibrational entropy obtained from the phonons over the entire Brillion zone. Moreover, the effects of thermal expansion and defects in the crystal on its ionic conduction behavior are also revealed.

The understanding of the atomic mechanism responsible for various anomalous thermodynamic properties in crystalline solids using the computational techniques will help in the development and engineering of battery materials with very low thermal expansion, high ionic conductivity, good mechanical properties and with a wide range of temperature pressure conditions without undergoing the structural phase transitions. The study of low density framework compounds will be useful for designing temperature and pressure sensors, artificial muscles and in piezoelectric applications¹⁴.

References

1. F. Bridges, T. Keiber, P. Juhas, S. J. L. Billinge, L. Sutton, J. Wilde and G. R. Kowach, *Physical Review Letters*, 2014, **112**, 045505.
2. R. Mittal, M. K. Gupta and S. L. Chaplot, *Progress in Materials Science*, 2018, **92**, 360-445.
3. S. L. Chaplot, R. Mittal and N. Choudhury, *Thermodynamic Properties of Solids: Experiments and Modeling*, John Wiley & Sons, 2010.
4. L. Zhang, Y. Wang, J. Lv and Y. Ma, *Nature Reviews Materials*, 2017, **2**, 17005.
5. G. Grimvall, *Thermophysical properties of materials*, Elsevier, 1999.
6. B. Cheng and M. Ceriotti, *Physical Review B*, 2018, **97**, 054102.
7. J. B. Goodenough and K.-S. Park, *Journal of the American Chemical Society*, 2013, **135**, 1167-1176.
8. R. Hausbrand, G. Cherkashinin, H. Ehrenberg, M. Gröting, K. Albe, C. Hess and W. Jaegermann, *Materials Science and Engineering: B*, 2015, **192**, 3-25.
9. G. Ceder, Y. M. Chiang, D. R. Sadoway, M. K. Aydinol, Y. I. Jang and B. Huang, *Nature*, 1998, **392**, 694-696.
10. J. Zheng, P. Xu, M. Gu, J. Xiao, N. D. Browning, P. Yan, C. Wang and J.-G. Zhang, *Chemistry of Materials*, 2015, **27**, 1381-1390.

11. M. H. Braga, N. S. Grundish, A. J. Murchison and J. B. Goodenough, *Energy & Environmental Science*, 2017, **10**, 331-336.
12. W. Zhou, Y. Li, S. Xin and J. B. Goodenough, *ACS Central Science*, 2017, **3**, 52-57.
13. J. Y. Hwang, S. T. Myung and Y. K. Sun, *Chemical Society Reviews*, 2017, **46**, 3529-3614.
14. A. B. Cairns and A. L. Goodwin, *Physical Chemistry Chemical Physics*, 2015, **17**, 20449-20465.
15. N. C. Burtch, J. Heinen, T. D. Bennett, D. Dubbeldam and M. D. Allendorf, *Advanced Materials*, 2017.
16. S. M. Mirvakili and I. W. Hunter, *Advanced Materials*, 2017, **29**.
17. A. L. Goodwin, M. Calleja, M. J. Conterio, M. T. Dove, J. S. O. Evans, D. A. Keen, L. Peters and M. G. Tucker, *Science*, 2008, **319**, 794-797.
18. A. B. Cairns, J. Catafesta, C. Levelut, J. Rouquette, A. van der Lee, L. Peters, A. L. Thompson, V. Dmitriev, J. Haines and A. L. Goodwin, *Nat Mater*, 2013, **12**, 212-216.
19. A. L. Goodwin, D. A. Keen and M. G. Tucker, *Proceedings of the National Academy of Sciences*, 2008, **105**, 18708-18713.
20. A. L. Goodwin, B. J. Kennedy and C. J. Kepert, *Journal of the American Chemical Society*, 2009, **131**, 6334-6335.
21. M. K. Gupta, B. Singh, R. Mittal, S. Rols and S. L. Chaplot, *Physical Review B*, 2016, **93**, 134307.
22. J. Bréger, N. Dupré, P. J. Chupas, P. L. Lee, T. Proffen, J. B. Parise and C. P. Grey, *Journal of the American Chemical Society*, 2005, **127**, 7529-7537.
23. D. Wiedemann, S. Indris, M. Meven, B. Pedersen, H. Boysen, R. Uecker, P. Heitjans and M. Lerch, *Zeitschrift für Kristallographie-Crystalline Materials*, 2016, **231**, 189-193.
24. Y. Mo, S. P. Ong and G. Ceder, *Chemistry of Materials*, 2011, **24**, 15-17.
25. M. M. Islam and T. Bredow, *The journal of physical chemistry letters*, 2015, **6**, 4622-4626.
26. M. M. Islam, J. Uhlendorf, E. Witt, H. Schmidt, P. Heitjans and T. Bredow, *The Journal of Physical Chemistry C*, 2017, **121**, 27788-27796.

27. B. Singh, M. K. Gupta, R. Mittal, M. Zbiri, S. Rols, S. J. Patwe, S. N. Achary, H. Schober, A. K. Tyagi and S. L. Chaplot, *Journal of Applied Physics*, 2017, **121**, 085106.
28. B. Singh, M. K. Gupta, R. Mittal, M. Zbiri, S. Rols, S. J. Patwe, S. N. Achary, H. Schober, A. K. Tyagi and S. L. Chaplot, *Physical Chemistry Chemical Physics*, 2017, **19**, 15512-15520.
29. B. Singh, M. K. Gupta, R. Mittal and S. L. Chaplot, *Journal of Materials Chemistry A*, 2018, **6**, 5052-5064.
30. B. Singh, M. K. Gupta, R. Mittal and S. L. Chaplot, *Physical Chemistry Chemical Physics*, 2018, **20**, 12248-12259.
31. B. Singh, M. K. Gupta, S. K. Mishra, R. Mittal, P. U. Sastry, S. Rols and S. L. Chaplot, *Physical Chemistry Chemical Physics*, 2017, **19**, 17967-17984.
32. R. J. D. Tilley and B. G. Hyde, *Journal of Physics and Chemistry of Solids*, 1970, **31**, 1613-1619.
33. D. S. Su and R. Schlögl, *Catalysis Letters*, **83**, 115-119.
34. G. Sai Gautam, P. Canepa, A. Abdellahi, A. Urban, R. Malik and G. Ceder, *Chemistry of Materials*, 2015, **27**, 3733-3742.
35. M. K. Gupta, B. Singh, R. Mittal, M. Zbiri, A. B. Cairns, A. L. Goodwin, H. Schober and S. L. Chaplot, *Physical Review B*, 2017, **96**, 214303.
36. B. Singh, M. K. Gupta, R. Mittal and S. L. Chaplot, *The Journal of Physical Chemistry C*, 2018, **122**, 15575-15581.
37. M. K. Gupta, B. Singh, R. Mittal and S. L. Chaplot, *Physical Review B*, 2018, **98**, 014301.
38. M. K. Gupta, R. Mittal, Baltej Singh, S. K. Mishra, D. T. Adroja, A. D. Fortes and S. L. Chaplot, *Phys. Rev. B* **98**, 104301 (2018).

LIST OF FIGURES

FIG 1.1 The interconnection between various fields of material research.

FIG 1.2 Schematic diagrams of the IN4C and IN6 time of flight neutron spectrometer at ILL, Grenoble, France (after www.ill.fr).

FIG 1.3 The atomic displacement patterns corresponding to longitudinal and transverse vibrational phonon modes.

FIG 1.4 A flow chart of PHONON calculation using density functional theory techniques.

FIG 1.5 A flowchart of density functional theory calculations scheme for convergence.

FIG 1.6 (Left) Potential energy surface of solid in three dimensions (Right) Elaboration of procedure to calculate the minimum energy pathway for a reaction and various types of forces which are optimized in this process (after Ref. [85]).

FIG 1.7 A flowchart for Molecular dynamical simulations.

FIG 2.1 Schematic representation of (Top)the unit cell structure of room temperature phase of β -eucryptite, projected along different axes, Li1(Red) occupies A-type channel while Li2 & Li3 (Blue & Green) occupy S-type channels. (Bottom) the unit cell structure of high temperature phase (supercell $2 \times 2 \times 1$) of β -eucryptite, projected along different axes. AlO_4 and SiO_4 tetrahedra are in blue and red colour respectively.

FIG 2.2 Temperature dependent (a) experimental inelastic neutron scattering spectra, and (b) calculated neutron weighted spectra using MD simulations. For clarity, the spectra are shifted vertically. The peak corresponding to Li vibrations in the phonon spectra is highlighted by dotted line.

FIG 2.3 Temperature dependent partial phonon densities of states for various atoms in β -eucryptite obtained from MD simulations. For clarity, the spectra are vertically shifted.

FIG 2.4 (a) The position of vacant sites of various atoms in (6×6×3) supercell of high temperature phase of LiAlSiO₄, **(b)** The calculated mean square displacement as a function of time for the different atoms of β-eucryptite at various temperatures for (Left) perfect crystal and (Right) the structure with a vacancy.

FIG 2.5 The diffusion coefficient for Li as a function of temperature for perfect crystal and the structure with a vacancy for β-eucryptite as calculated using MD simulations.

FIG 2.6 The activation energy for Li jump diffusion obtained from Arrhenius plot of diffusion coefficient as a function of temperature.

FIG 2.7 Trajectory of selected Li atoms in a perfect crystal of LiAlSiO₄ at 1400 K is given in Cartesian coordinate. The hexagonal *c*-axis is along the *z*-direction.

FIG 2.8 The calculated and experimental [29] temperature dependent lattice parameters of high temperature phase of LiAlSiO₄.

FIG 2.9 (a) The calculated Grüneisen parameters (Γ_l , $l=a, c$) as obtained from anisotropic stress along *a*- and *c*-axes. **(b)** Linear thermal expansion coefficients as a function of temperature **(c)** The calculated and experimental variation of the lattice parameters ($l= a$ or c) with temperature **(d)** The contribution of phonons of energy *E* to the linear thermal expansion coefficients (α_a and α_c), at 300 K, in the RT phase.

FIG 2.10 Phonon dispersion curves of β-eucryptite, at ambient (solid line) and 0.5 GPa (dash line) pressures, along the high symmetry directions in the Brillion zone of hexagonal unit cell. The Bradley-Cracknell notation is used for the high-symmetry points: Γ (0,0,0), M(1/2,0,0), K(1/3,1/3,0), A (0, 0, 1/2), H (1/3,1/3,1/2) and L (1/2,0,1/2).

FIG 2.11 Schematic representation of the polarization vectors of selected zone centre optic phonon modes in β-eucryptite. The first, and second and third values specified below each plot indicate the phonon energy and Grüneisen parameters, respectively. The

tetrahedral units around Al and Si are colour-coded by blue and red respectively, while the Li atoms are represented by a green colour.

FIG 2.12 Comparison between the barrier heights for the Li channels movement along *a* (or *b*-) and *c*-axis of β -eucryptite. “Site 1” and “Site 2” represent the initial and final positions of Li atoms movement as indicated by arrows in the left panel. Key: Li, Green sphere; Al, Blue sphere; Si Red sphere; O, Black sphere.

FIG 2.13 (a) The ABIMD calculated and experimental phonon spectra[39] of β -eucryptite at 300 K. (b) The calculated and experimental[60] (neutron diffraction) lattice parameters of β -eucryptite.

FIG 2.14 The AIMD calculated MSD ($\langle u^2 \rangle$) of various atoms of RT phase of β -eucryptite as a function of time (a) at 300K and (b) 600K. (c) Anisotropic MSD ($\langle u^2 \rangle$) of Li averaged over all the Li atoms in the supercell and (d) u^2 of each individual Li atoms along *c*-axis at 600K as a function of time.

FIG 2.15 Trajectory of Li atoms in channels of β -eucryptite (RT-Phase) at temperatures like (a) 300K, (b) 600K. Key: AlO_4 -Blue, SiO_4 -Red, Initial Position of Li- Black, Time Evolution of Li- Green balls.

FIG 2.16 The AIMD calculated u^2 of each individual Li atoms of HT- phase of β -eucryptite as a function of time along *c*-axis at (a) 800K, (b) 1000K

FIG 2.17 Trajectory of Li atoms in channels of β -eucryptite (HT-Phase) at various temperatures like (a) 800K, (b) 1000K and (c) 1200K. Key: AlO_4 -Blue, SiO_4 -Red, Initial Position of Li- Black, Time Evolution of Li- Green balls.

FIG 2.18 The AIMD calculated (a) one dimensional diffusion coefficient as a function of temperature and (b) Arrhenius plot of diffusion coefficient and temperature to obtain activation energy for Li diffusion.

FIG 2.19 The AIMD calculated temperature dependence of pair distribution function for various atomic pair of β -eucryptite. The information about different coloured lines is valid for all the subplots.

FIG 2.20 The AIMD calculated temperature dependence of angular distribution function for various polyhedral angles in β -eucryptite.

FIG 2.21 (a) A cartoon showing the effect of decreasing c/a ratio on structure of β -eucryptite and (b) AIMD calculated time evolution of MSD of Li atoms averaged over all the atoms in the super cell of HT- phase of β -eucryptite at various c/a ratio at T=800 K.

FIG 2.22 The AIMD calculated time evolution of u^2 of each individual Li along the hexagonal c -axis in the supercell ($3 \times 3 \times 1$) of HT- phase of β -eucryptite at various c/a ratios at T=800 K.

FIG 2.23 The *ab-initio* DFT calculated static activation energy barrier for Li channel diffusion in HT phase of β -eucryptite at various c/a ratios. The calculations are performed by using climbing image nudged elastic band method.

FIG 2.24 The AIMD calculated time evolution of anisotropic u^2 of each individual Li in the supercell ($3 \times 3 \times 1$) of HT- phase containing one additional Li at tetrahedral void in the central channel at 800K.

FIG 2.25 The AIMD calculated time evolution of u^2 of each individual Li in the super cell ($3 \times 3 \times 1$) of HT- phase containing one Li vacancy in the central channel at 800K.

FIG 2.26 The AIMD calculated time evolution of u^2 of each individual Li in the super cell ($3 \times 3 \times 1$) of HT- phase containing one O vacancy near the centre of the cell at 800K.

FIG 3.1 The crystal structure of (a) γ -Phase, (b) β -Phase, (c) α -Phase and (d) δ -phase of LiAlO_2 . The Li and Al polyhedral units are shown in green and blue colour, respectively.

FIG 3.2 Electronic band structure of various high-pressure phases of LiAlO_2 as calculated using *ab-initio* DFT. The high-symmetry points are chosen according to the crystal symmetry [60]. EDOS stand for electronic density of states.

FIG 3.3 Calculated pressure dependent band gap in various phases of LiAlO_2 at 0 K.

FIG 3.4 Calculated internal energy (Φ), enthalpy (H) and their differences with respect to that of γ -phase, for various phases of LiAlO_2 , as a function of pressure at 0K.

FIG 3.5 The calculated phonon dispersion curves along various high-symmetry directions [60] for various phases of LiAlO_2 , using *ab-initio* lattice dynamics.

FIG 3.6 The calculated partial and total phonon density of state in various phases of LiAlO_2 using *ab-initio* lattice dynamics.

FIG 3.7 Calculated Gibbs free-energy difference for various phases of LiAlO_2 compared to the γ -phase as a function of pressure at 600 K.

FIG 3.8 Calculated pressure-temperature phase diagram of LiAlO_2 . The phase boundaries are calculated from the Gibbs free-energy differences for various phases.

FIG 3.9 Calculated pressure dependence of volume and various atomic-pair distances for the various phases of LiAlO_2 .

FIG 3.10 Calculated transition pathways, through Path-I and Path-II, for γ to β - LiAlO_2 phase transition using *ab-initio* DFT nudged elastic band method. The solid squares represent the intervening images at which calculations are performed.

FIG 3.11 Calculated phonon dispersion curves of α - LiAlO_2 for the expanded volume. The eigenvector pattern of corresponding unstable phonon modes at Γ point are given on the right. The high-symmetry points are chosen according to the crystal symmetry[60].

FIG 3.12 Calculated phonon dispersion curves of δ - LiAlO_2 for the expanded volume. The eigenvector pattern of corresponding unstable phonon modes at Γ point is given on the right. The high-symmetry points are chosen according to the crystal symmetry[60].

FIG 3.13 (a) The calculated Grüneisen parameter, and (b) the temperature-dependent experimental and calculated lattice parameters and volume $[(l-l_{300\text{ K}}/l_{300\text{ K}}), l= a, c, V]$.

FIG 3.14 The displacements pattern of the zone-centre optic mode which makes a large contribution to thermal expansion in (a) a - b plane, and (b) along c -axis.

FIG 3.15 (a) The experimentally measured phonon density of states at various temperatures obtained using inelastic neutron scattering measurements (b) Multiphonon corrected experimental(473K) and MD calculated(300K) phonon density of states.

FIG 3.16 The *ab-initio* molecular dynamics calculated partial phonon density of states for different atoms in LiAlO_2 , at various temperatures.

FIG 3.17 The *ab-initio* calculated (a-c) mean square displacements of various atoms, Li, O and Al and (d) anisotropic mean square displacement of Li in a - b plane and along c -axis at various temperatures.

FIG 3.18 (Top) The calculated jumps in terms of squared displacements of individual atoms in a - b plane and along c -axis at 2000K (Bottom) The *ab-initio* calculated trajectories of Li atoms at 2000K projected along various crystal directions.

FIG 3.19 The *ab-initio* calculated mean square displacements of Li in vacancy containing structure in a - b plane and along c -axis at 1200K and 1600K.

FIG 4.1 (a) structure of α - V_2O_5 , containing square pyramids (b) α - V_2O_5 containing pseudo octahedra (for comparison) (c) β - V_2O_5 containing two different types of VO_6 octahedra (d) δ - V_2O_5 containing VO_6 octahedra.

FIG 4.2 (a) Evolution of X-Ray diffraction pattern with temperature (b-d) Observed (circle) and calculated (line) profiles obtained after the Rietveld refinement of V_2O_5 using orthorhombic structure with space group Pmmn at 853 K, 300 K and 12 K, respectively. (e) Evolution of structural parameters with temperature.

FIG 4.3 The atomic charge density plot of α -V₂O₅, in the a - c plane, for calculations performed considering (Top) GGA, (Middle) GGA+vdW, and (Bottom) GGA+vdW+U. The charge density scale is displayed on the right. The atomic positions in the space group Pmmn are O1 at 2a(x,y,z), O2 at 4f(x,y,z), O3 at 4f(x,y,z), and V at 4f(x,y,z) Wyckoff site.

FIG 4.4 (a) Experimental and calculated (GGA+vdW+U) neutron-weighted phonon density of states in α -V₂O₅. (b) Phonon density of states calculated using various types of interactions in α -V₂O₅.

FIG 4.5 Calculated (GGA+vdW+U) partial phonon density of states of atoms at various Wyckoff sites in α -V₂O₅. The atomic positions in the space group Pmmn are O1 at 2a(x,y,z), O2 at 4f(x,y,z), O3 at 4f(x,y,z), and V at 4f(x,y,z) Wyckoff site.

FIG 4.6 (a) The calculated anisotropic Grüneisen parameters. (b) The experimental and calculated lattice parameters as a function of temperature. (c) & (d) calculated linear thermal expansion coefficient as a function of phonon mode energy and temperature.

FIG 4.7 The displacement pattern and energies (in meV) of phonon modes responsible for negative thermal expansion in the a - b plane. The values of the frequencies correspond to the GGA+vdW+U calculations. Key: V(violet), O1(red), O2(blue) and O3(green).

FIG 4.8 Calculated and experimental [70] pressure dependence of lattice parameters, bond lengths and bond angles of orthorhombic α -V₂O₅. The calculations are shown in the pressure range of stability as observed experimentally [22,70].

FIG 4.9 Calculated Gibbs free energy per atom in various phases of V₂O₅ as a function of pressure at various temperatures.

FIG 4.10 Calculated and experimental [22] pressure/temperature phase diagram of V₂O₅. The experimental data points and calculated colour region are shown.

FIG 4.11 Calculated volume per atom as a function of pressure for the α , β and δ - V_2O_5 .

The calculations are shown in experimental stability range [22,70] of various phases.

FIG 4.12 The calculated eigenvector of unstable phonon modes in (a) $Li_{0.08}V_2O_5$ and (b, c) $Li_{0.16}V_2O_5$ obtained from density functional perturbation theory approach.

FIG 4.13 The calculated trajectories of Li in (a) $Li_{0.08}V_2O_5$ and (b) $Li_{0.16}V_2O_5$ obtained from *ab-initio* MD simulations at 1000K.

FIG 5.1 Crystal structure of the ambient pressure phase of $ZnAu_2(CN)_4$. Zn atoms are at the centre of tetrahedral units (red colour). Key: N, green sphere; C, blue sphere; Au yellow sphere; Zn, red sphere.

FIG 5.2 The temperature-dependent measured spectra of the ambient pressure phase of $ZnAu_2(CN)_4$ along with the calculated neutron-weighted phonon spectrum.

FIG 5.3 The calculated neutron weighted partial and total phonon spectra compared with measured inelastic spectra at $T=300$ K, in the ambient pressure phase of $ZnAu_2(CN)_4$.

FIG 5.4 The calculated Grüneisen parameters of $ZnAu_2(CN)_4$, Γ_a and Γ_c , averaged over the entire Brillouin zone on application of anisotropic pressure along a - (HP_a) and c - axes(HP_c), respectively.

FIG 5.5 The calculated linear and volume thermal expansion as a function of temperature in the ambient pressure phase of $ZnAu_2(CN)_4$.

FIG 5.6 (a)The calculated and measured[6] fractional change in lattice parameters and volume as a function of temperature, in the ambient pressure phase of $ZnAu_2(CN)_4$, and (b) the calculated contribution of various phonons of energy E to the linear thermal expansion along the a - and c -axes at 300 K.

FIG 5.7 (a) The calculated and experimental [3] mean square displacement of various atoms in the ambient pressure phase of $ZnAu_2(CN)_4$. (b) The calculated mean square

displacement of various atoms as a function of phonon energy in the ambient pressure phase of $\text{ZnAu}_2(\text{CN})_4$ at 300K.

FIG 5.8 The calculated eigenvectors of selected phonon modes in the Brillouin zone in the ambient pressure phase of $\text{ZnAu}_2(\text{CN})_4$. The c -axis is along the chain direction, while a - and b -axes are in the horizontal plane. Zn atoms are at the centre of tetrahedral units (yellow colour). Key: C1, red sphere; C2, green sphere; N1, blue sphere; N2, cyan sphere; Au purple sphere; Zn, yellow sphere.

FIG 5.9 (a) The calculated difference in enthalpy between the ambient and high-pressure phases, as a function of pressure. (b) The calculated distortion in terms of the amplitude of eigenvector of phonon modes as a function of pressure in the ambient pressure phase of $\text{ZnAu}_2(\text{CN})_4$. The symbols represent the points at which calculations are performed.

FIG 5.10 The calculated and experimental unit cell volumes of the ambient and high-pressure phases as a function of pressure. The calculated volumes of ambient and high-pressure phases have been normalized with respect to the volume of the ambient phase volume at zero pressure.

FIG 5.11 The calculated and measured[3] change in lattice parameters with pressure in the ambient and high pressure phases of $\text{ZnAu}_2(\text{CN})_4$. The high-pressure structural unit cell is a $2 \times 2 \times 2$ supercell of the ambient pressure phase. $a_i = a_0(2a_0)$ and $c_i = c_0(2c_0)$ are for the ambient(high) pressure phase. a_0 and c_0 are the lattice constants of ambient pressure phase at 0 GPa.

FIG 6.1 The crystal structure of AgC_8N_5 containing two types of AgN_4 (Poly-1: Black, and Poly-2: Blue) tetrahedra connected through C (Red) and N (Green) atoms.

FIG 6.2 The calculated pressure dependence of lattice parameters (l), unit cell volume, bond lengths and total energy/atom for AgC_8N_5 .

FIG 6.3 The calculated displacement pattern giving rise to negative linear compressibility along *c*-axis of AgC₈N₅. The arrow represents the displacement vector for Ag as obtained from the difference in atomic coordinates of all the atoms corresponding to ambient pressure and 4 GPa structure.

FIG 6.4 The calculated pressure dependence of bond length (C-C) and bond angles (<C-C=N) of hard building block (C₈N₅) planer unit in AgC₈N₅.

FIG 6.5 The calculated total and partial phonon density of states for various atoms of AgC₈N₅.

FIG 6.6 (a) The calculated energy dependence of anisotropic Grüneisen parameters Γ for AgC₈N₅. (b) The contribution of phonon mode of energy *E* to the linear thermal expansion coefficients. (c, e) The calculated temperature dependence of linear and volume thermal expansion coefficients respectively (d, f) The calculated temperature dependence of lattice parameters and unit cell volume respectively.

FIG 6.7 The calculated total and anisotropic mean square displacements for various atoms as a function of temperature for AgC₈N₅.

FIG 6.8 The calculated anisotropic and total mean square displacements for various atoms as a function of phonon energy for AgC₈N₅.

FIG 6.9 The displacement pattern of optic phonon modes projected in *a-b* plane of AgC₈N₅. The arrow represents the displacement vector for Ag atoms. The displacement vectors for C and N atoms are negligible and are not shown for clarity.

FIG 7.1 Calculated phonon dispersion relation of MZrF₆ (M=Ca, Mg and Sr). The high symmetry points in the cubic Brillouin zone are defined as $\Gamma(0\ 0\ 0)$, $X(1\ 0\ 0)$, $L(1/2\ 1/2\ 1/2)$, $W(1/2\ 1\ 0)$.

FIG 7.2 Calculated partial phonon density of states of various atoms and the total phonon density of states in MZrF₆ (M=Ca, Mg and Sr).

FIG 7.3 Calculated Grüneisen parameter as a function of phonon energy (E) of MZrF₆ (M=Ca, Mg and Sr); (a) plotted for individual phonons, and (b) averaged for all phonons around energy E in the entire Brillouin zone.

FIG 7.4 The calculated and experimental volume thermal expansion coefficient in the cubic phase of MZrF₆ (M=Ca, Mg and Sr) as a function of temperature. The cubic phase of MgZrF₆ is known to be stable only above ~100 K [22]. The open circles[22], solid circles[23] and solid squares[18] correspond to experimental data, respectively.

FIG 7.5 The contribution to the calculated volume thermal expansion coefficient of MZrF₆ (M=Ca, Mg and Sr) from phonons of energy E averaged over the BZ at 300K.

FIG 7.6 The calculated (solid line) and experimental (symbols) [18,22,23] fractional change in volume with respect to the volume at 300 K in the cubic phase of MZrF₆ (M=Ca, Mg and Sr) as a function of temperature. The cubic phase of MgZrF₆ is known to be stable only above ~100 K [22]. The open circles, solid circles and solid squares correspond to experimental data from Refs[22], [23] and [18] respectively.

FIG 7.7 (a) The calculated mean squared displacement of various atoms in MZrF₆ (M=Ca, Mg and Sr) as a function of temperature (b) The calculated anisotropic mean squared displacement of fluorine atoms, along (u_{\parallel}^2) and perpendicular (u_{\perp}^2) to the Zr-F bond, in MZrF₆ (M=Ca, Mg and Sr) compounds as a function of temperature.

FIG 7.8 The displacement pattern of typical phonon modes having large negative Grüneisen parameter at $\Gamma(0\ 0\ 0)$ and $X(1\ 0\ 0)$ points in the Brillouin zone. The energy of the $\Gamma(0\ 0\ 0)$ point mode is 3.6, 3.87 and 3.31 meV and that of the X point mode is 3.66, 3.95 and 3.51 meV for CaZrF₆, MgZrF₆ and SrZrF₆ respectively. The orange and green octahedral units correspond to MF₆ and ZrF₆ respectively.

FIG 7.9 The calculated potential energy profile (black lines) of specific phonon modes at $\Gamma(0\ 0\ 0)$ and $X(1\ 0\ 0)$ points in the BZ. The red line shows the harmonic profile of respective phonon modes. The corresponding phonon energy of each mode is also given.

FIG 7.10 The low energy part of experimental phonon spectra, in the *Ih* phase of H₂O and D₂O ice, as a function of temperature. The calculated neutron weighted phonon spectra as well as partial phonon contributions of H/D and O atoms are also shown. The inelastic neutron scattering measurements are performed by Dr. M. K. Gupta using the MERLIN spectrometer at ISIS Facility, Rutherford Appleton Laboratory, UK.

FIG 7.11 The calculated total and partial phonon density of states in the *Ih* phase of H₂O and D₂O ice.

FIG 7.12 The calculated anisotropic Grüneisen parameters in the *Ih* phase of H₂O and D₂O ice.

FIG 7.13 The calculated linear and volume thermal expansion coefficients the *Ih* phase of H₂O and D₂O ice.

FIG 7.14 The calculated and measured [45] lattice parameter change (l/l_{10} ; $l = a, c$) of ice with temperature. Inset in the left panel shows the calculated volume thermal expansion coefficient (α_v) of H₂O and D₂O ice up to 60K.

Fig 7.15 The calculated mean square displacement as a function of phonon energy averaged over Brillouin zone.

FIG 7.16 The atomic displacement pattern of selected phonon modes of H₂O/D₂O in *Ih* phase of ice. The number below the figure gives the phonon energies, Γ_a , Γ_c and Γ_v respectively. Key- H/D: Green and O: Red.

LIST OF TABLES

TABLE 1.1 Various physical variable (left) and corresponding physical properties obtained from derivatives of total energy with respect to these physical variables.

TABLE 2.1 The partial ionic charges and potential parameters[42] used in MD simulations. The charge q_i for Li, Al, Si and O are 1.0, 1.4, 2.4 and -1.2, respectively.

TABLE 2.2 The experimentally refined and calculated structure of β -eucryptite. The atomic positions in the space group $P6_422$ are Li1 at $3b(x,y,z)$, Li2 at $3c(x,y,z)$, Li3 at $6f(x,y,z)$, and O1, O2, O3 and O4 at $12k(x,y,z)$, and Al1 at $6h(x,y,z)$, Al2 at $6j(x,y,z)$, and Si1 at $6g(x,y,z)$ and Si2 at $6i(x,y,z)$ Wyckoff site.

TABLE 2.3 Calculated and experimental elastic constants in GPa units in β -eucryptite.

TABLE 2.4 The calculated elastic compliance matrix components (s_{ij}) in GPa^{-1} units for β -eucryptite.

TABLE 2.5 The calculated activation energy for Li channel diffusion in different crystal directions, from *ab-initio* DFT using climbing image nudged elastic band method.

TABLE 2.6 Comparison of enthalpy (H) per formula unit (f. u.) and lattice parameters (a & c) for some of the possible structural configurations with different distribution of Li atoms in the hexagonal channels of β -eucryptite. N_A and N_S represent the number of A and S type Li channels respectively in single unit cell containing 84 atoms. These structures are relaxed for all the degree of freedoms under the framework of DFT. ΔH represents the difference in enthalpy (meV/atom) with respect to that of the RT-phase.

TABLE 3.1 Crystal structure for various phases of LiAlO_2 as calculated at zero pressure and temperature. The calculated parameters are comparable with experiments[27].

TABLE 3.2 The calculated non-zero components of elastic compliance (GPa^{-1}) matrix for the γ -phase at ambient pressure.

TABLE 4.1 Calculated (0K) and experimental (12K) lattice parameters and bond lengths (VO₅ Polyhedra) of α -V₂O₅. The c-axis is perpendicular to layers of VO₅ square pyramids. V-O2 (pseudo octahedral bond) represents the bond length of V in the one layer and oxygen in the next layer.

TABLE 4.2 Calculated Born effective charges for atoms present at various Wyckoff sites in α -V₂O₅. $Z_{i,XX}$, $Z_{i,YY}$ and $Z_{i,ZZ}$ are the diagonal components of Born charge tensor.

TABLE 4.3 Calculated and experimental frequencies of zone centre phonon modes in α -phase of V₂O₅. The calculations in the present study are performed using the optimized minimum energy structures while the previous calculations [32-34] were performed at experimental fixed volumes.

TABLE 4.4 Calculated and experimental thermal expansion coefficients of α -V₂O₅.

TABLE 4.5 Experimental and calculated octahedral distortions in terms of bond length. For comparison, α -V₂O₅ is also considered to be made up of VO₆ octahedra instead of VO₅ square pyramids. The experimental parameters[22] are obtained at room temperature and ambient pressure while calculations are at 0K and 0 GPa.

TABLE 5.1 The calculated and measured[3] structure and elastic properties of the ambient pressure phase of ZnAu₂(CN)₄.

TABLE 5.2 The calculated elastic properties of the ambient pressure phase of ZnAu₂(CN)₄ as a function of pressure.

TABLE 5.3 The calculated and experimental [3] structure of high pressure phase of ZnAu₂(CN)₄. For easy comparison, the ambient phase structure in a 2×2×2 supercell is presented. The distortion vector (i.e. difference between ambient and high-pressure phases) at 4 GPa is also presented.

TABLE 5.4 A linear combination of the distortions corresponding to the Γ_1 , L_2 and M_1 points in the Brillouin zone with appropriate weight factors is used to generate the observed distortion vector at 4 GPa as given in Table 5.3.

TABLE 5.5 The calculated elastic constants in the ambient pressure phase of $\text{ZnAu}_2(\text{CN})_4$ as a function of pressure

TABLE 5.6 The calculated Born stability criteria in the ambient pressure phase of $\text{ZnAu}_2(\text{CN})_4$ as a function of pressure. For an elastically stable hexagonal crystal all the four Born criteria (elastic constants equations) must be positive.

TABLE 6.1 The experimental unit cell volume per atom, density and linear thermal expansion coefficients (α_l) at 300 K of metal cyanides from literature. The values of α_l ($l=a, b, c$) for AgC_8N_5 are obtained from our ab-initio calculations.

TABLE 6.2 The comparison of calculated and experimental lattice parameters in AgC_8N_5 .

TABLE 7.1 The comparison of calculated lattice parameter and bulk modulus of MZrF_6 ($M=\text{Ca, Mg and Sr}$) with previously reported [18,22] experimental and calculated values.

TABLE 7.2 The calculated anharmonicity parameters in the potential of certain phonon modes. The values of the parameters ‘ $a_{4,j}$ ’ are extracted from fitting of $V(\theta_j) = a_{0,j} + a_{2,j}\theta_j^2 + a_{3,j}\theta_j^3 + a_{4,j}\theta_j^4$ to the potential energy profile of the mode with fixed value of ‘ $a_{2,j}$ ’ as determined from the harmonic phonon energies. The calculated Grüneisen parameter $\Gamma(E)$ of the respective mode is also given.

TABLE 7.3 The calculated anisotropic Grüneisen parameter of a few phonons having large Grüneisen parameters in the BZ of an ordered analogue (space group $\text{P6}_3\text{cm}$) of ice I_h . E and Γ are the energy and Grüneisen parameter respectively. The wave-vectors are $\Gamma(0\ 0\ 0)$, $A(0\ 0\ 0.5)$, $K(.33\ 0.33\ 0)$, $H(.33\ 0.33\ 0.5)$, $M(0.5\ 0.5\ 0)$ and $L(0.5\ 0.5\ 0.5)$.

TABLE 7.4 The calculated elastic properties of the *Ih* phase of H₂O ice as a function of pressure.

TABLE 7.5 The calculated and experimental[79] elastic constants of H₂O ice *Ih* in kbar units. The calculations are performed in ordered analogue of H₂O ice *Ih*.

TABLE 7.6 The calculated Born stability criteria in the *Ih* phase of H₂O ice as a function of pressure. For elastically stable hexagonal crystal all three Born criteria (elastic constants equations) must be positive.

LIST OF ABBREVIATIONS

AIMD	Ab-initio Molecular Dynamics
BO	Born-Oppenheimer
BOMD	Born-Oppenheimer Molecular Dynamics
BZ	Brillouin Zone
DFPT	Density functional perturbation theory
DFT	Density functional theory
1,2,3-D	One, Two, Three-Dimensional
GGA	Generalized Gradient Approximation
HF	Hellman-Feynman
HK	Hohenberg–Kohn
HO	Harmonic oscillator
HT	High temperature
HP	High Pressure
ILL	Institut Laue Langevin
INS	Inelastic neutron scattering
IR	Infrared spectroscopy
IXS	Inelastic X-ray scattering
KS	Kohn–Sham
LA	Longitudinal acoustic
LD	Lattice Dynamics
LDA	Local–density approximation
LO-TO	Longitudinal optic and transverse optic
LT	Low temperature

MD	Molecular Dynamics
MEP	Minimum Energy Path
MOF	Metal Organic Framework
MSD	Mean-squared Displacements
NEB	Nudged Elastic Band
NTE	Negative thermal expansion
NLC	Negative Linear Compressibility
PAW	Projector-Augmented wave method
PBE	Perdew Burke Ernzerhof
PES	Potential Energy Surface
TA	Transverse acoustic
TOF	Time of Flight
TST	Transition State Theory
VASP	Vienna Ab-initio Simulation Package
vdW	Van der Waal

CHAPTER 1

Materials, Physical Properties and Techniques

“Everything in life is vibration”-Albert Einstein

1.1 Introduction

All material objects in this universe are made up of atoms and these atoms are in a state of continuous vibrations. The amplitude of these vibrations is governed by the temperature of the surroundings. In case of solids, especially the crystalline solids, the vibrations of atomic species form a collective pattern. The quanta of the collective vibrations are called phonons which are fingerprint for characterization of crystalline solids and give rise to propagation of sound waves, elastic properties, lattice specific heat, thermal expansion, thermal conductivity, and many more properties of the materials[1,2]. The application of pressure or temperature on a material affects the phonons and may be responsible for interesting thermodynamic behaviour and phase transitions in the solids[2,3]. The consideration of vibrational entropy of a system enables one to accurately calculate the free energy of the system[4,5] which is very important to calculate the phase stability and temperature-pressure phase diagram of crystalline solids. The research work presented in this thesis aims at studying the role of phonons (lattice vibrations) in giving rise to various thermodynamic and transport properties like thermal expansion, compressibility, ionic diffusion and phase transitions in crystalline solids. The understanding of the atomic level mechanisms [3,5-7] responsible for above functionalities of the materials is important to improve their performance in order to use them in various applications.

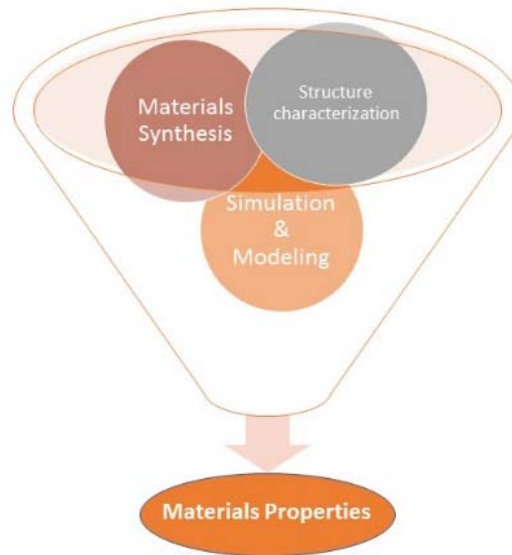


FIG 1.1 *The interconnection between various fields of material research.*

The research in material science involves synthesizing, simulating, studying the structure of materials and relating them to their properties (Fig 1.1). The study of structure-property correlation enables the material scientists to determine the relative performance of materials in a given application[8]. The structure of a material arises from the constituting chemical elements and the way in which they have been arranged. The diffraction experiments provide the structure, and dynamics can be obtained from various spectroscopic studies of crystalline solids. The designing of experiment for a particular purpose is not always simple and cheap, even sometimes not accessible. So, some alternative sources for characteristic studies of material properties are required.

The increase in computing power enabled materials scientists to simulate the behaviour of materials, discovering formerly unknown properties, as well as to design new materials [9,10]. The advancement in computational methods could drastically reduce the time-consuming trial and error processes to tailor material's properties. This involves simulating materials[11,12] at all length scales, using methods such as density functional theory (DFT), molecular dynamics (MD), Monte Carlo simulations and many other tools.

In the current research work, the structural and dynamical properties of crystalline solids are studied by a variety of experimental techniques. Theoretical models and computer simulations are used along with experiments to provide the microscopic mechanisms of thermo-dynamical and transport properties of functionally important materials. The following sections describe the materials and physical properties studied in the thesis along with various techniques used to perform these studies.

1.2 Materials of Interest

The research work presented in this thesis deals with study of framework compounds basically belonging to two categories. These are (i) Materials for Li ion battery applications and (ii) Materials with low density framework structures. Both types of materials are of current research interest in the field of material science [13-16]. The current state of art, functional properties and motivation for studying these classes of materials are discussed below.

1.2.1 Battery Materials

The efficient storage of energy to fulfil the increasing energy demands accompanied along the controlled pollution has become the necessity of today's world. Batteries are most eligible devices for this purpose [13,15,17]. A variety of batteries are available but Li-ion battery overtakes in terms of price-per-cycle and energy density[18]. Although, today's battery fulfils most of the portable applications[19], a suitable battery for electric vehicle is not yet made. The batteries are being optimized [17,20-22] for long runtime, long service life, small size, low cost, high load capability and improved reliability since its invention by Alessandro Volta in 1800. There are relatively a few gains

that can be made to the battery besides directly improving component materials[18,23]. The stability, safety and performance of these materials can be controlled by controlling their thermal expansion and elastic properties, enhancing ionic diffusion inside the solid material and avoiding the phase transitions in operational temperature and pressure range of battery [19,20,23,24]. For example, the efficient electrode for battery[23-25] should not undergo large changes in the structure during the battery operation (intercalation/deintercalation of ions) or accidental high pressure/temperature conditions. To design or investigate a battery material with above mentioned properties, there is a need for the materials with near zero thermal expansion, nil compressibility, sufficient ionic diffusion and large stability region in the phase diagram. For this purpose, the mechanism governing these properties needs to be understood in a better way.

Typically, a Li-ion battery is made up of two electrodes in which an electrolyte is sandwiched. The negative electrode [12,18,26] also called anode is generally made up of carbon (Graphite) and lithium alloyed (e.g. $\text{Li}_4\text{Ti}_5\text{O}_{12}$) materials. The cathode in the battery highly characterizes the capacity and power delivery of the battery [18,23-25] . Originally, the primary active component of the cathode was cobalt. Today, cobalt is frequently being partially substituted with nickel [7,13,27]. Cathode materials require extremely high purity levels and must be almost entirely free of unwanted metal impurities- notably iron, vanadium and sulphur. The major problem with current cathode materials is that they contain cobalt in sufficient amount and hence limited by toxicity, high cost, low thermal stability, and fast capacity fade at high current rates[13,27]. Therefore, material scientists are discovering for cobalt free alternate cathode material. In this category, physical properties of two potential cathode materials LiAlO_2 (Chapter 3) and V_2O_5 (Chapter 4) has been studied in the present thesis. The cathode and anode of a battery communicate through the intertwining electrolyte material. In Li-ion battery,

generally a liquid, gel or dry polymer electrolyte is used [18,28]. Liquid electrolyte is made up of a solution of lithium salts with organic solvents like ethylene carbonate and is highly flammable. With the aging of the battery, the drying of the electrolyte happens; which further reduce the performance of the battery[17,29,30]. Moreover, there is a limit on the power storage of liquid or polymer electrolyte-based battery which limits its use for electric vehicle applications.

A very good alternative to the major problems of liquid or gel electrolytes is the replacement by a solid electrolyte with very large ionic conductivity[20,31]. The solid electrolytes have ionic conductivity of the order of 0.0001 to $0.1 \text{ Ohm}^{-1} \text{ cm}^{-1}$ at 300 K and, are called superionic conductors. The activation energy barrier of about 0.1 eV exists for ionic diffusion in these materials. The solid electrolyte[32], being more stable[15,21,28,33] than liquids, could resolve the issue of leakage, chemical stability, vaporization, flammability and dendrites formation to a great extent. It will also enable the use of metallic Li as anode material[21,29] and will enhance the current charge capacities. The batteries which use a solid electrolyte are called all solid-state batteries. The solid state batteries [15,17,21,28,33] offer a most compact and safe version to store energy at various scales.

However, solid electrolytes possess a higher activation energy[15,28] for ionic diffusion through their body and hence offer smaller ionic conductivity values in comparison to liquid and salt-polymer based electrolytes[34]. Inflation in the magnitude of Li ionic conductivity in solid electrolytes[13,15,28,30] at room temperature is essential for engineering highly efficient[35] solid state batteries for electric vehicles applications. An enormous amount of research is underway to investigate and engineer a best suitable solid electrolyte for this purpose. Sulphides and oxides are the main classes[31,33,36-38] of materials possessing a liquid-like Li ionic conduction. Oxide electrolytes[32] possess

slightly lower ionic conductivity as compared to sulphides, but they can be used in high voltage batteries due to their wide range of stability in comparison to that of sulphides. Based on the topology and geometry[39-41], solid electrolytes have isotropic (3-D), planar (2-D) and channel-like (1-D) Li diffusion pathways. The present thesis work approach to deal with the study of various thermo-dynamical and diffusional properties of a 1-D superionic conductor, LiAlSiO_4 , which is a potential solid electrolyte (Chapter 2) for Li-ion battery.

1.2.2 Low Density Framework Structures

The framework solids exhibiting open structures have many potential applications in the field of catalysis, sensors and actuators[16]. Following the aluminosilicate zeolites, many other inorganic silicates, germanates, phosphates, sulphates, borates and selenites are discovered to exhibit open framework structures[42]. They are found to occur in variety of 1-D, 2-D and 3-D geometries. The presence of open space in these materials gives rise to low crystal density and sometimes give rise to interesting temperature and pressure dependent lattice behaviour[3,43-45]. By intuition, material should contract (or expand) on application of hydrostatic pressure (or temperature), yet a small number of crystals show opposite behaviour in a few directions. This type of anomalous behaviour with pressure (or temperature) is called negative linear compressibility (or negative thermal expansion) behaviour[14]. This property of negative linear compressibility (NLC) and negative thermal expansion (NTE) is observed in a few open inorganic framework structures[14].

Most of these polyhedral structures are connected through their vertices. The introduction of other anions between the polyhedral units increases the flexibility of

structures through hinge like movements. This type of structural flexibility has been identified in some metal organic framework structures (MOF) [14,16,46]. A unique combination of polyhedral units of metal ions coupled to organic linkages give rise to MOF compounds which exhibits interesting lattice behaviour[46-48]. The flexibility, porous nature and anisotropic bonding give rise to interesting mechanism of NLC, NTE as well as phase transitions in MOF's when exposed to the varying temperature-pressure environments. Different mechanisms responsible for NTE behaviour in metal inorganic and metal organic framework structures give rise to difference in magnitude of thermal expansion coefficients in these compounds[43,45,47,49]. MOF show very large NTE coefficient and large compressibilities due to their highly anisotropic and flexible structures. The MOF's exhibiting NLC along particular crystal direction; show NTE along the same direction with similar mechanism[14,47].

The above mentioned anomalous lattice behaviours are governed by arrangements and dynamics of atoms and molecules in the crystal lattice. The theoretical tools facilitate to investigate the underlying mechanisms responsible for anomalous lattice behaviour. The lattice dynamics (LD) calculations provide the phonon modes in the crystal which provide various possible directions for atomic movements[3,5]. The softening of phonon modes changes the entropy and free energy of crystal. The final configurations of compounds are related to the eigenvectors of the soft modes.

In this thesis, both inorganic and organic low-density framework compounds are studied to investigate the mechanism responsible for NTE, NLC and high-pressure phase transition. The studies primarily aim to correlate the anomalous lattice behavior with low energy phonons, nature of bonding, open structure, elastic constants and compressibilities. The materials include terminally connected polyhedral network structures like $MZrF_6$ ($M=Mg, Ca, Sr$) and Ice *Ih*. The second class of compounds are metal cyanides

frameworks such as $\text{ZnAu}_2(\text{CN})_4$ and AgC_8N_5 . Metal cyanides belong to MOF category and exhibits anisotropy due to strong $-\text{C}\equiv\text{N}$ and comparatively weak metal and carbon/nitrogen bonds.

1.3 Experimental Techniques

X-ray diffraction and inelastic neutron scattering (INS) techniques are used in the present work to study structural and dynamical properties of above mentioned framework compounds, respectively. The details of these techniques along with data analysis procedure are given in detail below.

1.3.1 X-ray Diffraction

X-ray diffraction is a powerful characterization technique used in the analysis of crystalline solids. When Bragg's law ($n\lambda = 2d \sin\theta$) is satisfied, diffraction is observed through the constructive interference of diffracted radiations by the electron clouds of atoms. The resultant pattern is obtained as intensity versus 2θ . This pattern gives the complete information of lattice spacing and the size of the crystal lattice. The intensities of the pattern determine the position of the atoms in the lattice. The thermal motion of the atoms as well as the resolution of instrument may produce broadening in the diffraction peaks. The single crystal as well as powder samples can be studied using X-ray diffraction. The further details of X-ray diffraction technique can be found elsewhere[50].

In the present case, the X-ray diffraction studies are carried out using 18KW rotating Cu anode-based powder diffractometer operating in the Bragg-Brentano focusing geometry with a curved crystal monochromator. For the high temperature X-ray diffraction experiments, the sample was placed on a flat platinum sample holder and

heated in a dynamically evacuated furnace. The temperature was measured using Pt-Rh thermocouples. At each temperature, the crystal structures were analysed using the Rietveld refinement program FULLPROF[51]. A Thompson-Cox-Hastings pseudo-Voigt with axial divergence asymmetry function was used to model the peak profiles. The background was fitted using a sixth order polynomial. Except for the occupancy parameters of the atoms, which were fixed corresponding to the nominal composition, all other parameters, i.e., scale factor, zero displacement and structural parameters were refined. X-ray diffraction is used to obtain the thermal expansion behaviour of V₂O₅ from 12K to 873K (Chapter 3).

1.3.2 Inelastic Neutron Scattering

The lattice vibrations can be experimentally investigated using techniques such as Raman spectroscopy, infrared absorption, inelastic X-ray and inelastic neutron scattering. Unlike Raman and infrared experiments, which probe only the long wavelength excitations in one-phonon scattering, inelastic neutron and inelastic X-ray scattering can directly probe the phonons in the entire Brillouin zone. The inelastic neutron scattering is used in the present work to measure the phonon spectra of solids.

Thermal neutrons have typical energy of about 1-500 meV and wavelength around 0.04 to 1nm. While scattering from a sample, thermal neutrons can exchange a part of their energy and momentum with an excitation in the system. During the process, the sum of energy and momentum of the neutron and system will remain conserved. This can be expressed mathematically by using following equations[52,53]:

$$E_i - E_f = \pm \hbar \omega(\mathbf{q}, j) \quad (1.1)$$

$$\hbar(\mathbf{k}_i - \mathbf{k}_f) = \hbar \mathbf{Q} = \hbar(\mathbf{G} \pm \mathbf{q}) \quad (1.2)$$

Where, \mathbf{k}_i , \mathbf{k}_f , are incident and the scattered neutron wavevectors and \mathbf{Q} is the wavevector transfer (scattering vector) associated with the scattering process. \mathbf{q} is the wavevector of the excitation with energy $\hbar\omega$ and \mathbf{G} is a reciprocal lattice vector of the system under study. E_i and E_f are the incident and scattered neutron energies and $\hbar\omega$ is the energy transfer to the system in the scattering process. The \pm sign indicates that the excitation is annihilated (created) in the scattering process.

In the scattering process, the inelastic scattering cross-section of the process is measured and this is directly proportional to the dynamical structure factor $S(\mathbf{Q}, \omega)$ (characteristic of the system), which is the double Fourier transform of the space-time correlation function of the constituents of the system. Peaks in $S(\mathbf{Q}, \omega)$ correspond to these elementary excitations[52,54,55]. The measurements on single crystals give information about the \mathbf{q} dependence of phonon (phonon dispersion relation), while polycrystalline samples provide frequency distribution of the phonons (phonon density of states $g(\omega)$). In order to obtain a complete picture of the dynamics, it is useful to determine the phonon density of states.

The coherent inelastic neutron scattering data from a sample are usually analysed in the incoherent approximation. In this approximation, one neglects the correlations between the motions of atoms and treats the scattering from each atom as incoherent with the scattering amplitude b_k^{coh} . However, this is valid only for large \mathbf{Q} . In practice, the data are averaged over a large range of \mathbf{Q} values. The data include scattering from both the one-phonon and multi-phonon processes; however, corrections can be made for the multi-phonon scattering. In the incoherent approximation, the expression[2,52,55-57] for coherent one-phonon scattering ($S_{\text{coh}}^{(1)}(\mathbf{Q}, \omega)$) from a powder sample is given by

$$S_{\text{coh}}^{(1)}(\mathbf{Q}, \omega) = A \sum_{\mathbf{qj}} \frac{\hbar}{2\omega(\mathbf{qj})} \left\{ n(\omega) + \frac{1}{2} \pm \frac{1}{2} \right\} |F_j^{(1)}(\mathbf{Q})|^2 \delta(\mathbf{Q} - \mathbf{G} \pm \mathbf{q}) \delta(\omega \mp \omega(\mathbf{qj})) \quad (1.3)$$

$$\text{Where, } F_j^{(1)}(\mathbf{Q}) = \sum_k b_k^{\text{coh}} \frac{\mathbf{Q} \cdot \xi(\pm \mathbf{qj}, k)}{\sqrt{m_k}} \exp\{-W_k(\mathbf{Q})\} \exp(i\mathbf{G} \cdot \mathbf{r}(k)) \quad (1.4)$$

Where, A' is the normalization constant, b_k and m_k are neutron scattering length and mass of the k^{th} atom, respectively. ξ is eigenvector of excitation, $\exp(-2W_k(\mathbf{Q}))$ is the Debye-Waller factor. $\hbar \mathbf{Q}$ and $\hbar \omega$ are the momentum and energy transfer on scattering of the neutron, respectively, while $n(\omega)$ is the phonon population factor.

Incoherent inelastic scattering also contributes to the scattering from a powder sample in almost the same way as coherent scattering in the incoherent approximation. Thus, the so-called neutron-weighted density of states involves weighting by the total scattering cross-section of the constituent atoms. The measured scattering function [2,52,55-57] in the incoherent approximation is therefore given by

$$S_{\text{inc}}^{(1)}(\mathbf{Q}, \omega) = \sum_k \frac{b_k^2}{\langle b^2 \rangle} e^{-2W_k(\mathbf{Q})} \frac{Q^2}{2m_k} \frac{g_k(\omega)}{\hbar\omega} \left(n(\omega) + \frac{1}{2} \pm \frac{1}{2} \right) \quad (1.5)$$

Where, the partial density of states $g_k(\omega)$ is given by

$$g_k(\omega) = \int \sum_j |\xi(\mathbf{qj}, k)|^2 \delta(\omega - \omega_j(\mathbf{q})) d\mathbf{q} \quad (1.6)$$

Thus, the scattered neutrons provide the information of the density of one-phonon states weighted by the scattering lengths and the population factor. The observed neutron-weighted phonon density of states is a sum of the partial components of the density of states due to the various atoms, weighted by their scattering length squares.

$$g^n(\omega) = B' \sum_k \left\{ \frac{4\pi b_k^2}{m_k} \right\} g_k(\omega) \quad (1.7)$$

Where, B' is normalization constant. By comparing the experimental phonon spectra with the calculated neutron-weighted density of states obtained from a lattice-dynamical

model, the dynamical contribution to frequency distribution from various atomic and molecular species can be understood. As the inelastic neutron scattering spectrum from a powder sample also contains a contribution from multiphonon scattering and we are interested to measure only the one-phonon spectrum; the multiphonon component has to be estimated and subtracted from the measured spectrum. This correction is done by using Sjolander's formalism[58].

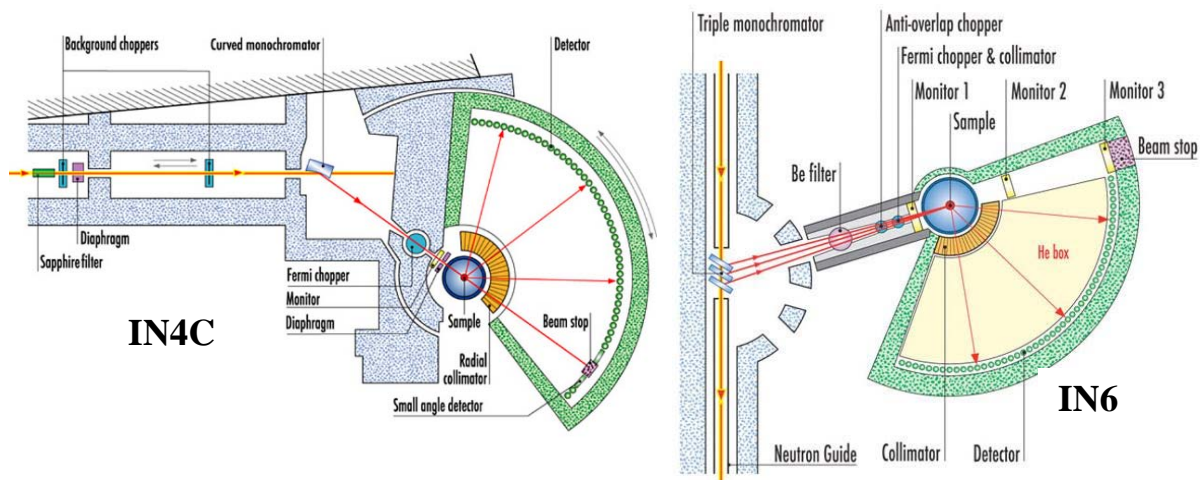


FIG 1.2 Schematic diagrams of the IN4C and IN6 time of flight neutron spectrometer at ILL, Grenoble, France (after www.ill.fr).

A number of different techniques [52,54-56,59] have been developed at steady and pulsed neutron sources to obtain the vibrational spectra of compounds. For the polycrystalline samples, the neutron time-of-flight technique (TOF) is rather convenient for the measurements. A typical time-of-flight spectrometer, namely, IN6 and IN4C at the Institut Laue Langevin (ILL), Grenoble, France are shown in Fig 1.2. The IN4C spectrometer uses thermal neutrons in energy range 10-100 meV while IN6 spectrometer works with cold neutrons in wavelength range of 4 to 6 Å. Similar spectrometers are available at many of the reactors and also at the spallation neutron sources at ISIS, Oak

Ridge, JPARC, etc. The energy of the neutrons is fixed either before or after the scattering process. The change in energy and the scattering vector \mathbf{Q} is obtained by measuring the flight time and the scattering angle of the neutrons from a beam pulsing device (chopper) to the detectors. For measurement of phonon density of states, the scattered neutrons from the sample are collected over a wide range of scattering angles, typically from 10° to 110° . By choosing a suitable incident neutron energy, measurement of the scattering function $S(\mathbf{Q}, \omega)$ over a wide range of momentum and energy transfers can be undertaken and the data can be averaged over a wide range of \mathbf{Q} . In the present thesis, the phonon density of state measurements for LiAlSiO_4 (Chapter 2), LiAlO_2 (Chapter 3), V_2O_5 (Chapter 4) and $\text{ZnAu}_2(\text{CN})_4$ (Chapter 5) are carried out using IN4C and IN6 time of flight neutron spectrometers at ILL, Grenoble, France

1.4 Theoretical Methods

The theoretical modelling of a phenomenon is based on empirical observations and some form of axioms to establish one or more relationships between various measurable quantities. The quality of a physical theory is judged on its ability to make new predictions which can be verified by new observations. Unfortunately, it is often the case that solving the mathematical model for a particular system in order to produce a useful prediction is not feasible. This can occur, for instance, when the solution does not have a closed form expression, or is too complicated. In such cases, numerical approximations are required. The study and implementation of numerical analysis to solve a particular problem, for which a quantitative theory already exists, give rise to a different branch which started with the upbringing of modern computers. Presently, these computational tools are very much advanced and can easily be implemented for pre-

experimental simulations and they can even replace some otherwise experiments[7,10,11,60].

The mechanism responsible for various transport and thermo-dynamical properties like ionic diffusion, elastic constant, compressibility, specific heat, thermal expansion and various phase transitions require analysis and interpretation of the measured data. The character and energy of atomic dynamics in solid as well as the individual atomic contribution to the overall spectra and other thermo-dynamical properties are difficult to obtain from the experimental measurements. Theory is well-established to understand the measured spectra and their atomic origin. The following theoretical techniques are applied in the present work.

1.4.1 Lattice Dynamics

The study of vibrations of the atoms in a crystal is called lattice dynamics. The frequency of these vibrations is related to the binding of atoms with their surrounding atoms as well as on atomic masses. Lattice dynamics gives us properties such as propagation of sound waves in crystals, the interaction of materials with light, thermodynamics, phase transitions, thermal conductivity, and thermal expansion.

The theory of lattice dynamics can be explained best by the Born and Karman formalism[61,62] which assumes the atoms as point masses, with no internal structure and attempts to analyse the dynamics of atoms, given the concept of the crystal potential function which describes the binding of atoms. It is essential to consider the Born Oppenheimer or adiabatic approximation. This approximation is backbone of lattice dynamics which assume that the electronic wave functions change adiabatically during the nuclear motion. The electrons essentially contribute an additional effective potential

for the nuclear motions and the lattice vibrations are associated only with nuclear motions. In this Chapter, a summary of the mathematical formalism for a perfect crystal is described. A complete account of the formal theory of lattice dynamics can be found in literature [2,59,61]. For small displacements of the atoms, $\mathbf{u} \begin{pmatrix} 1 \\ \mathbf{k} \end{pmatrix}$ about their equilibrium positions, $\mathbf{r} \begin{pmatrix} 1 \\ \mathbf{k} \end{pmatrix}$ (where, l denotes the l^{th} unit cell ($l = 1, 2, \dots, N$) and \mathbf{k} is the \mathbf{k}^{th} type of atom ($\mathbf{k}=1,2,\dots,n$) within the unit cell), the equation of motion of the $(lk)^{\text{th}}$ atom is

$$m_k \ddot{u}_\alpha \begin{pmatrix} 1 \\ \mathbf{k} \end{pmatrix} = - \sum_{l'k'\beta} \phi_{\alpha\beta} \begin{pmatrix} 1 & 1' \\ \mathbf{k} & \mathbf{k}' \end{pmatrix} \mathbf{u}_\beta \begin{pmatrix} 1' \\ \mathbf{k}' \end{pmatrix} \quad (1.8)$$

From eq. (1.8) it is clear that $\phi_{\alpha\beta} \begin{pmatrix} 1 & 1' \\ \mathbf{k} & \mathbf{k}' \end{pmatrix}$ is the negative of the force exerted on atom (lk) in the α direction due to unit displacement of the atom $(l'k')$ in the β direction. The quantity $-\phi_{\alpha\beta}$ is referred to as the force constant.

The equations of motion (eq. (1.8)) for periodic system can be solved by assuming wave like solutions of the type

$$\mathbf{u}_\alpha \begin{pmatrix} 1 \\ \mathbf{k} \end{pmatrix} = U_\alpha(\mathbf{k} | \mathbf{q}) \exp\{i(\mathbf{q} \cdot \mathbf{r} \begin{pmatrix} 1 \\ \mathbf{k} \end{pmatrix} - \omega(\mathbf{q})t\} \quad (1.9)$$

Here, \mathbf{q} is the wavevector and $\omega(\mathbf{q})$, the angular frequency associated with the wave.

Substituting (1.9) in (1.8)

$$m_k \omega^2(\mathbf{q}) U_\alpha(\mathbf{k} | \mathbf{q}) = \sum_{k'\beta} D_{\alpha\beta} \begin{pmatrix} \mathbf{q} \\ \mathbf{k}\mathbf{k}' \end{pmatrix} U_\beta(\mathbf{k}' | \mathbf{q}) \quad (1.10)$$

Where, m_k is the mass and $\mathbf{r} \begin{pmatrix} 1 \\ \mathbf{k} \end{pmatrix}$ the position coordinate of the \mathbf{k}^{th} atom.

Here, the dynamical matrix $D_{\alpha\beta} \left(\begin{smallmatrix} \mathbf{q} \\ \mathbf{k} \mathbf{k}' \end{smallmatrix} \right)$ is given by

$$D_{\alpha\beta} \left(\begin{smallmatrix} \mathbf{q} \\ \mathbf{k} \mathbf{k}' \end{smallmatrix} \right) = \sum_{l'} \phi_{\alpha\beta} \left(\begin{smallmatrix} l & l' \\ \mathbf{k} & \mathbf{k}' \end{smallmatrix} \right) \exp\{i(\mathbf{q} \cdot [\mathbf{r} \left(\begin{smallmatrix} l' \\ \mathbf{k}' \end{smallmatrix} \right) - \mathbf{r} \left(\begin{smallmatrix} l \\ \mathbf{k} \end{smallmatrix} \right)])\} \quad (1.11)$$

The frequencies of the normal modes and eigenvectors are determined by diagonalizing the dynamical matrix through a solution of the secular equation

$$\det | m_{\mathbf{k}} \omega^2(\mathbf{q}) \delta_{\mathbf{k}\mathbf{k}'} \delta_{\alpha\beta} - D_{\alpha\beta} \left(\begin{smallmatrix} \mathbf{q} \\ \mathbf{k} \mathbf{k}' \end{smallmatrix} \right) | = 0 \quad (1.12)$$

The dynamical matrix is a Hermitian matrix; hence the eigenvalues are real and its eigenvectors are orthonormal. Solving eq. (1.12), gives $3n$ eigenvalues $[\omega_j^2(\mathbf{q})]$, ($j=1,2,\dots,3n$) as well as $3n$ eigenvectors. The components of the eigenvectors $\xi_j(\mathbf{q})$ determine the displacement pattern of the atoms in a particular mode of vibration. The modes of vibrations may be divided into two categories called longitudinal and transverse vibration as illustrated in Fig 1.3.

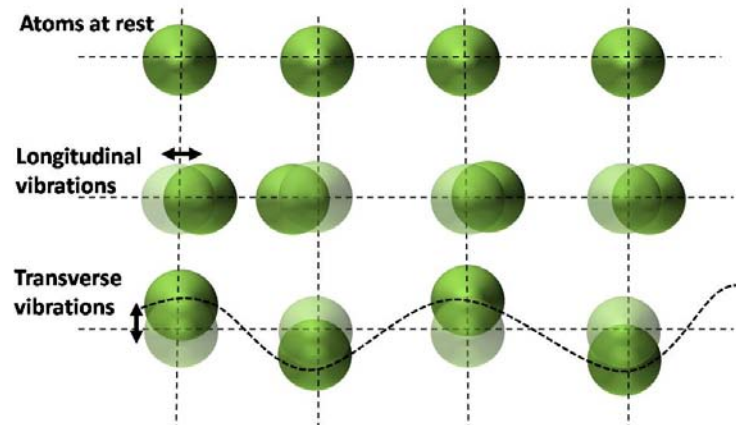


FIG 1.3 The atomic displacement patterns corresponding to longitudinal and transverse vibrational phonon modes.

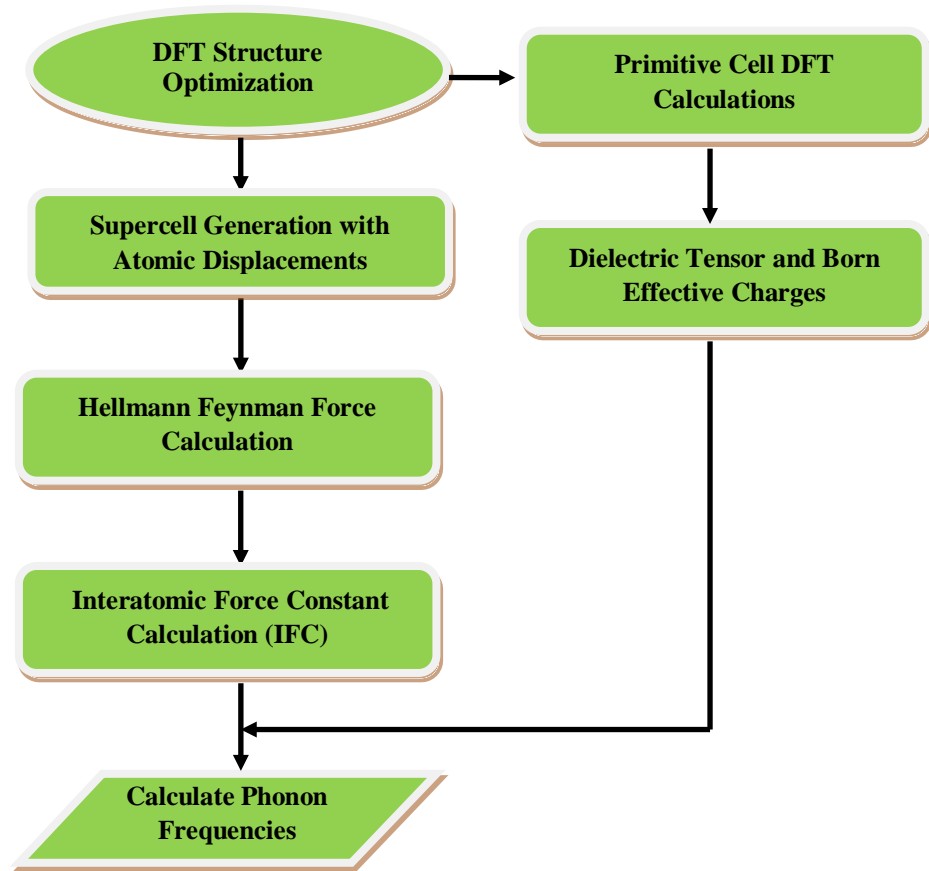


FIG 1.4 A flow chart of PHONON calculation using density functional theory techniques.

The most important step of the lattice dynamics problem is to calculate the force constants, which is usually done by constructing a suitable parametric potential model or *ab-initio* based density functional theory methods. Group-theoretical analysis at various high-symmetry points and directions in the Brillouin zone are used to derive the symmetry vectors. Which is used for block diagonalization of the dynamical matrix and hence the classification of the phonon modes into different irreducible representations enabling direct comparison with single crystal Raman, infrared and neutron scattering data.

The phonon density of states is defined by the equation

$$g(\omega) = \frac{1}{3nN} \lim_{\Delta\omega \rightarrow 0} \sum_{j,q} \delta(\omega - \omega_j(q)) \quad (1.13)$$

Here, $\delta(x)$ is the Dirac delta function.

The procedure for phonon calculations in framework of lattice dynamics is shown in flowchart (Fig 1.4). The phonon calculations are performed using PHONON-5.10 software package developed by K. Parlinski [63] for calculating phonon dispersion curves, and phonon density of states of crystals from a set of Hellmann-Feynman forces. The optimized structures are used for calculations of phonon spectra. An appropriate supercell of the optimized structure is generated. The calculation of force constants matrix (eq. (1.11)) for computation of phonon frequencies may be carried out using either density functional theory (DFT) approach or involving semi-empirical interatomic potentials. We have used the DFT method (using VASP software) for force constant calculations. The forces on atoms are calculated using Hellman-Feynman approach[64] by displacing the various atoms in different symmetry directions in a supercell. The calculated forces are used to compute the force constants matrices between various pairs of atoms. The phonon frequencies in the entire Brillouin zone are calculated using the interatomic force constants. The dielectric constants and Born effective charges can be used to calculate to longitudinal optical and transverse optic modes splitting. The PHONON-5.10 software is used to compute the phonon dispersion relation and phonon density of states for LiAlSiO_4 , LiAlO_2 , V_2O_5 , $\text{ZnAu}_2(\text{CN})_4$, MZrF_6 and Ice *Ih*.

1.4.2 Density Functional Theory

The density functional theory[65] is a *first-principles* electronic structure technique to accurately calculate the energy and structure-property relationships of many

electron systems. The popularity of DFT among the other computational techniques arises from its computationally cheap and accurate performance. DFT is based on two fundamental theorems of Hohenberg-Kohn[66] and Kohn-Sham equation[67]. The 1998 Nobel Prize in Chemistry was devoted to Walter Kohn for this wonderful breakthrough.

A quantum mechanical system is characterized by wave function (Ψ) and total energy (E) which follows the Schrödinger equation

$$\hat{H}\Psi = E\Psi \quad (1.14)$$

The wave function carries all the information about the positions and spins of the system. The many-body Hamiltonian operator (\hat{H}) that governs the behaviour of a system of interacting electrons and nuclei in atomic units takes the form (assuming $e, m_e=1$)

$$\begin{aligned} \hat{H} &= \hat{T}_e(r) + \hat{T}_N(R) + \hat{V}_{eN}(r, R) + \hat{V}_{ee}(r) + \hat{V}_{NN}(R), \\ &= -\frac{1}{2}\sum_i \nabla_i^2 - \sum_I \frac{\nabla_I^2}{2M_I} - \sum_{i,I} \frac{Z_I}{|r_i - R_I|} + \frac{1}{2}\sum_{i \neq j} \frac{1}{|r_i - r_j|} + \frac{1}{2}\sum_{I \neq J} \frac{Z_I Z_J}{|R_I - R_J|} \end{aligned} \quad (1.15)$$

Where, T_e and T_N are the kinetic energy operators of electron and nucleus, respectively. The potential energies due to electron-electron, nucleus-nucleus and electron-nucleus interactions are denoted by V_{ee} , V_{NN} and V_{Ne} respectively. The r_i , m_e and R_I , M_I represents the spatial coordinates and mass of electrons and nucleus, respectively and Z_I is the charge on nucleus. The solution of Schrodinger equation corresponding to above many bodies Hamiltonian is not simple and requires many approximations to be made. The very first of these is the Born-Oppenheimer or adiabatic approximation, which arises from the very high mass of nucleus as compared to that of electrons. It allows the nuclear and electron motions to be decoupled enabling the electrons to move about a fixed nuclear configuration. This transforms the Hamiltonian to

$$\hat{H} = \hat{T}_e + \hat{V}_{eN} + \hat{V}_{ee} + \hat{V}_{NN} = \hat{H}_e + E_{NN} \quad (1.16)$$

Where, H_e is the only electronic part of the many body Hamiltonian. V_{NN} is related to the nuclear degrees of freedoms. The electronic Hamiltonian now will operate on the electrons spins and positions within the system. The electronic part of the Hamiltonian is generally described in form of internal and external interactions with respect to electrons:

$$\hat{H}_e = \hat{T}_e(r) + \hat{V}_{int}(r) + \hat{V}_{ext}(r, R) \quad (1.17)$$

Where, \hat{V}_{int} describes the electron-electron interaction while the \hat{V}_{ext} represents the electron – nuclear interaction potentials. The stationary state electronic energy levels (E_e) can then be calculated by solving

$$\hat{H}_e \Psi = E_e \Psi \quad (1.18)$$

This complicated many-particle equation is not separable into simpler single-particle equations because of the interaction term V_{ee} . Many sophisticated methods for solving the many-body Schrödinger equation exist, based on the expansion of the wave function in Slater determinants, like, Hartree-Fock method, post-Hartree-Fock methods etc. However, the problem with these methods is the huge computational effort, which makes it virtually impossible to apply them efficiently to larger and more complex systems. DFT recasts the basic variable of our equations from being the ground state electronic normalized wave function $\Psi(r_1, \dots, r_N)$ to that of the ground state electron density $n_0(r)$,

$$n_0(r) = \int |\Psi(r, r_2, \dots, r_N)|^2 dr_2 \dots dr_N \quad (1.19)$$

and hence it effectively reduces the $3N$ degrees of freedom to just 3 for an N -electron system. Using the ground-state electron density, it is then possible to find other ground-state properties for the system. In principle, DFT is an exact theory of the ground state of a system, however, due to lack of the exact form of the exchange–correlation functional; the theory works on certain assumptions and approximations to this functional.

Hohenberg and Kohn used the variational principle to determine the ground state properties of an electronic system with the electron Hamiltonian from eq. (1.17) using the electron density of a system rather than the electron wave function on the basis of following two theorems.

1.4.2.1 Hohenberg–Kohn Theorems

Hohenberg–Kohn Theorem 1-For any system of multiple interacting particles in an external potential $V_{ext}(r)$, the potential $V_{ext}(r)$ is determined uniquely, except for a constant C , by the ground state particle density $n_0(r)$.

Hohenberg–Kohn Theorem 2-A universal functional for the energy $E[n(r)]$ in terms of the density $n(r)$ can be defined, valid for any external potential $V_{ext}(r)$. For any particular $V_{ext}(r)$, the exact ground state energy of the system is the global minimum value of this functional, and the density $n(r)$ that minimizes the functional is the exact ground state density $n_0(r)$.

For N electrons in an external potential, $\hat{V}_{ext}(r, R_0)$, with representable densities $n(r)$, a density functional can be defined as

$$F[n(r)] = \min_{\Psi \rightarrow n(r)} \langle \Psi(r) | \hat{T}_e(r) + \hat{V}_{int}(r) | \Psi(r) \rangle \quad (1.20)$$

The functional F is a universal in the sense that it does not depend on the external potential, $\hat{V}_{ext}(r, R_0)$, of the system. If we name E_0 and $n_0(r)$ to be the ground state energy and density, respectively, then the above said two basic theorems of DFT are

$$E[n(r)] = \int \hat{V}_{ext}(r, R_0) n(r) dr + F[n(r)] \geq E_0 \quad (1.21)$$

for all N -representable, $n(r)$, and

$$\int \hat{V}_{ext}(r, R_0) n_0(r) dr + F[n_0(r)] = E_0 \quad (1.22)$$

This implies that the density $n(\mathbf{r})$ is a basic variable, rather than the electronic wave function $\Psi(\mathbf{r})$ and constructing a satisfying approximation to the true functional $F[n(\mathbf{r})]$, one can obtain approximations to both the true ground state energy E_0 and the true ground state density $n_0(\mathbf{r})$.

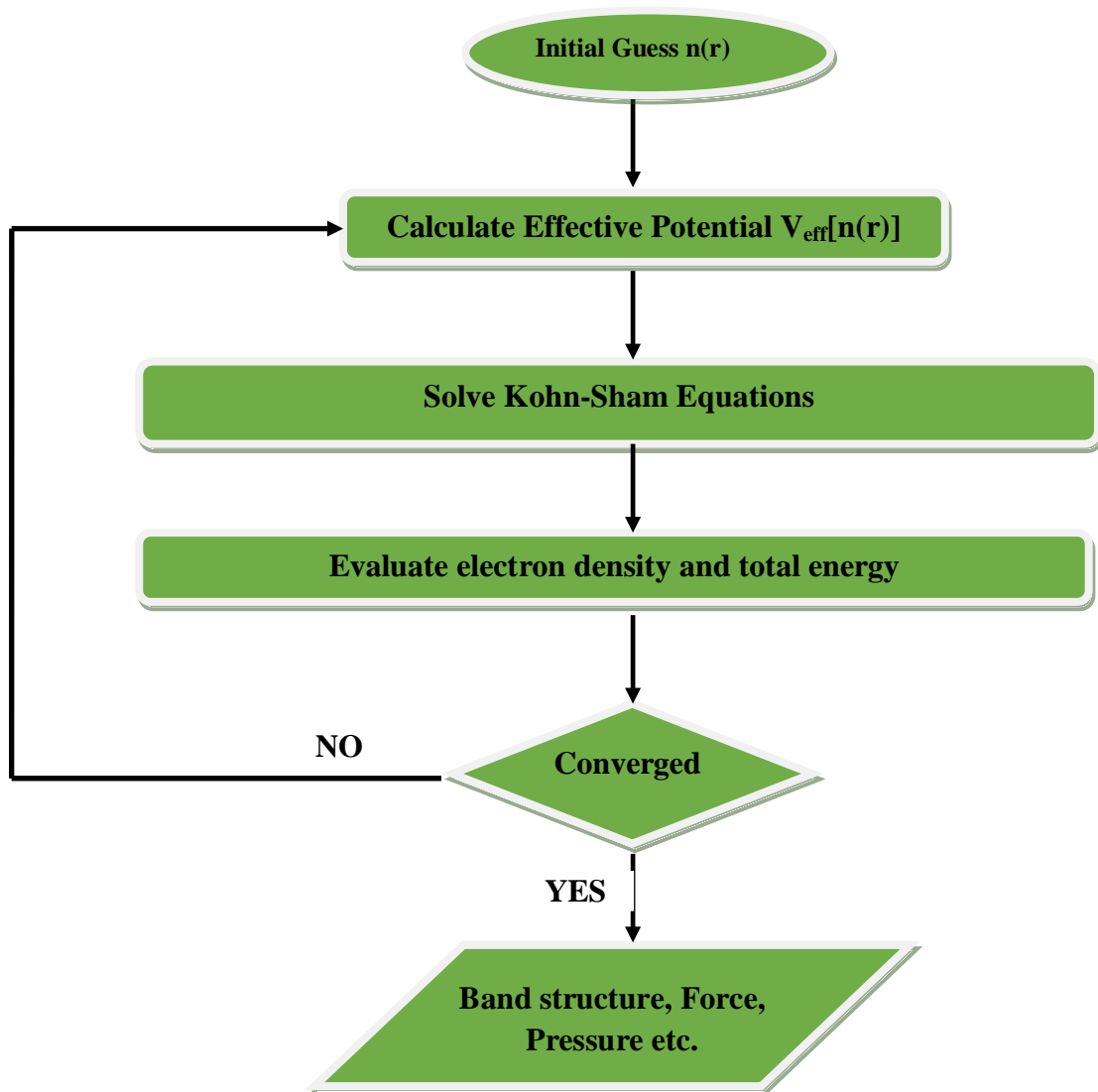


FIG 1.5 A flowchart of density functional theory calculations scheme for convergence.

1.4.2.2 Kohn-Sham Approach

Although Hohenberg-Kohn theorems laid the foundations for the development of modern DFT, their findings did not enable to actually solve the Schrödinger equation that

was later provided by Kohn-Sham equations. They provided a way to systematically map the many-body problem onto a single-body problem. They assumed that there exists an equivalent auxiliary system of non-interacting electrons with density $n(\mathbf{r})$ corresponding to a set of interacting electrons with electron density $n(\mathbf{r})$. This give the following form to the unknown energy functional term from the Hohenberg-Kohn theorem:

$$E_{KS}[n] = \hat{T}_0[n] + E_H[n] + E_{xc}[n] \quad (1.23)$$

and

$$E_H[n] = \frac{1}{2} \int \int \frac{n_1 n_2}{|r_1 - r_2|} dr_1 dr_2 \quad (1.24)$$

Where \hat{T}_0 is the kinetic energy of anon-interacting system of electrons with density, $n(\mathbf{r})$. The term E_H is the classical Coulomb potential for electron-electron interaction between the electron charge densities and does not account for correlation of electron motions, also known as the Hartree energy and E_{XC} is the so-called exchange-correlation energy. The first two terms can be calculated exactly, while the last term, the exchange-correlation functional, incorporates both the exchange and correlation energies, as well as the ‘remainder’ of electron kinetic energy and anything else that might be lacking in order for the energy functional E_{KS} to be the true energy functional $E(n(r))$ from eq. (1.21). It is only this term for which we need to construct a satisfying, approximate functional, since the form of the true functional is not known. The details of DFT can be found in many popular books[68,69]. A flowchart of DFT calculation is shown in Fig 1.5.

1.4.2.3 Exchange Correlation Approximations

The approximation of exchange and correlation energies term is considered to be a significant source of error. Therefore, the accuracy of the whole DFT technique relies upon finding a good approximation of this quantity. One of the simplest exchange–

correlation functional applied in DFT is the local-density approximation (LDA) functional [66]. This functional calculates the exchange–correlation energy of a point in a system to being the same as that of a point in a homogenous electron gas of the same density. It turns out that the kinetic energy term \hat{T}_0 for the non–interacting electrons can account for a large part of the full kinetic energy term \hat{T}_e for the many–body interacting system. Thus, only a relatively small part of the energy contributed to the functional E_{KS} comes from E_{XC} , and thus our calculated ground state properties become relatively well approximated despite a rough estimate of the exchange–correlation energy. That is why even for those inhomogeneous systems, for which the electron density does not resemble that of a homogeneous electron gas, the LDA is found to work well. LDA exchange correlations is given by

$$E_{xc}^{LDA}[n(r)] = \frac{1}{2} \int n(r) \varepsilon_{xc}^{hom}(n(r)) dr \quad (1.25)$$

which is derived from the homogeneous electron gas with density $n(r)$. Although LDA underestimates correlation energy and overestimates the exchange energy, yet the success of LDA can partly be attributed to systematic cancelation of errors involved in the calculation of $E_{xc}^{LDA}[n]$. However, there are several remaining problems with LDA which give rise to underestimating the band gaps of materials, overestimating binding energies and incorrect predictions for the structures of electronic ground-states.

The generalized gradient approximation (GGA) to calculation of exchange correlation energy[70,71] take care variations in the electron density with respect to the position. This attempt to include the dependence of exchange correlation on local charge density and its gradient as follow

$$E_{xc}^{GGA}[n] = \int n(r) \varepsilon_{xc}^{GGA}(n(r), \nabla n(r)) dr \quad (1.26)$$

Where ϵ_{xc}^{GGA} can take many potential alternative parameters, LDA is one of them. Therefore, many different types of GGA functional exist; however, for all the calculations within this thesis a functional based on the work of Perdew, Burke and Ernzerhof (PBE)[72] is considered. GGA tend to reproduce the highly accurate lattice parameters, improved band gaps and bond lengths, especially for the non-metallic systems and inorganic oxides, in comparison to LDA.

The calculated structure and properties of materials containing strongly correlated electrons need special attention, due to localized d- and f-orbitals, which is not very well taken care in usual DFT method. The effect can be implemented by inclusion of strong onsite Hubbard interaction (LDA/GGA +U) [73,74] for correlated d- and f-electrons. This especially plays very important role in Li ion battery cathode materials which are generally the compounds with transition metal. For these types of compounds, LDA/GGA provides partially filled d-bands with metallic type electronic structure with wandering d-electrons contrary to the experimentally observed localized d- and f-electrons with separated occupied and unoccupied electron bands. The inclusion of strong onsite Hubbard interaction (LDA/GGA +U) for correlated d- and f-electrons alters the exchange correlation functional, significantly. This treats the d- and f-electrons with Hartree-Fock type (mean field) Columbic interactions. The strength of correction made to the exchange correlation functional is controlled by the Hubbard Coefficient, U.

The popular density functional like LDA/GGA is unable to incorporate the van der Waals interactions resulting from fluctuating charge distributions. Therefore, many battery cathodes with layered structures and the open framework compounds generally give overestimated lattice parameters in the DFT calculations. A pragmatic method to work around this problem is to add a correction to the conventional Kohn-Sham DFT energy as

$$E_{DFT-disp} = E_{KS-DFT} + E_{disp} \quad (1.27)$$

There are various approximate methods to calculate the dispersion corrections. In the DFT-D2 method of Grimme[75], the van der Waals interactions are described via a simple pair-wise force field, which is optimized for several popular DFT functional. Another method of vdW-DF, proposed by Dion et. al.[76], is a non-local correlation functional that approximately accounts for dispersion interactions. The original vdW-DF, the “opt” functional (optPBE-vdW, optB88-vdW, and optB86b-vdW) where the exchange functional were optimised for the correlation part, and the vdW-DF2 of Langreth and Lundqvist groups[77] gives the accurate structures.

For the density functional theory calculations, plane wave-based Vienna *ab-initio* Simulation Package (VASP)[78,79] has been used in the present research work. The interactions between the electrons and ions are described using the projector-augmented-wave method. VASP is used to compute the total energy, pressure, Born effective charges, charge density and Hellman-Feynman forces for LiAlSiO₄, LiAlO₂, V₂O₅, ZnAu₂(CN)₄, AgC₈N₅, MZrF₆ and Ice-*Ih*.

1.4.3 Thermodynamic and Elastic Properties

The calculated phonon spectra from the lattice dynamics calculations provide the various thermodynamical properties of the crystalline materials. The harmonic approximation for atomic vibrations fails to account for thermal expansion, thermal conductivity, specific heat at high temperatures and multiphonon processes etc. These properties can be modelled by considering anharmonic nature of potential energy curve responsible for bonding. Anharmonic effects are negligible at low temperatures. The population of phonon states at temperature T, are governed by Bose-Einstein distribution

as $n(\omega_j) = \frac{1}{\exp\left(\frac{\hbar\omega_j}{k_B T}\right) - 1}$. At high temperatures, $\hbar\omega_j \ll k_B T$, implying $n(\omega_j) \propto \frac{k_B T}{\hbar\omega_j}$.

Therefore, the anharmonic effects become more important at high temperatures and affect the physical properties of the crystal.

The quasiharmonic approximation[2] is one of the methods to partially deal with the anharmonic nature of the potential energy curves up to moderate temperature. It assumes the vibrations of atoms at different volumes to be harmonic appropriate to the corresponding temperature or pressure. In the quasiharmonic approximation, the thermodynamic properties of a crystal are based on the averages of energies associated with the $3nN$ vibrations corresponding to the number of degrees of freedom of the n atomic constituents in the N unit cells of the crystal. The crystalline solids can be assumed as a combination of large number of harmonic oscillators. The partition function of a crystalline system looks like

$$Z = \exp - \phi(V) \prod_{jq} \frac{\exp^{-\hbar\omega_{jq}/2k_B T}}{1 - \exp^{-\hbar\omega_{jq}/k_B T}} \quad (1.28)$$

Various thermodynamic properties of the crystal derived from the partition function, involve summations over the phonon frequencies in the entire Brillouin zone and can be expressed as averages over the phonon density of states. One may derive all the thermodynamical quantities using the partition function mentioned above.

The linear thermal expansion coefficients along a , b and c -axes can be calculated within the quasiharmonic approximation. The calculations require anisotropic pressure dependence of phonon energies in the entire Brillouin zone. These calculations are subsequently used to obtain the anisotropic mode Grüneisen parameters. According to Grüneisen's original work for anisotropic system[80], the Grüneisen parameter is given by a general expression as

$$\Gamma_l(E_{q,j}) = - \left(\frac{\partial \ln E_{q,j}}{\partial \ln l} \right)_{T,l'} ; l, l' = a, b, c \& l \neq l' \quad (1.29)$$

Where, $E_{q,j}(= \hbar \omega_j(q))$ is the energy of j^{th} phonon mode at point q in the Brillouin zone. The anisotropic Grüneisen parameters are calculated by applying a small anisotropic stress by changing one of the lattice constants keeping others fixed, and vice versa, where temperature is held constant at zero. The symmetry of the unit cell is kept invariant on introduction of strain, while performing the calculations. The anisotropic linear thermal expansion coefficients are given by[1,80]

$$\alpha_l(T) = \frac{1}{V_0} \sum_{q,j} C_v(q,j,T) \sum_{l'} S_{ll'} \Gamma_l \quad (1.30)$$

Where, $S_{ll'}$ are elements of elastic compliances matrix $S=C^{-1}$, V_0 is volume at ambient conditions and $C_v(q,j,T)$ is the specific heat at constant volume for j^{th} phonon mode at point q in the Brillouin zone. The anisotropy of Grüneisen parameters and elasticity give rise to the anisotropic thermal expansion behaviour of the compound. Since $C_v(T)$ is positive for all modes at all temperatures, it is clear that the NTE would result only from large negative values of the Grüneisen parameter for certain phonons; the values should be large enough to compensate for the normal positive values of all other phonons. The frequencies of such phonons should decrease on compression of the crystal rather than increase which is the usual behaviour. It is very interesting to note that the quantization of the phonon energies is important to the phenomena of NTE, just as in the case of specific heat. Although thermal expansion and specific heat are highly averaged quantities, their temperature dependence involves progressively the role of low energy to higher energy phonons.

The elastic constants are calculated using the symmetry-general least square method[81]. The values are derived from the strain-stress relationships obtained from

finite distortions of the equilibrium lattice. If a crystal system is given a strain ϵ_{ij} which produce stress σ_{kl} in the system, then the elastic constant tensor is given by

$$\sigma_{kl} = C_{ijkl} \epsilon_{ij} \quad (1.31)$$

Where, C_{ijkl} is positive definite with symmetry properties. In matrix notation, it can be represented as

$$\sigma_i = C_{ij} \epsilon_j \quad (1.32)$$

Which gives 6×6 matrix for C_{ij} . Three tensile and three shear strains are manually applied to the crystal structure and corresponding stress components of final relaxed structure are calculated. For a crystalline solid, to be stable at any conditions, all the phonon frequencies must be positive and the Born elastic stability criteria must be fulfilled. The Born stability criteria demand the elastic constant matrix to be positive definite which give rise to different simplified expressions for different symmetry structures [82].

TABLE 1.1 Various physical variable (left) and corresponding physical properties obtained from derivatives of total energy with respect to these physical variables.

Derivative of Total energy	Physical Property
<i>1st Ordered</i>	<i>Forces, Stresses, Dipole Moments</i>
<i>2nd Ordered</i>	<i>Dynamical Matrix, Elastic Constants, Dielectric Susceptibility, Born Effective Charges, Piezoelectricity, Internal Strains</i>
<i>3rd Ordered</i>	<i>Non-Linear dielectric Susceptibility, Phonon-Phonon Interaction, Grüneisen Parameters</i>

Many physical properties like polarizabilities, phonons, Raman intensities and infra-red absorption cross-sections depend upon a system response to some form of perturbation. Density functional perturbation theory (DFPT)[83,84] is a particularly

powerful and flexible theoretical technique that allows calculation of such properties within the density functional framework providing a rigorous testing ground for theoretical developments. System responses to external perturbations may be calculated using DFT with the addition of some perturbing potential obtaining the system response through a series of single-point energy calculations. The physical properties are the derivative of total energy with respect to perturbations as given in Table 1.1. The calculation of complete phonon spectra in the entire Brillouin zone is computationally expensive for a large system. The zone centre phonon spectrum in conventional unit cell using linear response density functional perturbation theory (DFPT), as implemented in VASP, is used in those cases. This technique is used to calculate the vibrational frequencies of AgC_8N_5 which has 336 atoms in the unit cell.

1.4.4 Transition State theory

The atoms in a crystal have some thermal energy which causes them to vibrate on a typical timescale of femto-seconds. Energy is free to move from one atom to another, and sometimes a particular atom will get a relatively large amount of energy and it can cause bonds to break i.e. an atom can move to a new lattice site within the solid. These processes take place on a much longer timescale than the vibrational timescale. The atoms will vibrate on average 10^{12} times in between such reactions. It takes long time to simulate the motion of the atoms on a computer to see a single event happening.

Transition state theory (TST) is a concept that provides some relief from this problem. Within TST only those rare events that lead to reactions are statistically described. TST assumes the system as a small ball rolling on landscape known as potential energy surface (PES), which is a high dimensional surface and is hard to

visualize, however the two-dimensional PES is shown in Fig 1.6. The major effort in calculating a rate of a process with TST is required in identifying bottle neck regions or transition states through which the system must pass to get to another PEM. In the present research work I have used the nudged elastic band method for saddle point calculations. The saddle point is the highest energy point that must be crossed to get from one PEM to another while staying as low in energy as possible. The NEB method finds the entire minimum energy path (MEP) between two minima. Both the initial and final states of the system should be well known to perform the NEB calculations. The NEB works by creating a number of images connecting the initial and final states. These images are connected by springs to keep them equally spaced (Fig 1.6). The path of springs acts like an elastic band. The images on the band feel the forces due to the springs, but they also feel the forces due to the potential so that each image tries to minimize its potential energy. The details of TST can be found in literature[85].

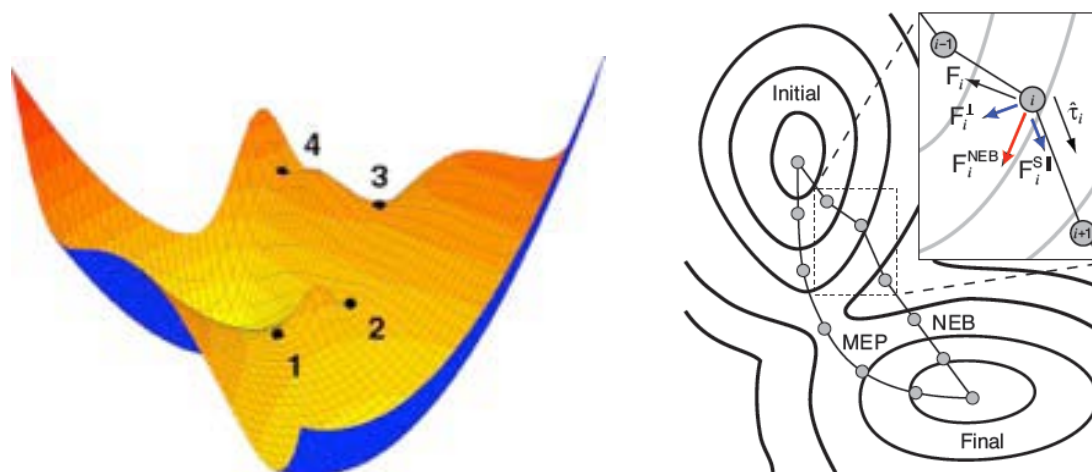


FIG 1.6 (Left) Potential energy surface of solid in three dimensions (Right) Elaboration of procedure to calculate the minimum energy pathway for a reaction and various types of forces which are optimized in this process (after Ref. [85]).

An important part of the method is the nudging or force projection scheme. The spring forces are only allowed to act along the band so that constant image spacing is ensured, and the potential forces are only allowed to act in all directions perpendicular to the band, ensuring that the band comes to rest on the MEP between the minima. The NEB method would develop oscillations in the band in which one image would be on one side of the MEP, and the next would be on the other and hence it does not find the exact saddle point along the path, which is used to calculate the activation energy of the process. It is possible to put down many images in the band so that the saddle point can be found by interpolation between the images, but having many images adds to the computational cost. A way of moving the highest energy image on the band right to the saddle point is adopted. This image is also freed of the spring forces so that it can move exactly to the saddle point. This modification, called the climbing image NEB, extends the NEB so that saddle points can be found with fewer images in the band.

Let $[R_0, R_1, R_2, \dots, R_N]$ be the $N+1$ images on an elastic band with initial and final points, R_0 and R_N at corresponding potential energy minima. Two adjacent images R_{i+1} and R_{i-1} are used to estimate the tangent at an i^{th} image by bisecting two unit vectors

$$\boldsymbol{\tau}_i = \frac{R_i - R_{i-1}}{|R_i - R_{i-1}|} + \frac{R_{i+1} - R_i}{|R_{i+1} - R_i|} \quad (1.33)$$

The direction of this tangent is obtained as

$$\hat{\boldsymbol{\tau}} = \frac{\boldsymbol{\tau}}{|\boldsymbol{\tau}|} \quad (1.34)$$

This formalism give rise to equi-spaced images even in the highly curvature PES. The total force acting on an image is the sum of the spring force along the tangent and the true force perpendicular to the tangent

$$\mathbf{F}_i = \mathbf{F}_i^s|_{||} - \nabla V(\mathbf{R}_i)|_{\perp} \quad (1.35)$$

Where the true force is given by

$$\nabla V(\mathbf{R}_i)|_{\perp} = \nabla V(\mathbf{R}_i) - \nabla V(\mathbf{R}_i) \cdot \hat{\tau}_i \quad (1.36)$$

And the spring forces, when the perpendicular component of the spring force is not included, are given as

$$\mathbf{F}_i^s|_{\parallel} = k[(R_{i+1} - R_i) - (R_i - R_{i-1})] \cdot \hat{\tau}_i \quad (1.37)$$

The method of climbing image advances the NEB techniques by fixing one of the nearest images to the actual saddle point without adding any extra computational cost to the calculations. This gives the accurate determination of activation energy barrier for the transition. These methods can be further advanced using variable spring forces instead of the fixed one to be closer to the actual transition pathways. This method is used to calculate the activation energy for Li diffusion in LiAlSiO₄ and that for high pressure phase transitions in LiAlO₂.

1.4.5 Molecular Dynamics Simulations

The DFT, LD and TST are the static calculations techniques which only deal with the potential energy of the system and describe the system at 0K; hence no kinetic behaviour or temperature effect is involved. On the other hand, molecular dynamics (MD) is a computer simulation method for studying the physical movements of atoms and molecules as a function of time. The atoms and molecules are allowed to interact for a fixed period of time, giving a view of the dynamic evolution of the system. All atoms are assigned a velocity; therefore, the kinetic energy of the atoms is included explicitly in MD simulations. The combined effect of all the velocities provides a macroscopic temperature to the system. The kinetic energy of particles in MD simulations allows the system to

overcome local energy barrier of a few kT to attain a thermodynamically stable configuration. The details of MD simulations are given in Ref. [86]

MD simulations provide the time averaged structures and ionic diffusion in the solids by covering a large part of the potential energy surface of the system. MD determines the atomic trajectories, velocities, vibrational spectra using the Newton's equations of motion. The energy function allows us to calculate the force experienced by any atom given the positions of the other atoms. Newton's laws tell us how those forces will affect the motions of the atoms. By dividing time into step of femto-seconds MD compute the forces acting on each atom, using provided force fields. Then the atoms are moved a little bit: updating position and velocity of each atom using Newton's laws of motion

$$\mathbf{F}(r_i) = -\nabla U(r_i) \quad (1.38)$$

Where, r_i represents coordinates of i^{th} atom, and U is the potential energy function. From the forces, velocities and position can be calculated for given initial conditions as follow:

$$\frac{dv(r_i)}{dt} = \frac{F(r_i)}{m_i} = a_i \& \frac{dr_i}{dt} = v_i \quad (1.39)$$

This gives system of ordinary differential equations containing $3N$ position coordinates and $3N$ velocity coordinates for system of N atoms. The analytical solution to these equations is impossible while the numerical solution is very straight forward by advanced integration algorithms which have been developed to increase computational efficiencies like Leapfrog Verlet, Trapezoidal rule, Beeman's algorithm, Midpoint method, Heun's method, Newmark-beta method etc. In MD simulations, atoms are in continuous motion and will never stay in energy minima. However, sufficiently large simulation time samples the Boltzmann distribution for probability of observing a particular arrangement of atoms depending on the potential energy of the configurations.

The total energy (Kinetic + potential) of system is conserved in MD simulations, i.e., in atomic arrangements with lower potential energy, atoms move faster. In practice total energy tends to grow slowly with time due to numerical errors. Therefore, one adds a mechanism to keep the temperature roughly constant called a thermostat. There are many types of thermostats or barostats in MD simulations and these are characterized by the appropriate ensembles. These ensembles describe the set of constraints applied to a system that gives rise to the distribution of accessible states.

The micro-canonical (NVE) ensemble maintains a constant number of atoms (N), volume (V) of the simulation cell and total energy (E). Although the total energy of the micro-canonical (NVE) ensemble remains constant yet the potential and kinetic energy contributions can be mutually exchanged. The rounding and truncation errors during the integration process always give rise to a slight drift in energy. The NVE ensemble is not recommended for achieving temperature and equilibrium as it does not allow any flow of energy in the system. The canonical ensemble (NVT) controls the temperature of the system through direct temperature scaling during the initialization stage and by temperature-bath coupling during the data collection phase. The canonical ensemble allows the system under study to be probed as a function of temperature. On the other hand, isobaric-isothermal (NPT) ensemble allows control over both the temperature and pressure. The unit cell vectors are allowed to change and the pressure is adjusted by adjusting the volume. This is the ensemble of choice when the correct pressure, volume, and densities are important in the simulation. This ensemble can also be used during equilibration to achieve the desired temperature and pressure before changing to the constant-volume or constant-energy ensemble when data collection starts.

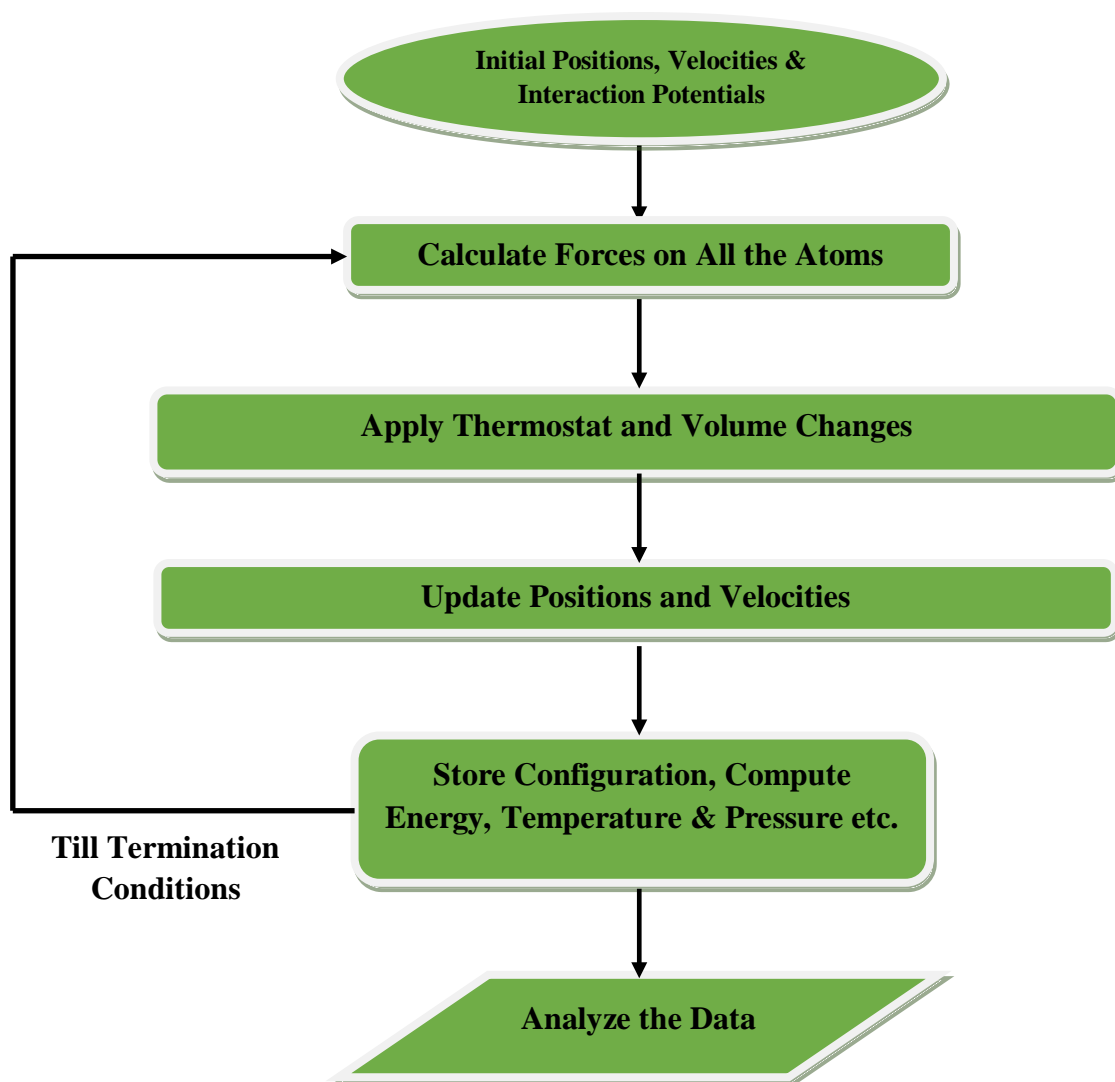


FIG 1.7 A flowchart for molecular dynamics simulations.

Two different types of molecular dynamics (MD) methods i.e. classical MD and *ab-initio* Born Oppenheimer MD (BOMD), are used in the present research work. Classical MD uses classical force fields to define interactions among the species of the system. It is computationally cheaper but compromise with accuracy unless or until an accurate force field is known for the system. We can simulate a thousand of atoms with classical MD simulations. On the other hand, BOMD also called *ab-initio* MD (ABIMD)[87,88] uses pseudo-potential for total energy and forces calculations. It solves the electronic structure with stationary ions for each time step and then calculates the

ionic movement with stationary electronic structure and recalculates the electronic structure with new ionic positions. The old electronic densities of few past steps are commonly used to calculate the initial guess for the self-consistent loop. This helps in reaching the convergence, and in practice, a single BO-MD step in the middle of a simulation requires much less computational effort than the calculation of electronic density of the same ionic structure from scratch. The complete flowchart of MD simulations is shown in Fig 1.7.

In the present thesis, classical molecular dynamics is used to study Li ion diffusion in LiAlSiO_4 while *ab-initio* molecular dynamics simulations are performed for LiAlSiO_4 to study high temperature phase transition and various factors affecting superionic Li conduction. The ABIMD is also used to study diffusion of Li in LiAlO_2 and alkali intercalated V_2O_5 . For classical molecular dynamical simulations, the DL_POLY-4 software[89] is used. On the other hand VASP software[78,79] is used for ABIMD simulations. The ABIMD in VASP is also used to calculate the thermal expansion behavior of LiAlSiO_4 and AgC_8N_5 .

1.4.6 Ionic Diffusion in Solids

The atomistic of solid state diffusion had to wait for the birth date of solid-state physics heralded by the experiments of Max von Laue. Equally important was the perception of the Russian and German scientists Jakov Frenkel and Walter Schottky that point defects play an important role for diffusion properties of crystalline substances. Albert Einstein provided the statistical cornerstone of diffusion and bridged the gap between mechanics and thermodynamics. Fick's laws and continuity equations form the basis of diffusion studies. The diffusion of atoms in solids represents the sum of a large

number of particles or atoms that each makes a large number of jumps. In the diffusion process it is not possible to observe the individual jumps of the atoms, and it is necessary to find a relation between the individual atom jumps for large number of atoms and the diffusion phenomena which may be observed on a macroscopic scale. The problem is to find how far a large number of atoms will move from their original sites after having made a large number of jumps. Such relations may be derived statistically by means of the so-called random walk method, according to which the diffusion coefficients are related to the averaged mean-squared displacements (MSD). The details of diffusion in solids can be found in book by Helmut Mehrer[90].

For the calculation of diffusion coefficient, the squared displacements (u^2) are averaged over all the diffusing atoms and over a large number of time origins. This averaging gives rise to disappearance of step like behaviour in the u^2 curve. The slope of the mean-squared displacement (MSD) versus time plot is used to get the diffusion coefficients in accordance with Einstein's formula

$$2Dt = \frac{1}{N_D} \langle |r_i(t) - r_i(0)|^2 \rangle \quad (1.40)$$

Where, r_i is the position vector of the diffusing species, t is the time and N_D represent the dimensionality of diffusion, and $u^2 = |r_i(t) - r_i(0)|^2$. The quantity within the brackets has been averaged over different initial times. The activation energy for atomic jump diffusion can be obtained from the Arrhenius plot of diffusion coefficient as a function of temperature as given by [90]

$$D = D_0 e^{-\frac{E_a}{k_B T}} \quad (1.41)$$

Where D_0 is the pre-exponential factor, k_B is the Boltzmann constant and T is the temperature. The logarithm of this equation is

$$\ln(D) = \ln(D_0) - \frac{E_a}{k_B T} \quad (1.42)$$

Although the single symbol, D , has been used to denote the diffusion coefficient, there are several variants of this property. They are classified as follows:

- (i) **The Self-Diffusion Coefficient, D_{self}** -This property refers to the migration of the atoms of a pure element or ion of an ionic solid in the absence of a concentration gradient. This term is commonly assumed to be equal to the tracer diffusion determined by watching the movement of an isotope in the material of interest. There is no direct method for measuring the self-diffusion coefficient.
- (ii) **The Tracer Diffusion Coefficient, D_{tr}** -This diffusivity is subject to the same conditions as the self-diffusion coefficient except that some of the atoms are radioactive isotopes of the host element or ion. Measurement of D_{tr} requires a gradient (and hence a flux) of the tracer but there is no gradient or flux of the combined radioactive and nonradioactive element or ion. The diffusivities of these two forms are equal i.e. $D_{\text{self}} = D_{\text{tr}}$
- (iii) **The Intrinsic Diffusion Coefficient, D_{In}** : This quantity refers to the diffusion of a species in a binary solid. Each species possesses an intrinsic diffusion coefficient, designated as D_X and D_Y for the components X and Y , respectively. The intrinsic diffusivities of the components of a binary solid are in general not equal. These diffusivities imply concentration gradients of the species X and Y , in contrast to the self and tracer diffusion coefficients.

Besides the correlated diffusion of ions in the solids, diffusion can take place through the movement of point defects. The presence of different types of defects gives rise to different mechanisms of diffusion. The commonly observed diffusion via defect in solids includes vacancy, interstitial, and interstitialcy mechanisms.

1.5 Objectives of Research

The main objectives of the thesis are to extensively study the phonon spectra of battery materials and low density metal organic/inorganic framework compounds. The battery materials include cathode materials (LiAlO_2 and V_2O_5) and solid electrolyte (LiAlSiO_4). On the other hand, the low density framework compounds include inorganic frameworks (MZrF_6 ($\text{M}=\text{Mg}$, Ca , Sr) and H_2O & D_2O Ice *Ih*) and metal organic frameworks ($\text{ZnAu}_2(\text{CN})_4$ and AgC_8N_5). The phonon studies in these compounds are performed to understand the mechanisms responsible for ionic conduction, NTE, NLC and high temperature-pressure phase transitions. The various factors affecting the ionic diffusion in these materials are also studied. Moreover, the accurate calculations of vibrational free energy (considering contributions only from vibrational entropy) is used to calculate temperature pressure phase diagrams and specific phonon modes responsible for these phase transitions are identified.

1.6 Summary

This chapter describes the basic introduction, motivation and objectives of the work along with experimental and theoretical tools used to study the thermodynamical properties of interest. The inelastic neutron scattering (INS) technique to study dynamics, and X-ray diffraction for structural study of materials has been explained briefly. Thermal neutrons have a wavelength and energy of the order of atomic spacing and lattice vibrations, respectively and thus are suitable to study the phonons in the materials. The phonon dispersion and phonon density of states [3,5] can be measured using the single crystal and polycrystalline samples, respectively. The measurements of temperature dependence of phonon density of states using the polycrystalline samples are performed

using the IN4 and IN6 time-of-flight spectrometer at high flux reactor of Institut Laue-Langevin, Grenoble, France as described. The theoretical techniques like quantum-mechanical *ab-initio* density functional theory (DFT), lattice dynamics, molecular dynamics (*ab-initio* as well as empirical potential based), density functional perturbation theory and transition state theory are discussed. These techniques have been used to calculate the phonon spectra, diffusion coefficients, diffusion pathways and activation energy for these pathways in the compounds of interest. The equilibrium structures, total energy and force constants in any given atomic configuration of the system are calculated. The basic formalism for the calculation of elastic properties and anisotropic linear thermal expansion coefficients of a crystalline system is provided in detail.

References

- [1] G. Grimvall, *Thermophysical properties of materials* (Elsevier, 1999).
- [2] G. Venkataraman, L. A. Feldkamp, and V. C. Sahni, *Dynamics of perfect crystals* (MIT Press, Cambridge, 1975).
- [3] R. Mittal, M. K. Gupta, and S. L. Chaplot, *Progress in Materials Science* **92**, 360 (2018).
- [4] B. Cheng and M. Ceriotti, *Physical Review B* **97**, 054102 (2018).
- [5] S. L. Chaplot, R. Mittal, and N. Choudhury, *Thermodynamic Properties of Solids: Experiments and Modeling* (John Wiley & Sons, 2010).
- [6] F. Bridges, T. Keiber, P. Juhas, S. J. L. Billinge, L. Sutton, J. Wilde, and G. R. Kowach, *Physical Review Letters* **112**, 045505 (2014).
- [7] H. Sun, Y. Zhang, J. Zhang, X. Sun, and H. Peng, *Nature Reviews Materials* **2**, 17023 (2017).
- [8] E. Cubuk *et al.*, *Science* **358**, 1033 (2017).
- [9] S. Curtarolo, G. L. W. Hart, M. B. Nardelli, N. Mingo, S. Sanvito, and O. Levy, *Nature Materials* **12**, 191 (2013).
- [10] D. P. Tabor *et al.*, *Nature Reviews Materials* **3**, 5 (2018).
- [11] M. Asta, *JOM* **66**, 364 (2014).
- [12] S. Kirklin, B. Meredig, and C. Wolverton, *Advanced Energy Materials* **3**, 252 (2013).
- [13] J. B. Goodenough and K. S. Park, *Journal of the American Chemical Society* **135**, 1167 (2013).
- [14] A. B. Cairns and A. L. Goodwin, *Physical Chemistry Chemical Physics* **17**, 20449 (2015).
- [15] W. Zhou, Y. Li, S. Xin, and J. B. Goodenough, *ACS Central Science* **3**, 52 (2017).
- [16] N. C. Burtch, J. Heinen, T. D. Bennett, D. Dubbeldam, and M. D. Allendorf, *Advanced Materials*, 1704124 (2017).
- [17] J. Janek and W. G. Zeier, *Nature Energy* , **1**, 16141 (2016).
- [18] R. Schmich, R. Wagner, G. Hörpel, T. Placke, and M. Winter, *Nature Energy* **3**, 267 (2018).
- [19] N. Nitta, F. Wu, J. T. Lee, and G. Yushin, *Materials Today* **18**, 252 (2015).
- [20] M. D. Bhatt and C. O'Dwyer, *Physical Chemistry Chemical Physics* **17**, 4799 (2015).
- [21] M. H. Braga, N. S. Grundish, A. J. Murchison, and J. B. Goodenough, *Energy & Environmental Science* **10**, 331 (2017).
- [22] J.-M. Tarascon, *Philosophical Transactions of the Royal Society of London A: Mathematical, Physical and Engineering Sciences* **368**, 3227 (2010).
- [23] R. Hausbrand, G. Cherkashinin, H. Ehrenberg, M. Gröting, K. Albe, C. Hess, and W. Jaegermann, *Materials Science and Engineering: B* **192**, 3 (2015).
- [24] J. Zheng, P. Xu, M. Gu, J. Xiao, N. D. Browning, P. Yan, C. Wang, and J.-G. Zhang, *Chemistry of Materials* **27**, 1381 (2015).
- [25] A. Mukherjee, N. Sa, P. J. Phillips, A. Burrell, J. Vaughey, and R. F. Klie, *Chemistry of Materials* **29**, 2218 (2017).

- [26] L. Ji, Z. Lin, M. Alcoutlabi, and X. Zhang, *Energy & Environmental Science* **4**, 2682 (2011).
- [27] Y.-K. Sun, S.-T. Myung, B.-C. Park, J. Prakash, I. Belharouak, and K. Amine, *Nature Materials* **8**, 320 (2009).
- [28] C. Sun, J. Liu, Y. Gong, D. P. Wilkinson, and J. Zhang, *Nano Energy* **33**, 363 (2017).
- [29] J. Y. Hwang, S. T. Myung, and Y. K. Sun, *Chemical Society Reviews* **46**, 3529 (2017).
- [30] D. Larcher and J. M. Tarascon, *Nature Chemistry* **7**, 19 (2015).
- [31] J. Yang and J. S. Tse, *Computational Materials Science* **107**, 134 (2015).
- [32] V. Thangadurai, S. Narayanan, and D. Pinzarú, *Chemical Society Reviews* **43**, 4714 (2014).
- [33] Y. Kato, S. Hori, T. Saito, K. Suzuki, M. Hirayama, A. Mitsui, M. Yonemura, H. Iba, and R. Kanno, *Nature Energy* **1**, 16030 (2016).
- [34] L. Yue, J. Ma, J. Zhang, J. Zhao, S. Dong, Z. Liu, G. Cui, and L. Chen, *Energy Storage Materials* **5**, 139 (2016).
- [35] E. D. Wachsman and K. T. Lee, *Science* **334**, 935 (2011).
- [36] G. K. Phani Dathar, J. Balachandran, P. R. C. Kent, A. J. Rondinone, and P. Ganesh, *Journal of Materials Chemistry A* **5**, 1153 (2017).
- [37] U. V. Alpen, E. Schönherr, H. Schulz, and G. H. Talat, *Electrochimica Acta* **22**, 805 (1977).
- [38] N. Kamaya *et al.*, *Nature Materials* **10**, 682 (2011).
- [39] E. Kendrick, J. Kendrick, K. S. Knight, M. S. Islam, and P. R. Slater, *Nature Materials* **6**, 871 (2007).
- [40] P. Goel, M. K. Gupta, R. Mittal, S. Rols, S. J. Patwe, S. N. Achary, A. K. Tyagi, and S. L. Chaplot, *Journal of Materials Chemistry A* **2**, 14729 (2014).
- [41] M. K. Gupta, P. Goel, R. Mittal, N. Choudhury, and S. L. Chaplot, *Physical Review B* **85**, 184304 (2012).
- [42] A. K. Cheetham, G. Férey, and T. Loiseau, *Angewandte Chemie International Edition* **38**, 3268 (1999).
- [43] A. W. Sleight, *Annual Review of Materials Science* **28**, 29 (1998).
- [44] K. Takenaka, *Science and Technology of Advanced Materials* **13**, 013001 (2012).
- [45] W. Miller, C. Smith, D. Mackenzie, and K. Evans, *Journal of Materials Science* **44**, 5441 (2009).
- [46] A. B. Cairns, A. L. Thompson, M. G. Tucker, J. Haines, and A. L. Goodwin, *Journal of the American Chemical Society* **134**, 4454 (2012).
- [47] A. L. Goodwin, M. Calleja, M. J. Conterio, M. T. Dove, J. S. O. Evans, D. A. Keen, L. Peters, and M. G. Tucker, *Science* **319**, 794 (2008).
- [48] A. B. Cairns *et al.*, *Nature Materials* **12**, 212 (2013).
- [49] A. U. Ortiz, A. Boutin, A. H. Fuchs, and F.-X. Coudert, *Physical Review Letters*, **109**, 195502 (2012).
- [50] B. D. Cullity, *Elements of X-Ray Diffraction* (Addison-Wesley Publishing Company, Inc. 1978).

- [51] J. Rodriguez-Carvajal, in *satellite meeting on powder diffraction of the XV congress of the IUCr* (Toulouse, France:[sn], 1990).
- [52] P. Brüesch, *Phonons: Theory and Experiments II: Experiments and Interpretation of Experimental Results* (Springer Science & Business Media, 2012), Vol. 65.
- [53] G. E. Bacon, *Neutron Diffraction* (Clarendon Press, Oxford, 1975).
- [54] J. M. Carpenter and D. L. Price, *Physical Review Letters* **54**, 441 (1985).
- [55] Price, David Long. *Methods of Experimental Physics*. (Academic Press, 1986).
- [56] G. L. Squires, *Introduction to the theory of thermal neutron scattering* (Cambridge university press, 2012).
- [57] S. L. Chaplot, N. Choudhury, S. Ghose, R. Mittal, and G. Prabhathasree, *European Journal of Mineralogy* **14**, 291 (2002).
- [58] A. Sjolander, *Arkiv Fysik* **14** (1958).
- [59] P. Brüesch, *Phonons: Theory and Experiments I* (Springer-Verlag Berlin Heidelberg New York, 1982), Vol. 34.
- [60] L.-Q. Chen, L.-D. Chen, S. V. Kalinin, G. Klimeck, S. K. Kumar, J. Neugebauer, and I. Terasaki, *NPJ Computational Materials* **1**, 15007 (2015).
- [61] M. Born and K. Huang, *Dynamical Theory of Crystal Lattices* (Clarendon Press, 1998).
- [62] M. Born, *Annalen der Physik* **349**, 605 (1914).
- [63] K. Parlinski, *PHONON*, 2003.
- [64] R. P. Feynman, *Physical Review* **56**, 340 (1939).
- [65] W. Kohn, A. D. Becke, and R. G. Parr, *The Journal of Physical Chemistry* **100**, 12974 (1996).
- [66] P. Hohenberg and W. Kohn, *Physical Review* **136**, B864 (1964).
- [67] W. Kohn and L. J. Sham, *Physical Review* **140**, A1133 (1965).
- [68] W. Koch and M. C. Holthausen, *A chemist's guide to density functional theory* (John Wiley & Sons, 2015).
- [69] R. G. Parr and W. Yang, (Oxford University Press, New York, 1989).
- [70] D. C. Langreth and M. Mehl, *Physical Review B* **28**, 1809 (1983).
- [71] A. D. Becke, *Physical Review A* **38**, 3098 (1988).
- [72] J. P. Perdew, K. Burke, and M. Ernzerhof, *Physical Review Letters* **77**, 3865 (1996).
- [73] A. I. Lichtenstein, R. O. Jones, H. Xu, and P. J. Heaney, *Physical Review B* **58**, 6219 (1998).
- [74] S. Dudarev, G. Botton, S. Savrasov, C. Humphreys, and A. Sutton, *Physical Review B* **57**, 1505 (1998).
- [75] S. Grimme, *Journal of Computational Chemistry* **27**, 1787 (2006).
- [76] M. Dion, H. Rydberg, E. Schröder, D. C. Langreth, and B. I. Lundqvist, *Physical Review Letters* **92**, 246401 (2004).
- [77] K. Lee, É. D. Murray, L. Kong, B. I. Lundqvist, and D. C. Langreth, *Physical Review B* **82**, 081101 (2010).
- [78] G. Kresse and J. Furthmüller, *Computational Materials Science* **6**, 15 (1996).
- [79] G. Kresse and J. Furthmüller, *Physical Review B* **54**, 11169 (1996).

- [80] E. Grüneisen and E. Goens, *Z. Phys.* **29**, 141 (1924).
- [81] Y. Le Page and P. Saxe, *Physical Review B* **65**, 104104 (2002).
- [82] F. Mouhat and F.-X. Coudert, *Physical Review B* **90**, 224104 (2014).
- [83] S. Baroni, P. Giannozzi, and A. Testa, *Physical Review Letters* **58**, 1861 (1987).
- [84] X. Gonze, *Physical Review A* **52**, 1086 (1995).
- [85] G. Henkelman, (www.hankelmanlab.org) 2001.
- [86] M. P. Allen and D. J. Tildesley, *Computer Simulation of Liquids* (Oxford university press, 2017).
- [87] J. Hafner, *Journal of Computational Chemistry* **29**, 2044 (2008).
- [88] M. E. Tuckerman, *Journal of Physics: Condensed Matter* **14**, R1297 (2002).
- [89] I. Todorov, W. Smith, and U. Cheshire, STFC, STFC Daresbury Laboratory, Daresbury, Warrington, Cheshire, WA4 4AD, United Kingdom, version **4** (2011).
- [90] H. Mehrer, *Diffusion in solids: fundamentals, methods, materials, diffusion-controlled processes* (Springer Science & Business Media, 2007), Vol. 155.

CHAPTER 2

β -Eucryptite, LiAlSiO_4 : A Potential Solid Electrolyte for Li-ion Battery

2.1 Introduction

Clean and green storage of energy is achievable by various energy storage technologies[1-4]. Batteries are one of the most eligible devices[5-8] for this purpose. The solid state batteries[6,9-12] offer a most compact and safe version to store energy at various scales. These batteries contain a solid electrolyte between two electrode materials and hence no separator is required to fabricate these batteries. The solid electrolyte[13], being more stable[6,9-11] than liquids, could resolve the issue of leakage, chemical stability, vaporization, flammability and dendrites formation to a great extent. It will also enable the use of metallic Li as anode material[9,14] and will enhance the current charge capacities.

LiAlSiO_4 (β -eucryptite) is one of the most promising candidate in this category of ionic conductors[15-17]. It shows a large ionic conductivity, very low volume thermal expansion[18,19] and good mechanically stability which make it a potential electrolyte in Li-ion batteries[20]. These properties also make it useful in domestic cookware, high-precision machines, optical devices and as a good thermal shock resistance material. The current chapter involves the study of mechanism responsible for NTE, high temperature phase transition, superionic conductivity and various factors enhancing the ionic conductivity in β -eucryptite.

2.1.1 Structural Details

β -eucryptite crystallizes[21,22] in a hexagonal structure with the space group- $P6_222$. It is basically a stuffed derivative of β -quartz[23]. It contains double helices of SiO_4 and AlO_4 tetrahedra. This produces alternating layers of Al and Si normal to the hexagonal c -axis[21,24].

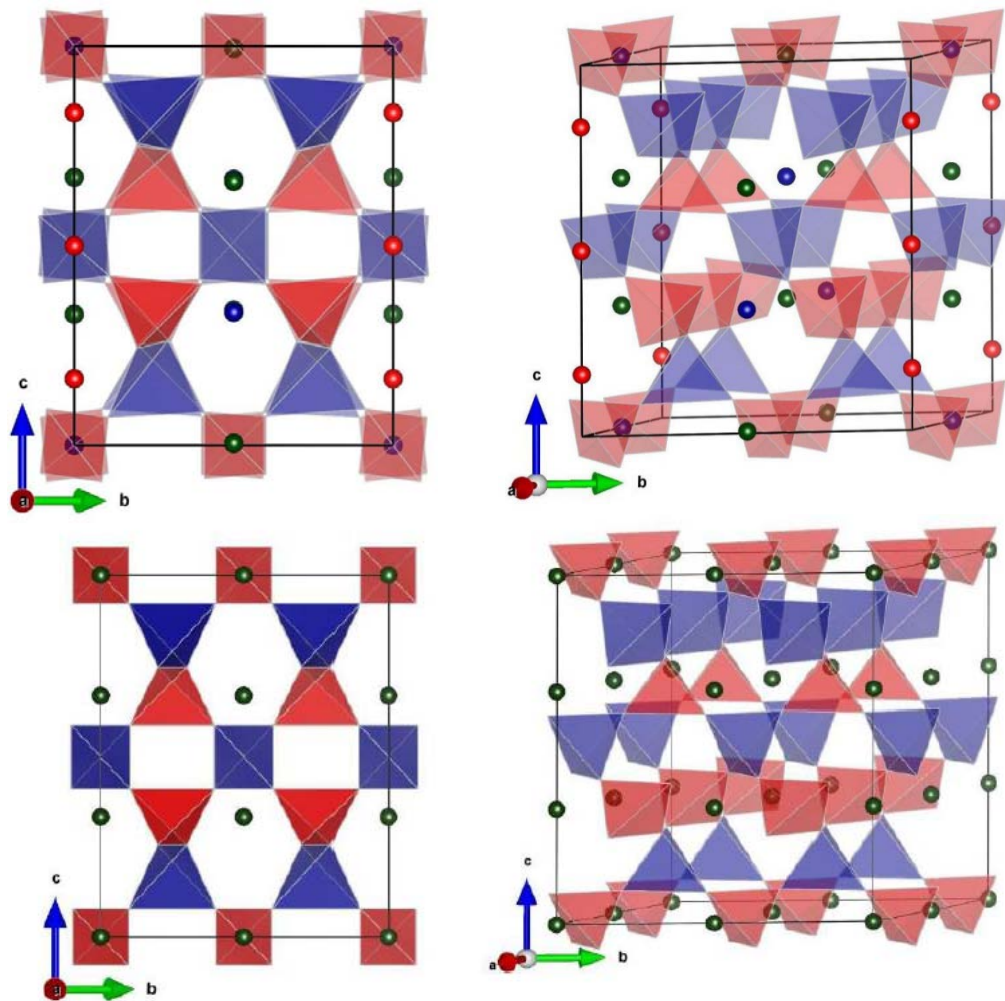


FIG 2.1 Schematic representation of (Top)the unit cell structure of room temperature phase of β -eucryptite, projected along different axes, Li1(Red) occupies A-type channel while Li2 & Li3 (Blue & Green) occupy S-type channels. (Bottom) the unit cell structure of high temperature phase (supercell $2 \times 2 \times 1$) of β -eucryptite, projected along different axes. AlO_4 and SiO_4 tetrahedra are in blue and red colour respectively.

The room temperature phase of β -eucryptite[22] (Fig 2.1) contains 12 *Li* atoms which are present at three different Wyckoff sites namely *3b*, *3c* and *6f*. These *Li* atoms are distributed in the channels along the hexagonal *c*-axis. Each channel has six available tetrahedral sites; however, at ambient temperature, only three of the available sites are occupied[22] in an alternating sequence. There are two types of channels[22], namely, ‘S’ type and ‘A’ type. In ‘S’ type channel *Li* atoms are coplanar with the *Si* atoms while in ‘A’ type channel *Li* atoms are coplanar with the *Al* atoms. There are three secondary (*S*) and one primary (*A*) channel in a single unit cell of the room temperature structure[22]. Another difference between these channels is that the ‘A’ type channel contains *Li* which are present at $3b(x,y,z)$ Wyckoff site and is named as *Li1*, while the ‘S’ type channels have a distribution of *Li* over $3c(x,y,z)$ and $6f(x,y,z)$ sites and are named as *Li2* and *Li3* respectively. Moreover, when ‘A’ type channel is moved by $c/6$ along the hexagonal *c*-axis, it becomes ‘S’ type channel[22]. β -eucryptite shows an isostructural phase transition at high temperature (above 673K) as studied by X-ray and neutron diffraction[19,22,25-28]. This transition is accompanied with a large increase in the conductivity of the compound. This reversible isostructural phase transition involves the disordering of *Li*-sites and geometrical changes in the framework through *Al/Si* tetrahedral deformation and tilting. The high-temperature form is accompanied by a statistical distribution of *Li* over all the available tetrahedral sites among the channels[27,28]. The average structure of the high-temperature phase (Fig 2.1) has three formula units (21 atoms in the unit cell), with all the *Li* atoms lying in the *Si* layers[22,25].

2.1.2 Motivations and Objectives of Research

The compound β -eucryptite shows a strong anisotropic thermal expansion behavior[19,22,29]^(a) ($\alpha_c \approx -2\alpha_a$) with linear thermal expansion coefficients of about $\alpha_a=8.6 \times 10^{-6} \text{K}^{-1}$ and $\alpha_c=-18.4 \times 10^{-6} \text{K}^{-1}$, which results in a very low volume thermal expansion over a wide temperature range of 300-1400 K. Earlier lattice dynamics calculations[29] of β -eucryptite provided a fair description of the thermal expansion behavior. Perhaps due to limited computational resources at that time and structural complexity, the accuracy of the calculation was limited. However, it was clear that an improved description of the phonon spectrum in the entire Brillouin zone is needed to accurately reproduce the observed anomalous thermal expansion in β -eucryptite. Moreover, it is necessary to identify the specific phonon modes to understand the microscopic mechanism of the anomalous thermal expansion.

The high temperature phase shows a large one-dimensional ionic conductivity[15,16,30-32] along the hexagonal c -axis. The ionic conductivity is reported to be due to inter- and intra-channel correlated motions of Li along the c -axis[16,26,30,31]. Single crystal electrochemical transport measurements show 30 times higher conductivity along the c -axis than within the a - b plane at about 773K[15,16]. The intra-channel correlation of Li-Li is reported to be much stronger than the inter-channel correlation[26], which corroborates the cooperative motion of Li along the channel in the superionic regime. Quasi-elastic neutron scattering studies[31] of β -eucryptite show jump diffusion of Li by $c/3$, along the hexagonal c -axis. The temperature dependent phonon spectra across the phase transition temperature is required to find the phonon modes governing the high temperature phase transitions and superionic conduction of Li in this compound.

It is rather difficult to determine the structural and dynamical behaviour of Li atoms experimentally[33]. Li has a small atomic number ($Z=3$), which makes it poor scatterer in x-ray experiments. Further, the low scattering cross section ($= 1.37$ barns) and high absorption cross section ($= 70.5$ barns) of Lithium for neutrons makes it difficult to perform neutron scattering experiment. The Li atoms become highly anharmonic at higher temperatures due to its low atomic mass (3 a.m.u.). Computational tool provide a good alternative to study the atomic scale behaviour of Li atom[34,35]. The calculation of the phonon spectra within molecular dynamics (MD) simulation directly considers the effect of temperature on the phonons, or phonon anharmonicity[36,37]. In this chapter, a combination of inelastic neutron scattering and state of art computational tools like DFT, LD and MD are used to study[38-40] NTE, high temperature phase transition and superionic properties of β -eucryptite. The anisotropic pressure dependence of phonon spectra calculated using *ab-initio* lattice dynamics are coupled with the elastic tensor of β -eucryptite to obtain the role of phonon in NTE along c -axis. The temperature dependent inelastic neutron scattering measurements in β -eucryptite over the extended temperature range from 313 K to 898 K to cover the reported anomaly in ionic conductivity. We have performed molecular dynamics simulations[38,40] at various temperatures for the analysis of temperature dependent inelastic neutron spectra. The calculated phonon spectra, partial phonon density of states, mean square displacements, diffusion coefficient and pair correlation functions are discussed in relation to observed superionic Li conduction in β -eucryptite. The various factors affecting the diffusion of Li in the high temperature phase of β -eucryptite are discussed. The anisotropy of diffusion pathways and the correlated diffusion are analysed from the trajectory of Li atoms at high temperature. All the calculations are performed by considering an ordered average structure of high temperature phase of β -eucryptite.

2.2 Experimental and Computational Details

About 10 grams of polycrystalline sample of β -eucryptite is used for the inelastic neutron scattering measurements. The sample was put inside a cylindrical niobium sample holder and mounted in a furnace for measurements at temperatures, 313, 498, 673 and 898 K, respectively. The experiments are carried out using the high-flux time-of-flight (IN4C) spectrometer at the Institut Laue Langevin (ILL), France. Thermal neutrons of wavelength 2.4 Å (14.2 meV) are used for the measurements. The scattering function $S(Q, E)$ is measured in the neutron energy gain mode.

The classical molecular dynamics (MD) simulations has been performed using $6 \times 6 \times 3$ supercell (2268 atoms) of high temperature phase β -eucryptite with periodic boundaries using DL_POLY[41] simulation package. The system was first thermally equilibrated using NPT ensemble for 50ps to achieve the required temperature and 0 kbar pressure. The Langevin Thermostat with friction parameter 0.1 ps^{-1} is used to achieve and maintain the desired temperature. The velocity was rescaled every 10 steps during the equilibration process. After the equilibration, the system was allowed to relax for 50 ps. Finally, a MD production run of 200 ps is performed in microcanonical ensemble (NVE) where the temperature was monitored and found to be constant with minor fluctuations. A time step of 1 fs was used for the integration of the equations of motion. The radial distribution function was calculated after every 50 steps. We have used the Columbic and Buckingham type inter atomic potential[42] as given below

$$V(r_{ij}) = -\frac{1}{4\pi\epsilon_0} \frac{q_i q_j}{r_{ij}^2} + \left(A e^{-\frac{r_{ij}}{\rho}} - \frac{B}{r_{ij}^6} \right)$$

Where, $r_{ij} = |r_i - r_j|$, q_i, q_j are ionic charges, A, B and ρ are potential parameters. The parameters of the potential (Table 2.1) are taken from S. Asel et al.[43].

TABLE 2.1 The partial ionic charges and potential parameters[43] used in MD simulations. The charge q_i for Li, Al, Si and O are 1.0, 1.4, 2.4 and -1.2, respectively.

Interacting Atom Pairs(i,j)	A_{ij} (eV)	ρ_{ij} (\AA^{-1})	C_{ij} (eV \AA^{-6})
Li-O	1149.4126	0.28048	0.0
O-O	1388.773	0.3623	175.0
Al-O	16008.5345	0.20847	130.5659
Si-O	18003.75	0.2052	133.538

For the accurate calculations of structure and dynamics, *ab-initio* DFT calculations are performed using VASP software[44,45]. The plane wave pseudo-potential with a plane wave kinetic energy cutoff of 820 eV was adopted. The integration over the Brillouin zone is sampled using a k-point grid of $2 \times 2 \times 2$, generated automatically using the Monkhorst-Pack method[46]. The above parameters were found to be sufficient to obtain a total energy convergence of less than 0.1 meV for the fully relaxed geometries. The Hellman-Feynman forces are calculated in the finite displacement method (displacement 0.04 \AA). The convergence criteria for the total energy and ionic forces were set to 10^{-8} eV and 10^{-5} eV \AA^{-1} . The phonon energies were extracted from subsequent calculations using the PHONON software [47]. The anisotropic thermal expansion behaviour is calculated from the anisotropic pressure dependent phonon spectra in the framework of quasiharmonic approximations[48]. The activation energy for the Li movement was calculated with the climbing-image nudged-elastic-band [49] method.

The *ab-initio* molecular dynamics simulations (ABIMD) are also performed as a function of temperature for LiAlSiO_4 using VASP. The thermal expansion of LiAlSiO_4 is obtained from Parrinello-Rahman (NPT) dynamics[50,51] with Langevin thermostat[52]. The Newton's equations of motion are integrated using the Verlet's algorithm with a time step of 2 fs. A unit cell of 84 atoms for the room temperature (RT) phase and a supercell of 189 atoms, equivalent to $3 \times 3 \times 1$ supercell of the high-temperature phase (21 atoms per

unit cell), subject to the periodic boundary conditions are used. Further, to study the RT to HT phase transition and lithium diffusion in the HT phase, NVT ensemble with Nosé thermostat[53] is used. Initially, the structure was equilibrated for 2 ps to attain the required temperature in NVT simulations. Then the production runs up to 10 ps in NVE simulation are performed (the temperature remained essentially constant). Simulations are performed for a series of temperatures from 300 to 1200 K. At each temperature, a well-equilibrated configuration is observed during the 10 ps simulation.

2.3 Results and Discussions

First, the results from the inelastic neutron scattering (INS) measurements and classical MD simulations are given followed by the *ab-initio* calculations. This section will also cover the limitations of classical MD simulations and requirements of *ab-initio* MD calculations in LiAlSiO_4 .

2.3.1 Inelastic Neutron Scattering Measurements

The temperature dependent measurements of inelastic neutron spectra (Fig 2.2(a)) of LiAlSiO_4 are carried out at temperatures, namely, 313 K, 498 K, 673 K and 898 K, across the order-disorder and superionic phase transition reported around 698-755 K[28]. At 313 K, the high energy phonon modes do not populate significantly; hence, the data have poor statistics for these modes, which prevents us to obtain the full-energy range of the phonon spectra. Upon heating, the high-energy phonon modes get populated, and therefore data can map the full energy range up to 150 meV. The data are corrected for multiphonon contribution as calculated using Sjolander[54] formalism. The temperature-dependent spectra consist of several peaks around 15, 25, 40, 55, 85 and 125 meV (Fig 2.2(a)). A

previous infrared study of β - LiAlSiO_4 showed absorption peaks in the energy range of 100 - 1200 cm^{-1} (12 to 150 meV)[32], which is consistent with the neutron data.

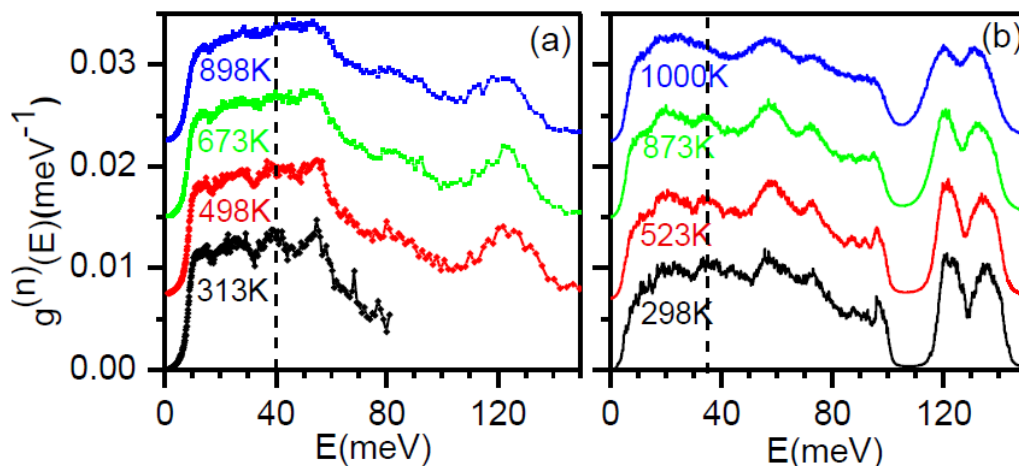


FIG 2.2 Temperature dependent (a) experimental inelastic neutron scattering spectra, and (b) calculated neutron weighted spectra using MD simulations. For clarity, the spectra are shifted vertically. The peak corresponding to Li vibrations in the phonon spectra is highlighted by dotted line.

2.3.2 Classical Molecular Dynamical Simulations

2.3.2.1 Phonon Spectra

In order to analyse the experimental phonon spectra, the MD simulation are performed at various temperatures. The phonon spectra obtained from MD incorporate the temperature effects [37] which helps us to better understand the temperature dependent inelastic neutron spectra and Li diffusion. The calculated neutron weighted total phonon density of states (Fig 2.2 (b)) is in good agreement with the experimental spectra and validated the MD simulations.

The calculated as well as the experimental phonon spectra show that the phonon modes belong to two distinct regions and exhibit a significant band gap. The first region

extends up to 100 meV and has contributions from the vibrations of all the atoms in the unit cell. On the other hand, the high-energy part of the spectrum, between 110-150 meV, largely corresponds to the internal vibrations of the SiO_4 and AlO_4 tetrahedra. The available IR measurements show that the IR bands around 246 (30.5 meV) and 300 cm^{-1} (37.2 meV) broaden and weaken dramatically at around 715 K. Moreover, a change in slope in the temperature dependence of the IR phonon frequency near 300 cm^{-1} (37.2 meV) and the line width of the 760 cm^{-1} (94 meV) band at 715 K is observed.

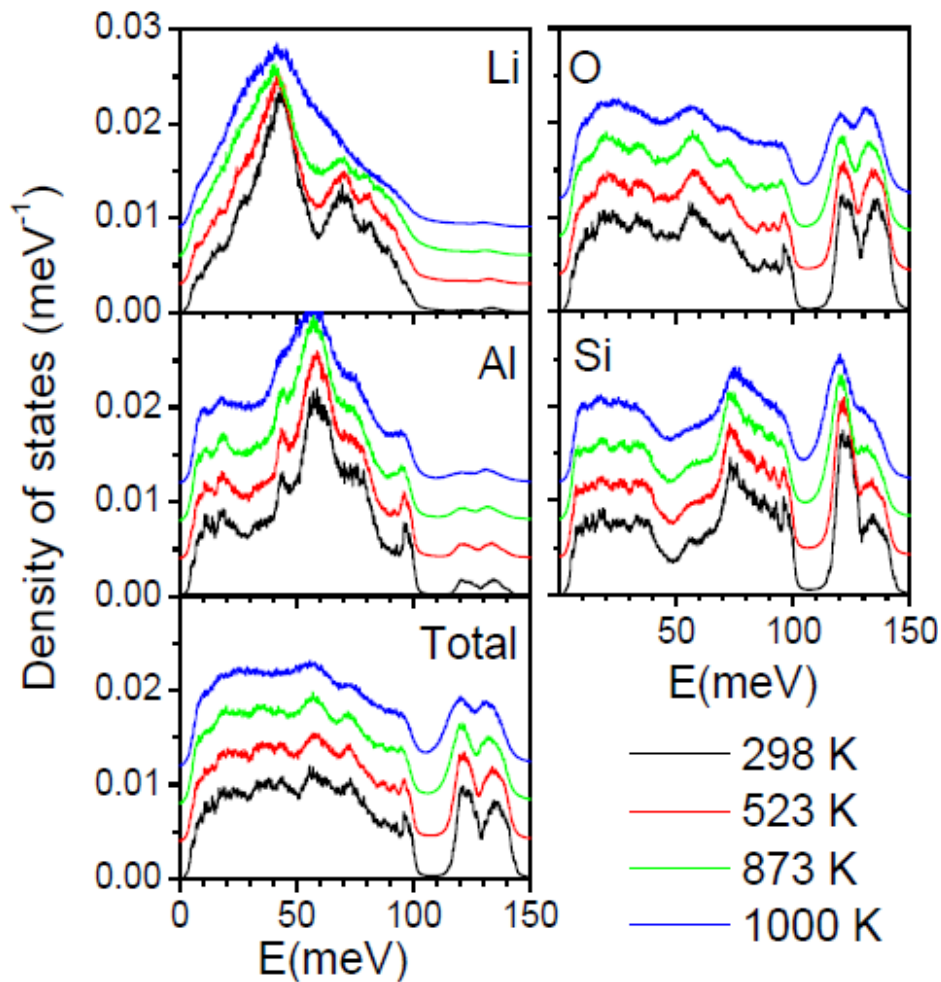


FIG 2.3 Temperature dependent partial phonon densities of states for various atoms in β -eucryptite obtained from MD simulations. For clarity, the spectra are vertically shifted.

The calculated partial density of states using molecular dynamics (Fig 2.3) show that the phonon spectra in energy range from 30 meV-50 meV are highly contributed by Li dynamics. This region in the phonon spectra is broadened with increase in temperature, which can be seen from the experimental (Fig 2.2(a)) as well as calculated phonon density of states (Fig 2.2(b)). The reason for this broadening may be the large increase in mean squared displacement of Li atom as a function of increase in temperature.

2.3.2.2 Lithium Diffusion and Thermal Expansion

At high temperature, the anharmonic contributions are significantly large. To account these effects, we have calculated mean square displacements (MSD) of various atoms in LiAlSiO_4 , using the MD simulations. At 1200 K, the calculated MSD (Fig 2.4 (b)) of Al, Si and O atoms saturate with time. However, for Li atoms it is found to increase with time. The continuous increase in MSD of Li atom signifies the diffusion of Li inside the crystal.

The calculated diffusion coefficients at various temperatures for Li atoms show an anomalous jump in the (Fig 2.5) above 1200 K. The calculated diffusion coefficients are of the order of $10^{-10} \text{ m}^2\text{s}^{-1}$ which is in the regime of superionic conductors. The high temperature structure of LiAlSiO_4 may have vacancies. So, the calculation of diffusion coefficients is also performed for structure with Li vacancy. In order to have a neutral structure, we have removed a complete formula unit in the supercell ($6 \times 6 \times 3$, 2268 atoms) of the HT phase of LiAlSiO_4 . The supercell dimension was $\approx (31 \text{ \AA} \times 31 \text{ \AA} \times 33 \text{ \AA})$. The snapshot of vacant positions is given in Fig 2.4(a). The distance between any two vacant sites is more than 13 \AA which is sufficient to avoid any unusual effect due to vacancy-vacancy interactions during the simulations.

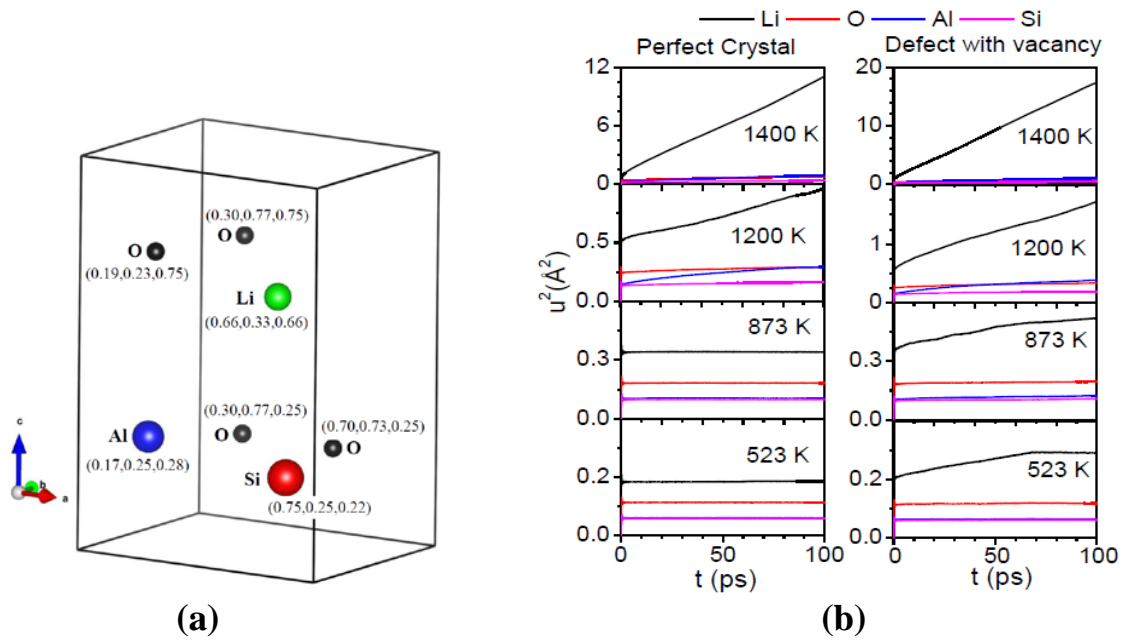


FIG 2.4 (a) The position of vacant sites of various atoms in $(6 \times 6 \times 3)$ supercell of high temperature phase of LiAlSiO_4 , (b) The calculated mean square displacement as a function of time for the different atoms of β -eucryptite at various temperatures for (Left) perfect crystal and (Right) the structure with a vacancy.

The calculated diffusion coefficients for the vacancy containing (defected) structure (Fig 2.5) show that the diffusion of Li atom in structure with vacancy starts at 1100 K as compared to that of 1200 K in the perfect structure. When the vacancies are created in the crystal of LiAlSiO_4 supercell, the available volume/atom increases and a concentration gradient is developed in the neighbourhood of a vacant site. This decreases the randomness in jumping processes because vacancy induces a directional jump. As the vacant site attracts the Li ion from its neighbouring site, the energy barrier for Li diffusion decreases and hence diffusion of Li occurs at lower temperature as compared to that in the perfect crystal.

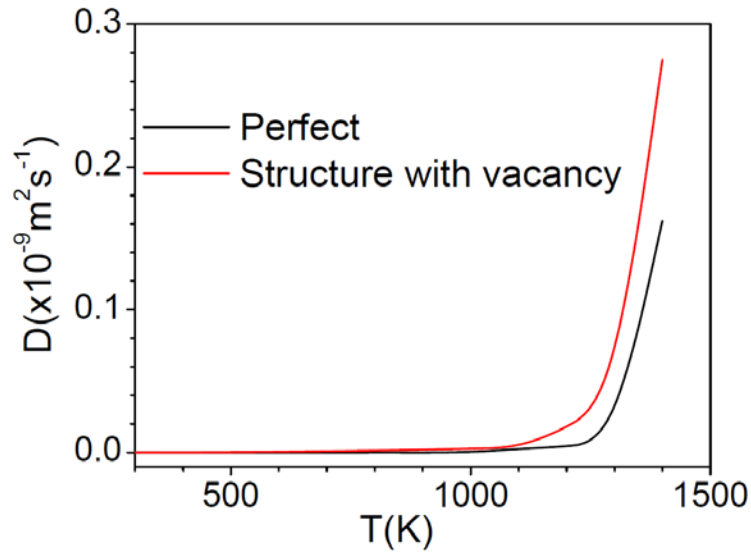


FIG 2.5 The diffusion coefficient for Li as a function of temperature for perfect crystal and the structure with a vacancy for β -eucryptite as calculated using MD simulations.

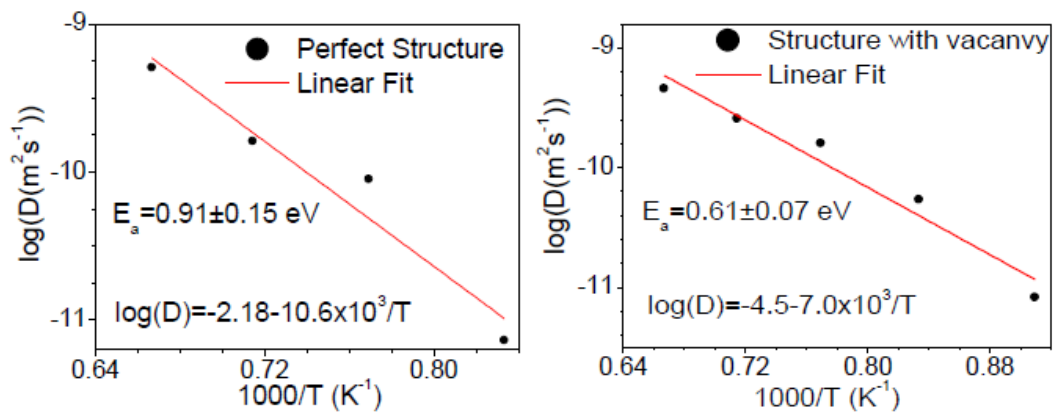


FIG 2.6 The activation energy for Li jump diffusion obtained from Arrhenius plot of diffusion coefficient as a function of temperature.

The slope of Arrhenius plot of diffusion coefficients versus temperature provides the activation energy for Li diffusion in β -eucryptite (Fig 2.6). The activation energy for Li diffusion in perfect as well as in defected structure is calculated to be 0.91 ± 0.15 eV and 0.61 ± 0.07 eV respectively.

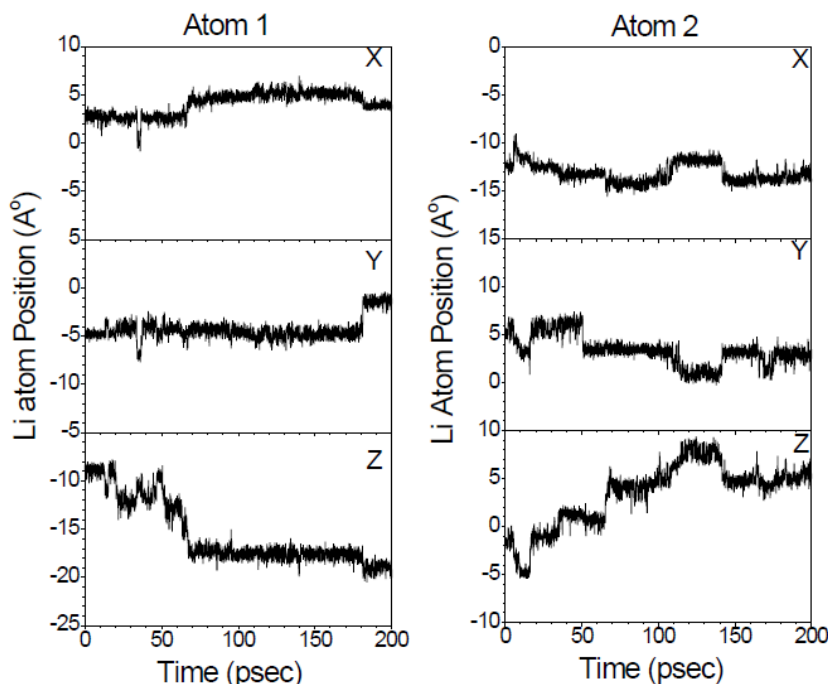


FIG 2.7 Trajectory of selected Li atoms in a perfect crystal of LiAlSiO_4 at 1400 K is given in Cartesian coordinate. The hexagonal c -axis is along the z -direction.

In order to understand the microscopic mechanism of superionic conduction in β -eucryptite, the trajectories of Li atoms are analyzed at 1400 K. Fig 2.7 shows the trajectories of a few Li atoms with high mean square displacements. It can be seen that with increase in time, Li atoms show large jumps in the position coordinates. The jump like behavior is more pronounced along the z -direction (along the hexagonal c -axis) as compared to that along the x - or y -axis (in the a - b plane). So, the diffusion process at 1400 K seems to be small anisotropic. The anisotropy is less pronounced due to the isotropic nature of the Columbic and Buckingham type interatomic potentials[43].

These simulations enabled us to calculate the thermal expansion behavior of this compound. At room temperature, the calculations (Fig 2.8) underestimated the ' a ' lattice parameter while ' c ' parameter is in very good agreement with the experimental values[29]. The calculated temperature dependence of ' a ' lattice parameter shows positive

thermal expansion behavior in line with the experiments. On the other hand, along c -axis, the calculations show positive thermal expansion behavior contrary to the experimentally observed negative thermal expansion along this axis (Fig 2.8). Since both the thermal expansion and superionic diffusion are temperature driven phenomenon, therefore discrepancy of calculated anisotropy in diffusion and thermal expansion may arise from the same reason which is suspected to be the isotropic nature of force field used in these calculations. This motivated us to perform the *ab-initio* calculations which are known to provide a very accurate measure of anisotropy in solids.

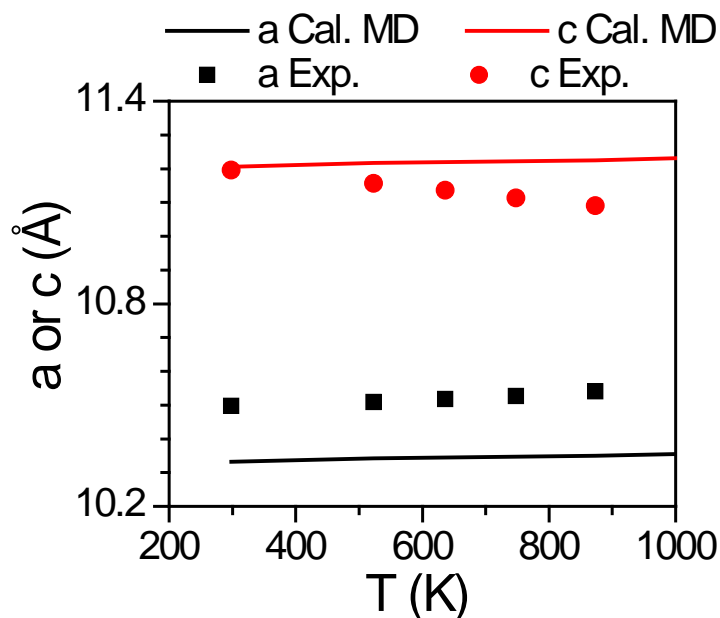


FIG 2.8 The calculated and experimental [29] temperature dependent lattice parameters of high temperature phase of LiAlSiO_4 .

2.3.3 First-Principles Calculations

In order to know the shortcomings of classical force fields and to understand the mechanism of experimentally observed anisotropy in the thermal expansion and superionic conduction behavior of β -eucryptite, the *ab-initio* DFT, lattice dynamics (LD)

as well as *ab-initio* molecular dynamical simulations are performed. The *ab-initio* optimized structure of ambient temperature phase of β -eucryptite is compared with the experimental structure (Table 2.2) and is used for all further calculations. The results from these calculations are discussed in the following subsections.

2.3.3.1 Mechanism of Negative Thermal Expansion

The anisotropic thermal expansion behavior can be calculated using the elastic constant tensor and anisotropic Grüneisen parameters. The elastic constants (Table 2.3) are calculated using the symmetry-general least square method[55] as implemented in VASP. The calculated elastic constants and bulk modulus are in good agreement with the reported experimental[56] data as well as other estimations from the literature[57].

TABLE 2.2 *The experimentally refined and calculated structure of β -eucryptite. The atomic positions in the space group $P6_422$ are Li1 at $3b(x,y,z)$, Li2 at $3c(x,y,z)$, Li3 at $6f(x,y,z)$, and O1, O2, O3 and O4 at $12k(x,y,z)$, and Al1 at $6h(x,y,z)$, Al2 at $6j(x,y,z)$, and Si1 at $6g(x,y,z)$ and Si2 at $6i(x,y,z)$ Wyckoff site.*

		Experimental[22]			Calculated		
a (Å)		10.497			10.574		
c (Å)		11.200			11.410		
Atoms	Wyckoff site	x	y	z	x	y	z
Li(1)	3b	0	0	0.5	0	0	0.5
Li(2)	3c	0.5	0	0	0.5	0	0
Li(3)	6f	0.5	0	0.324	0.5	0	0.328
O(1)	12k	0.0853	0.1942	0.2428	0.087	0.198	0.242
O(2)	12k	0.6023	0.7008	0.2651	0.601	0.697	0.261
O(3)	12k	0.1101	0.7099	0.2597	0.106	0.706	0.263
O(4)	12k	0.5902	0.2011	0.2494	0.592	0.1998	0.251
Al(1)	6h	0.2520	0	0.5	0.251	0	0.5
Al(2)	6j	0.2506	0.5012	0.5	0.251	0.502	0.5
Si(1)	6g	0.2486	0	0	0.248	0	0
Si(2)	6i	0.2477	0.4954	0	0.248	0.496	0

The anisotropic Grüneisen parameters are calculated by applying an anisotropic stress of 0.25 GPa by changing the lattice constant ‘ a ’ and keeping the ‘ c ’ parameter constant, and vice versa, where temperature is held constant at zero. The symmetry of the unit cell is kept invariant on introduction of strain, while performing the calculations. The calculated mode Grüneisen parameters as a function of phonon energy along different directions are shown in Fig 2.9 (a). The Grüneisen parameters has large negative value for the low-energy phonon modes around 10 meV and has positive value for the high-energy modes in the range 30 to 70 meV.

TABLE 2.3 Calculated and experimental elastic constants in GPa units in β -eucryptite.

	C_{11}	C_{12}	C_{13}	C_{33}	C_{44}	C_{66}	Bulk Modulus
Our Calculations	171.6	79.0	92.9	140.0	60.0	46.3	113.1
Experimental[56]	176.3	68.5	89.8	139.9	61.2	53.9	109.9
Calculation[58]	178.9	102.8	118.3	181.3	47.4	38.1	134.9
Calculation[57]	165.6	71.0	78.6	132.8	58.7	47.3	101.5

The calculated linear thermal expansion coefficients and the lattice parameters as a function of temperature are shown in Fig 2.9(b) and 2.9(c) respectively. The calculated temperature dependence of the lattice parameters is in excellent agreement (Fig 2.9(c)) with the experimental data[19,29]. The calculated linear thermal expansion coefficients at 300 K are $\alpha_a = 6.0 \times 10^{-6} \text{ K}^{-1}$ and $\alpha_c = -13.7 \times 10^{-6} \text{ K}^{-1}$. The thermal expansion coefficient for the RT phase in the a - b plane ($\alpha_a(T)$), upto 200 K, has a small negative value (Fig 2.9(b)). It evolves to a positive value at higher temperatures.

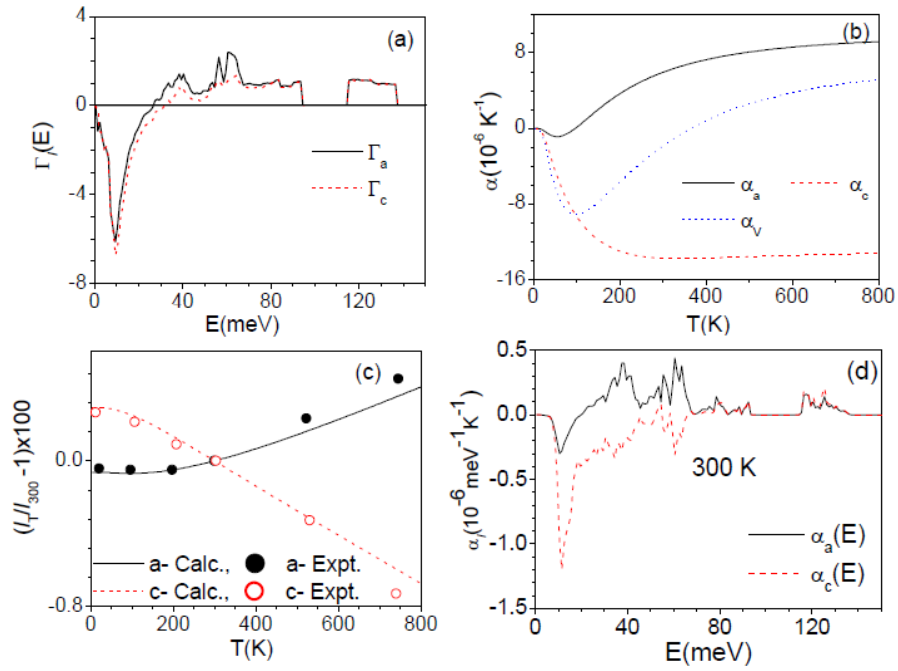


FIG 2.9 (a) The calculated Grüneisen parameters (Γ_l , $l=a, c$) as obtained from anisotropic stress along a - and c -axes. (b) Linear thermal expansion coefficients as a function of temperature (c) The calculated and experimental variation of the lattice parameters ($l= a$ or c) with temperature (d) The contribution of phonons of energy E to the linear thermal expansion coefficients (α_a and α_c), at 300 K, in the RT phase.

The calculated lattice parameters show a very good agreement with the available experimental data up to 600 K but deviate slightly (Fig 2.9(c)) from the experiments at higher temperatures. This might be due to the fact that at high temperature the explicit anharmonicity of phonons plays an important role. This effect has not been considered in the thermal expansion calculation. It can be seen that the compound shows negative volume thermal expansion behaviour below 300 K, and a positive expansion at higher temperatures. The compound has a very small volume thermal expansion coefficient ($\alpha_v = -1.7 \times 10^{-6} \text{ K}^{-1}$) at 300 K, which makes it suitable for application as a high thermal shock resistance material.

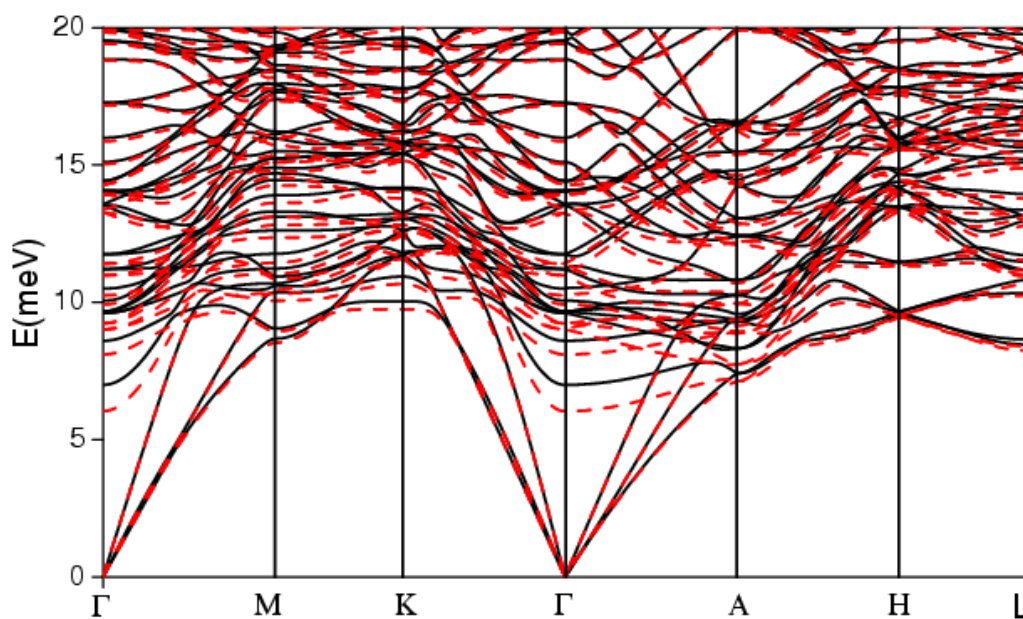


FIG 2.10 Phonon dispersion curves of β -eucryptite, at ambient (solid line) and 0.5 GPa (dash line) pressures, along the high symmetry directions in the Brillouin zone of hexagonal unit cell. The Bradley-Cracknell notation is used for the high-symmetry points: $\Gamma(0,0,0)$, $M(1/2,0,0)$, $K(1/3,1/3,0)$, $A(0,0,1/2)$, $H(1/3,1/3,1/2)$ and $L(1/2,0,1/2)$.

The phonon dispersion relation (Fig 2.10) in the RT phase has been calculated along the high symmetry directions of the hexagonal cell at ambient, as well as at 0.5 GPa. It can be seen that some of the zone centre modes are highly anharmonic. The eigenvectors of some of these anharmonic modes are analyzed (Fig 2.11) to understand the mechanism of anisotropy in the thermal expansion behavior of the compound. The Γ -point mode of 7.0 meV (Fig 2.11) has Grüneisen parameters values of $\Gamma_a=-31.0$ and $\Gamma_c=-30.8$. This mode shows an anti-phase rotation of adjacent polyhedral units (AlO_4 or SiO_4) about all the three directions. The central atom (Al or Si) of the polyhedral units has a small displacement in comparison with oxygen atoms. The next Γ -point mode of 9.6 meV ($\Gamma_a=-13.6$, $\Gamma_c=-15.3$) also involves anti-phase rotation of AlO_4 and SiO_4 but only

about b -axis. Here, the amplitude of rotation for SiO_4 is large in comparison to AlO_4 polyhedral units. The Li atoms in both these modes vibrate in the a - b plane.

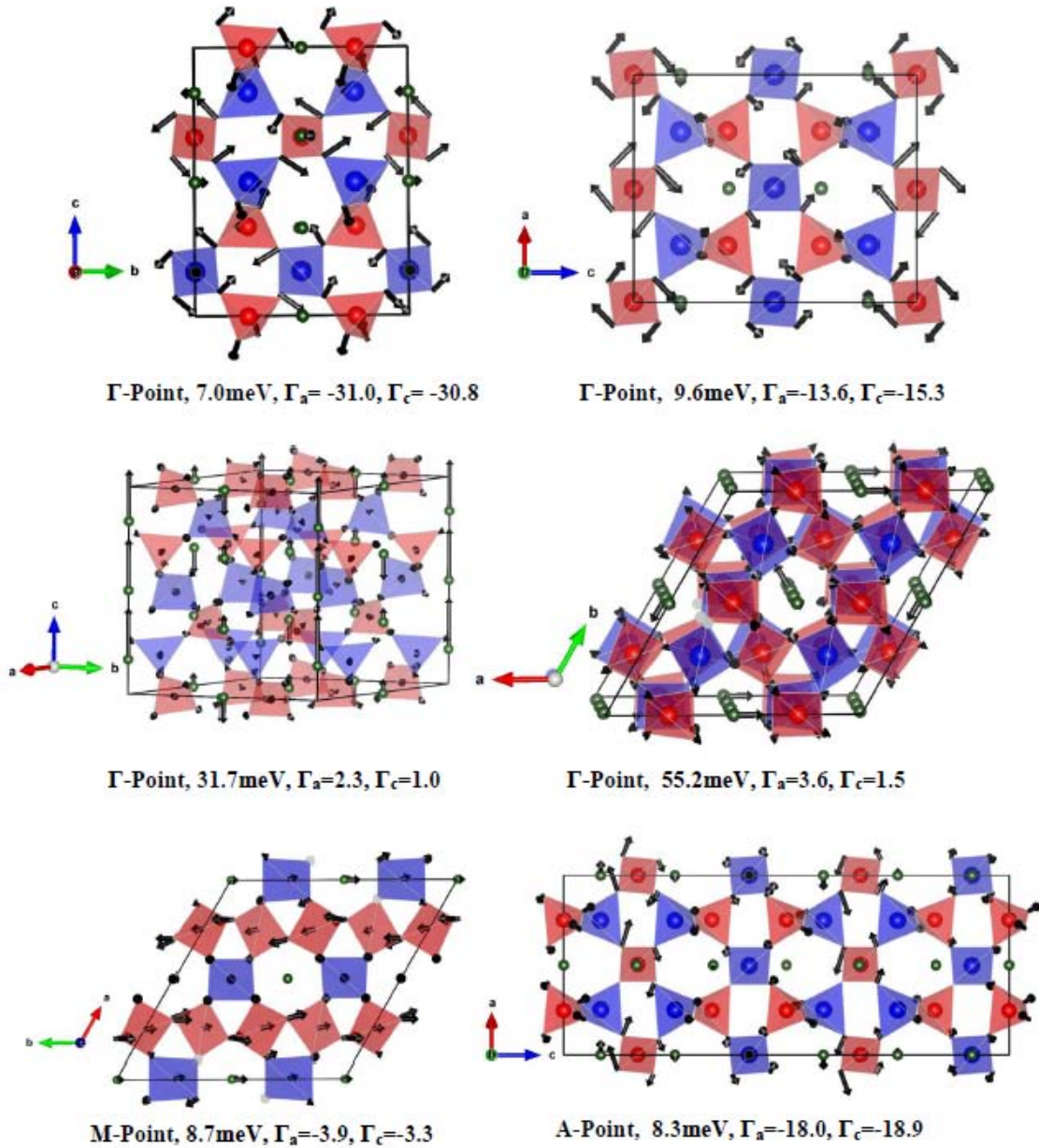


FIG 2.11 Schematic representation of the polarization vectors of selected zone centre optic phonon modes in β - eucryptite. The first, and second and third values specified below each plot indicate the phonon energy and Grüneisen parameters, respectively. The tetrahedral units around Al and Si are color-coded by blue and red respectively, while the Li atoms are represented by a green color.

The high energy, Γ -point, modes of energy 31.7 meV ($\Gamma_a=2.3$, $\Gamma_c=1.0$) and 55.2 meV ($\Gamma_a=3.6$, $\Gamma_c=1.5$) (Fig 2.11) have significant positive Grüneisen parameter value. These modes get populated as temperature is increased and might give expansion in the a - b plane, at higher temperature. These modes are highly contributed by Li motion with very small component of Al and Si tetrahedral rotation and distortions. The mode at 31.7 meV involve the translational motion of Li along the hexagonal channel and might be correlated with the Li diffusion along c -axis, while the other mode at 55.2 meV, involves the Li translation motion in a - b plane.

The M-Point mode (Fig 2.11) of 8.7 meV ($\Gamma_a=-3.9$, $\Gamma_c=-3.3$) reflects a sliding motion of SiO_4 tetrahedral units in the a - b plane. The adjacent SiO_4 layers move in opposite directions along the b -axis. This gives rise to a rotation of the involved AlO_4 polyhedra. The Li atoms in adjacent layers move along b - and c -axis. This type of dynamics induces folding of spirals containing (Al, Si) O_4 polyhedra producing contraction in the system. The A-Point mode at 8.3 meV ($\Gamma_a=-18.0$, $\Gamma_c=-18.9$) shows (Fig 2.10) AlO_4 polyhedral rotation about a -axis while SiO_4 polyhedral rotation about b -axis. Here, oxygen atoms connected to the tetrahedral units have different amplitude and may produce polyhedral distortion. The lithium motion lies in the a - b plane.

TABLE 2.4 The calculated elastic compliance matrix components (s_{ij}) in GPa^{-1} units for β -eucryptite.

S₁₁	S₁₂	S₁₃	S₃₃	S₄₄	S₆₆
0.00932	-0.00148	-0.00520	0.01405	0.01668	0.02163

At low temperature, low-energy modes contribute significantly to the thermal expansion behavior. Although the above mentioned low-energy modes have almost

similar values of Γ_a and Γ_c ($\Gamma_a \approx \Gamma_c$), yet the anisotropy in thermal expansion behavior is there (Fig 2.9(b-d)). This anisotropy can be understood in terms of elastic properties of β -eucryptite (eq.(1.30)). We have,

$$\alpha_a \propto [s_{11} + s_{12}]\Gamma_a + s_{13}\Gamma_c = 0.008\Gamma_a - 0.005\Gamma_c \quad (2.1)$$

$$\text{and, } \alpha_c \propto [s_{31} + s_{32}]\Gamma_a + s_{33}\Gamma_c = -0.010\Gamma_a + 0.014\Gamma_c \quad (2.2)$$

where, $[s_{11} + s_{12}] = 0.008$, $[s_{31} + s_{32}] = -0.010$, $s_{13} = -0.005$ and $s_{33} = 0.014$ in GPa^{-1} units (Table 2.4).

We note that for low-energy modes $\Gamma_a \approx \Gamma_c < 0$, which imply a negative thermal expansion both along a - and c -axis at low temperatures [Fig 2.9(b-c)]. However, at high temperatures the entire spectra will contribute to the thermal expansion behaviour and larger positive values of Γ_a than those of Γ_c result in a positive thermal expansion in a - b plane and negative thermal expansion along c -axis.

2.3.3.2 Activation Energy Barrier for Li Diffusion

Our classical MD simulations do not show anisotropy in the Li motion as observed in conductivity measurements [27,30] (above 773K up to 875K). For understanding of experimentally observed anisotropic conduction we have calculated energy barrier for Li motion using the DFT. We have calculated the barrier height for Li chain motion along the c -axis and in the a - b plane. The energy profiles for Li-ion diffusion are calculated using the standard climbing-image nudged elastic band method [49]. The search for the saddle point is implemented by assuming 6–10 intermediate “images” between each pair of local minima. Each of the images is relaxed until the forces perpendicular to the minimum energy path are less than 0.01 eV/\AA .

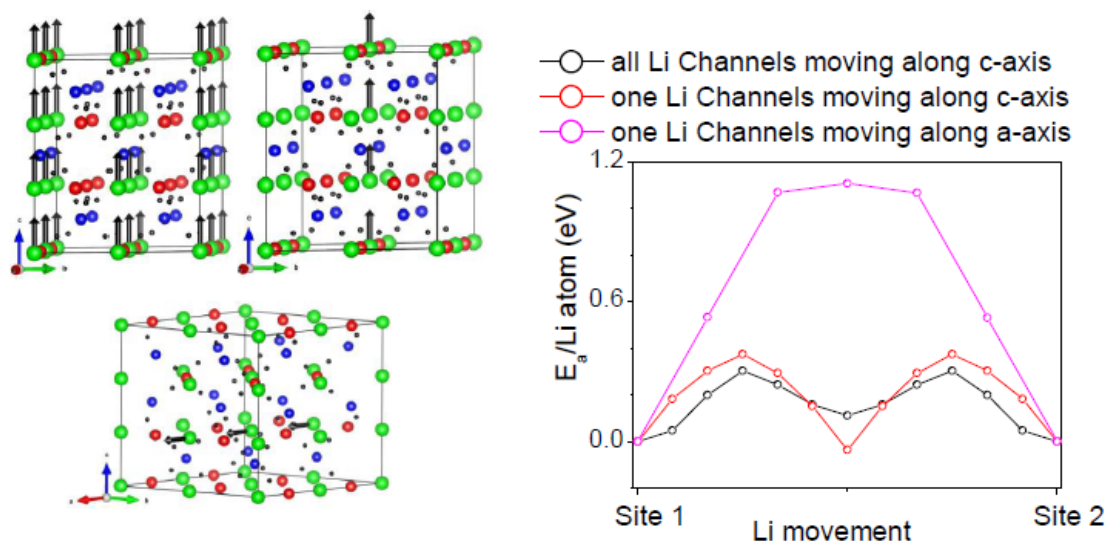


FIG 2.12 Comparison between the barrier heights for the Li channels movement along a (or b -) and c -axis of β -eucryptite. “Site 1” and “Site 2” represent the initial and final positions of Li atoms movement as indicated by arrows in the left panel. Key: Li, Green sphere; Al, Blue sphere; Si Red sphere; O, Black sphere.

In the high temperature phase, all the channels containing Li are equivalent and there are six available sites for Li in each channel[25]. The energy profile for Li channel diffusion is calculated for the cooperative Li motion in the possible ways, namely, by moving (i) all Li containing channels along c -axis (ii) One channel containing Li atoms along c -axis, and (iii) one channel containing Li atoms along a -axis (or b -axis). It can be seen (Fig 2.12 & Table 2.5) that the energy for Li channel motion along a -axis (or b -axis) is an order of magnitude higher than that along the c -axis. Hence, the c -axis provides a minimum energy pathway for Li channel diffusion in LiAlSiO_4 . Moreover, the activation energy barrier per Li atom for the motion of all Li channels (inter-channel correlation) and single Li channel (intra-channel correlated) is almost equal. This implies that both the intrachannel and interchannel correlated motion of Li along c -axis are favourable. This agrees with the reported anisotropic conductivity along c -axis in this compound[15,16].

TABLE 2.5 The calculated activation energy for Li channel diffusion in different crystal directions, from *ab-initio* DFT using climbing image nudged elastic band method.

Diffusion Mechanism (Channel)	Activation Energy
All Li containing Channels moving together along c-axis	0.30 eV/Li atom
One Li Channel moving independently along c- axis	0.37 eV/Li atom
One Li Channel moving along a-axis	1.10 eV/Li atom

2.3.4 *Ab-initio* Molecular Dynamics Simulations

In order to investigate the nature of diffusion, diffusion coefficients and high temperature phase transition in β - eucryptite, *ab-initio* MD simulations are performed at various temperatures. Although quasiharmonic lattice dynamics is a good tool[59] to calculate the phonon spectrum, it does not include the anharmonic contribution coming from the temperature. The ABIMD directly encounters the anharmonic effect[36,60] and hence provides accurate determination of phonon spectrum at any temperature. We have calculated and compared the phonon spectrum (Fig 2.13(a)) of β -eucryptite at ambient temperature (for RT- phase) and pressure with our INS measurements[39].

The peak structure in the calculated phonon spectrum (Fig 2.13(a)) agrees very well with the experimental spectrum. Moreover, both the spectra extend up to the same maximum energy. A very small underestimation in the calculated stretching modes comes from the slightly overestimated bond lengths in the framework of GGA approximation. The overall match of the phonon spectra validates our simulations cell and other input parameters for further calculations of various physical properties. In contrary to the classical force field calculations, ABIMD reproduce the experimental thermal expansion behaviour (Fig 2.13 (b)), which show contraction along the *c*-axis and expansion along *a*-axis. Even at higher temperature the thermal expansion behaviour is accurately reproduced which was little underestimated in quasiharmonic LD calculations.

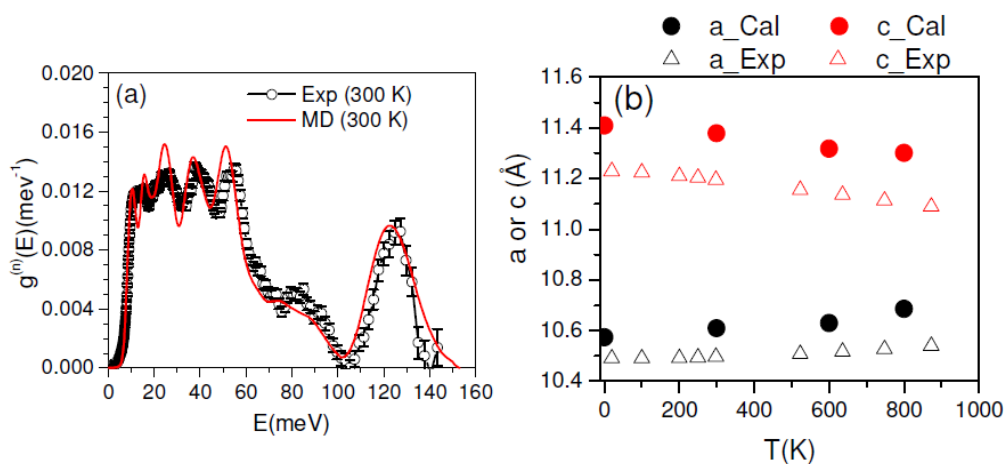


FIG 2.13 (a) The ABIMD calculated and experimental phonon spectra[39] of β -eucryptite at 300 K. (b) The calculated and experimental[61] (neutron diffraction) lattice parameters of β -eucryptite.

2.3.4.1 High Temperature Phase Transition

The mean square displacements of various atoms (Li, O, Al & Si) are calculated from the time evolution of the trajectory of these atoms at room temperature (300K). These calculations are performed in micro canonical ensemble (NVE) and the volume of unit cell is held constant to that of relaxed structure at 0K. The calculations show that the Li being lightest element has the highest but Al and Si being heavier has lower mean square amplitudes (Fig 2.14(a)). At 300K, the atoms are vibrating about their equilibrium positions with small amplitudes and hence the structure is stable in this configuration.

As simulation temperature is increased to 600K, we see (Fig 2.14(b) & 2.15(b)) that although Al, Si, and O atoms have very small and almost constant values of MSD, Li atom show a sudden increase after 4 ps. We analysed the anisotropic MSD (Fig 2.14(c) & 2.15(b)) for Li atoms and found that the MSD's show an anomalous value only along the hexagonal c -axis while it is negligible in the a - b plane. This implies that Li atoms start moving along the hexagonal c -axis with a jump like behaviour. When all individual

atom's trajectory (Fig 2.14(d)) are analysed, we found that three Li atoms are moving altogether. These groups of three Li atoms belong to the same channel.

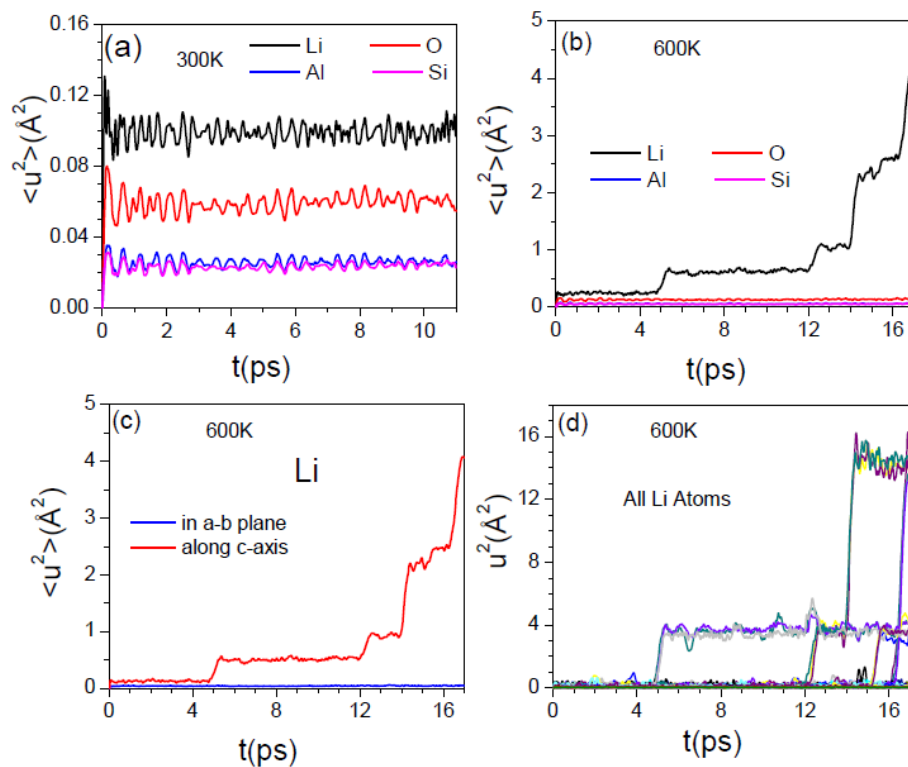
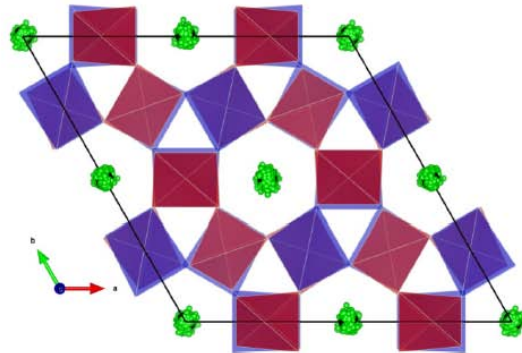
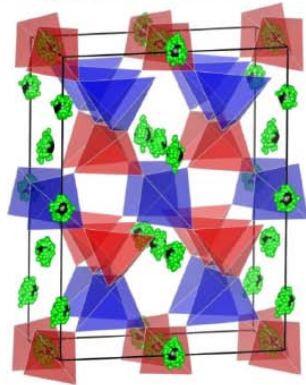


FIG 2.14 The ABIMD calculated MSD ($\langle u^2 \rangle$) of various atoms of RT phase of β -eucryptite as a function of time (a) at 300K and (b) 600K. (c) Anisotropic MSD ($\langle u^2 \rangle$) of Li averaged over all the Li atoms in the supercell and (d) u^2 of each individual Li atoms along c-axis at 600K as a function of time.

The very first channel movement (Fig 2.14(d)) occur around a simulation time of 4 ps. This is found to be the ‘A’ type channel. All the Li atoms in this ‘A’ type channel are found to have squared-displacement of $\sim 3.6 \text{\AA}^2$ which corresponds to a displacement of $\sim 1.9 \text{\AA}$. This displacement is equal to $c/6$. This indicates that the ‘A’ type channel is transformed to the ‘S’ type channel. Afterwards, the Li atoms (three atoms together) in other channels also start moving along c-axis with displacement amplitude of about $c/6$

and $c/3$ etc. Hence Li atoms have a possibility to be present in all the available sites along the channels at 600K. The entire channels become equivalent with a distribution of Li atoms at all the available sites. This gives rise to the high- temperature phase transition in β -eucryptite. This transition was experimentally reported[62,63] at around 698-758 K. In the high temperature phase, all the channels become equivalent and the hence the new symmetry reduces the ‘a’ (or ‘b’) lattice parameter to half of their original values. Experimentally[62] the high temperature structure of β -eucryptite is also known to have Li atoms positional disordering along the hexagonal c-axis.

(a) T=300K, RT Phase Unit Cell



(b) T=600K, RT Phase Unit Cell

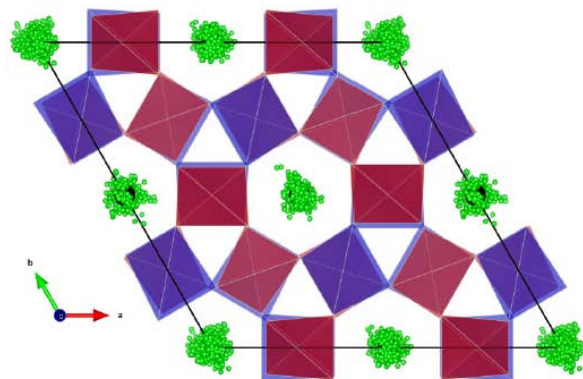
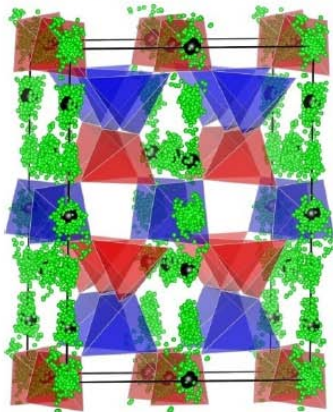


FIG 2.15 Trajectory of Li atoms in channels of β -eucryptite (RT-Phase) at temperatures like (a) 300K, (b) 600K. Key: AlO_4 -Blue, SiO_4 -Red, Initial Position of Li- Black, Time Evolution of Li- Green balls.

The favourable movement of Li atoms in the 'A' type channel in comparison to that in the 'S' type channel may be statistical or may be related to their activation energy barriers. We have calculated the activation energy barrier for motion of Li atoms in these channels using climbing image nudged elastic band method and found that the activation energy barrier for both types of channels is almost equal. This indicates that activation energy provides an equal probability for movement of both types of Li channels. However, the calculated energy shows that the final state obtained after moving channel A is energetically more favourable in comparison to that for S type channel by an enthalpy difference of 0.35 meV.

Further, we have calculated the total enthalpy of final structural configurations (Table 2.6) obtained from the shift of 'A' and 'S' type channels by $c/6$ along the c -axis. N_A and N_S represent the number of A and S type Li channels respectively in single unit cell containing 84 atoms. The calculated enthalpy is compared for the following configurations: (i) when $N_S: N_A:: 3: 1$, this corresponds to actual room temperature phase unit cell, (ii) when all Li atoms are coplanar with Si atoms ($N_S: N_A:: 4: 0$), this is obtained by shifting all Li atoms in A- type channel by $c/6$ along c -axis, (iii) when $N_S: N_A:: 2: 2$, there are equal number of Li atoms in Al and Si planes, (iv) when $N_S: N_A:: 1: 3$, and (v) when $N_S: N_A:: 0: 4$, (vi) Li occupying three consecutive sites at 0, $c/6$ and $c/3$ in one of the four channels while all other Li are present at their equilibrium positions, (vii) Li occupying three consecutive sites at 0, $c/6$ and $c/3$ in all of the four channels. The calculated (0 K) enthalpy and lattice parameters for various possible combinations of Li occupancy in the channels are given in Table 2.6. The RT-Phase possesses the minimum enthalpy and hence represents the most stable configuration. Moreover, some of the other possible configurations have fairly low enthalpy. Hence Li in the channels of the high temperature phase may occur at all the available sites with some finite probability. The

high temperature phase is characterised by the statistical distribution of Li atoms in all the available sites in the hexagonal channels. The Li atoms seem to be disordered in channels and the high temperature phase transition may be of order-disorder nature[62].

TABLE 2.6 Comparison of enthalpy (H) per formula unit (f. u.) and lattice parameters (a & c) for some of the possible structural configurations with different distribution of Li atoms in the hexagonal channels of β -eucryptite. N_A and N_S represent the number of A and S type Li channels respectively in single unit cell containing 84 atoms. These structures are relaxed for all the degree of freedoms under the framework of DFT. ΔH represents the difference in enthalpy (meV/atom) with respect to that of the RT-phase.

Sr. No.	Phase Description	N_A : N_S	H(eV)/f.u.	ΔH (meV)/f.u.	a(Å)	c(Å)
(i)	RT-Phase	1:3	-50.6072	0	10.5735	11.4100
(ii)	All Li in Si Plane	0:4	-50.5981	9.1	10.5702	11.4763
(iii)	Equal number of Li in Al and Si planes	2:2	-50.5953	11.9	10.5772	11.3156
(iv)	One Li channel coplanar with Si	3:1	-50.5680	39.2	10.6317	11.2108
(v)	All Li in Al plane	4:0	-50.5064	100.8	10.6934	11.1189
(vi)	Li at 0, $c/6$ and $c/3$ in One channel.		-50.3937	213.15	10.5252	11.5990
(vii)	Li at 0, $c/6$ and $c/3$ in all channels.		-49.5628	1044.4	10.4656	11.7154

If an ordered structure is assumed for the HT phase (configuration (ii) (Table 2.6)) it gives rise to a calculated c parameter which is larger than that of the RT-phase. However, when various possible configurations ((iii), (iv) & (v) (Table 2.6)) of structure with Li at different sites are considered we get lower c lattice parameter. Hence, Li in the channels of the high temperature phase would have a distribution over all the sites. This

implies that the HT-phase transition occurs by disordering of Li atoms and produces little change in the lattice parameters. We have also calculated the phonon spectra of β -Eucryptite for structural parameters close to the Li-diffusion temperature (800 K). However, we didn't get any unstable phonon mode implying that phonons do not contribute to this transition.

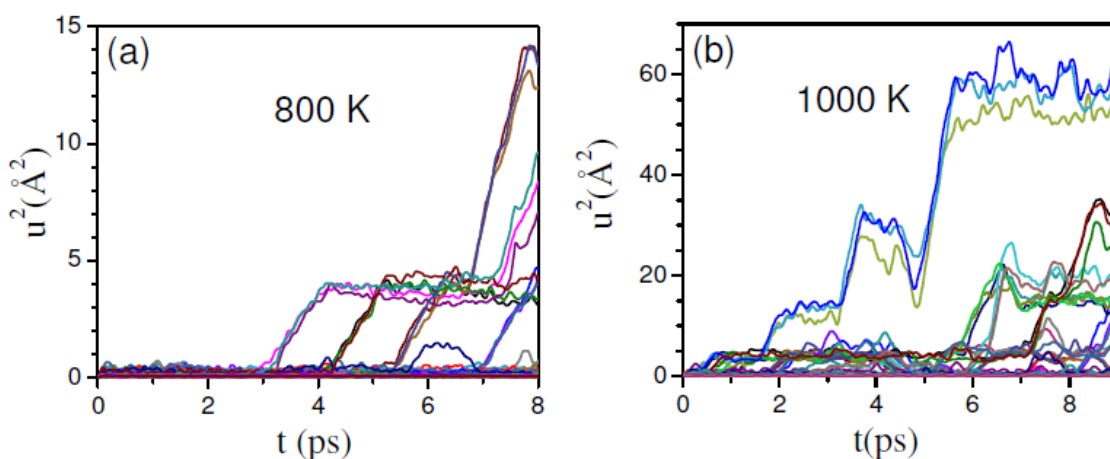


FIG 2.16 The ABIMD calculated u^2 of each individual Li atoms of HT- phase of β -eucryptite as a function of time along c -axis at (a) 800K, (b) 1000K

2.3.4.2 Superionic Conductivity in HT Phase

The simulations performed at 800 K indicate increase in Li channel movements. At 800K (Fig 2.16(a) & Fig 2.17(a)), the compound is already in the high temperature structure, so all the Li containing channels are equivalent. The channel movement begins at smaller simulation time in comparison to that for 600K, and some channels start moving coherently at same time. The increasing squared displacements (u^2) of Li atoms in these channels signify the diffusion in Li channels along the hexagonal c -axis. When temperature is further raised to 1000K (Fig 2.16(b) & Fig 2.17(b)), more numbers of channels are seen to be diffusing at even smaller simulation times. During the diffusion,

there is correlation between the Li atoms in each channel which can be seen at 1000K. The diffusion of Li channels in this compound is found to be one- dimensional jump- like rather than continuous diffusion. At sufficiently high temperature of 1200 K (Fig 2.17(c)), some of the Li atoms also started diffusing in the ab-plane; hence at high temperatures the intra- channel correlation of Li atoms decreases.

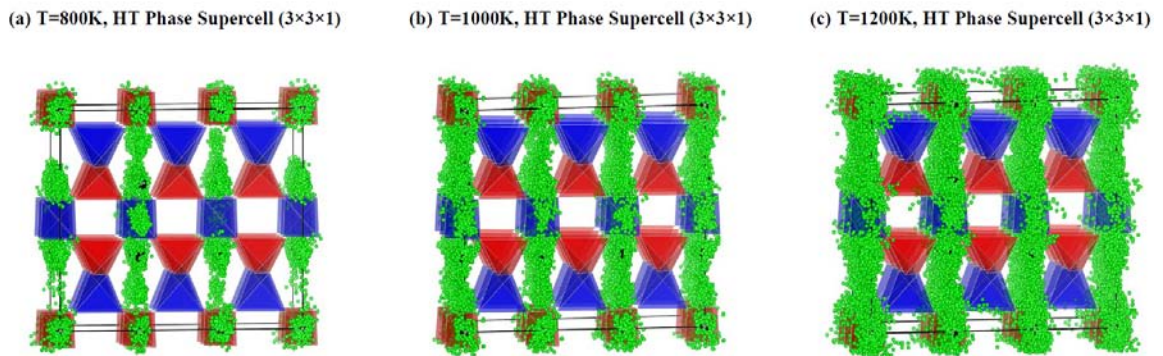


FIG 2.17 Trajectory of Li atoms in channels of β -eucryptite (HT-Phase) at various temperatures like (a) 800K, (b) 1000K and (c) 1200K. Key: AlO_4 -Blue, SiO_4 -Red, Initial Position of Li- Black, Time Evolution of Li- Green balls.

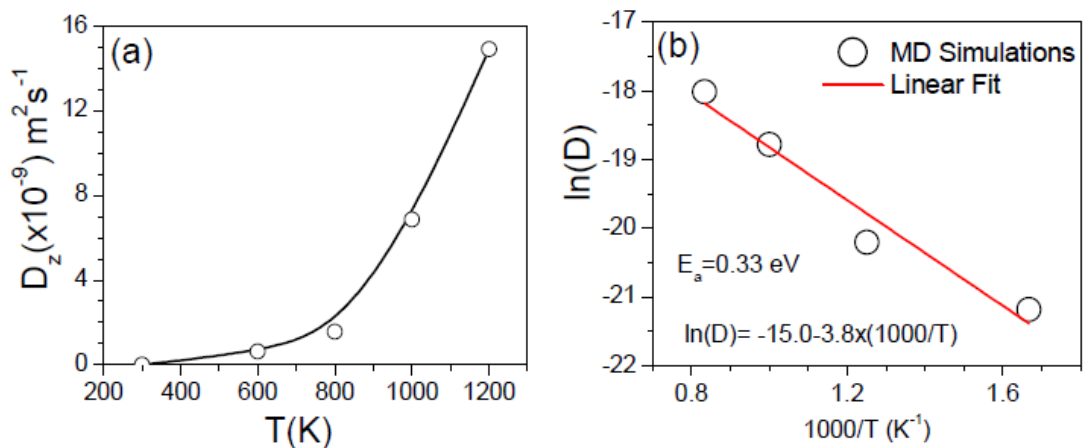


FIG 2.18 The ABIMD calculated (a) one dimensional diffusion coefficient as a function of temperature and (b) Arrhenius plot of diffusion coefficient and temperature to obtain activation energy for Li diffusion.

For the calculation of diffusion coefficient, we have averaged the squared displacements (u^2) over all the Li atoms and over a large number of time origins. This averaging gives rise to disappearance of step like behaviour in the u^2 curve. We have calculated the average diffusion coefficient for all the Li atoms in the supercell. The calculated diffusion coefficient (Fig 2.18 (a)) shows a sharp increase in magnitude around 600K. The calculated value of diffusion coefficient has magnitude ($10^{-9} \text{ m}^2\text{s}^{-1}$) comparable to that of atoms in liquids. So, the high temperature structure of β -eucryptite possesses a superionic Li conduction which is one dimensional in nature. In Fig 2.14 & 2.16, the step-like behaviour of squared-displacements (u^2) of Li ions shows the correlated Li jumps along the hexagonal c-axis with typical jump distances of $c/6$ (1.9\AA), $c/3$ (3.8\AA) and so on. The flatness of u^2 curve signifies the resting time of Li atoms in between the jumps. The resting time decreases with increase in temperature, and typical resting time at 600 K varies from 2 to 4 ps (Fig 2.14). The jump distances correlate to the structure because there are filled and vacant Li sites along the channel at $c/6$ separation. The calculated jump distances are consistent with the experimental quasi-elastic neutron scattering results[64]. The calculated activation energy (Fig 2.18(b)) for diffusion of Li atoms is 0.33 eV which agrees with those calculated from the nudged elastic band method (0.3-0.4 eV) calculations[40] and with the experimental[65] values of 0.6-0.8 eV.

2.3.4.3 Calculated Pair Distribution Functions

The pair distribution function (PDF) for various atomic pairs of β -eucryptite is calculated (Fig 2.19) as a function of temperature. The PDF for Al-O and Si-O pairs does not seem to change with temperature. This indicates that Al-O and Si-O bonds remain nearly rigid up to high temperatures of 1200 K. On the other hand, the PDF for Li related

atomic pairs are highly affected with increasing temperature. This gives a signature that at high temperature the superionic phase transition in β -eucryptite mainly arises from the dynamical behaviour of Li atoms.

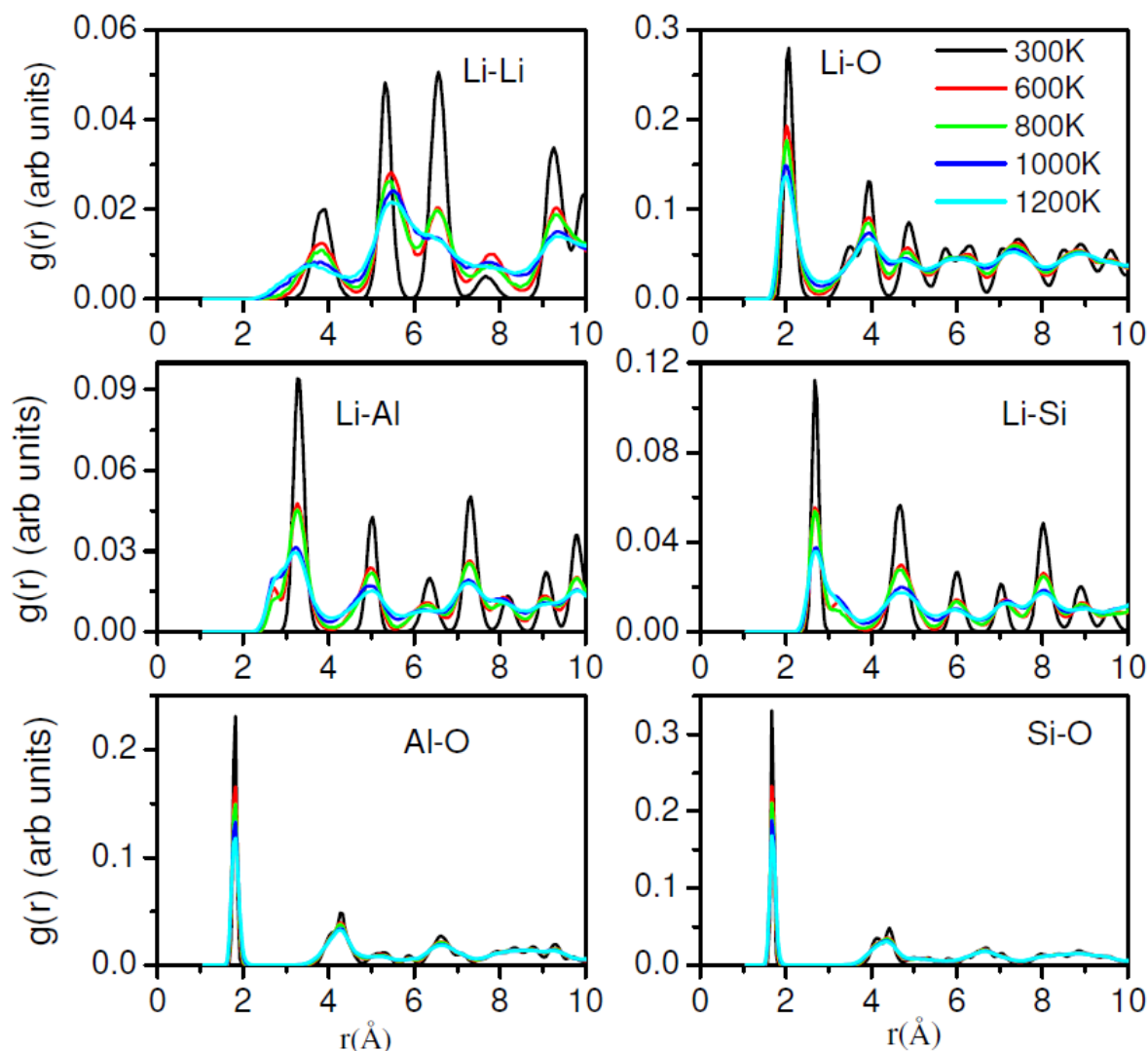


FIG 2.19 The ABIMD calculated temperature dependence of pair distribution function for various atomic pair of β -eucryptite. The information about different coloured lines is valid for all the subplots.

The polyhedral angles (Fig 2.20) as a function of temperature are calculated from the time evolution of structure as obtained from molecular dynamical simulations. At 300 K, the O-Al-O bond angles have an average value of 109.2° . The O-Si-O bonds exhibit two

peaks around 113.8° and 100.6° corresponding to two types of bond angles around Si atoms. The spread in bond angles shows that the AlO_4 and SiO_4 polyhedral units are irregular in nature. However, as a function of temperature the double peak structure of O-Si-O bonds merges to single peak. With increase in temperature, the configurational entropy increases and the structure has more possible values of O-Si-O angles. This in turn creates a broad distribution of O-Si-O bond angles and the two peak structures disappear in this broadening. The total spread of O-Al/Si-O bond angles does not change significantly with increasing temperature.

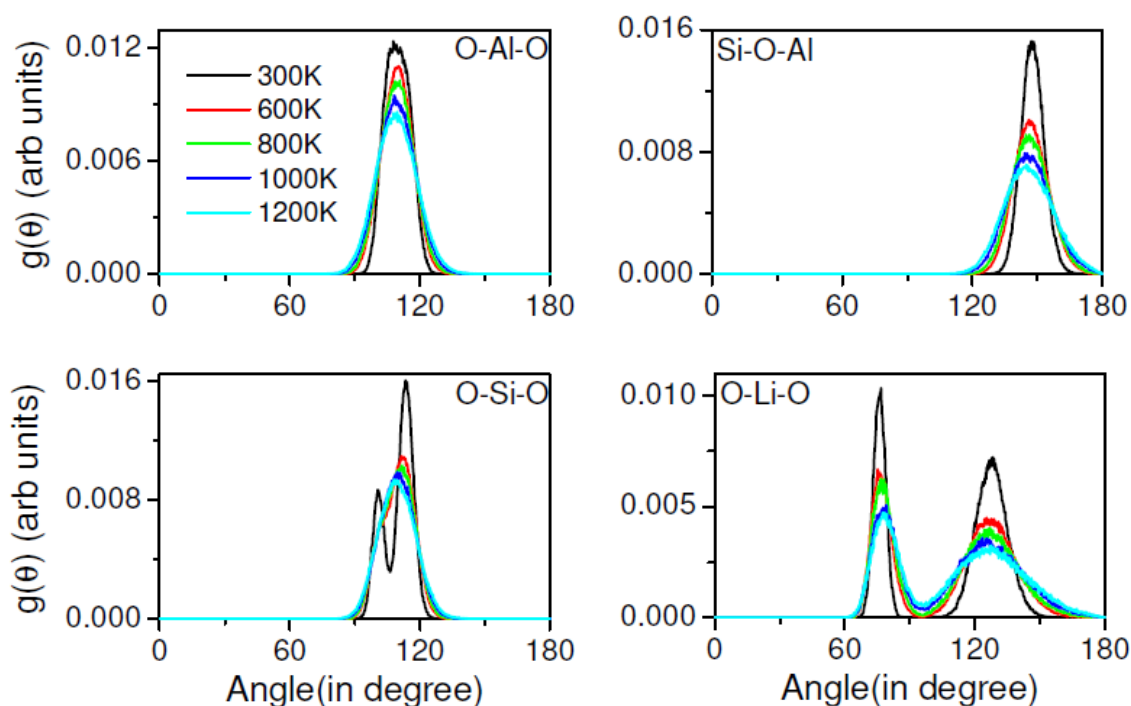


FIG 2.20 The ABIMD calculated temperature dependence of angular distribution function for various polyhedral angles in β -eucryptite.

This implies that the irregularity of $(\text{Al/Si})\text{O}_4$ polyhedral units do not increase at high temperature. However, the bond angles Si-O-Al show significant increase in spread with increase in temperature. This indicates increase in flexibility for the rotation of corner

shared AlO_4 and SiO_4 polyhedra about the shared O atom. This would give rise to a flexible network which favours the movement of Li atoms. Li atom bond with O atoms shows two types of widely spread O-Li-O angles showing a highly irregular polyhedral nature. The two O-Li-O bond angles show some spread with temperature, but the two peak structure is preserved. This suggests that the Li- jumps are quite fast and Li remains at definite positions $(0, c/6, c/3, c/2, 2c/3, 5c/6)$ at most of the time.

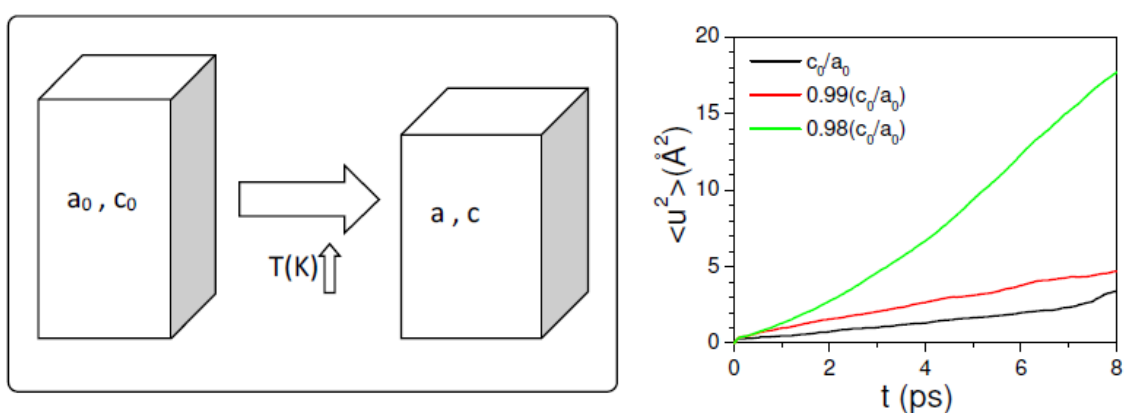


FIG 2.21 (a) A cartoon showing the effect of decreasing c/a ratio on structure of β -eucryptite and (b) ABIMD calculated time evolution of MSD of Li atoms averaged over all the atoms in the super cell of HT- phase at various c/a ratio at $T=800\text{K}$.

2.3.4.4 Role of NTE in Superionic Conduction

β -Eucryptite is a unique superionic conductor exhibiting the anisotropic negative thermal expansion (Fig 2.21(a)) behaviour. The negative thermal expansion and superionic conduction in β -eucryptite are temperature driven phenomenon. So, there is a need to find the relation between these two phenomena. In order to see the effect on Li diffusion due to the anisotropic negative thermal expansion behaviour we have performed a series of ABIMD simulations in NVE ensemble at 800 K for calculated structure with c_0/a_0 (as at 0K), $0.99c_0/a_0$ and $0.98c_0/a_0$. These values of c/a reflect the actual thermal

expansion behaviour of β -eucryptite as a function of increasing temperature. The study is performed in a well determined (HT-phase) superionic state of β -eucryptite.

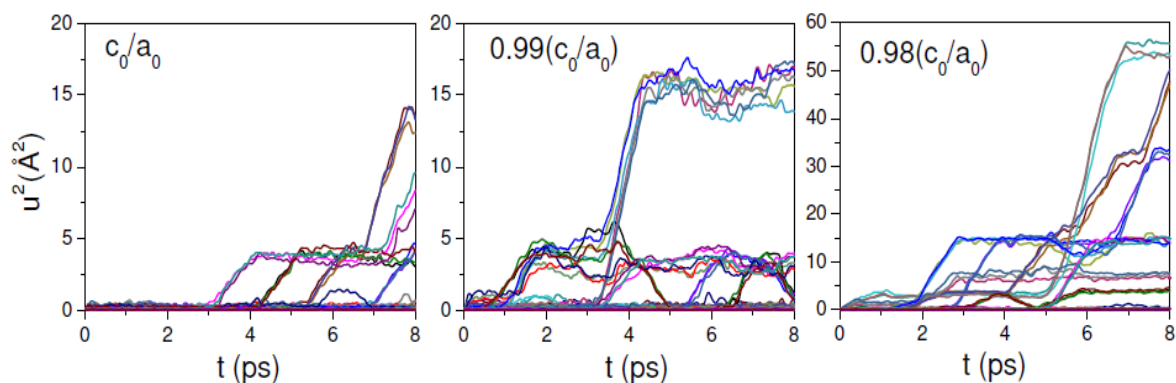


FIG 2.22 The ABIMD calculated time evolution of u^2 of each individual Li along the hexagonal c -axis in the supercell ($3 \times 3 \times 1$) of HT- phase of β -eucryptite at various c/a ratios at $T=800\text{K}$.

We have calculated the mean square displacement (Fig 2.21(b), MSD integrated over different initial times) as a function of simulation time for structure with different c/a ratios. Fig 2.21(b) shows MSD averaged over all the Li atoms and implies that MSD value is enhanced by decreasing c/a ratio. We have further analysed the Li channel motions in structures with different c/a ratios. The magnitudes of MSD for Li channels diffusion are found (Fig 2.22) to increase with decreasing c/a ratio. The increase in diffusion with decreasing c/a ratio happens since expansion in the a - b plane opens the free space for Li movement along the c -axis. Also, the contraction of the c -axis reduced the available jump distance along the c -axis. We have also calculated the activation energy for Li channel diffusion in all the considered structure configurations using static climbing image nudged elastic band method (Fig 2.23). The increase in diffusion with decreasing c/a ratio comes from the decrease in activation energy for Li channel diffusion.

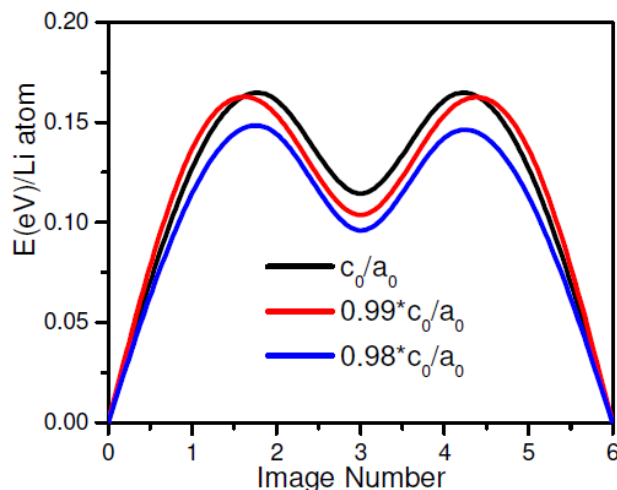


FIG 2.23 The *ab initio* DFT calculated static activation energy barrier for Li channel diffusion in HT phase of β -eucryptite at various c/a ratios. The calculations are performed by using climbing image nudged elastic band method.

2.3.4.5 Role of Defects in Superionic Conduction

There may be many factors affecting ionic motion in a crystal. We have considered three types of defects in the crystal to study Li diffusion. These defects are (i) Li excess (interstitial) (ii) Li vacancy and (iii) O vacancy. This study is performed at $T=800\text{K}$ which corresponds to a well determined superionic state of β -eucryptite.

Li Excess: For Li excess case, a Li atom is inserted in the hexagonal channel in a vacant tetrahedral site of $3\times 3\times 1$ supercell of HT phase structure. The system is equilibrated for 3ps and the excess Li is found to settle at position in between the already present Li atoms along c - axis, but slightly displaced in a - b plane from the channel along the c -axis. The molecular dynamical simulations (NVE) are performed for 15 ps and MSD (averaged over all Li atoms) from these simulations are plotted in Fig 2.24. Contrary to the earlier cases, Li atoms also show movement in the a - b plane. However, even in this case, the diffusion of Li is dominated along the hexagonal c -axis.

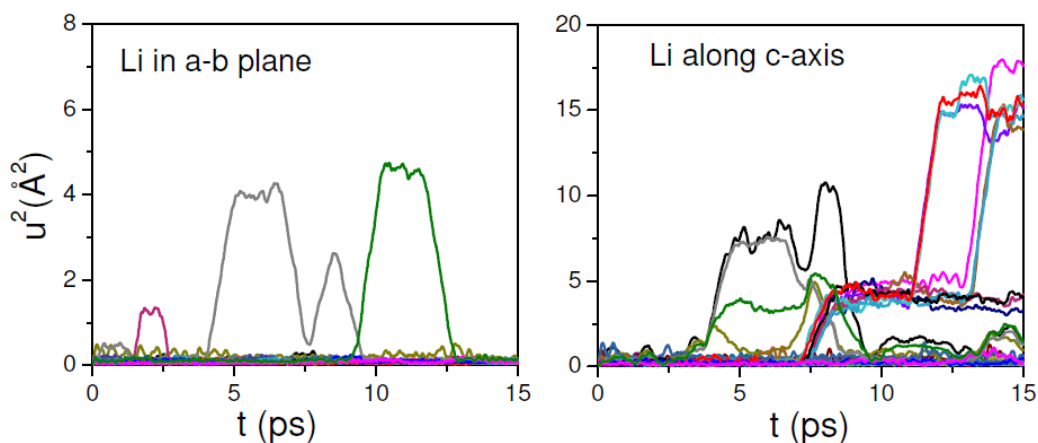


FIG 2.24 The ABIMD calculated time evolution of anisotropic u^2 of each individual Li in the supercell ($3 \times 3 \times 1$) of HT- phase containing one additional Li at tetrahedral void in the central channel at 800K.

The atom- wise analysis of the MSD for Li atoms along the various directions is shown in Fig 2.24. We note that three Li atoms show jumps in the ab -plane and return to their original positions. Among these three Li atoms, two Li atoms belong to the channel where excess Li atom was inserted and the third Li atom belongs to its nearest channel. It can be seen that the movement of Li in a - b plane does not give any net diffusion; however, it only decouples the correlated motion of Li atoms in a channel. Due to this decoupling, the Li atoms which were moving together earlier now show different displacements along the c -axis. Therefore, the presence of excess Li atom in the tetrahedral void in β -eucryptite gives rise to extra diffusion and decouples the correlated dynamics of Li atoms in channels along the hexagonal c -axis.

Li Vacancy: A Li vacancy is created at the centre of $3 \times 3 \times 1$ supercell of the HT phase of β -eucryptite by removing a Li atom. Now there are 26 Li atoms in the simulation cell. The structure is equilibrated to obtain a temperature of 800 K in NVE ensemble. The simulation shows that the Li atoms in the vacancy-containing channel come slightly closer

to the central vacancy. The simulation results (Fig 2.25) show that there is no translation or diffusional motion of Li in the a - b plane. However, diffusion of Li is observed along the hexagonal c -axis like that in a perfect HT-phase. The diffusion is found to be enhanced in magnitude in comparison to that in the perfect crystal. Li atoms in the vacancy containing channel show the largest displacements and initialize the diffusion process. We observe that the intra-channel correlation between the diffusing Li atoms is decreased as compared to that in the perfect crystal. This might happen because of the increased freedom of motion of Li atoms in vacancy-containing channel due to availability of more number of tetrahedral sites when Li vacancy is created.

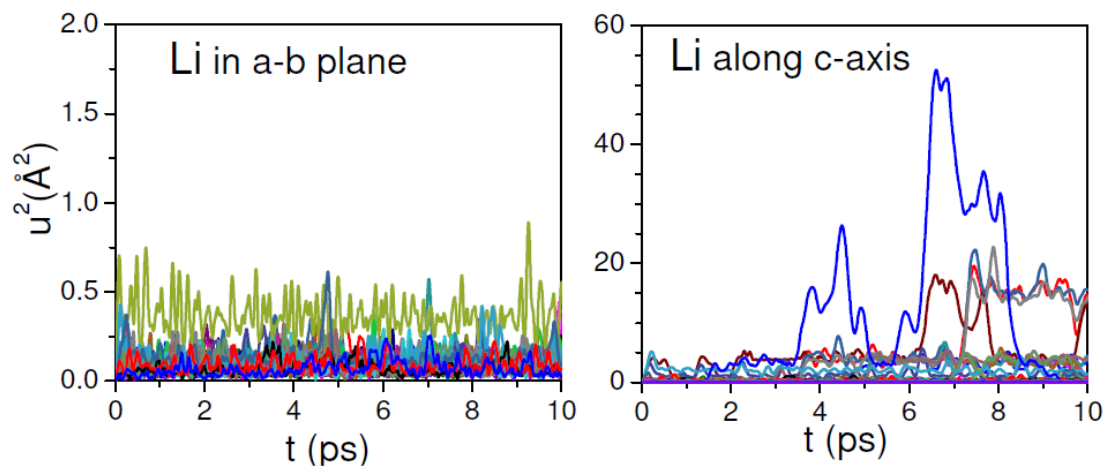


FIG 2.25 The ABIMD calculated time evolution of u^2 of each individual Li in the super cell ($3 \times 3 \times 1$) of HT- phase containing one Li vacancy in the central channel at 800K.

O Vacancy: Several oxides are found to be oxygen deficit [66-68] even in normal synthesis processes although oxygen deficiency can be easily introduced by synthesis in a reduced environment. Here we have calculated the effect of oxygen vacancy on Li diffusion. Oxygen vacancy was created near the centre of $3 \times 3 \times 1$ super cell of the HT phase of β -eucryptite by removing an O atom from 144 O atoms. The structure is

equilibrated in NVE ensemble and then a production run is performed. The calculated anisotropic displacements of all Li atoms in the structure are plotted (Fig 2.26) as a function of time. It can be seen that similar to the perfect crystal there is no diffusion of Li in a - b plane. However, the magnitude of diffusion along the hexagonal c -axis increases substantially in comparison to that of the perfect crystal. Moreover, there is still very good intra- channel correlation between the Li atoms in all the channels. Oxygen vacancy enhances the diffusion of Li without interrupting the intra- channel correlation.

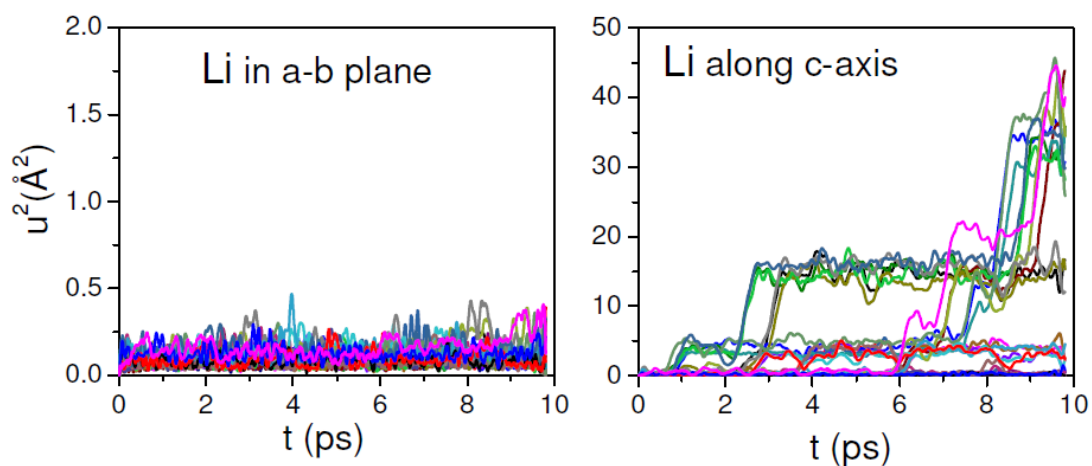


FIG 2.26 The ABIMD calculated time evolution of u^2 of each individual Li in the supercell ($3 \times 3 \times 1$) of HT- phase containing one O vacancy near the centre of the cell at 800K.

2.4 Conclusions

Measurements of the temperature dependent phonon spectra together with molecular dynamics and lattice dynamics simulations have been successfully used to understand the vibrational dynamics of β -eucryptite. Although, classical MD simulations provide a clear indication of superionic Li diffusion at high temperature, the anisotropy of diffusion pathways and anisotropic thermal expansion behaviour are not obtained. The pressure dependence of the phonon spectra using *ab-initio* lattice dynamics calculations

successfully provided the anisotropic thermal expansion behaviour of β -eucryptite. Such an anisotropic behaviour is a result of anisotropic elasticity and anisotropic Grüneisen parameters. We find that the high-energy modes involving translational motions of Li result in a positive thermal expansion along the a -axis and contraction along the c -axis; on the other hand, low-energy phonons involving rotational degrees of freedom as well as a distortion of polyhedral are responsible for the negative thermal expansion behaviour at low temperature both along a - and c -axis.

The *ab-initio* DFT calculation shows that the activation energy barrier for the intrachannel correlated motion of lithium atoms along the hexagonal c -axis is an order of magnitude lower than that in the a - b plane and hence should be the major process for Li conduction. The *ab-initio* MD simulations show a transition to the high temperature phase at around 600K initiated by the movement of Li atoms in the A type channel. The high temperature phase is found to have disordered Li atoms over all the six available sites in each channel of the unit cell. The reason for Li disorder in HT phase is elucidated by the calculated enthalpy of various possible structures. The compound is found to exhibit a one-dimensional Li superionic conduction in the HT phase along the hexagonal c -axis. The correct nature of anisotropy in superionicity is very well reproduced by *ab-initio* calculations as compared to somewhat less satisfactory results obtained from classical MD simulations. The anisotropic negative thermal expansion along the hexagonal c -axis is found to enhance Li ionic conductivity along the c -axis. The introductions of defects in the crystal are found to increase the ionic conductivity and hence might reduce the temperature of HT superionic phase transition in this material. The synthesis of the structure with Li or O atoms vacancies might provide a possibility to achieve a nearly room temperature solid electrolyte.

References

- [1] J.-H. Lee, J. Kim, T. Y. Kim, M. S. Al Hossain, S.-W. Kim, and J. H. Kim, *Journal of Materials Chemistry A* **4**, 7983 (2016).
- [2] X. Luo, J. Wang, M. Dooner, and J. Clarke, *Applied Energy* **137**, 511 (2015).
- [3] M. R. Lukatskaya, B. Dunn, and Y. Gogotsi, *Nature Communications* **7**, 12647 (2016).
- [4] H. Sun, Y. Zhang, J. Zhang, X. Sun, and H. Peng, *Nature Reviews Materials* **2**, 17023 (2017).
- [5] K. C. Divya and J. Ostergaard, *Electric Power Systems Research* **79**, 511 (2009).
- [6] W. Zhou, Y. Li, S. Xin, and J. B. Goodenough, *ACS Central Science* **3**, 52 (2017).
- [7] J. B. Goodenough and K.-S. Park, *Journal of the American Chemical Society* **135**, 1167 (2013).
- [8] D. Larcher and J. M. Tarascon, *Nature Chemistry* **7**, 19 (2015).
- [9] M. H. Braga, N. S. Grundish, A. J. Murchison, and J. B. Goodenough, *Energy & Environmental Science* **10**, 331 (2017).
- [10] C. Sun, J. Liu, Y. Gong, D. P. Wilkinson, and J. Zhang, *Nano Energy* **33**, 363 (2017).
- [11] Y. Kato, S. Hori, T. Saito, K. Suzuki, M. Hirayama, A. Mitsui, M. Yonemura, H. Iba, and R. Kanno, *Nature Energy* **1**, 16030 (2016).
- [12] J. Janek and W. G. Zeier, *Nature Energy* , **1**, 16141 (2016).
- [13] V. Thangadurai, S. Narayanan, and D. Pinzar, *Chemical Society Reviews* **43**, 4714 (2014).
- [14] J. Y. Hwang, S. T. Myung, and Y. K. Sun, *Chemical Society Reviews* **46**, 3529 (2017).
- [15] U. V. Alpen, E. Schönherr, H. Schulz, and G. H. Talat, *Electrochimica Acta* **22**, 805 (1977).
- [16] U. v. Alpen, H. Schulz, G. H. Talat, and H. Böhm, *Solid State Communications* **23**, 911 (1977).
- [17] B. Ziebarth, M. Klinsmann, T. Eckl, and C. Elsässer, *Physical Review B* **89**, 174301 (2014).
- [18] L. Xia, G. W. Wen, C. L. Qin, X. Y. Wang, and L. Song, *Materials & Design* **32**, 2526 (2011).
- [19] H. Xu, P. J. Heaney, D. M. Yates, R. B. Von Dreele, and M. A. Bourke, *Journal of Materials Research* **14**, 3138 (1999).
- [20] R. T. Johnson, B. Morosin, M. L. Knotek, and R. M. Biefeld, *Physics Letters A* **54**, 403 (1975).
- [21] H. Schulz and V. Tscherry, *Acta Crystallographica Section B* **28**, 2168 (1972).
- [22] W. W. Pillars and D. R. Peacor, *American Mineralogist* **58**, 681 (1973).
- [23] M. J. Buerger, *The Journal of Chemical Physics* **15**, 1 (1947).
- [24] V. Tscherry, H. Schulz, and F. Laves, *Zeitschrift für Kristallographie - Crystalline Materials*

- 135**, 175 (1972).
- [25] H. Schulz and V. Tscherry, *Acta Crystallographica Section B* **28**, 2174 (1972).
- [26] W. Press, B. Renker, H. Schulz, and H. Böhm, *Physical Review B* **21**, 1250 (1980).
- [27] S. Asel, A. T. R. Simon, and T. L. William, *Journal of Physics: Condensed Matter* **16**, 5267 (2004).
- [28] H. Guth and G. Heger, in *Fast Ion Transport in Solids*, edited by Vashishta, mundy, and shenoy; (Elsevier, North-Holland, 1979), p. 499.
- [29] A. I. Lichtenstein, R. O. Jones, H. Xu, and P. J. Heaney, *Physical Review B* **58**, 6219 (1998).
- [30] D. M. Follstaedt and P. M. Richards, *Physical Review Letters*, **37**, 1571 (1976).
- [31] B. Renker, H. Bernotat, G. Heger, N. Lehner, and W. Press, *Solid State Ionics* **9–10, Part 2**, 1341 (1983).
- [32] M. Zhang, H. Xu, E. K. H. Salje, and P. J. Heaney, *Physics and Chemistry of Minerals* **30**, 457 (2003).
- [33] J. A. Anta and P. A. Madden, *Journal of Physics: Condensed Matter* **11**, 6099 (1999).
- [34] G. K. Phani Dathar, J. Balachandran, P. R. C. Kent, A. J. Rondinone, and P. Ganesh, *Journal of Materials Chemistry A* **5**, 1153 (2017).
- [35] J. Yang and J. S. Tse, *Computational Materials Science* **107**, 134 (2015).
- [36] G. Cardini, P. Procacci, and R. Righini, *Chemical Physics* **117**, 355 (1987).
- [37] J. E. Turney, E. S. Landry, A. J. H. McGaughey, and C. H. Amon, *Physical Review B* **79**, 064301 (2009).
- [38] B. Singh, M. K. Gupta, R. Mittal, and S. L. Chaplot, *Journal of Materials Chemistry A* **6**, 5052 (2018).
- [39] B. Singh *et al.*, *Journal of Applied Physics* **121**, 085106 (2017).
- [40] B. Singh *et al.*, *Physical Chemistry Chemical Physics* **19**, 15512 (2017).
- [41] I. T. Todorov, W. Smith, K. Trachenko, and M. T. Dove, *Journal of Materials Chemistry* **16**, 1911 (2006).
- [42] S. L. Chaplot, R. Mittal, and N. Choudhury, *Thermodynamic Properties of Solids: Experiments and Modeling* (John Wiley & Sons, 2010).
- [43] S. Asel, A. W. Stephen, and A. T. R. Simon, *Journal of Physics: Condensed Matter* **16**, 8173 (2004).
- [44] G. Kresse and J. Furthmüller, *Computational Materials Science* **6**, 15 (1996).
- [45] G. Kresse and D. Joubert, *Physical Review B* **59**, 1758 (1999).
- [46] H. J. Monkhorst and J. D. Pack, *Physical Review B* **13**, 5188 (1976).
- [47] K. Parlinski, PHONON Software (2003).
- [48] G. Venkataraman, L. A. Feldkamp, and V. C. Sahni, *Dynamics of perfect crystals* (MIT Press, Cambridge, 1975).
- [49] G. Henkelman and H. Jónsson, *The Journal of Chemical Physics* **113**, 9978 (2000).
- [50] M. Parrinello and A. Rahman, *Journal of Applied physics* **52**, 7182 (1981).
- [51] M. Parrinello and A. Rahman, *Physical Review Letters* **45**, 1196 (1980).

- [52] M. P. Allen and D. J. Tildesley, *Computer simulation of liquids* (Oxford university press, 2017).
- [53] S. Nosé, *The Journal of Chemical Physics* **81**, 511 (1984).
- [54] A. Sjolander, *Arkiv für Fysik* **14**, 315 (1958).
- [55] Y. Le Page and P. Saxe, *Physical Review B* **65**, 104104 (2002).
- [56] S. Haussühl, W. Nagel, and H. Böhm, *Zeitschrift für Kristallographie* **169**, 299 (1984).
- [57] B. Narayanan, I. E. Reimanis, E. R. Fuller, and C. V. Ciobanu, *Physical Review B* **81**, 104106 (2010).
- [58] N. Badri, C. T. v. D. Adri, B. K. Branden, E. R. Ivar, and V. C. Cristian, *Modelling and Simulation in Materials Science and Engineering* **20**, 015002 (2012).
- [59] S. L. Chaplot, N. Choudhury, S. Ghose, R. Mittal, and G. Prabhathasree, *European Journal of Mineralogy* **14**, 291 (2002).
- [60] J. Turney, E. Landry, A. McGaughey, and C. Amon, *Physical Review B* **79**, 064301 (2009).
- [61] A. Lichtenstein, R. Jones, H. Xu, and P. Heaney, *Physical Review B* **58**, 6219 (1998).
- [62] A. Sartbaeva, S. A. Redfern, and W. T. Lee, *Journal of Physics: Condensed Matter* **16**, 5267 (2004).
- [63] H. Guth and G. Heger, North-Holland, (1979).
- [64] B. Renker, H. Bernotat, G. Heger, N. Lehner, and W. Press, *Solid State Ionics* **9-10**, 1341 (1983).
- [65] H. Böhm, *Physica Status Solidi (a)* **30**, 531 (1975).
- [66] A. Padilha, H. Raebiger, A. Rocha, and G. Dalpian, *Scientific Reports* **6**, 28871 (2016).
- [67] O. Bierwagen, A. Proessdorf, M. Niehle, F. Grosse, A. Trampert, and M. Klingsporn, *Crystal Growth & Design* **13**, 3645 (2013).
- [68] R. Chatten, A. V. Chadwick, A. Rougier, and P. J. Lindan, *The Journal of Physical Chemistry B* **109**, 3146 (2005).

CHAPTER 3

Thermodynamic Properties and Li Diffusion in Cathode Material, LiAlO_2

3.1 Introduction

The stability and performance of battery is directly related to its components electrodes and electrolyte[1,2]. The present battery technology uses lithium cobalt oxide (LiCoO_2) and various doped combinations like NMC ($\text{LiNi}_{0.33}\text{Co}_{0.33}\text{Mn}_{0.33}\text{O}_2$), NCA ($\text{LiNi}_{0.8}\text{Co}_{0.15}\text{Al}_{0.05}\text{O}_2$) etc. as a cathode[1-4]. The major problem with these materials is that they contain cobalt in sufficient amount and hence limited by toxicity, high cost, low thermal stability, and fast capacity fade at high current rates. Therefore, many other alternative materials are being studied for this purpose[3,5-7]. LiAlO_2 belong to this family and compositionally similar to LiCoO_2 . The γ - LiAlO_2 is stable up to 1873 K and is cost effective. It is even more stable towards intercalation/deintercalations of Li from the structure[8,9]. The Li diffusion in this material occurs with a migration barrier of 0.72(5) eV[8,9]. LiAlO_2 exhibits very small lattice changes during lithium diffusion. This property also makes it suitable for use as a substrate material for epitaxial growth of III-V semiconductors like GaN[10]. It is also used as a tritium-breeder material in the blanket for fusion reactors [11,12].

3.1.1 Structural Details

LiMO_2 (M=B, Al, Ga, In) compounds are widely studied due to their rich phase diagrams. The polymorphism in these compounds arises from the cation order disorder as well as coordination changes[13-15]. The transitions in these systems occur by large

lattice mismatch and are accompanied by enormous stress in the crystals[13,14]. LiAlO_2 finds several important applications as a coating material for Li based electrodes [16-18] and as an additive in composite electrolytes[19]. This material is a lithium ion conductor[8,9]at high temperature.

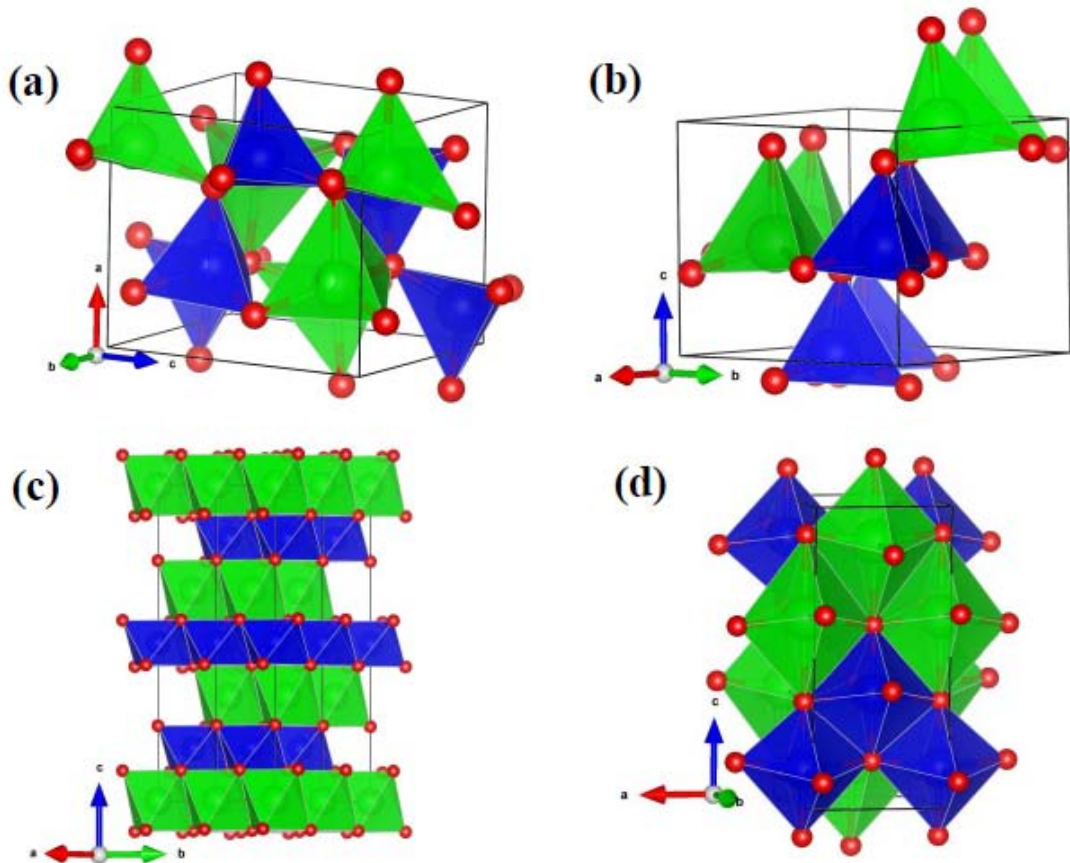


FIG 3.1 The crystal structure of (a) γ -Phase, (b) β -Phase, (c) α -Phase and (d) δ -phase of LiAlO_2 . The Li and Al polyhedral units are shown in green and blue colour, respectively.

3.1.2 Motivations and Objectives of Research

LiAlO_2 is extensively studied using various experimental and computational techniques[8,9,20-25] in recent years for its interesting properties as a Li ion battery material. The stability, safety and performance of battery materials are related to their

thermodynamical behaviour and transport properties (Li diffusion, thermal expansion and phase transitions) in the temperature and pressure range of interest[26]. The phase diagram of LiAlO_2 as obtained from the X-ray diffraction experiments is reported over a range of temperature and pressure[27]. LiAlO_2 is known to have six polymorphs of which the structure (Fig 3.1) of only four (α , β , γ and δ) is known[27]. The most stable form of LiAlO_2 under ambient conditions is γ - LiAlO_2 . The α and β polymorphs begin to convert to the γ -polymorph above 700°C [28,29]. The occurrence of $\alpha \rightarrow \gamma$ - LiAlO_2 phase transformation is one of the crucial problems of application of this compound as solid phase matrix for electrolyte in molten carbonate fuel cells (MCFC). γ - LiAlO_2 is strongly considered as a breeder material because of its thermophysical, chemical and mechanical stability at high temperatures. The dilatometer measurements[30] for γ - LiAlO_2 yielded values of the anisotropic thermal expansion coefficient to be $\alpha_a=7.1 \times 10^{-6} \text{K}^{-1}$ and $\alpha_c=15 \times 10^{-6} \text{K}^{-1}$, while $\alpha_a=10.8 \times 10^{-6} \text{K}^{-1}$ and $\alpha_c=17.97 \times 10^{-6} \text{K}^{-1}$ are from recent neutron diffraction studies[9].

The energetic and atomistic picture of the phase transitions is not well understood. Here, a picture through study of the phase stability and phase transitions among various forms of LiAlO_2 is reported. *Ab-initio* density functional calculations provide a very good alternative[31-36] to accurately study the energetic and properties of material under extreme pressure conditions[37]. The *ab-initio* calculated enthalpy is widely used to obtain the pressure stability region of many crystalline solids[31,38-40]. To be more accurate, the entropy contribution can be added to enthalpy in order to obtain the free energy of the system[34]. *Ab-initio* lattice dynamics calculations of phonon spectra[41-45] can provide the phonon entropy contribution to the free energy of solid and hence the pressure-temperature phase diagram and stability range of crystalline solids[34,46,47].

The pressure and temperature dependence of vibrational modes[33,35,48,49][50,51] can be used to understand the atomistic picture of phase transition.

In the present work [52,53], the pressure dependent electronic band structure, phonon band structure and energetic of various phases of LiAlO_2 have been studied. Phonon spectra calculations at various pressures are performed in order to understand the role of phonon entropy in stability of phases and their phase transformation. The mechanism of high temperature phase transitions from high pressure phases to ambient phase is studied in terms of phonon modes instability. The anisotropic thermal expansion is calculated for $\gamma\text{-LiAlO}_2$ in the framework of quasiharmonic approximation. The experimentally measured temperature dependent phonon spectra are interpreted by the *ab-initio* molecular dynamics calculations to understand the role of phonon in Li diffusion. Moreover, Li diffusion coefficients and pathways for Li diffusion in this compound are calculated[52] using the *ab-initio* MD simulations.

3.2 Experimental and Computational Details

The inelastic neutron scattering measurements on γ -phase of LiAlO_2 were carried out using time of flight IN4C spectrometer at the Institut Laue Langevin (ILL), France. Thermal neutrons of wavelength 2.4 Å in neutron energy gain mode are used for the measurements. The data were collected at several temperatures from 473 K to 1073 K.

The VASP software [54,55] was used for structure optimization and total energy calculations. The kinetic energy cutoff of 820 eV is adapted for plane wave pseudo-potential. A k-point sampling with a grid of $4 \times 4 \times 4$, generated using the Monkhorst-Pack method[56], is used for structure optimizations. For lattice dynamics calculations, the Hellman-Feynman forces are calculated by the finite displacement method (displacement

$\pm 0.03 \text{ \AA}$). The convergence criteria for the total energy and ionic forces were set to 10^{-8} eV and $10^{-4} \text{ eV \AA}^{-1}$. The phonon frequencies were obtained from subsequent calculations using the PHONON software[57]. The phonon density of states is obtained by homogenous sampling of Brillouin zone over 8000 points. The *ab-initio* molecular dynamics simulations are performed at various temperatures using VASP software[54,55]. We have first achieved the desired temperature using NVT simulation, afterward NVE ensemble is used for production run. We have performed the simulation using a $2 \times 2 \times 2$ supercell of ambient phase structure of $\gamma\text{-LiAlO}_2$.

TABLE 3.1 Crystal structure for various phases of LiAlO_2 as calculated at zero pressure and temperature. The calculated parameters are comparable with experiments[27].

	$\gamma\text{-LiAlO}_2$		$\beta\text{-LiAlO}_2$		$\delta\text{-LiAlO}_2$		$\alpha\text{-LiAlO}_2$	
Structure	Tetragonal		Orthorhombic		Tetragonal		Hexagonal	
Space Group	P4 ₁ 2 ₁ 2 (92)		Pna2 ₁ (33)		I4 ₁ /amd (141)		R-3m (166)	
	Exp.	Calc.	Exp.	Calc.	Exp.	Calc.	Exp.	Calc.
a(Å)	5.169	5.226	5.280	5.316	3.887	3.906	2.799	2.827
b(Å)	5.169	5.226	6.300	6.335	3.887	3.906	2.799	2.827
c(Å)	6.268	6.300	4.900	4.946	8.300	8.452	14.180	14.348
V/Z (Å ³)	41.59	43.02	40.75	41.65	31.35	32.23	32.07	33.11
$\rho(\text{g/cm}^3)$	2.615		2.685		3.510		3.401	
α, β, γ (°)	90, 90, 90		90, 90, 90		90, 90, 90		90, 90, 120	
Z	4		4		4		3	
Polyhedral units	LiO ₄ , AlO ₄		LiO ₄ , AlO ₄		LiO ₆ , AlO ₆		LiO ₆ , AlO ₆	

3.3 Results and Discussions

LiAlO_2 occurs in several phases[27]and the crystal structures are known for the α , β , γ and δ -phase. The γ -phase is the most stable phase at ambient condition and crystallizes in a tetragonal structure[27]. It consists of LiO₄ and AlO₄ tetrahedral units (Fig 3.1(a)). The α , β and δ -phases are the high pressure-temperature phases[27]. The β -

LiAlO_2 , also called as the low-temperature form[58] which is stable below 0 °C, crystallizes in orthorhombic structure and it also consists of LiO_4 and AlO_4 tetrahedral units (Fig 3.1(b)). In high pressure experiments[27], β -phase can be obtained from the γ -phase at 0.8 GPa and 623K. The stability region for β -phase is quite narrow, so it possibly coexists with other phases[27]. The AlO_4 and LiO_4 polyhedral units share one edge in γ -phase while these polyhedra are corner shared in β -phase.

α - LiAlO_2 crystallizes in hexagonal symmetry[28] and consists of LiO_6 and AlO_6 octahedra (Fig 3.1(c)). It can be experimentally obtained from γ -phase at high temperature and pressure range (0.5-3.5 GPa and 933-1123 K). α -phase can reversibly transform[28,29] to γ -phase when heated above 600°C at zero pressure. δ -phase is experimentally obtained, at 4GPa using static pressure[14] and at 9 GPa, by dynamic shock compression[59] of γ -phase. It crystallizes in tetragonal structure and consists of LiO_6 and AlO_6 octahedral units (Fig 3.1(d)). The structure of δ -phase is known to possess small amount of Li/Al anti-site disorder. The δ - LiAlO_2 is stable up to 773K and it transforms to α and γ - LiAlO_2 at higher temperatures. The high pressure reconstructive transition from γ to δ -phase is reported as of displacive nature accompanied by enormous stresses stemming from the lattice mismatch[14]. Table 3.1 gives the experimental and calculated structures of the various phases, which also provides some idea of the structural correlation among the various phases. The calculated structures are found to be in good agreement with the available experimental data.

3.3.1 Electronic Structure

The electronic band structure calculations (Fig 3.2) of various phases of LiAlO_2 are performed using *ab-initio* DFT method. These calculations are performed with a very

high dense k-point mesh of $20 \times 20 \times 20$ to ensure the fine curvature of electronic bands. The electronic densities of states are obtained by integrating the band structure over complete Brillion zone. The negative energy of bands signifies the filled valence band while the empty conduction bands have the positive energy.

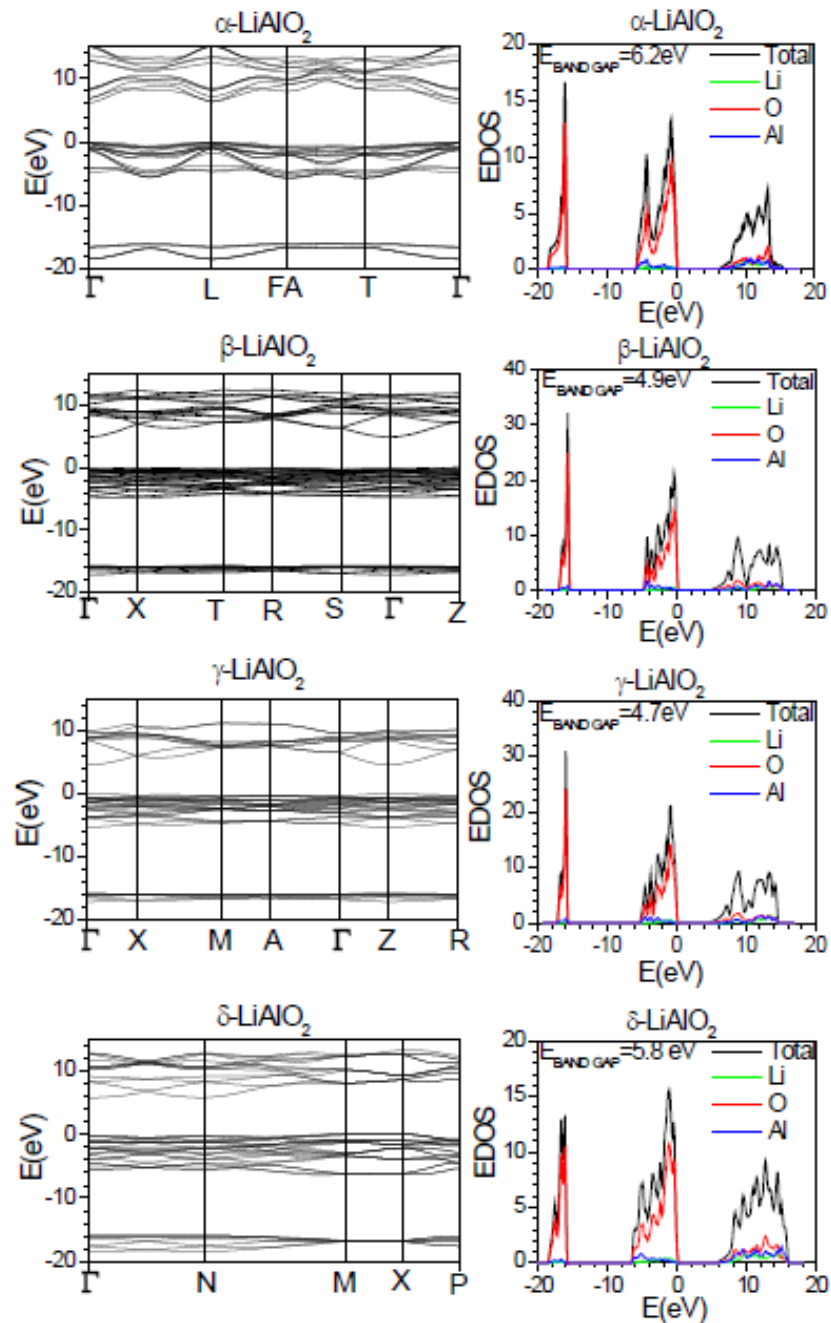


FIG 3.2 Electronic band structure of various high-pressure phases of LiAlO_2 as calculated using *ab-initio* DFT. The high-symmetry points are chosen according to the crystal symmetry[60]. EDOS stand for electronic density of states.

For all the phases, the minimum of conduction band and the maxima of valence band are least separated at zone centre (Γ -point) of the Brillion zone. It can be seen that all the phases show a direct band gap (Fig 3.2) higher than 4 eV and signify insulating behavior. The γ -phase has the least value of band gap of 4.7 eV among all the phases. Therefore, as compared to other phases, the γ -phase maybe most easily tuned for battery electrode applications, by creating defects in the crystal.

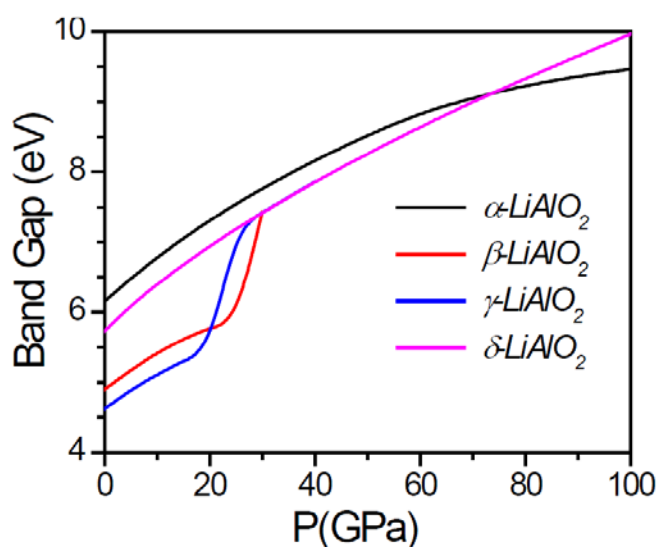


FIG 3.3 Calculated pressure dependent band gap in various phases of LiAlO₂ at 0 K.

As pressure is applied, γ -phase transforms to β -phase with band gap of 4.9 eV. The band gap for δ -phase(5.8 eV) and α -phase (6.2 eV) are further higher than that of γ - and β -phases which may be related to the increasing coordination (4 to 6) of Al and Li atoms in these high-pressure phases. The cathode materials for Li ion battery are required to behave as a good electronic and ionic conductor. Although α -phase has a layered distribution of Li in which Li ionic movement could be favourable, yet the high coordination and high band gap could limit the applications of this phase as a cathode material in the Li ion battery. The calculations reveal increase in electronic band gap in all the phases of LiAlO₂ (Fig 3.3) on application of hydrostatic pressure. Above 20 GPa, the

band gap for γ and β phases shows a sudden increase and takes the value which is equal to that for the δ -phase. However, the corresponding phase transitions occur at much lower pressures. The band-gap crossing between α and δ phases occurs at very high pressure above 70 GPa.

3.3.2 Enthalpy and Phase Transitions

The total energy and enthalpy for various phases of LiAlO_2 are calculated as a function of pressure to find the stability region of these phases at high pressures at zero temperature (while the zero-point phonon energy is ignored). The difference in enthalpy is calculated with respect to that of the ambient pressure stable phase (γ - LiAlO_2) is shown in Fig 3.4. It can be seen that the γ and β phase possess nearly same energy and enthalpy at ambient pressure and hence are likely to be found at ambient pressure conditions. However, with increase in pressure, β phase lowers its enthalpy as compared to that of γ phase and hence is favourably found in this ($0.0 < P < 1.2$ GPa) pressure range. As pressure is further increased, enthalpy of α -phase gets lowered than that of γ and β -phases. Therefore, the α -phase is favoured above 1.3GPa. At further higher pressure, enthalpy shows the lowest value for highest pressure δ -phase. The calculated total energy and enthalpy show several crossovers which may indicate possible phase transitions, among metastable states, namely, from γ - to α , γ - to δ , β - to α , β - to δ and α to δ -phase. The enthalpy crossover shows a phase transition from γ - to α at around 1.3 GPa and γ - to δ -phase transition at around 3.2 GPa. The transitions from β - to α and β - to δ are observed from the enthalpy plot at around 1.6 and 3.7 GPa respectively.

The critical pressures for the high pressure phase transition as calculated from the enthalpy crossover are only slightly different from the experimental values[27]. However,

enthalpy curve implies that β -phase is more stable in comparison to γ -phase at zero pressure (at zero temperature). Experimentally, β -phase was reported to be stable at low temperature[58] (<273K). The α to δ -phase transition is found at about 30 GPa. For more accurate picture of phase stability at finite temperatures, one need to include the entropy and calculate the Gibbs free energy in various phases (Section 3.3.3). Since these are crystalline solids hence most of the entropy is contributed by phonon vibrations.

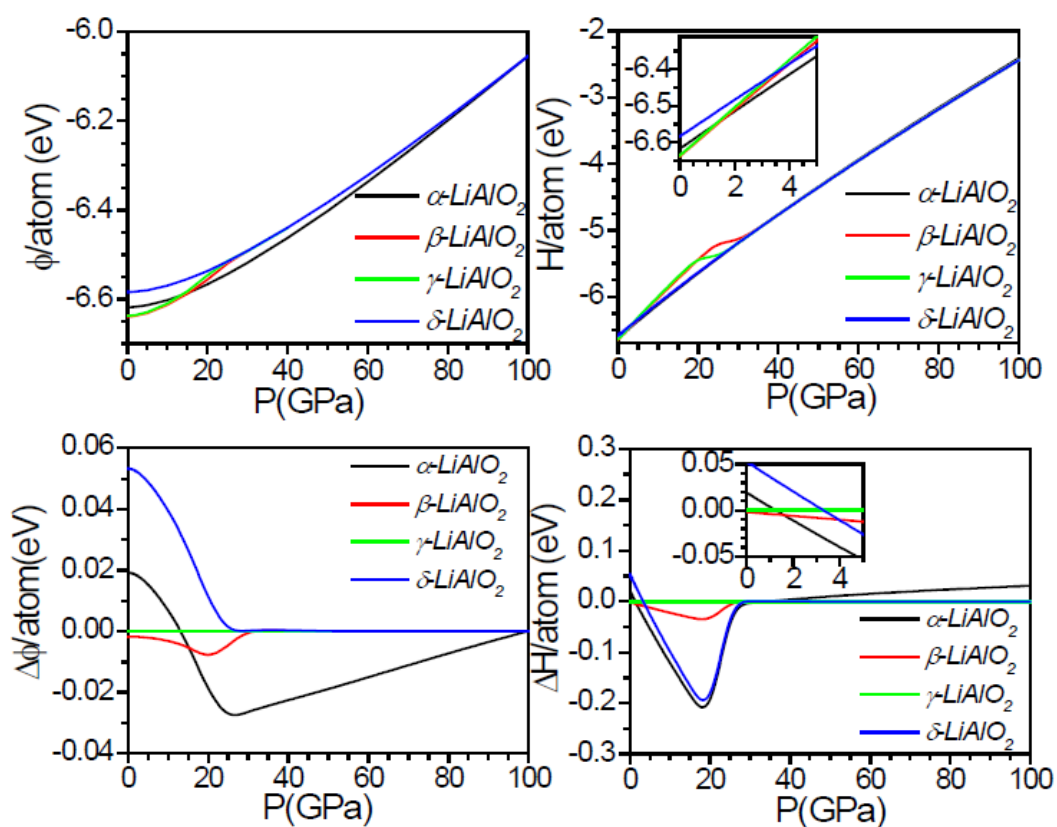


FIG 3.4 Calculated internal energy (Φ), enthalpy (H) and their differences with respect to that of γ -phase, for various phases of LiAlO_2 , as a function of pressure at 0K.

3.3.3 Phonon Spectra of Various Phases of LiAlO_2

The phonon dispersion curves along the high symmetry directions in the Brillion zone of various high-pressure phases of LiAlO_2 are shown in Fig 3.5. The various high

symmetry directions are chosen according to crystal symmetry[60]. The numbers of phonon branches are different for each phase as these branches are related to the number of atoms and symmetry of the primitive unit cell. The slope of the acoustic phonon modes is related to the elastic properties of the crystal.

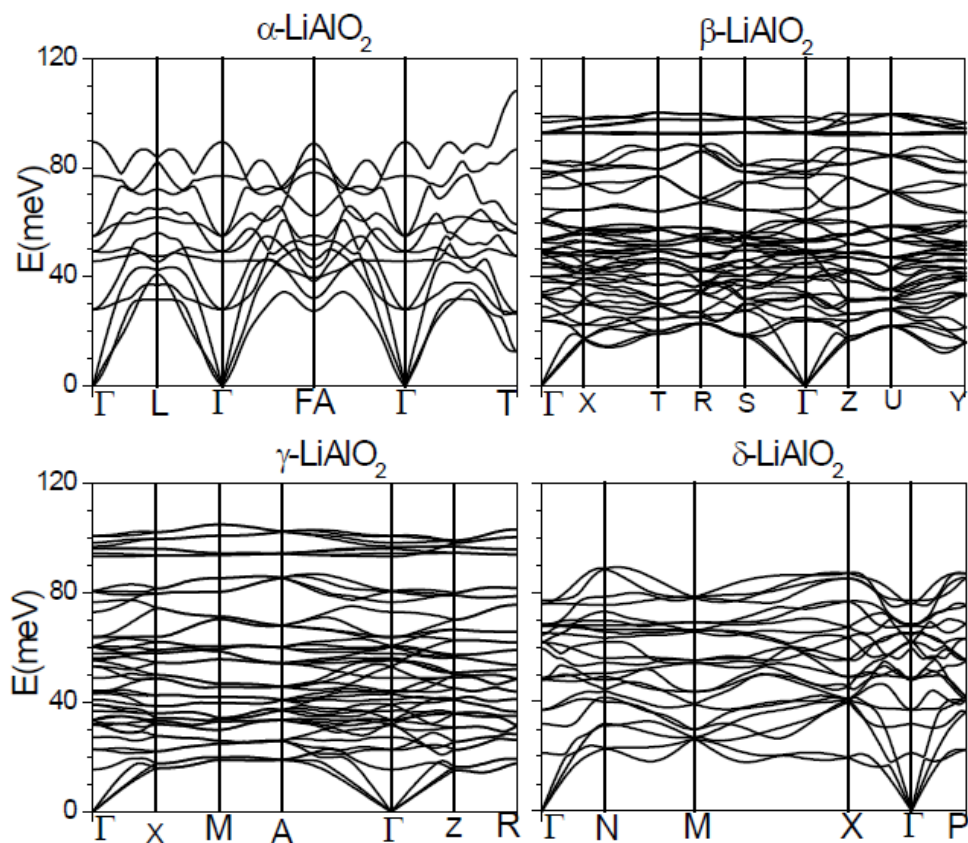


FIG 3.5 The calculated phonon dispersion curves along various high-symmetry directions[60] for various phases of LiAlO_2 , using *ab-initio* lattice dynamics.

As seen from Fig 3.5, the slope of acoustic phonon modes for α , β and δ phases are large as compared to that of γ -phase. This indicates comparatively hard nature of these phases, which is related to their lower volume and high-pressure stability. The highest energy phonon bands signify the polyhedral stretching vibrations of Al-O and Li-O bonds. There exists a significant band gap in the phonon dispersion and phonon density of states (from 80 to 90 meV) for γ -phase which reduces in the first high pressure phase (β -phase)

and ultimately disappears in the successive high-pressure phases (α and δ phases). This disappearance of phonon band gap and shifting of highest energy phonon branches towards lower energy signify delocalization of phonon bands due to tetrahedral to octahedral coordination as one goes for the high-pressure phases. The lowering of Al-O and Li-O stretching frequencies in the high-pressure phases may come from the longer octahedral bonds as compared to tetrahedral bonds.

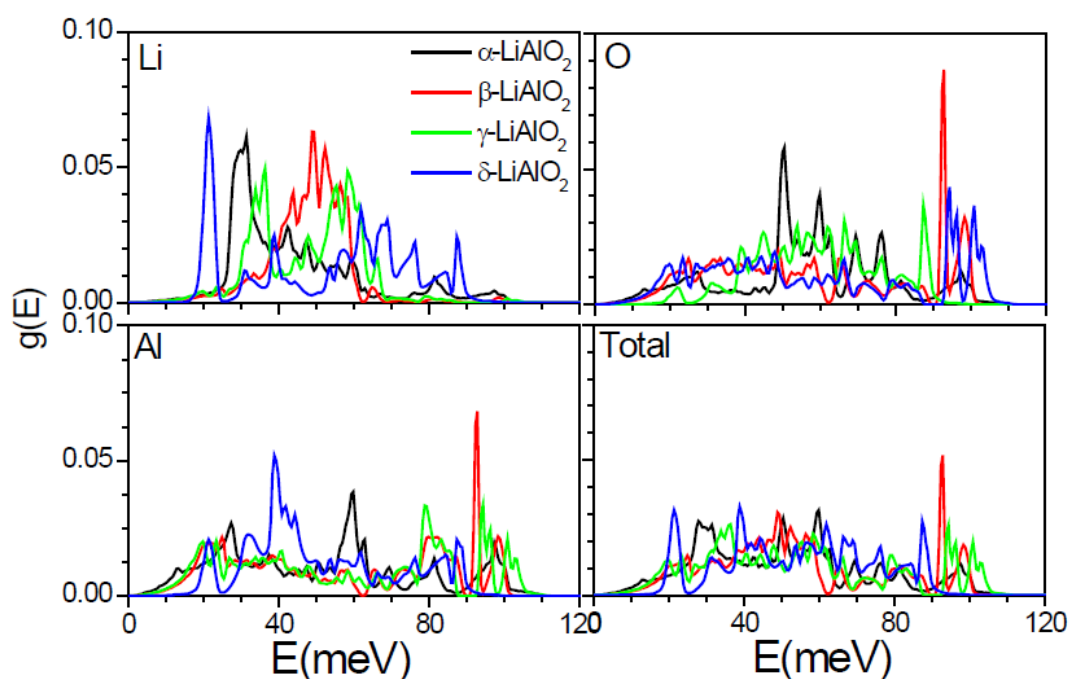


FIG 3.6 The calculated partial and total phonon density of state in various phases of LiAlO_2 using *ab-initio* lattice dynamics.

The calculated total and partial (atom wise) phonon density of states for the various high pressure/temperature phases of LiAlO_2 , are given in Fig 3.6. It is clear that different atoms contribute in different energy interval to the total phonon density of states. The comparison of total phonon density of states for various phases reveals a peak like behavior in low energy range for α and δ phases as compared to that of γ and β phases. This will give rise to high entropy contribution to the free energy in α and δ phases. This

arises from the low energy peaks in the partial phonon density of states associated with Li atoms. However, the comparison of phonon spectra of γ and β phases shows that the phonon spectrum in the ambient pressure phase (γ -phase) is more populated in the low energy region as compared to that of first high pressure phase (β -phase). This gives higher entropy at ambient pressure for γ -phase than that for β -phase.

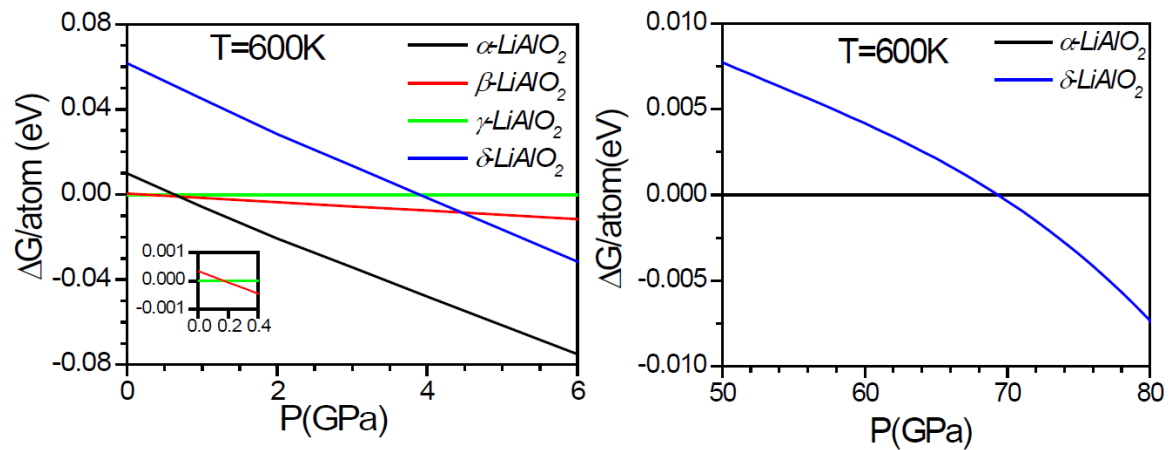


FIG 3.7 Calculated Gibbs free-energy difference for various phases of LiAlO_2 compared to the γ -phase as a function of pressure at 600 K.

3.3.4 Pressure Temperature Phase Diagram of LiAlO_2

The free energy as a function of pressure at different temperatures for the various phases of LiAlO_2 is calculated. It can be seen (Fig 3.7) as temperature increases to 600K, the phonon entropy starts playing a significant role in stabilizing the various phases. Due to this entropy contribution, the free energy of γ -phase is slightly lower than that of β -phase unlike the enthalpy behaviour discussed above. Therefore, free energy reflects the stability of γ -phase at ambient pressure conditions. The calculated phase transition pressure for γ to β -phase at 600K is found to be 0.2 GPa. This transition was experimentally obtained at 0.8 GPa and 623K[27]. Therefore, phonon entropy plays an

important role in γ to β phase transition. This is a first order phase transition with increase in density from 2.61 to 2.68 g/cm³. However, as the free energies of the γ and β phases are very close, both the phases could coexist at ambient pressure as observed experimentally.

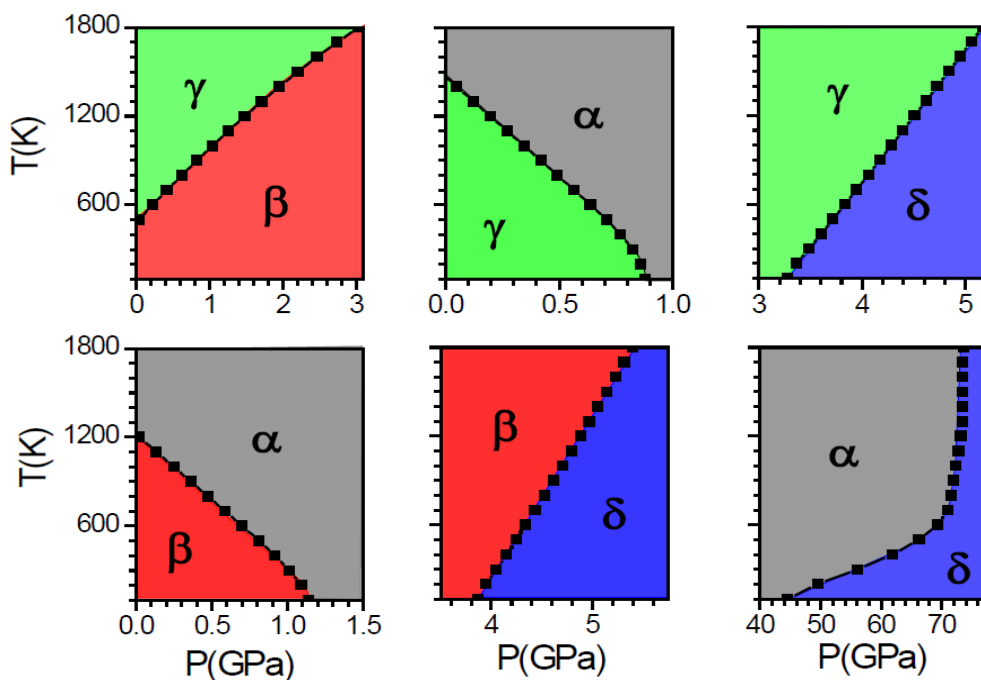


FIG 3.8 Calculated pressure-temperature phase diagram of LiAlO_2 . The phase boundaries are calculated from the Gibbs free-energy differences for various phases.

Further, the critical pressure for γ (or β) to α phase transition is obtained to be 0.6 (or 0.7) GPa at 600K. This transition is experimentally reported at 0.5-3.5 GPa and 933-1123 K[27]. The γ to α phase transformation is of order as it involve volume drop of about 20%. This transition takes place by increasing the coordination numbers of both the Li and Al atoms from four to six (more details in Section 3.3.5). The structure of the α - LiAlO_2 is hexagonal containing AlO_6 and LiO_6 octahedral units. The octahedral units in α phase are found to be square bipyramidal in nature with different planner and axial bond lengths. If the γ to α phase transition is prevented, it is found from the energy crossover that γ - LiAlO_2 could transform to a δ - LiAlO_2 phase around 4GPa and 600K. The δ -phase is

experimentally obtained from γ -phase with static pressure 4.0 GPa as well with dynamic shock pressure of 9.0 GPa. The earlier calculations[61] using different pseudo potentials underestimated this value to 2.3 GPa. This phase is also made up of (Li, Al)O₆ octahedra. Free energy crossovers also suggest β to α and β to δ phase transitions as earlier discussed in enthalpy plots. The α to δ -phase transition at very high pressure is found at about 40GPa from the free-energy crossover. The experimental data for this phase transition is not yet available. The complete pressure-temperature phase diagrams (Fig 3.8), for transition between various phases, are also calculated from the Gibbs free energy.

3.3.5 Structural Changes during Phase Transitions

The high-pressure structure optimization is performed for various phases of LiAlO₂. These calculations are used to extract the pressure dependence of volume (Fig 3.9(a)) and bond lengths (Fig 3.9(b-f)) in all the phases. The different phases of LiAlO₂ have different number of atoms in the unit cell, so for the sake of comparison, the volume per atom (Fig 3.9(a)) is plotted. It can be seen that, at low pressures, the ambient pressure phase (γ -phase) has the highest volume/atom among all the phases. β -phase has lower volume/atom as compared to that of γ -LiAlO₂. This gives a signature of high pressure stability of β -phase than that of γ -phase as observed from the Gibbs free energy calculations. Similarly, volume/atom for α and δ phases are further lower because they are further higher-pressure phases. At around 21 GPa the volume/atom for γ -LiAlO₂, which would be in a metastable state at this pressure, becomes equal to that for β -LiAlO₂. Further at around 25GPa, the volume/atom for both γ -LiAlO₂ and β -LiAlO₂ becomes equal to the highest pressure (δ -LiAlO₂) phase. The volume/atoms for α -LiAlO₂ and δ -LiAlO₂ phases become equal at very high pressure of 100GPa.

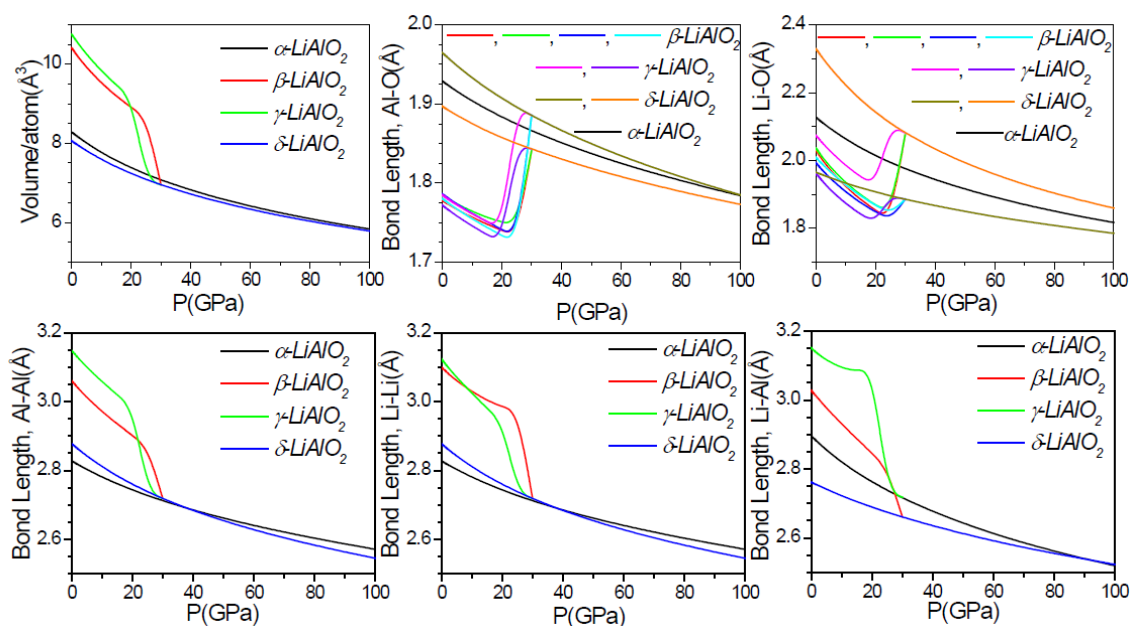


FIG 3.9 Calculated pressure dependence of volume and various atomic-pair distances for the various phases of LiAlO_2 .

The sharp decrease in volume/atom of $\gamma\text{-LiAlO}_2$ and $\beta\text{-LiAlO}_2$ in comparison to that of $\delta\text{-LiAlO}_2$ actually happen due to the increase in coordination of Li and Al from 4 to 6. This can be understood in terms of change in bond lengths (Fig 3.9(b-f)) with pressure. The calculated bond lengths (Fig 3.9(b-f)) show that the AlO_4 (and LiO_4) tetrahedra are not regular in γ and β phase, due to the different Al-O (and Li-O) bond lengths of the tetrahedral units. The tetrahedral bond lengths decrease with increasing pressure and show a sudden increase at around 25 GPa. This sharp increase in Li-O and Al-O bond lengths signify the transformation of LiO_4 and AlO_4 tetrahedral units to corresponding LiO_6 and AlO_6 octahedra of $\delta\text{-LiAlO}_2$. The two different values of each Li-O (and Al-O) bond lengths still implies the irregular nature of octahedral units, which tend to become regular with further increase in pressure up to 100 GPa. Moreover, the atomic pairs like Al-Al, Li-Li and Li-Al are well separated in $\gamma\text{-LiAlO}_2$ and $\beta\text{-LiAlO}_2$ at ambient pressure. These distances also show a sudden jump at around 25 GPa and

converge to corresponding values for δ -LiAlO₂. It is interesting to note that even up to very high pressure of 100 GPa, the bond lengths of α -LiAlO₂ do not converge to that of corresponding δ -LiAlO₂ phase.

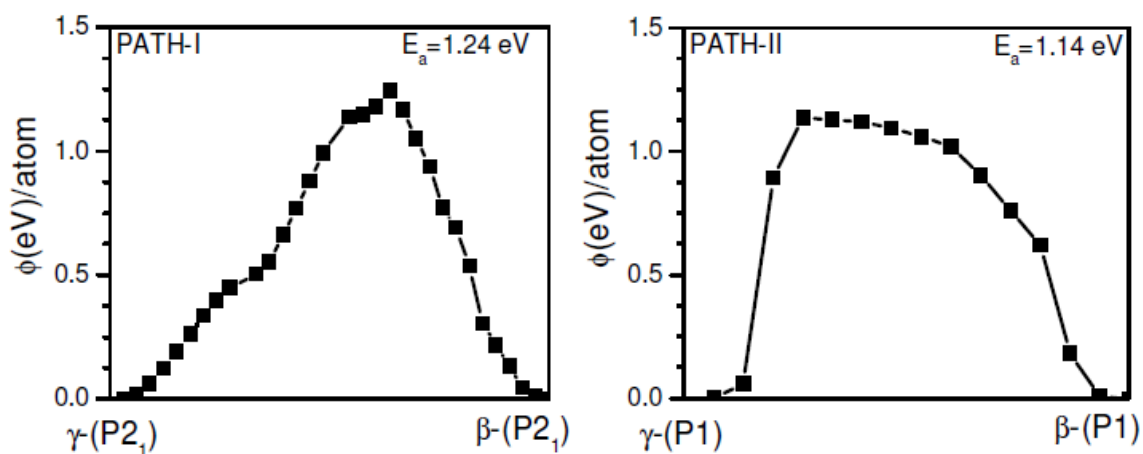


FIG 3.10 Calculated transition pathways, through Path-I and Path-II, for γ to β -LiAlO₂ phase transition using *ab-initio* DFT nudged elastic band method. The solid squares represent the intervening images at which calculations are performed.

3.3.6 Energy Barrier for γ to β Phase Transition

The activation energy barrier for the γ to β phase transformation is calculated using the nudged elastic band method calculations as implemented in the USPEX software[62]. Group theory analysis shows that the transition from γ (P4₁2₁2) to β (Pna2₁) phase can take place through either of the two common subgroups, namely, P2₁ and P1, of both the phases. These transition paths are designated as Path-I and Path-II respectively. The group-subgroup transformation from P4₁2₁2 to P2₁ occurs through Wyckoff site splitting from 4a (Li), 8b (O) and 4a (Al) in P4₁2₁2 to corresponding all 2a (Li, O & Al) sites in P2₁. Similarly, group-subgroup transformation from Pna2₁ to P2₁ takes place through all 4a (Li, O, Al) sites to all 2a (Li, O, Al) sites. For γ to β -LiAlO₂ transition

through their common subgroup P1, all the Wyckoff sites in P4₁2₁2 (γ -LiAlO₂) and Pna2₁ (β -LiAlO₂) split in 1a sites of corresponding P1 subgroup. The total energies for Path-I and Path-II as calculated using DFT are shown in Fig 3.10. An activation energy per atom of 1.24 eV is required for this transformation through Path-I. Similarly, the activation energy per atom of 1.14 eV is calculated for the Path-II. These calculated values for the γ to β phase transition are lower in comparison to the activation energy barrier of 1.8 eV, for the γ to α phase transition[61], as reported from previous calculations which may be expected since the latter transition also involves large coordination changes.

3.3.7 Phonons and High Temperature Phase Transitions

The high pressure phases of LiAlO₂ become unstable on heating and transform to the ambient pressure phase[28,29,58,59]. The α -phase, which is used in molten carbonate fuel cells, undergoes α to γ phase transition[28,29] above 600°C. The slow kinetics of this transition makes it difficult to identify the transition temperature. However, the transformation is generally complete by 900°C. In this transition the structural volume expands. The phonon dispersion curve (Fig 3.11) in the α -phase by expanding the unit cell of α -phase to the corresponding volume of γ -phase. Three optic phonon branches are found to become unstable. These phonon modes may be responsible for the high temperature instability of the structure and might lead to α to γ phase transition. The eigenvectors of these modes are analyzed (Fig 3.11) at the zone centre of the Brillouin zone. These modes are highly contributed by the vibrations of Li atoms with small contribution from the oxygen atoms. The first phonon mode involves the Li vibrations perpendicular to the layers of AlO₆ octahedra and may break the layered structure. The other phonon mode involves the sliding motion of Li in between the successive layers of

AlO_6 octahedra. These types of motion may cause the diffusion of Li in the 2D layers. This may give rise to the observed low binding energy of Li in $\alpha\text{-LiAlO}_2$ as observed experimentally[63]. The diffusion of Li breaks the Li-O octrahedral bonds. In a molten carbonate fuel cell, as the cell works, the temperature increases, this may cause large amplitude vibrations of Li atoms. These vibrations may trigger the phase transition from α to γ -phase.

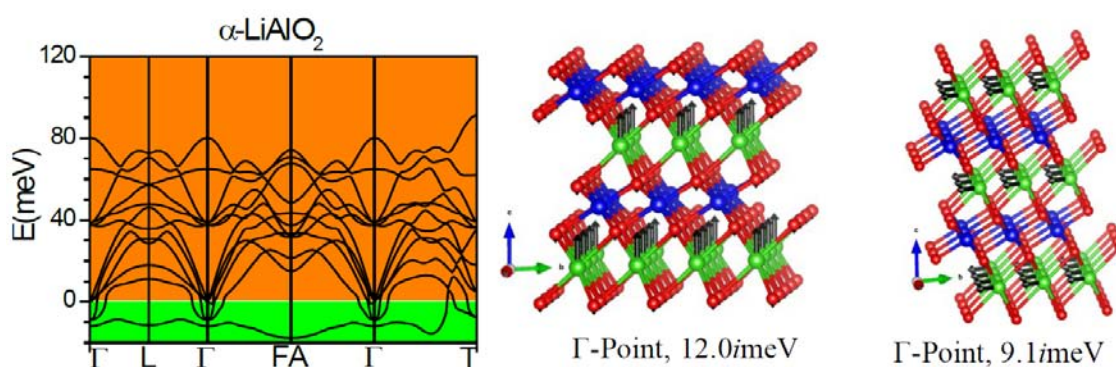


FIG 3.11 Calculated phonon dispersion curves of $\alpha\text{-LiAlO}_2$ for the expanded volume. The eigenvector pattern of corresponding unstable phonon modes at Γ point are given on the right. The high-symmetry points are chosen according to the crystal symmetry[60].

The δ -phase is experimentally known to transform to γ -phase at around 1173K[59]. In order to understand the mechanism of the phase transition, the phonon dispersion for δ -phase (Fig 3.12) is calculated at expanded volume corresponding to that of γ -phase. Two optic phonon branches become unstable which are degenerate at zone centre of the Brillion zone. The eigenvectors of these modes involve (Fig 3.12) large amplitudes of oxygen atoms along with some contribution from Al atoms. The Li atoms are found to remain steady in these particular phonon modes. Two of the oxygen atoms out of six in AlO_6 octahedra show the outward vibrations which may results in breaking of Al-O bonds. All other four oxygen show bending of Al-O bonds about Al atom. This type

of vibrations may give rise to formation of tetrahedral form from the existing AlO_6 octahedra. Moreover, the vibration of Al atoms towards the centre of the tetrahedral geometry will give rise to the shortening of Al-O bond lengths. Therefore, both the high-pressure phases transform to the ambient phase through very different mechanisms, one initiated by Li vibrations and the other by O and Al vibrational motion.

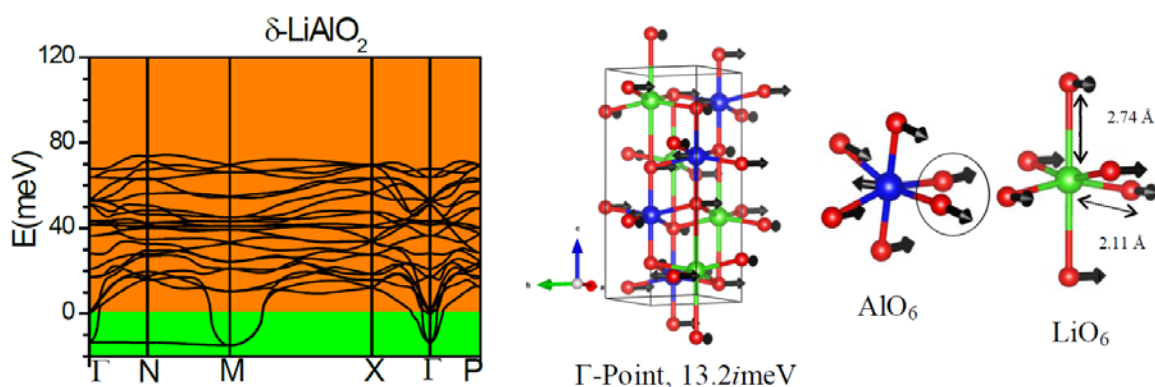


FIG 3.12 Calculated phonon dispersion curves of $\delta\text{-LiAlO}_2$ for the expanded volume. The eigenvector pattern of corresponding unstable phonon modes at Γ point is given on the right. The high-symmetry points are chosen according to the crystal symmetry[60].

3.3.8 Thermal Expansion Behavior of $\gamma\text{-LiAlO}_2$

The linear thermal expansion coefficients along the ‘a’ and ‘c’ -axes have been calculated within the quasiharmonic approximation[64-66]. The calculations require anisotropic pressure dependence of phonon energies in the entire Brillouin zone[67]. An anisotropic stress of 5 kbar is implemented by changing the lattice constant ‘a’ and keeping the ‘c’ parameter constant; and vice versa. The calculated mode Grüneisen parameters as a function of phonon energy along different crystal directions are shown in Fig 3.13(a). The calculated elastic compliances matrix is given in Table 3.2.

TABLE 3.2 The calculated non-zero components of elastic compliance (GPa^{-1}) matrix for the γ -phase at ambient pressure.

$S_{11}=S_{22}$	$S_{12}=S_{21}$	$S_{13}=S_{23}=S_{31}=S_{32}$	S_{33}	$S_{44}=S_{55}$	S_{66}
0.00984	-0.00332	-0.00253	0.00785	0.01679	0.01599

The calculated temperature dependence of the lattice parameters is in excellent agreement (Fig 3.13(b)) with the recent experimental neutron diffraction data[9]. The calculated linear thermal expansion coefficients at 300 K are $\alpha_a=10.1 \times 10^{-6} \text{ K}^{-1}$ and $\alpha_c=16.5 \times 10^{-6} \text{ K}^{-1}$. They compare very well with available experimental values[9,30]. The thermal expansion along c -axis is large in comparison to that in the a - b plane. The calculated lattice parameters are in a very good agreement with the available experimental data even at very high temperatures up to 1500 K. This implies that the quasiharmonic approximation for this compound is valid even at very high temperature.

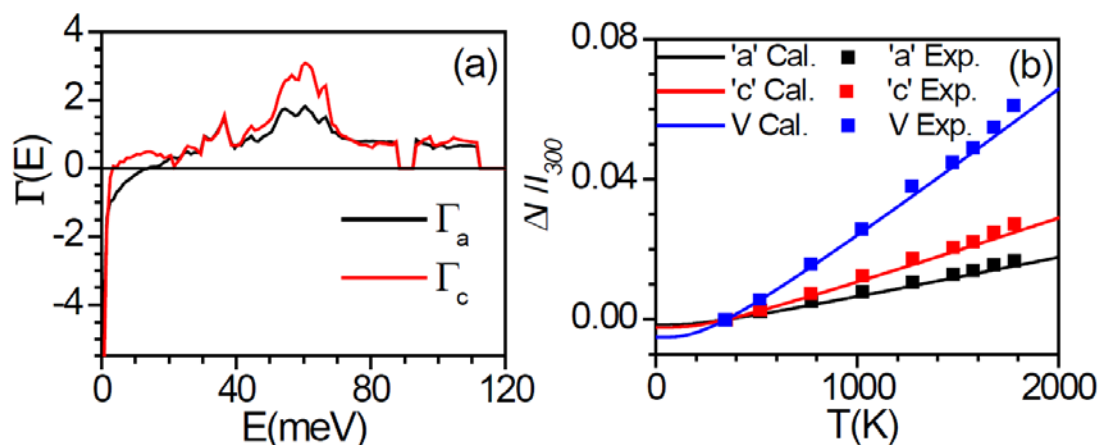


FIG 3.13 (a) The calculated Grüneisen parameter, and (b) the temperature-dependent experimental and calculated lattice parameters and volume [$(l-l_{300} \text{ K})/l_{300} \text{ K}$], $l = a, c, V$].

The phonon modes around 35 and 55 meV have a large positive value of Grüneisen parameter (Fig 3.13(a)). The displacement patterns of two of the zone centre modes in this energy range are shown in Fig 3.14. The eigenvector of the first mode (36.9

meV) shows (Fig 3.14) that the mode is highly contributed by the Li motion in a-b plane along with a small component of AlO_4 polyhedral vibrations. So, this mode can give an expansion in the a-b plane. The other mode of 55.7 meV (Fig 3.14) has a high value of Γ_c and involves Li motion in a-c and b-c planes along with some component of AlO_4 polyhedral rotation. This type of mode can give an expansion along the c-axis.

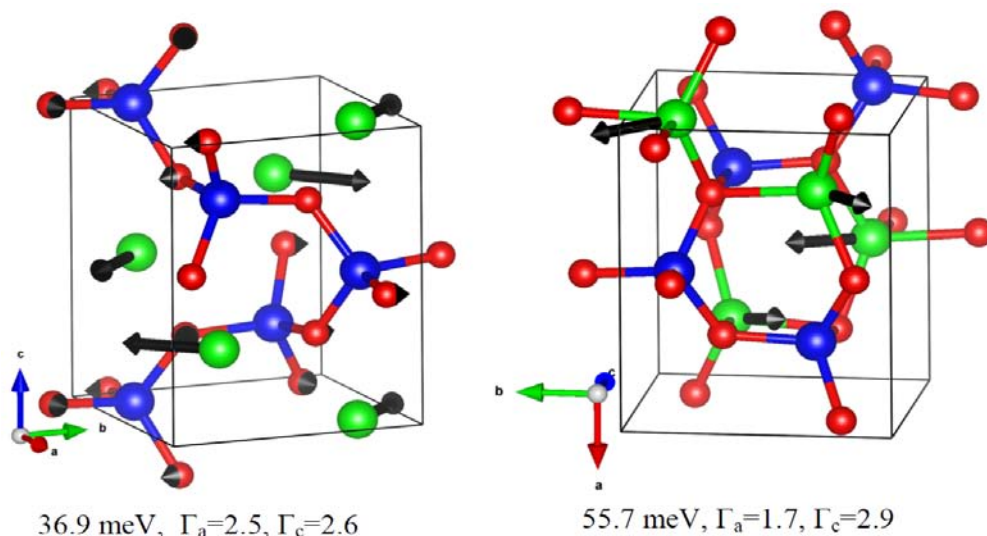


FIG 3.14 The displacements pattern of the zone-centre optic mode which makes a large contribution to thermal expansion in (a) a-b plane, and (b) along c-axis.

3.3.9 Li Diffusion in $\gamma\text{-LiAlO}_2$

The experimentally measured temperature dependent phonon density of states (DOS) using inelastic neutron scattering is shown in Fig 3.15(a). To identify the various peaks and partial atomic contribution from various species in LiAlO_2 in the measured spectra, the phonon spectra is calculated using *ab-initio* molecular dynamics (MD) simulations. The multiphonon corrected experimental phonon DOS of 473K is compared with the MD calculations at 300K (Fig 3.15(b)). Various peaks in the experimental spectra are very well reproduced by the calculations.

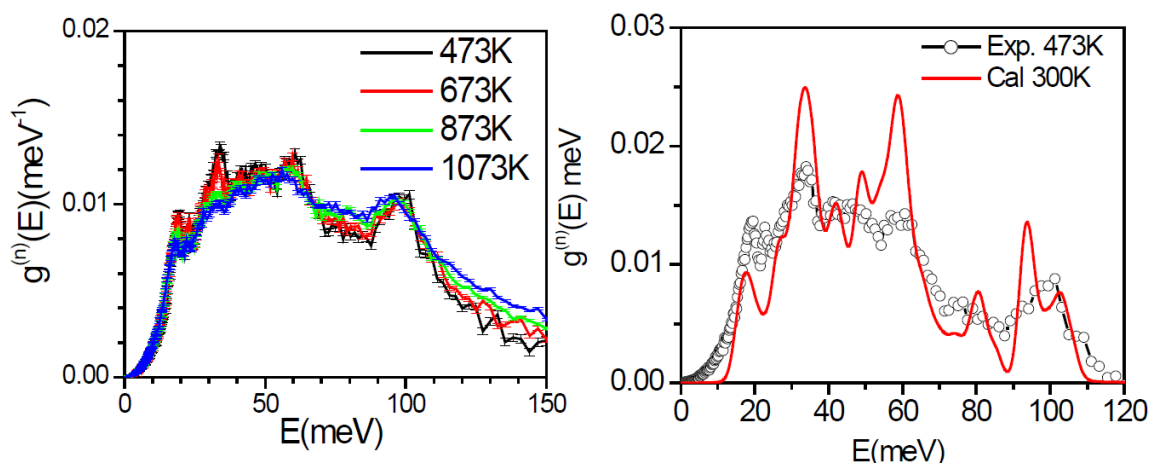


FIG 3.15 (a) The experimentally measured phonon density of states at various temperatures obtained using inelastic neutron scattering measurements (b) Multiphonon corrected experimental(473K) and MD calculated(300K) phonon density of states.

The partial phonon density of states (Fig 3.16) of each atom provides the contribution of individual atoms to total phonon spectra and provides the energy range of dynamics of various atoms in the compound. The peak in spectra around 100 meV arises from the stretching vibrations of strong Al-O bonds because this region is only contributed by Al and O atoms. But the peaks around 35 and 55 meV are largely contributed by dynamics of Li atoms.

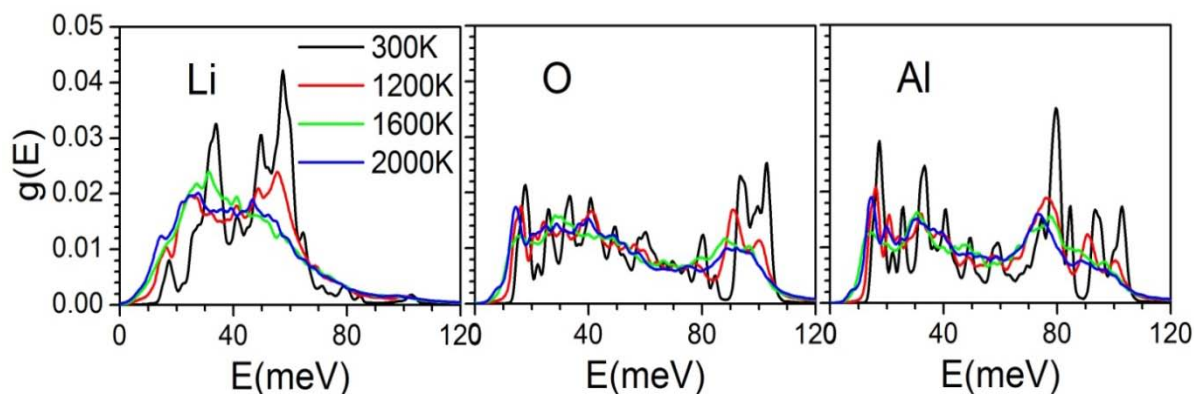


FIG 3.16 The ab-initio molecular dynamics calculated partial phonon density of states for different atoms in LiAlO_2 , at various temperatures.

The sharp decrease in the intensity of peaks in the experimentally measured phonon spectra around 35 and 55 meV may be arises from the large vibrational amplitude as well as diffusion of Li in the lattice. Hence in order to get the microscopic understanding of the experimental observation, we have performed the *ab-initio* MD simulations at various temperatures at 300K, 1200K, 1600K and 2000K. The calculated temperature dependent partial phonon density of states (Fig 3.16) shows significant decay in the peak intensity in Li partial density of states.

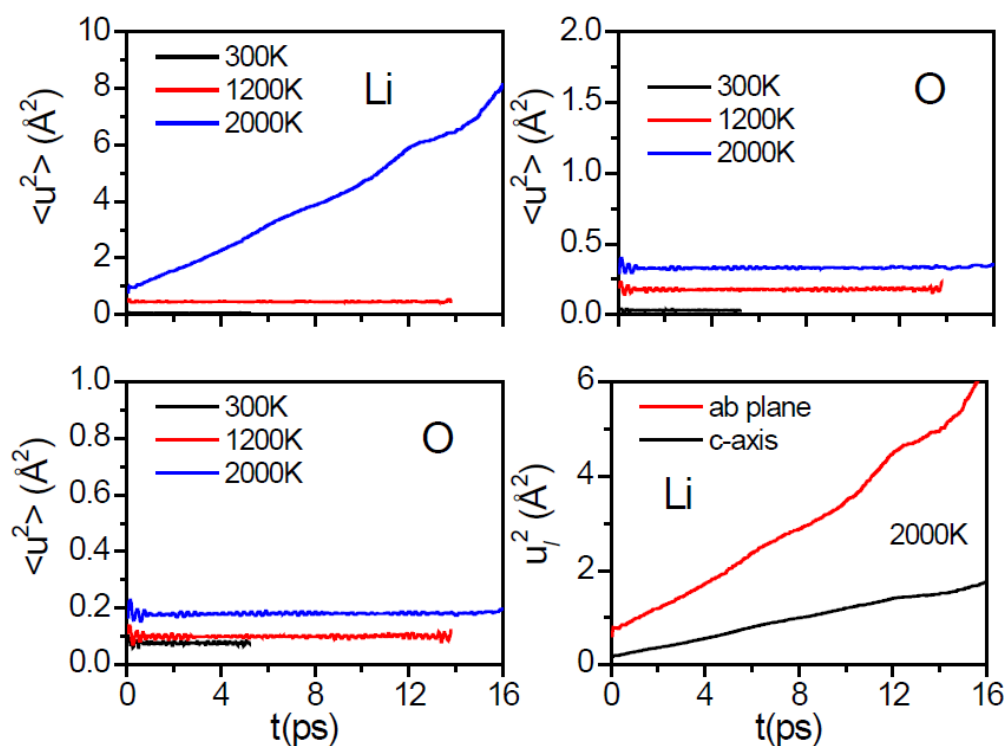


FIG 3.17 The *ab-initio* calculated (a-c) mean square displacements ($\langle u^2 \rangle$) of various atoms, Li, O and Al and (d) anisotropic mean square displacement of Li in a-b plane and along c-axis at various temperatures.

To investigate this further, we have calculated mean squared displacements (MSD) of various type of atom averaged over number of atoms of a given type as a function of time at various temperatures are shown in Fig 3.17. It can be seen that all the

atoms i.e. Li, O and Al shows very small MSD indicating normal vibration about their corresponding mean positions up to 1200K. However, at 2000K, although Al and Si show normal vibrations but Li atoms show an increasing trend in calculated MSD with time, this is a signature of diffusion. Hence, we confirmed that at 2000K, the Li atom started diffusing in the compound while other atoms remain intact and provide host structure for diffusion. Further the calculated anisotropy in MSD of Li atoms show that the diffusion of Li atoms is more pronounced in *a-b* plane than that along the *c*-axis of the unit cell.

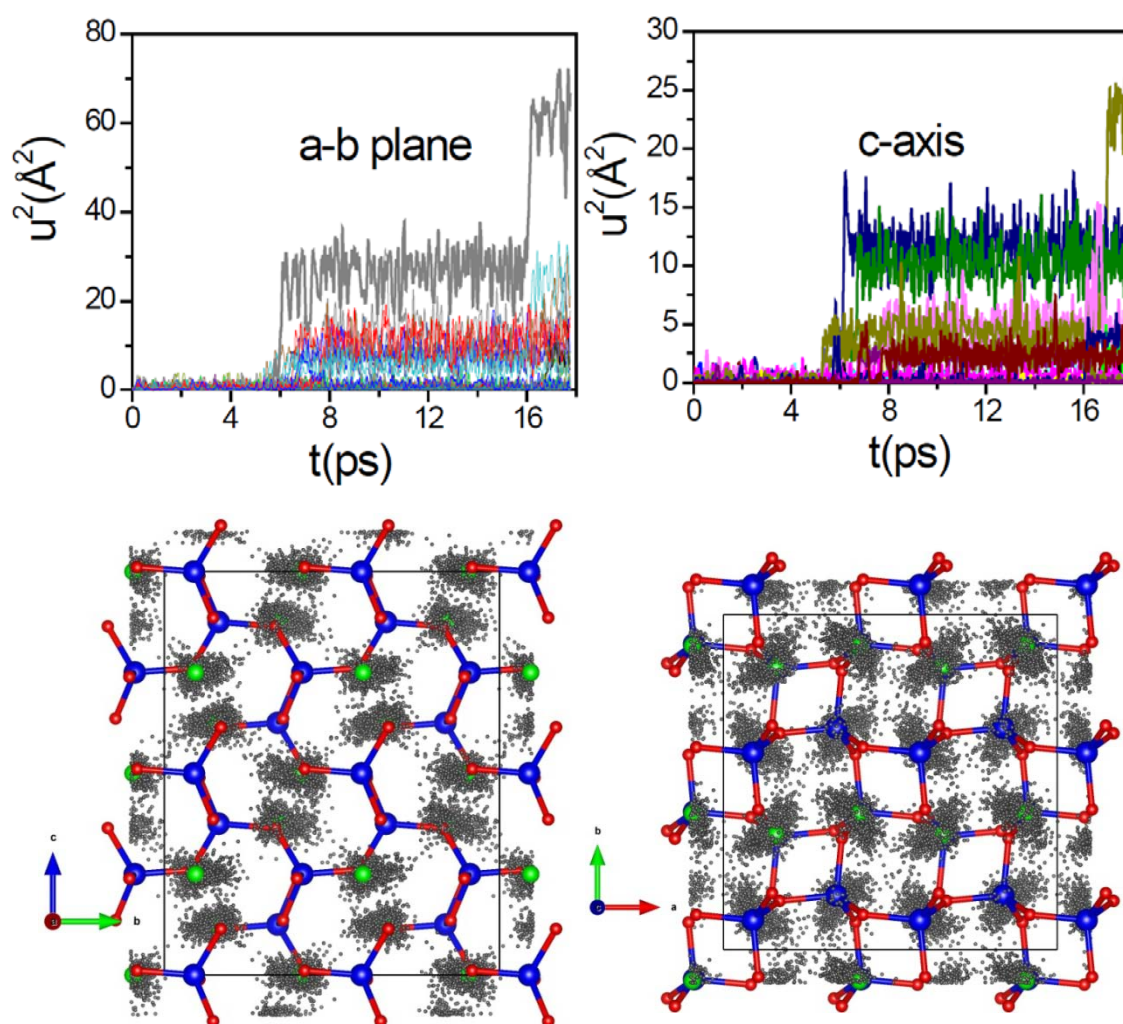


FIG 3.18 (Top) The calculated jumps in terms of squared displacements (u^2) of individual atoms in *a-b* plane and along *c*-axis at 2000K (Bottom)The *ab-initio* calculated trajectories of Li atoms at 2000K projected along various crystal directions.

The calculated jump displacements of individual Li atoms along various directions are shown in Fig 3.18. It can be seen that there are more number of Li atoms jumping in *a-b* plane than that along *c*-direction. This can also be seen from the trajectories of Li atoms projected along various crystal directions. These trajectories show that significant Li atom diffusion in *a-b* plane attributed to large number of jumps in *a-b* plane than that along the *c*-axis. From structural point of view, it can be related to closer Li sites and more open channels in *a-b* plane for Li ion migration than that along *c*-axis.

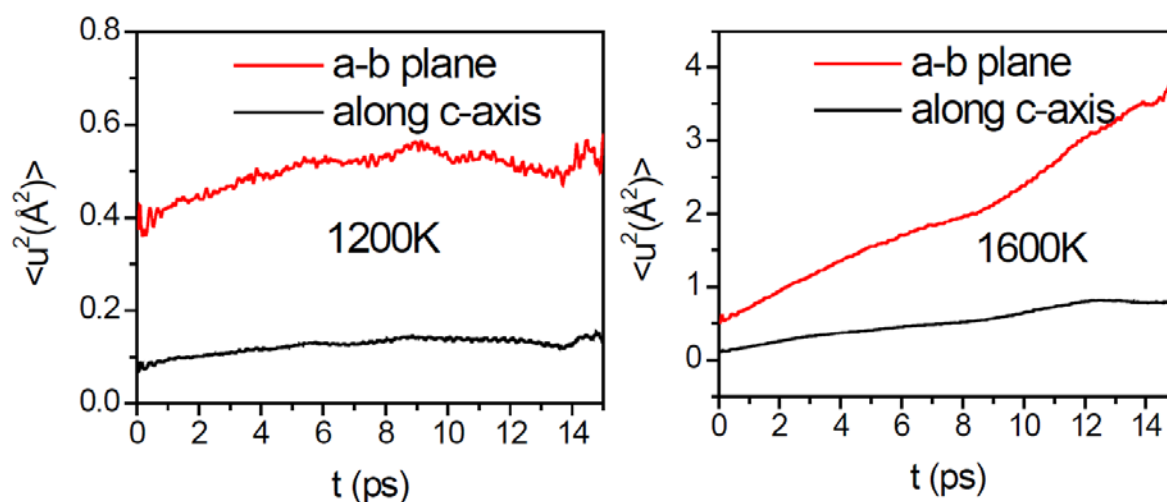


FIG 3.19 The *ab-initio* calculated mean square displacements of Li in vacancy containing structure in *a-b* plane and along *c*-axis at 1200K and 1600K.

Further, to explore the possibility of enhancement of Li ion diffusion in the compound we have performed the molecular dynamics simulation with Li vacancy in the structure. For this purpose, one of Li from $2 \times 2 \times 2$ supercell of LiAlO_2 is removed (i.e., one Li out of 32 Li is removed) and structure is relaxed. These calculations show that the diffusion of Li initiates at lower temperatures than that for the perfect crystal (Fig 3.19). Although there are signatures of Li vacancy diffusion at 1200 K where there is small slope in calculated MSD, but at 1600 K the diffusion is clearly visible. The increase in

diffusion with vacancy in structure favours at low temperature because vacancy creates the frustration in bonding of nearest Li atoms and enhanced the Li ion migration probability in the structure.

3.4 Conclusions

Ab-initio density functional theory techniques are used to calculate the structural parameters of various phases of LiAlO_2 with pressure. The application of pressure leads to structural changes in γ -phase through tetrahedral to octahedral coordination change about Li/Al atoms, which give rise to the high pressure α and δ phases. The phonon entropy is found to play an important role in phase stability and transitions among various phases. On the basis of calculated free energy, the complete phase diagram of LiAlO_2 is obtained. Moreover, the phonon modes which are responsible for phase transition (upon heating) from α to γ are found to be dominated by the Li dynamics. This dynamics at high temperature could give rise to Li diffusion and hence the phase transformation to low density γ phase. On the other hand, phonon mode responsible for δ - to γ -phase transformation, upon heating, is dominated by Al and O atoms dynamics. This is accompanied by breaking of two Al-O bonds of AlO_6 octahedra while converting to AlO_4 tetrahedra. Moreover, the calculated anisotropic thermal expansion behaviour of γ - LiAlO_2 using *ab-initio* lattice dynamics agrees very well with experimental measurements and the thermal expansion behaviour is highly governed by phonon modes which involve the Li dynamics. The temperature dependent inelastic neutron scattering and *ab-initio* molecular dynamics simulations shows Li diffusion in γ - LiAlO_2 which is more pronounced in *a-b* plane than that along *c*-axis. The presence of Li vacancy is found to lower the temperature for Li diffusion from 2000 K to 1600 K.

References

- [1] N. Nitta, F. Wu, J. T. Lee, and G. Yushin, *Materials Today* **18**, 252 (2015).
- [2] J. B. Goodenough and K.-S. Park, *Journal of the American Chemical Society* **135**, 1167 (2013).
- [3] J.-M. Tarascon, *Philosophical Transactions of the Royal Society of London A: Mathematical, Physical and Engineering Sciences* **368**, 3227 (2010).
- [4] M. D. Bhatt and C. O'Dwyer, *Physical Chemistry Chemical Physics* **17**, 4799 (2015).
- [5] M. H. Braga, N. S. Grundish, A. J. Murchison, and J. B. Goodenough, *Energy & Environmental Science* **10**, 331 (2017).
- [6] R. Hausbrand, G. Cherkashinin, H. Ehrenberg, M. Gröting, K. Albe, C. Hess, and W. Jaegermann, *Materials Science and Engineering: B* **192**, 3 (2015).
- [7] J. Janek and W. G. Zeier, *Nature Energy* , **1**, 16141 (2016).
- [8] D. Wiedemann, S. Indris, M. Meven, B. Pedersen, H. Boysen, R. Uecker, P. Heitjans, and M. Lerch, *Zeitschrift für Kristallographie-Crystalline Materials* **231**, 189 (2016).
- [9] D. Wiedemann *et al.*, *Chemistry of Materials* **28**, 915 (2016).
- [10] P. Waltereit, O. Brandt, A. Trampert, H. T. Grahn, J. Menniger, M. Ramsteiner, M. Reiche, and K. H. Ploog, *Nature* **406**, 865 (2000).
- [11] J. Charpin, F. Botter, M. Briec, B. Rasneur, E. Roth, N. Roux, and J. Sannier, *Fusion Engineering and Design* **8**, 407 (1989).
- [12] F. Botter, F. Lefevre, B. Rasneur, M. Trotabas, and E. Roth, *Journal of Nuclear Materials* **141–143, Part 1**, 364 (1986).
- [13] Q. Hu *et al.*, *Physical Review B* **97**, 014106 (2018).
- [14] Q. Hu, L. Lei, X. Yan, L. Zhang, X. Li, F. Peng, and D. He, *Applied Physics Letters* **109**, 071903 (2016).
- [15] L. Lei, T. Irifune, T. Shinmei, H. Ohfuji, and L. Fang, *Journal of Applied Physics* **108**, 083531 (2010).
- [16] H. Cao, B. Xia, Y. Zhang, and N. Xu, *Solid State Ionics* **176**, 911 (2005).
- [17] L. Li, Z. Chen, Q. Zhang, M. Xu, X. Zhou, H. Zhu, and K. Zhang, *Journal of Materials Chemistry A* **3**, 894 (2015).
- [18] G. Ceder, Y. M. Chiang, D. R. Sadoway, M. K. Aydinol, Y. I. Jang, and B. Huang, *Nature* **392**, 694 (1998).
- [19] M. A. K. Lakshman Dissanayake, *Ionics* **10**, 221.
- [20] M. M. Islam, J. Uhlendorf, E. Witt, H. Schmidt, P. Heitjans, and T. Bredow, *The Journal of Physical Chemistry C* **121**, 27788 (2017).
- [21] E. Witt, S. Nakhal, C. V. Chandran, M. Lerch, and P. Heitjans, *Zeitschrift für Physikalische Chemie* **229**, 1327 (2015).
- [22] M. M. Islam and T. Bredow, *The Journal of Physical Chemistry Letters* **6**, 4622 (2015).
- [23] D. Wohlmuth *et al.*, *Journal of Materials Chemistry A* **2**, 20295 (2014).

- [24] Q. Hu, L. Lei, X. Jiang, Z. C. Feng, M. Tang, and D. He, *Solid State Sciences* **37**, 103 (2014).
- [25] S. Indris, P. Heitjans, R. Uecker, and B. Roling, *The Journal of Physical Chemistry C* **116**, 14243 (2012).
- [26] B. Singh, M. K. Gupta, S. K. Mishra, R. Mittal, P. U. Sastry, S. Rols, and S. L. Chaplot, *Physical Chemistry Chemical Physics* **19**, 17967 (2017).
- [27] L. Lei, D. He, Y. Zou, W. Zhang, Z. Wang, M. Jiang, and M. Du, *Journal of Solid State Chemistry* **181**, 1810 (2008).
- [28] M. Marezio and J. Remeika, *The Journal of Chemical Physics* **44**, 3143 (1966).
- [29] V. Danek, M. Tarniowy, and L. Suski, *Journal of Materials Science* **39**, 2429 (2004).
- [30] B. Cockayne and B. Lent, *Journal of Crystal Growth* **54**, 546 (1981).
- [31] Y. X. Wang, Q. Wu, X. R. Chen, and H. Y. Geng, *Scientific Reports* **6**, 32419 (2016).
- [32] Y. Qi *et al.*, *npj Quantum Materials* **3**, 4 (2018).
- [33] W.-w. Peng, R. Tétot, G. Niu, E. Amzallag, B. Vilquin, J.-B. Brubach, and P. Roy, *Scientific Reports* **7**, 2160 (2017).
- [34] B. Cheng and M. Ceriotti, *Physical Review B* **97**, 054102 (2018).
- [35] V. Balédent *et al.*, *Physical Review B* **97**, 024107 (2018).
- [36] R. Zhang, P. Gao, X. Wang, and Y. Zhou, *AIP Advances* **5**, 107233 (2015).
- [37] Y. X. Wang, H. Y. Geng, Q. Wu, X. R. Chen, and Y. Sun, *Journal of Applied Physics* **122**, 235903 (2017).
- [38] D. Plašienka, R. Martoňák, and E. Tosatti, *Scientific Reports* **6**, 37694 (2016).
- [39] R. Lizárraga, F. Pan, L. Bergqvist, E. Holmström, Z. Gercsi, and L. Vitos, *Scientific Reports* **7**, 3778 (2017).
- [40] L. Yue, J. Ma, J. Zhang, J. Zhao, S. Dong, Z. Liu, G. Cui, and L. Chen, *Energy Storage Materials* **5**, 139 (2016).
- [41] G. A. S. Ribeiro, L. Paulatto, R. Bianco, I. Errea, F. Mauri, and M. Calandra, *Physical Review B* **97**, 014306 (2018).
- [42] E. Mozafari, B. Alling, M. P. Belov, and I. A. Abrikosov, *Physical Review B* **97**, 035152 (2018).
- [43] S. Li and Y. Chen, *Physical Review B* **96**, 134104 (2017).
- [44] G. Lan, B. Ouyang, Y. Xu, J. Song, and Y. Jiang, *Journal of Applied Physics* **119**, 235103 (2016).
- [45] N. Yedukondalu, G. Vaitheeswaran, P. Anees, and M. C. Valsakumar, *Physical Chemistry Chemical Physics* **17**, 29210 (2015).
- [46] S. Hirata, K. Gilliard, X. He, J. Li, and O. Sode, *Accounts of Chemical Research* **47**, 2721 (2014).
- [47] C. Cazorla, A. K. Sagotra, M. King, and D. Errandonea, *The Journal of Physical Chemistry C* **122**, 1267 (2018).
- [48] A. Erba, A. M. Navarrete-Lopez, V. Lacivita, P. D'Arco, and C. M. Zicovich-Wilson, *Physical Chemistry Chemical Physics* **17**, 2660 (2015).

- [49] C.-M. Lin, I. J. Hsu, S.-C. Lin, Y.-C. Chuang, W.-T. Chen, Y.-F. Liao, and J.-Y. Juang, *Scientific Reports* **8**, 1284 (2018).
- [50] J. Engelkemier and D. C. Fredrickson, *Chemistry of Materials* **28**, 3171 (2016).
- [51] R. Mittal, M. K. Gupta, and S. L. Chaplot, *Progress in Materials Science* **92**, 360 (2018).
- [52] B. Singh. et. al. (Unpublished).
- [53] B. Singh, M. Gupta, R. Mittal, and S. Chaplot, *Physical Chemistry Chemical Physics* **20**, 12248 (2018).
- [54] G. Kresse and J. Furthmüller, *Computational Materials Science* **6**, 15 (1996).
- [55] G. Kresse and J. Furthmüller, *Physical Review B* **54**, 11169 (1996).
- [56] H. J. Monkhorst and J. D. Pack, *Physical Review B* **13**, 5188 (1976).
- [57] K. Parlinski, PHONON, 2003.
- [58] J. Théry, A. Lejus, D. Briancon, and R. Collongues, *Bull. Soc. Chim. Fr.*, 973 (1961).
- [59] X. Li, T. Kobayashi, F. Zhang, K. Kimoto, and T. Sekine, *Journal of Solid State Chemistry* **177**, 1939 (2004).
- [60] M. I. Aroyo, J. Perez-Mato, D. Orobengoa, E. Tasci, G. De La Flor, and A. Kirov, *Bulg. Chem. Commun* **43**, 183 (2011).
- [61] W. Sailuam, K. Sarasamak, and S. Limpijumnong, *Integrated Ferroelectrics* **156**, 15 (2014).
- [62] A. O. Lyakhov, A. R. Oganov, H. T. Stokes, and Q. Zhu, *Computer Physics Communications* **184**, 1172 (2013).
- [63] R. Dronskowski, *Inorganic Chemistry* **32**, 1 (1993).
- [64] M. T. Dove, *Introduction to Lattice Dynamics* (Cambridge University Press, 1993).
- [65] S. L. Chaplot, R. Mittal, and N. Choudhury, *Thermodynamic Properties of Solids: Experiments and Modeling* (John Wiley & Sons, 2010).
- [66] G. Grimvall, *Thermophysical properties of materials* (Elsevier, 1999).
- [67] B. Singh *et al.*, *Journal of Applied Physics* **121**, 085106 (2017).

CHAPTER 4

Phonons, Anomalous Lattice Behaviour and Li-ion Diffusion in a Potential Battery Cathode, V_2O_5

4.1 Introduction

The battery research is progressively increasing for the efficient storage of energy. This demands the batteries to be lighter, quickly chargeable, safer, long lived, stable and cost effective[1,2]. There are relatively few gains that can be made to the battery besides directly improving component materials. In this respect many material scientists are searching for efficient electrodes and electrolyte materials. It has been calculated[3] that an increase of 57% in cell energy density can be obtained by doubling the capacity of cathode; however, only 47% gain is obtained by 10 times increasing the capacity of anode. Therefore, large focus of electrode material research is dedicated to the discovery of cathode materials[4]. Layered structure materials have been suggested best for battery cathode purpose.

Vanadium based oxides show a variety of interesting properties like catalytic behaviour[5], metal insulator transition[6] and super capacitor[7] properties. The low cost, high abundance, easy synthesis and high energy density[8] of vanadium pentoxide (V_2O_5) make it useful as a cathode material for Li and Na ion batteries[9-13]. It also finds application in solar cells[14] as window material, antireflection coatings, critical temperature sensors[15] and light detectors. The sheets made of entangled vanadium oxide nano fibers behave like actuators[16] (artificial muscles) that contract reversibly under an electrical signal due to its good mechanical properties.

4.1.1 Structural Details

At ambient condition, vanadium pentoxide crystallizes in orthorhombic phase (space group : $Pmmn$), known as α - V_2O_5 [17]. The structure (Fig 4 (a) & (b)) is build-up of zig-zag double chains of VO_5 square-based pyramids running along b -axis. These pyramids point alternately up and down and share an edge along the chain direction [010]. The chains are bridged, through corner sharing oxygen atoms along b -axis, to make a 2-D layered structure in x - y plane. The layers are weakly bonded along c -axis via V-O van der Waals interaction. There are three different types of O atoms named as: vanadyl (O2), chain (O3) and bridge (O1).

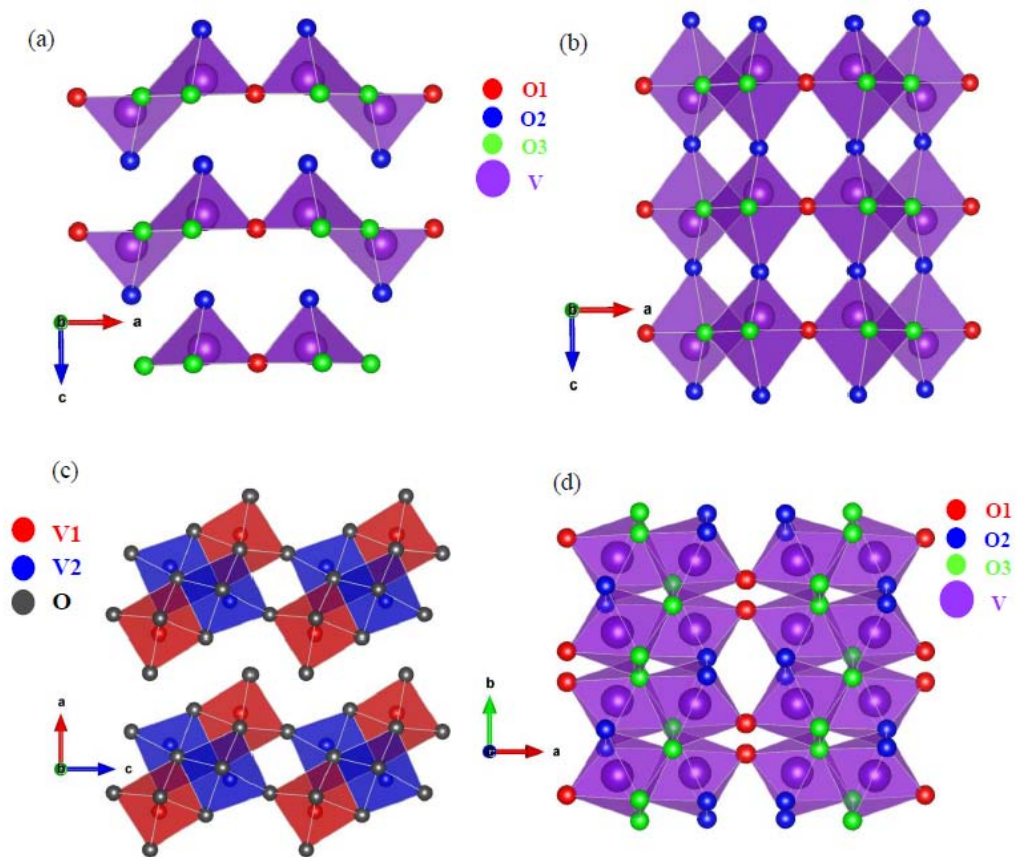


FIG 4.1 (a) structure of α - V_2O_5 , containing square pyramids (b) α - V_2O_5 containing pseudo octahedra (for comparison) (c) β - V_2O_5 containing two different types of VO octahedra (d) δ - V_2O_5 containing VO_6 octahedra.

4.1.2 Motivations and Objectives of Research

Vanadium pentoxide has been studied by a variety of experimental techniques over a range of temperatures. Thermal expansion coefficients of α -V₂O₅ as measured using dilatometer methods[18] in temperature range of 303-723K is found to be $0.63 \times 10^{-6} \text{ K}^{-1}$. On the other hand the value from X-ray powder diffraction[19] in temperature range 303-902K, is found to be $17.2 \pm 1.4 \times 10^{-6} \text{ K}^{-1}$. The thermal expansion behaviour is highly anisotropic with $\alpha_a = (9.5 \pm 0.9) \times 10^{-6} \text{ K}^{-1}$, $\alpha_b = (6.9 \pm 1.3) \times 10^{-6} \text{ K}^{-1}$ and $\alpha_c = (35.2 \pm 1.8) \times 10^{-6} \text{ K}^{-1}$. The large value of α_c may be due to weak van der Waals interaction between the layers along the c-axis [19]. There is a large discrepancy between the dilatometer and X-ray diffraction results of thermal expansion behaviour.

The transmission electron microscopy[20] (TEM) and electron energy loss spectroscopy (EELS)[21] experiments indicate that α -V₂O₅ undergoes decomposition above 673K in high vacuum environment. This decomposition indicates a number of new phases, which may be related to ordered super-lattices of anion (O²⁻) vacancies in vanadium pentoxide with no evidence of crystallographic shear[20]. The EELS measurements carried out up to 873K indicated transformation of V₂O₅ to VO₂ & V₂O₃, which was found to be different from electron beam induced reduction studies. The initial thermal decomposition of V₂O₅ to V₂O₃ is followed by a combination of diffusion, coalescence and stabilization process[21].

Vanadium pentoxide shows a rich phase diagram as a function of pressure. It exhibits variety of phase transitions[22,23] from α -V₂O₅ to β -V₂O₅ and δ -V₂O₅ (Fig 4.1). A metastable phase, γ' -V₂O₅, is also reported by deintercalating Li from γ -LiV₂O₅[24]. Balog et. al. report that β and δ phases could be quenched to ambient pressure and temperature. The zone-centre phonon spectrum of α -V₂O₅ has been studied by

spectroscopic experiments[25-31] and calculations based on density functional perturbation methods[32-35]. The calculated stretching modes frequencies in these studies are found to be either overestimated or underestimated depending upon the type of exchange correlation used. A comparative study[32] among bulk and monolayer structures has been made treating vanadium semi-core states 3s and 3p as bands. The relative intensities showed somewhat larger discrepancies compared to experimental Raman spectra. Moreover, high energy mode frequencies are highly overestimated[32].

In the present research work[36,37], the structure and dynamics of V_2O_5 are investigated through X-ray diffraction, inelastic neutron scattering (INS) and *ab-initio* calculations. The main motive for the high temperature studies is to obtain unambiguous temperature dependence of lattice parameters and to study the high temperature decomposition reported previously in the literature[20,21]. These studies provide the clarity about the reported[18,19] discrepancies in the thermal expansion behaviour of this compound. *ab-initio* DFT studies are done to study role of van der Waals (vdW) dispersion and Hubbard onsite interaction (U) for the d-electron of vanadium in layered structure of V_2O_5 . The neutron INS experiments validate the phonon calculations including vdW+U interactions. The areal negative thermal expansion at low temperatures and negative linear compressibility are discussed in relation to anisotropic Grüneisen parameters and elastic constants. The calculated Gibbs free energy and elastic constants as a function of pressure are used to calculate the pressure-temperature phase diagram and to understand the mechanism of the high-pressure transitions in this compound, respectively. Moreover, dynamics Li-ions among the V_2O_5 layers of these ions at high temperature has been studied[38] by performing *ab-initio* MD simulations. The diffusion pathways of these ions from the MD simulations are predicted to follow the eigenvectors of soft phonon modes obtained in the intercalated structure.

4.2 Experimental and Computational Details

X-ray diffraction studies from 12 to 853 K are carried out. Data were collected in the continuous scan mode at a scan speed of 1 degree per minute and step interval of 0.02 degree in the 2θ range of 10° – 120° . For the high temperature X-ray diffraction experiments, the sample was placed on a flat platinum sample holder and heated in a dynamically evacuated furnace. At each temperature, the crystal structures were analysed using the Rietveld refinement program FULLPROF[39]. In all the refinements, the data over full angular range has been used, although in the figures only a limited range has been shown to highlight the changes.

The inelastic neutron scattering measurements were carried out using time of flight IN4C spectrometer at the Institut Laue Langevin (ILL), France. Thermal neutrons of wavelength 2.4 \AA (14.2 meV) in neutron energy gain mode are used for the measurements. The momentum transfer, Q , extends up to 7 \AA^{-1} . The sample was placed in a cylindrical niobium sample holder and heated in dynamic vacuum in the furnace for temperature dependent measurements. The multi-phonon contribution has been calculated using the Sjolander[40] formalism and subtracted from the experimental data.

The Vienna based VASP software [41,42] is used to carry out the total energy calculation based on plane-wave pseudo potential methods. K-point sampling was performed using $2 \times 8 \times 6$ mesh Monkhorst-pack scheme[43] with a plane wave energy cutoff of 960 eV. The structure is optimized with atomic pseudo potential with s^2p^4 valence electrons and $p^6d^4s^1$ valence electrons in O and V atom respectively. DFT-D2 method of Grimme[44] was used, to account the van der Waals dispersive interaction. The values of C and R parameters are taken to be $C_6=0.70, 10.80 \text{ Joule.nm}^6.\text{mol}^{-1}$ and $R_0=1.342 \text{ \AA}, 1.562 \text{ \AA}$ for O and V atoms respectively. The on-site Coulomb interaction

was accounted within the Dudarev approach[45] using $U_{\text{eff}} = U - J = 4.0$ eV. The phonon frequencies in entire Brillouin zone are calculated using finite displacement method implemented in PHONON5.2[46]. Hellman-Feynman forces are calculated by the finite displacement of 0.03 Å. Free energy calculations are done at various pressures for the completely relaxed structure, which is used to understand the high-pressure phase transition in the compound.

4.3 Results and Discussions

4.3.1. X-Ray Diffraction Study

The powder X-ray diffraction measurements are performed (Fig 4.2) in the temperature range 12-853 K that extends beyond the reported decomposition[20] temperature 673 K. Fig 4.2 shows the evolution of powder diffraction pattern at selected temperatures. For clarity, the diffraction patterns are shown (Fig 4.2) only upto $2\theta=35^\circ$. It is evident from the figure there is not a dramatic change in the powder diffraction pattern with temperature. With increase in temperature from 12 K, the most intense peak in the diffraction pattern around ($2\theta=20.3^\circ$), corresponding to (001) Bragg reflection, shifts toward lower 2θ value. This peak corresponds to the interlayer distance of distorted square pyramids (VO_5) lying perpendicular to the orthorhombic c -axis. The shift is due to the expansion of the lattice along the c -axis (Fig 4.2), with increase of temperature. Moreover, the Bragg peaks (201) and (301) around $2\theta= 25.7$ and 31.1 degree respectively, also shift towards lower 2θ that imply an expansion in the a - c plane but with different rate. The Bragg profile at 31.1 degree corresponds to two peaks, (400) and (301), and show clear splitting above 573 K which is due to prominent increase in c -lattice parameter as compared to that of the a -lattice parameter.

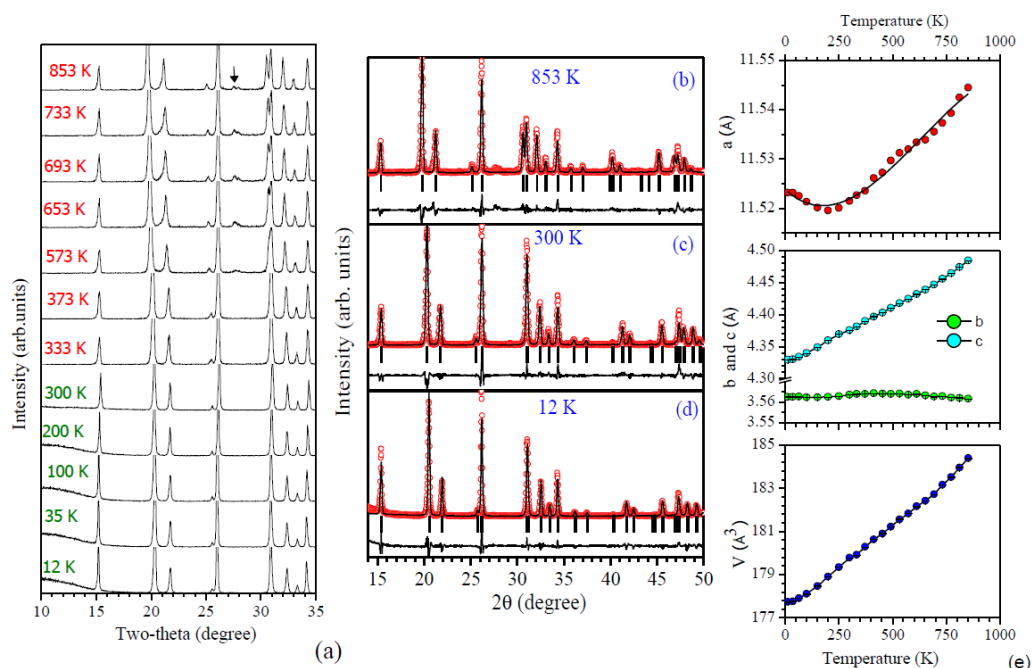


FIG 4.2 (a) Evolution of X-Ray diffraction pattern with temperature. (b-d) Observed (circle) and calculated (line) profiles obtained after the Rietveld refinement of V_2O_5 using orthorhombic structure with space group $Pmmn$ at 853 K, 300 K and 12 K, respectively. (e) Evolution of structural parameters with temperature.

In the diffraction pattern a very low intensity peak appears above 500K at around $2\theta=28^\circ$ marked with arrow (Fig 4.2). The diffraction pattern was compared with the reported[20] decomposed phases of V_2O_5 ; however, this did not signify the decomposition of V_2O_5 . All the peaks present in the diffraction patterns can be indexed with orthorhombic structure with $Pmmn$ space group and shown in Fig 4.2. The fitting of experimental data is shown in Fig 4.2 (b, c, d). The fit between the observed and calculated profiles is satisfactory and consistent with literature[17]. The refined lattice parameters, bond lengths and bond angles are given in Table 4.1. The variation of structural parameters with temperature is shown in Fig 4.2. On heating above 12 K, a -lattice parameter decreases up-to 250 K and then increases above 250 K. The c -parameter

increases in the entire temperature range; however, the b -parameter does not show significant temperature dependence.

TABLE 4.1 Calculated (0K) and experimental (12K) lattice parameters and bond lengths (VO_5 Polyhedra) of α - V_2O_5 . The c -axis is perpendicular to layers of VO_5 square pyramids. V-O2 (pseudo octahedral bond) represents the bond length of V in the one layer and oxygen in the next layer.

	Experimental	DFT (GGA)	DFT (GGA+ U)	DFT (GGA+ vdW)	DFT (GGA+ vdW+U)
a (Å)	11.523(2)	11.572	11.564	11.661	11.649
b (Å)	3.562(6)	3.577	3.638	3.544	3.608
c (Å)	4.330(1)	4.747	4.728	4.424	4.408
V (Å ³)	177.74(8)	196.50	198.88	182.83	185.25
E/atom (eV)		-8.41	-7.26	-8.53	-7.38
V-O1	1.791(8)	1.793	1.809	1.786	1.802
V-O2	1.554(8)	1.599	1.609	1.602	1.614
V-O3	1.877(0)	1.892	1.916	1.880	1.904
	2.027(6)	2.046	2.030	2.063	2.044
	1.877(0)	1.892	1.916	1.880	1.904
V-O2	2.775(1)	3.149	3.119	2.822	2.795
\angle V-O1-V	146.838(9)	146.5	146.2	149.5	149.4
\angle O1-V-O2	105.574(1)	105.1	105.0	104.6	104.5
\angle O2-V-O3	104.721(5)	105.1	104.7	105.2	104.7
	104.799(2)	107.9	107.9	105.9	105.9
	104.721(5)	105.1	104.7	105.2	104.7
\angle O1-V-O3	96.383(9)	97.0	96.5	97.7	97.1
	149.626(7)	147.1	147.0	149.5	149.6
	96.383(9)	97.0	96.5	97.7	97.1
\angle O3-V-O3	75.818(9)	74.5	75.2	74.3	75.2
	143.270(1)	141.9	143.3	141.1	142.8

It is evident from this study that the thermal expansion behaviour is highly anisotropic with $\alpha_a = (-1.9 \pm 0.1) \times 10^{-6} \text{K}^{-1}$ for temperature range 12-250 K and $\alpha_a = (3.3 \pm 0.1) \times 10^{-6} \text{K}^{-1}$ for above 250 K. Thermal expansion coefficient along b and c are $\alpha_b = (1.9 \pm$

$0.2) \times 10^{-6} \text{K}^{-1}$ for temperature below 413K and $\alpha_b = (-1.7 \pm 0.2) \times 10^{-6} \text{K}^{-1}$ above 413K and $\alpha_c = (42.2 \pm 0.5) \times 10^{-6} \text{K}^{-1}$, respectively. The large value of α_c may be due to weak van der Waals interaction between the layers along the c-axis. As a result, the VO_5 polyhedral layers move further apart from each other with increase of temperature. On the average, a 3.7 % change in volume is observed on increase of temperature from 12K up to 853 K. No signature of decomposition of V_2O_5 at around 673 K is observed contrary to previously reported [20] decomposition using transmission electron microscopy.

4.3.2. Role of van der Waals and Hubbard Interaction

$\alpha\text{-V}_2\text{O}_5$ is a layered compound and layered structures are generally bonded by weak van der Waals (vdW) interactions[47,48]. Moreover, V atom has strongly correlated d-electrons in its valence shell that contribute in bonding[49], which implies that the Hubbard onsite interaction (U) can play an important role in this compound. Earlier density functional theory calculations without the above interactions were performed for partially relaxed (at fixed volume) structure of V_2O_5 keeping lattice parameters fixed to experimental values[32-34,50-52]. Other first principles calculations on V_2O_5 highly overestimated the c-lattice parameters, and hence produced large discrepancies in physical properties[23,32-34,51,53-58]. Recent studies [38,59-65] considered the van der Waals interaction that shows a good agreement of the c lattice parameter with experiments. However, detailed investigation about the role of the van der Waals interaction on bonding, phonon spectra and other thermo-dynamical properties of V_2O_5 is not available. Since all the phases of V_2O_5 possess layered structures[23,51,66], it is expected that the van der Waals dispersion interactions would also play an important role in structural stability of high pressures phases of V_2O_5 . Being an important material for a wide range

of applications, it is important to study various thermodynamical properties of V_2O_5 over a range of pressures and temperatures.

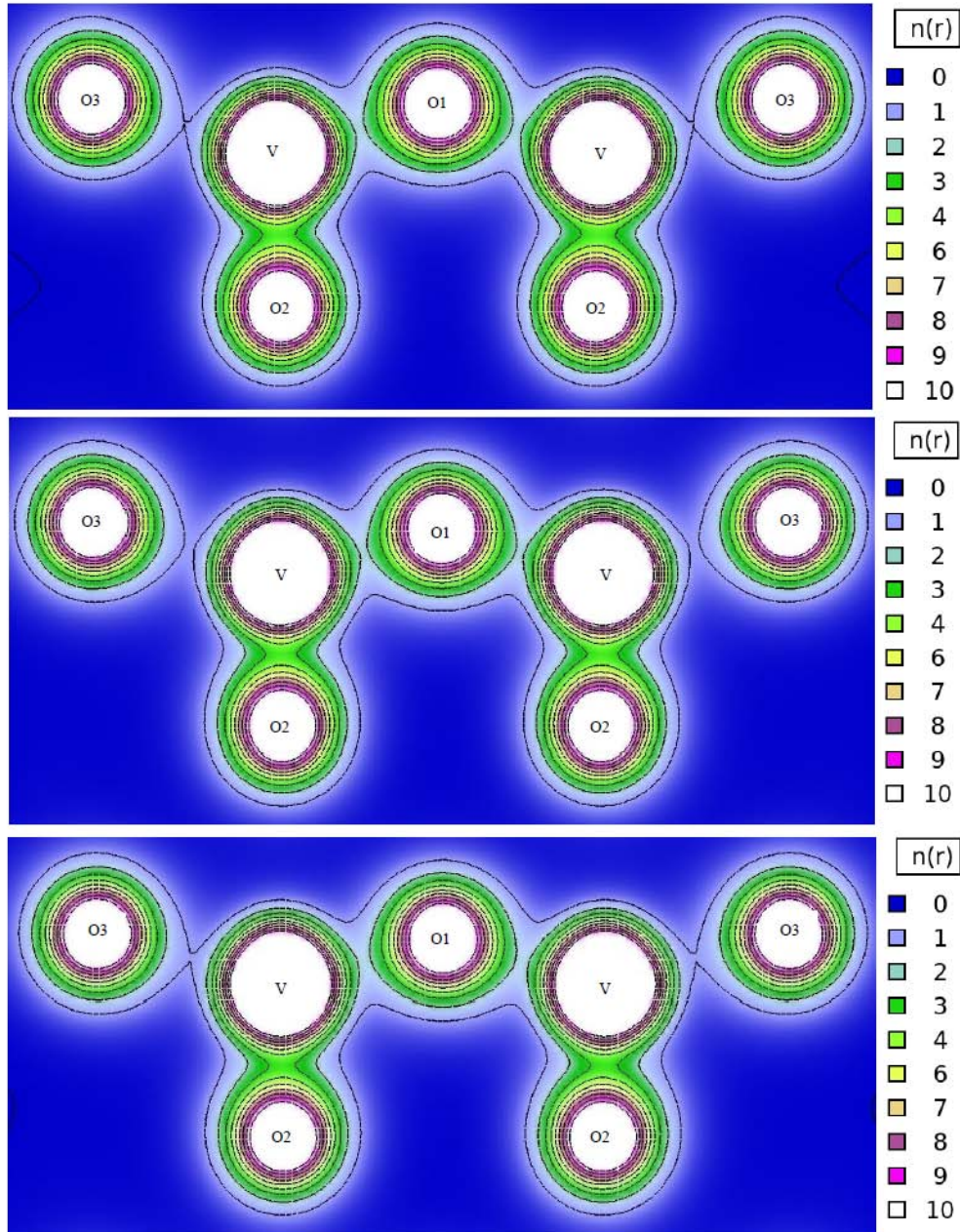


FIG 4.3 The atomic charge density plot of α - V_2O_5 , in the a - c plane, for calculations performed considering (Top) GGA, (Middle) GGA+vdW, and (Bottom) GGA+vdW+U. The charge density scale is displayed on the right. The atomic positions in the space group $Pmmn$ are O1 at $2a(x,y,z)$, O2 at $4f(x,y,z)$, O3 at $4f(x,y,z)$, and V at $4f(x,y,z)$ Wyckoff site.

In order to bring out the importance of the van der Waals(vdW) and the onsite Hubbard(U) interactions, various optimized structures of α -V₂O₅ with only GGA, GGA+U, GGA+vdW and GGA+vdW+U respectively are compared with the experimental values obtained from the X-ray diffraction experiments (Table 4.1). The structural data as obtained from GGA approximation gives highly overestimated ($\approx 10\%$) volume in comparison to the experimental value. The large deviation from the experimental lattice parameters, in particular the *c* parameter, is found when the van der Waals dispersion interactions are not considered. A parameter-based van der Waals approach implemented along with the GGA exchange correlation excellently reproduces the experimental lattice parameters (Table 4.1). Moreover, the calculated V-O bond lengths and bond angles by this approach agree very well with the experimental values.

The charge density in the *a-c* plane as obtained from GGA calculations is plotted in Fig 4.3. It can be seen that V-O2 bond is a very strong bond (along *c*-axis) with large electron density in between the bonded atoms. The calculated charge density (Fig 4.3 (a)) implies that V-O1 is stronger than V-O3 bond and is consistent with the experimental bond lengths (Table 4.1). The inclusion of the van der Waals interaction (Fig 4.3(b)) brings VO₅ layers closer along 'c' axis and also modifies (Table 4.1) the bond lengths and bond angles (\angle V-O1-V & \angle O1-V-O3).

The effect of vdW interaction is found to strengthen the V-O1 bond; however, it slightly weakens the V-O3 bond (Table 4.1). The decrease in V-O1 bond length may be due to the reason that the O1 atoms is shared between two long chains of VO₅ polyhedral and as a result of vdW interaction these chains come close in the similar way as that of VO₅ layers along *c*-axis. The weakest V-O3 bond expands significantly along *a*-axis. O₁ atom is covalently bonded to two V atoms along *a*-axis and does not allow expansion of the V-O1 bond. Moreover, O2 of next layer push the O1 atom of present layer in the *a-b*

plane, increasing electron density in V-O1 bond region; strengthen the bond (Fig 4.3 (b)). Due to the expansion of V-O3 bond lengths, *a*-lattice parameter increases slightly on inclusion of van der Waals interactions.

TABLE 4.2 Calculated Born effective charges for atoms present at various Wyckoff sites in α -V₂O₅. $Z_{I,xx}$, $Z_{I,yy}$ and $Z_{I,zz}$ are the diagonal components of Born charge tensor.

Atom	Calculation	$Z_{I,xx}$	$Z_{I,yy}$	$Z_{I,zz}$
V	GGA	7.34	5.76	2.40
	GGA+U	6.69	5.24	2.51
	GGA+vdW	6.55	6.07	2.46
	GGA+vdW+U	6.42	5.78	2.92
O1	GGA	-6.21	-0.87	-0.70
	GGA+U	-6.58	-0.74	-0.78
	GGA+vdW	-7.27	-0.85	-0.78
	GGA+vdW+U	-7.45	-0.80	-0.86
O2	GGA	-0.67	-0.56	-1.42
	GGA+U	-0.55	-0.56	-1.52
	GGA+vdW	-0.55	-0.61	-1.64
	GGA+vdW+U	-0.55	-0.59	-1.92
O3	GGA	-2.89	-4.78	-0.53
	GGA+U	-2.57	-4.32	-0.56
	GGA+vdW	-2.45	-5.04	-0.44
	GGA+vdW+U	-2.27	-4.79	-0.54

Further, the inclusion of the Hubbard onsite interaction (Table 4.1 & Fig 4.3(c)) for V atom results in localization of valence d-electrons. This will modify the angular alignment of valence d-orbital of V atom. This strengthens the V-O₃ bond but weakens the V-O₁ bond. Charge density between the atoms (Fig 4.3(c)) and bond lengths (Table 4.1) clearly show this feature which is consistent with the calculated Born effective charges (Table 4.2). Thus, van der Waals interaction along with Hubbard interactions plays a very important role in optimization of layered structure of α -V₂O₅ in line with earlier studies[33,51,57]. This optimized structure is further used for the calculation of other thermo-dynamical properties of α -V₂O₅.

4.3.3 Phonon Spectra of α -V₂O₅

The temperature dependent INS measurements (Fig 4.4) of α -V₂O₅ are carried out in neutron energy gain mode. So, at 313 K, the low population of high energy phonons restricted one to obtain the phonon spectra only up to 110 meV. As the temperature increases, the high energy phonons get populated and statistics of spectra at high energy improves. There is no significant change in the spectra at higher temperature, which is also corroborated from result of the X-ray studies, that there is no phase transition or decomposition in the temperature range of the study. The measured spectra are further used to validate the *ab-initio* DFT calculations. The *ab-initio* calculation calculated phonon spectra (Fig 4.4) under GGA+vdW+U are found to be in excellent agreement with the measurement. There band gap in the phonon spectra from 110-120meV (Fig 4.4), was also observed in previous IR and Raman measurements[27-29].

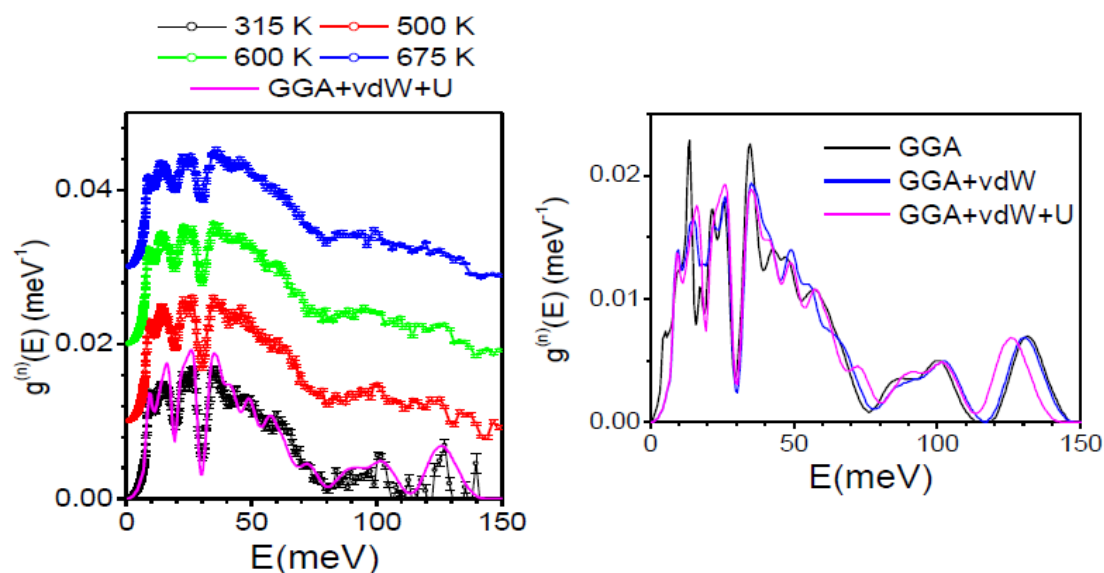


FIG 4.4 (a) Experimental and calculated (GGA+vdW+U) neutron-weighted phonon density of states in α -V₂O₅. (b) Phonon density of states calculated using various types of interactions in α -V₂O₅.

The calculated partial phonon densities of states of various atoms (Fig 4.5) are useful for understanding the dynamical contribution of various atoms to the total calculated phonon density of states. There are three types of O atoms: Vanadyl (O2) is bonded to a single vanadium and forms the apex of the pyramids; chain O3 binds to three vanadium (two along the chain direction and one in the adjacent chain), and bridge O1 is bonded to two vanadium atoms and couples the chains together. It can be seen that V-O1 and V-O3 polyhedral stretching modes are lower in energy than the V-O2 stretching mode. This behaviour confirms the relatively weaker bonding of O1 and O3 with V in comparison to that of O2, which is also obvious from the bond length data (Table 4.1). Various O (O1, O2 and O3) atoms are found to contribute (Fig 4.5) in different energy ranges in the spectrum, which may be related to difference in V-O bond lengths.

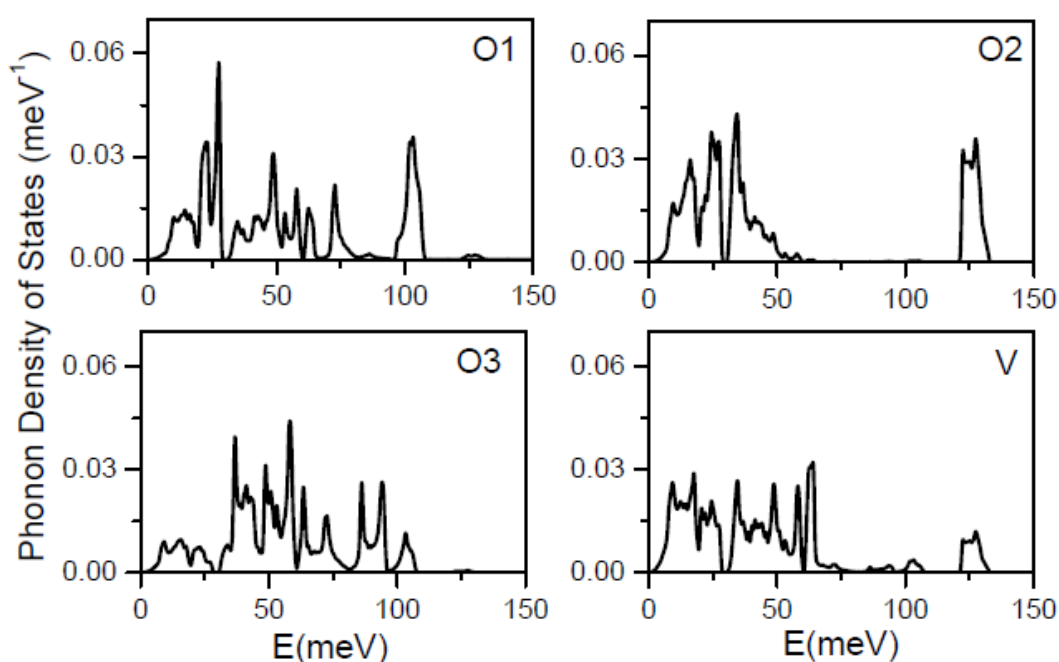


FIG 4.5 Calculated (*GGA+vdW+U*) partial phonon density of states of atoms at various Wyckoff sites in α - V_2O_5 . The atomic positions in the space group *Pmmn* are O1 at $2a(x,y,z)$, O2 at $4f(x,y,z)$, O3 at $4f(x,y,z)$, and V at $4f(x,y,z)$ Wyckoff site.

TABLE 4.3 Calculated and experimental frequencies of zone centre phonon modes in α -phase of V_2O_5 . The calculations in the present study are performed using the optimized minimum energy structures while the previous calculations[32-34] were performed at experimental fixed volumes.

	Expt. (Raman & IR)	GGA	GGA +U	GGA+ vdW	GGA+ vdW+U	LDA- FHI [33]	GGA [34]	LDA- HGH [32]
Au	76	66	70	66	70		127	
B3u(I)	72	57	57	71	73	74	102	72
Ag(R)	107	85	88	98	103	108	137	104
B2g(R)	147	125	130	134	140	146	143	145
B1u(I)	140	118	118	139	141	142	248	136
B1g(R)	147	139	152	150	162	167	169	147
B3g(R)	149	139	152	151	162	169	174	148
Ag(R)	200	172	179	189	197	193	291	185
B2g(R)	201	181	187	194	201	200	259	192
B2u(I)	213	208	210	210	210	205	254	217
B3g(R)	232	231	231	227	226	219	273	230
B3u(I)	259	244	242	258	256	255	327	267
Au	263	257	251	266	260		297	
B2u(I)	285	274	277	281	281	271	304	285
B1g(R)	290	273	273	282	281	277	305	285
B3g(R)	291	274	280	285	289	279	311	284
B1u(I)	290	275	276	286	289	295	329	291
B2g(R)	315	283	275	300	294	299	385	309
Ag(R)	310	286	279	301	295	294	383	303
B3u(I)	302	346	358	329	345	362	347	339
B1u(I)	354	349	342	347	340	338	439	358
B2g(R)	350	343	344	347	351	361	388	352
Ag(R)	404	387	381	389	385	382	454	396
B3u(I)	411	412	358	418	420	478	463	414
Ag(R)	483	466	381	452	468	528	484	467
B1u(I)	472	472	468	467	461	477	481	464
B2g(R)	507	480	494	478	487	529	500	482
Au	533	473	493	492	510		468	
B2u(I)	506	473	493	493	511	602	474	495
Ag(R)	528	514	515	520	518	542	539	518
B1u(I)	570	514	519	525	534	665	623	617
B3g(R)	702	676	687	685	696	772	676	693
B1g(R)	702	676	686	685	695	772	676	693
B3u(I)	766	758	758	778	779	849	768	758
B2g(R)	963	840	831	861	856	1010	936	929
B1u(I)	974	1046	1006	1029	985	1014	1007	1014

B3u(I)	981	1043	1002	1030	986	1011	1006	1011
B2g(R)	992	1060	1023	1044	1004	1030	1024	1029
Ag(R)	992	1066	1030	1050	1010	1029	1026	1031

The calculated frequencies of zone center phonon modes are compared with earlier spectroscopic[27-29] and DFPT [32-34] results (Table 4.3). The energy of modes as obtained from the previous calculations in the literature is highly overestimated in comparison to the experimental values, especially high energy modes around 1000 cm^{-1} . The phonon spectra are calculated in all the schemes discussed above namely GGA, GGA+U, GGA+vdW and GGA+vdW+U. It can be seen that the presence of van der Waals dispersion interactions along with the Hubbard onsite potential significantly improved (Table 4.5) the results. Especially the agreement between the experimental and calculations is much improved for the phonon modes below 350 cm^{-1} and above 900 cm^{-1} .

4.3.4 Elastic and Thermal Expansion Behavior of $\alpha\text{-V}_2\text{O}_5$

The elastic constants are calculated using the symmetry-general least square method[67] as implemented in VASP. The nine independent components of elastic constant (in GPa) for the orthorhombic[68] $\alpha\text{-V}_2\text{O}_5$ are calculated as:

$$\begin{pmatrix} 183.2 & 116.4 & 37.0 & 0 & 0 & 0 \\ 116.4 & 234.6 & 26.7 & 0 & 0 & 0 \\ 37.0 & 26.7 & 34.6 & 0 & 0 & 0 \\ 0 & 0 & 0 & 22.5 & 0 & 0 \\ 0 & 0 & 0 & 0 & 29.7 & 0 \\ 0 & 0 & 0 & 0 & 0 & 42.9 \end{pmatrix}$$

The very high values of C_{11} and C_{22} relative to C_{33} imply that the structure is less compressible along a - and b -crystallographic axes. C_{33} component is very small that

results in high compressibility of the structure along c-axis, which is due to the layered nature of the structure along c-axis.

The quasi-harmonic approximation is used to calculate the linear thermal expansion coefficients. The anisotropic Grüneisen parameters are calculated by applying an anisotropic stress of 0.5 GPa along one of the lattice parameters while keeping other lattice parameters constant, and vice versa. The calculated mode Grüneisen parameters averaged over phonon of a particular energy E as a function of phonon energy along different directions are shown in Fig 4.6 (a). The Grüneisen parameters along a and b axes show significant negative values for the low-energy phonon modes upto 30 meV and may give rise to negative thermal expansion along a and b axes.

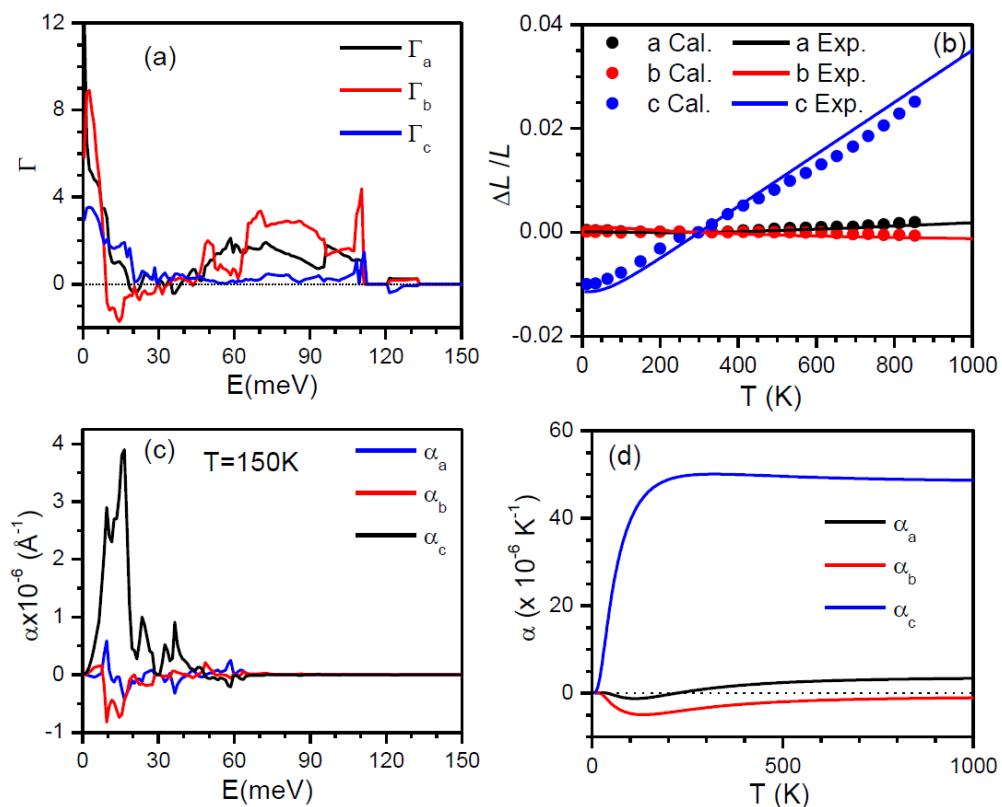


FIG 4.6 (a) The calculated anisotropic Grüneisen parameters. (b) The experimental and calculated lattice parameters as a function of temperature. (c) & (d) calculated linear thermal expansion coefficient as a function of phonon mode energy and temperature.

The elements of elastic compliances matrix $S=C^{-1}$ as given below:

$$\begin{pmatrix} 0.0093 & -0.0038 & -0.0070 & 0 & 0 & 0 \\ -0.0038 & 0.0062 & -0.0007 & 0 & 0 & 0 \\ -0.0070 & -0.0007 & 0.0369 & 0 & 0 & 0 \\ 0 & 0 & 0 & 0.0444 & 0 & 0 \\ 0 & 0 & 0 & 0 & 0.0337 & 0 \\ 0 & 0 & 0 & 0 & 0 & 0.0233 \end{pmatrix}$$

The anisotropy in the thermal expansion behaviour of this compound may arise from the anisotropy in Grüneisen parameters and elastic constants. At temperature below Debye temperature, the specific heat (C_V) shows a large variation with temperature, whereas the elastic compliance/constants and Grüneisen parameters don't show significant temperature dependence. The anisotropic Grüneisen parameters of various modes and the elastic constants are calculated at 0 K. The temperature dependence in the thermal expansion enters due to the specific heat, or, actually through the population of phonons. As the temperature increases, phonon modes of higher energy get populated, and so these higher energy modes begin to contribute to the anisotropic thermal expansion. Thus, the anisotropy of the net thermal expansion, which is the sum total due to all the highly populated modes, changes with temperature.

The calculated linear thermal expansion coefficients and the lattice parameters as a function of temperature are shown in Fig 4.6(b) and 4.6(c) respectively. The calculated temperature dependence of the lattice parameters is in good agreement (Fig 4.6(b)) with the experimental data. However, above 500 K, the calculated parameters deviate slightly from the experiments. This might be due to the fact that at high temperature the explicit anharmonicity of phonons plays an important role. This effect has not been considered in the thermal expansion calculation, which includes only the volume dependence of phonon energies (implicit contribution). The thermal expansion behaviour from eq. (1.30) can be expressed as

$$\alpha_a(T) \propto \sum_{q,i} C_V(q, i, T) [0.0093\Gamma_a - 0.0038\Gamma_b - 0.0070\Gamma_c] \quad (4.1)$$

$$\alpha_b(T) \propto \sum_{q,i} C_V(q, i, T) [-0.0038\Gamma_a + 0.0062\Gamma_b - 0.0007\Gamma_c] \quad (4.2)$$

$$\alpha_c(T) \propto \sum_{q,i} C_V(q, i, T) [0.0070\Gamma_a - 0.0007\Gamma_b + 0.0369\Gamma_c] \quad (4.3)$$

As seen from above relations, the negative Γ_a and positive Γ_b & Γ_c will enhance the NTE along a -axis. The b -axis shows a very small negative thermal expansion in the entire temperature range upto 1000 K. The NTE behaviour along b -axis is governed by the negative value of s_{21} and Γ_b . The c -axis shows a large positive value of thermal expansion in entire temperature range. As seen from above relation this behaviour is related to large value of Γ_c .

TABLE 4.4 Calculated and experimental thermal expansion coefficients of α - V_2O_5 .

Thermal Expansion Coefficient ($\times 10^{-6}$) K^{-1}	Dilatometer Measurements [18] (303-723K)	X-Ray Diffraction [19] (303-902K)	X-Ray Diffraction (This Study) 12-853K	<i>Ab-initio</i> Lattice Dynamical Calculations
α_a	9.5 \pm 0.9	-1.9 \pm 0.1 (12-250K) 3.3 \pm 0.1 (above 250K)	-1.3(110 K) 2.9(above 250K)
α_b	6.9 \pm 1.3	1.9 \pm 0.2(upto413K) -1.7 \pm 0.2 (above 413K)	-2.3
α_c	35.2 \pm 1.8	42.2 \pm 0.5	46.2
α_V	0.63	51.6 \pm 1.4	44.5 \pm 0.5	47.1

The calculated coefficients of thermal expansion are compared with the X- ray diffraction and previous literature (Table 4.4). There is a very good agreement of the calculated and measured anisotropic thermal expansion coefficient. The previous dilatometer measurements have largely underestimated the thermal expansion while the previous X-ray results did not show the negative thermal expansion behaviour. The

compound shows overall positive volume thermal expansion behaviour. The anisotropic thermal expansion behaviour is governed by the high anisotropy in Grüneisen parameters and elastic constants. The thermal expansion coefficient along a -axis ($\alpha_a(T)$) has a negative value upto 300 K (Fig 4.6 (d)) which becomes positive at higher temperatures.

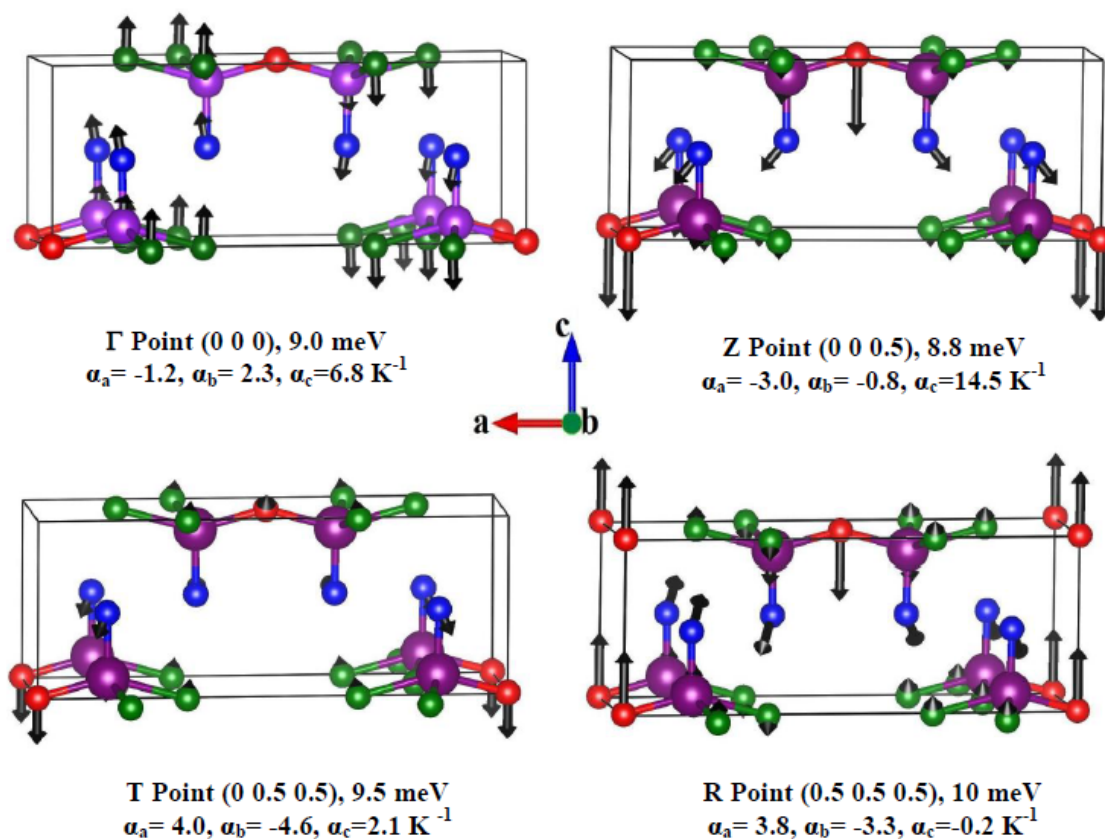


FIG 4.7 The displacement pattern and energies (in meV) of phonon modes responsible for negative thermal expansion in the a - b plane. The values of the frequencies correspond to the GGA+vdW+ U calculations. Key: V(violet), O1(red), O2(blue) and O3(green).

The low energy modes below 30 meV in this compound produce anisotropic thermal expansion behavior with NTE along the a - and b -axis at low temperatures and expansion along the c -axis in the entire temperature range. The displacement pattern of some of the selected low energy phonon modes, at various high symmetry points in the

Brillouin zone, highly contributing to negative thermal expansion in the a - b plane is shown in Fig 4.7. However it can be best visualized by animation[37]of the displacement pattern. The contribution to the thermal expansion coefficient, due to the Γ -point mode at around 9 meV (assuming it as an Einstein mode with one degree of freedom), along various axes is: $\alpha_a = -1.2 \times 10^{-6} \text{ K}^{-1}$, $\alpha_b = 2.3 \times 10^{-6} \text{ K}^{-1}$, $\alpha_c = 6.8 \times 10^{-6} \text{ K}^{-1}$. The mode produces contraction along a -axis. Basically, the mode involves in-phase bending of VO_5 polyhedral chains about O1 atoms in the a - c plane. All the atoms in the chain show in-phase motion. The Z-point (0 0 0.5) mode at 8.8meV ($\alpha_a = -3.0 \times 10^{-6} \text{ K}^{-1}$, $\alpha_b = -0.8 \times 10^{-6} \text{ K}^{-1}$, $\alpha_c = 14.5 \times 10^{-6} \text{ K}^{-1}$) involves out-of-phase bending of VO_5 polyhedral units in two consecutive layers. All the atoms in a chain show out-of-phase motion along c -axis. Another T-point (0 0.5 0.5) mode of 9.5meV ($\alpha_a = 4.0 \times 10^{-6} \text{ K}^{-1}$, $\alpha_b = -4.6 \times 10^{-6} \text{ K}^{-1}$, $\alpha_c = 2.1 \times 10^{-6} \text{ K}^{-1}$) is important for understanding NTE along the b -axis. The mode involves rotation and translation vibration of V_2O_5 units and creates buckling in the a - b plane. The successive layers show out-of-phase buckling. The phonon mode at high symmetry R-point (0.5 0.5 0.5) of 10 meV ($\alpha_a = 3.8 \times 10^{-6} \text{ K}^{-1}$, $\alpha_b = -3.3 \times 10^{-6} \text{ K}^{-1}$, $\alpha_c = -0.2 \times 10^{-6} \text{ K}^{-1}$) involves out-of-phase bending of successive layers containing VO_5 polyhedral units in a - b plane. Overall the buckling of V_2O_5 layers in a - b plane give rise to the contraction in the a - b plane and this contraction is also enhanced by the expansion along the c -axis.

4.3.5. High Pressure Study of V_2O_5

Orthorhombic, α - V_2O_5 is studied under high pressure by various experimental techniques like XRD[22,23,66,69,70], neutron powder diffraction[71], high-resolution transmission electron microscopy[71]spectroscopic[70,72] and theoretical *ab-initio* DFT[23,51,73] etc. Raman spectra and density functional calculations[51] provide the

identification of spectral finger prints specific to structural basic units of α - V_2O_5 and β - V_2O_5 . β - V_2O_5 phase is obtained from α - V_2O_5 by the application of isotropic pressure between 4 to 10 GPa at temperature between room temperature to 1023 K [64,70,72,74,75]. The structure [22,23,51,69,71,76,77] of β - V_2O_5 is monoclinic with space group $P2_1/m$. In another study [72], α - V_2O_5 to β - V_2O_5 phase transition is found to be an irreversible transition occurring above 7 GPa at ambient temperature and involves change in vanadium coordination number from 5 to 6. The microscopic mechanism of phase transition from α to β phase studied using density functional theory approach [73] indicated that the U_5 shear strain of the α phase causes this transition to happen via a gliding displacement of V_2O_5 layers. Further increase in pressure, beyond 7 GPa at ambient temperature, results in a recently discovered monoclinic δ - V_2O_5 phase. This phase was first obtained by Filonenko et al [76] between 8– 8.5 GPa and 873-1373 K which they have labelled B- V_2O_5 , later identified as δ - V_2O_5 . However, pure δ - V_2O_5 was not obtained even up to 10 GPa [77]. This phase transforms reversibly to α - V_2O_5 [76]. The phase was characterized at 10.1 GPa and 673 K using in-situ X-ray measurement. Another X-ray diffraction and Raman spectroscopy studies [22] up to 29 GPa and temperatures up to 1773 K on V_2O_5 is performed, which indicates that the structure of δ - V_2O_5 is monoclinic with space group $C2/c$. The δ -phase seems to be stable [22] from 10 up to 29 GPa, at temperatures higher than 473 K. Recently δ - V_2O_5 is obtained at $P = 8.0$ - 8.5 GPa, and $T = 973$ – 1373 K and structure is found to be independent of the synthesis method [69]. There is a large discrepancy in the reported pressures and temperatures of phase transitions in V_2O_5 .

Here, the study of the high-pressure behaviour of V_2O_5 from the *ab-initio* DFT calculations is reported. The calculated pressure dependent lattice parameters for α - V_2O_5 along with experimental values are compared in Fig 4.8. It can be seen that α - V_2O_5 shows

an anisotropic compressibility along different crystallographic axes. The a -lattice parameter is found to expand while c contracts. This gives an effective negative linear compressibility (NLC) along a -axis and positive linear compressibility along c -axis, while b -axis is almost invariable in the range of applied pressure up to 6 GPa. The positive compressibility along c axis is related to decreasing interlayer distance (V-O2 interlayer in Fig 4.8) along c -axis.

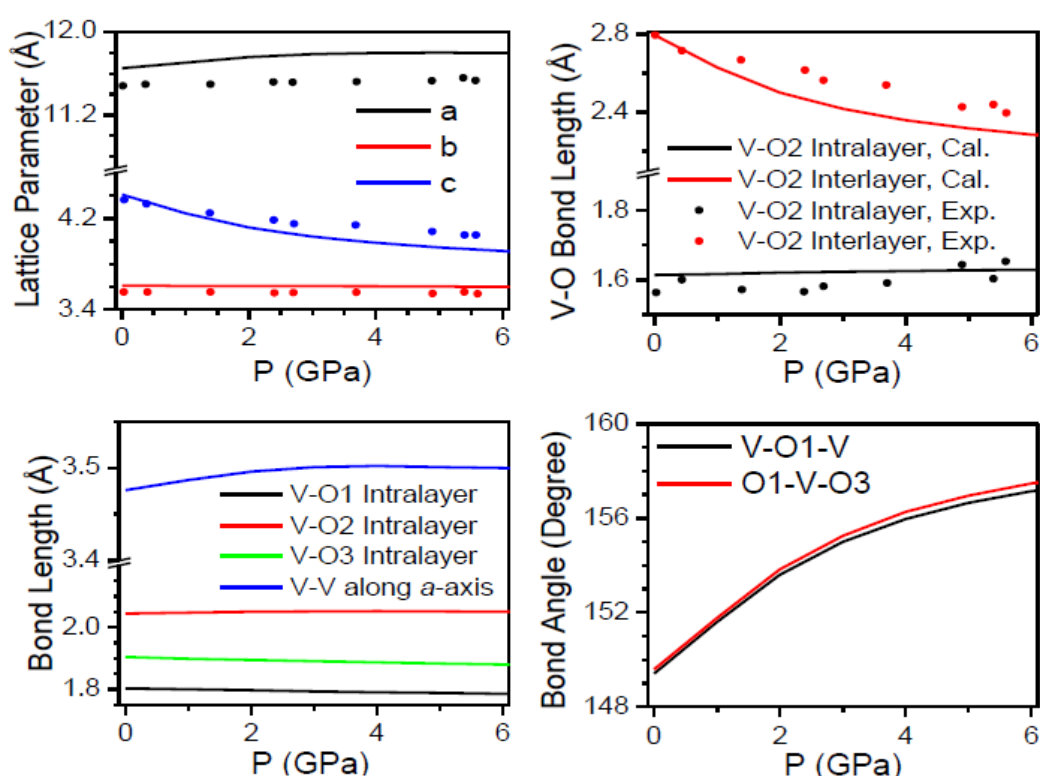


FIG 4.8 Calculated and experimental[70] pressure dependence of lattice parameters, bond lengths and bond angles of orthorhombic α - V_2O_5 . The calculations are shown in the pressure range of stability as observed experimentally[22,70].

On the other hand, an increase in V-O2 intralayer bond (V-O2 bond in VO_5 polyhedral unit lies along c -axis) length signifies that V is pushed more towards the plane of VO_5 square pyramid. This gives rise to an expansion of square pyramid in a - b plane

which can be seen from increasing V-V bond lengths (Fig 4.8) along a -axis. The effect of expanding square plane of VO_5 square pyramids is more pronounced along a axis in comparison to that along b -axis. The increase in V-V bond length along a -axis is governed by opening of the $\angle\text{V-O1-V}$ and $\angle\text{O1-V-O3}$ bond angles (Fig 4.8) with increase of pressure. This gives rise to a negative linear compressibility along a -axis of α - V_2O_5 . The diminishing difference between the b and c -lattice implies a continuous change of the V coordination from square pyramidal towards octahedral. The V-O2 interlayer bond length in the α -phase, which is 2.8 Å at $P=0$, gradually reduces to 2.3 Å up to 6 GPa approaching the value in the β -phase.

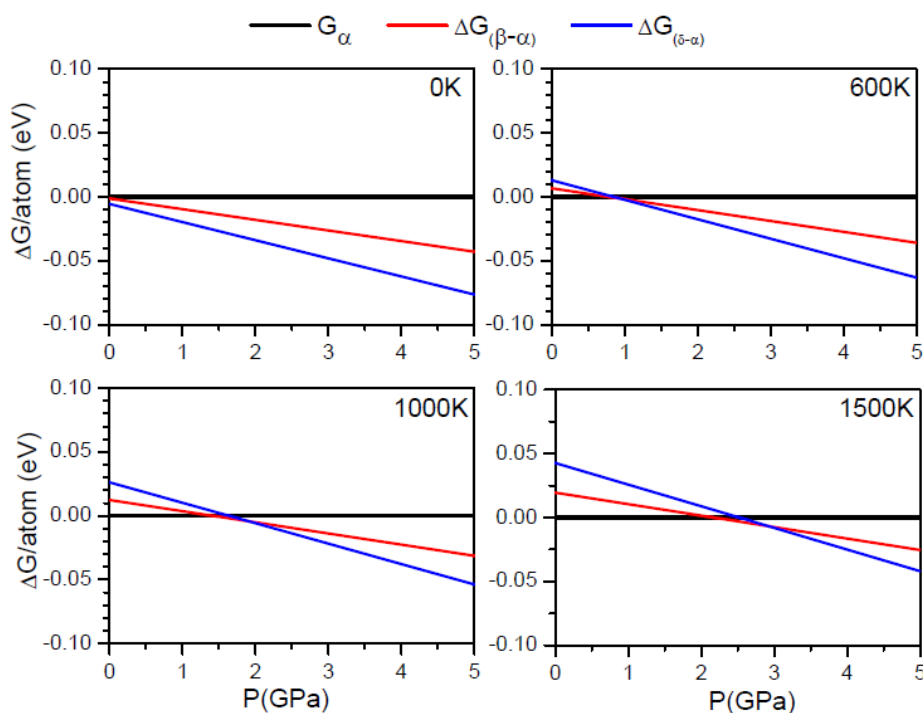


FIG 4.9 Calculated Gibbs free energy per atom in various phases of V_2O_5 as a function of pressure at various temperatures.

The investigation of likely phase transitions is studied by the minimization of Gibbs free energy, which is the basic requirement for the stability of one phase compared

to the other phases. The phonon spectra are first calculated as a function of pressure for the various phases using the GGA+vdW+U optimized structures. The Gibbs free energy has been calculated (Fig 4.9) for the three phases (α - V_2O_5 , β - V_2O_5 & δ - V_2O_5) as a function of pressure and temperature. Pressure is applied isotropically with a large enough cutoff to minimize the pulay stress. The dynamical stability of all the phases is observed at all the pressures upto 5 GPa when all the phonon frequencies are real.

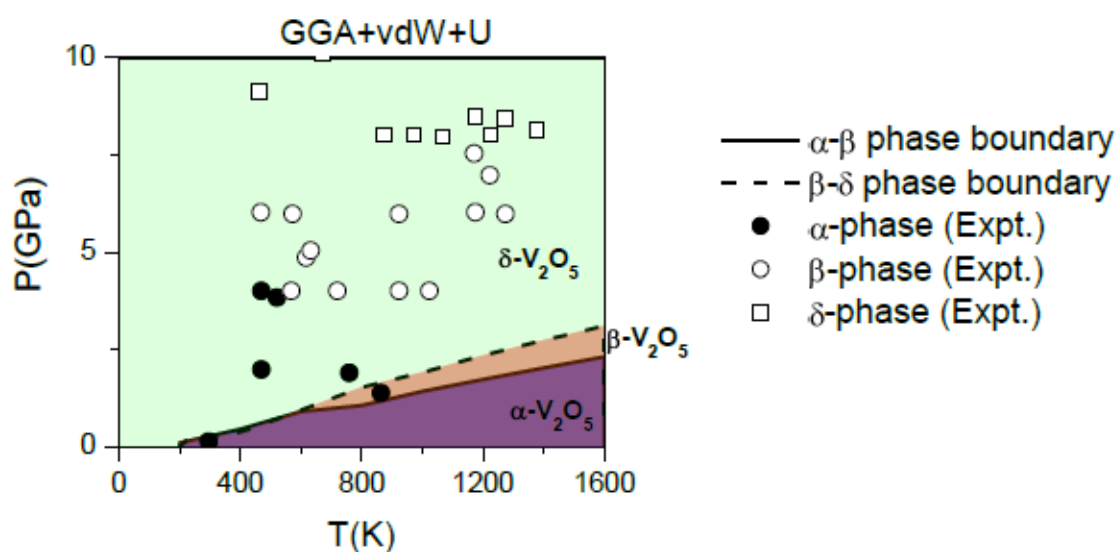


FIG 4.10 Calculated and experimental[22] pressure/temperature phase diagram of V_2O_5 . The experimental data points and calculated colour region are shown.

The free energy crossover (Fig 4.9) between α to β phases is obtained at around 1.5GPa at 1000K. The critical pressure for α - β transition is somewhat underestimated from the experimental value[23] of 4.0 GPa. The α to β phase transformation is of first order and involves volume drop of about $\sim 11\%$. The structure of the β phase is monoclinic containing VO_6 octahedral units. The VO_6 octahedra are found to be highly distorted. Further comparison of the free energy of β and δ phase (Fig 4.9) indicates that δ phase is stable above 3GPa and 1500 K. The β to δ transition is experimentally observed

at 10.1 GPa and 673 K[23]. The β to δ phase transition is a monoclinic to monoclinic transition which occurs by doubling the number of atoms per unit cell. The δ - V_2O_5 is about ~10 % denser in comparison to β -phase. δ - V_2O_5 is also made of VO_6 distorted octahedral. The calculated and experimental[22] phase diagram of V_2O_5 as a function of temperature and pressure is given in Fig 4.10. The DFT calculations reproduce the experimental phase diagram qualitatively. The phase boundaries in present calculations are somewhat underestimated in comparison to the experimental values[22] possibly due to the fact that the first-order transformations involve energy barriers and hysteresis phenomena. The α - β and β - δ phase transitions involve volume collapses. This results in a delay in emergence of the new phases due to the kinetic effects. Therefore, the transition pressure values predicted by the calculations are expected to be lower than those obtained in the experiments.

TABLE 4.5 *Experimental and calculated octahedral distortions in terms of bond length. For comparison, α - V_2O_5 is also considered to be made up of VO_6 octahedra instead of VO_5 square pyramids. The experimental parameters[22] are obtained at room temperature and ambient pressure while calculations are at 0K and 0 GPa.*

Phase	Experimental[22]			Calculated		
	Max. V-O	Min. V-O	Max-Min	Max. V-O	Min. V-O	Max-Min
α - V_2O_5	2.791	1.577	1.214	2.795	1.614	1.181
β - V_2O_5	2.325	1.634	0.691	2.364	1.592	0.772
δ - V_2O_5	2.145	1.628	0.517	2.189	1.657	0.532

As one goes from ' α ' to ' δ ' phase, V-O bond length among the layers start decreasing which decreases the distortion of VO_6 octahedral units. This can be seen from

the difference of $(V-O)_{max} - (V-O)_{min}$ (Table 4.5) for a VO_6 octahedral unit. In case of α - V_2O_5 , V is five coordinated with oxygen atoms. For the sake of comparison α - V_2O_5 is also considered to be made up of VO_6 pseudo octahedra instead of VO_5 square pyramids. The phase transition basically takes place by decrease in volume under pressure. The volume per atom as a function of pressure (Fig 4.11) shows that α - V_2O_5 would transform to β - V_2O_5 and then to δ - V_2O_5 at higher pressures.

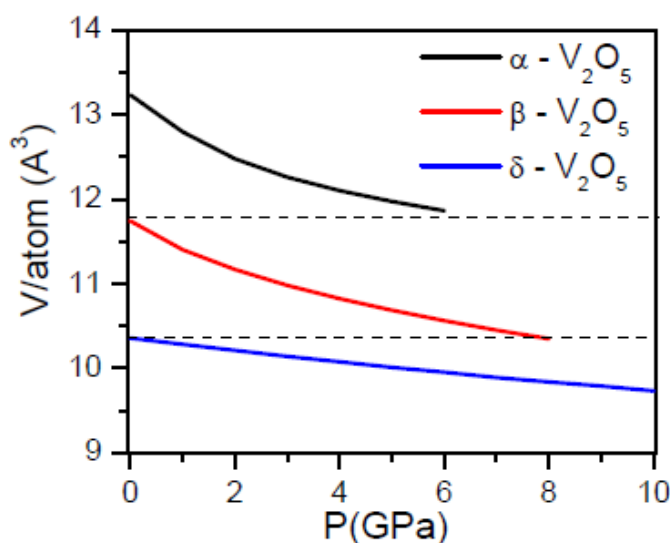


FIG 4.11 Calculated volume per atom as a function of pressure for the α , β and δ - V_2O_5 . The calculations are shown in experimental stability range [22,70] of various phases.

4.3.6 Dynamics of Li-ion in V_2O_5 Layers

The compound V_2O_5 , due to its layered structure, offer a large affinity to host and intercalate with small elements[38,78,79]. The alkali atoms, due to their smaller sizes and lower charge ionic states, are most eligible to intercalate in the structural layers of V_2O_5 . The lower charge states of these alkali ions favour their reversible intercalation. This type of intercalation is very useful for battery technology, where electrode materials are required to intercalate and deintercalate Li ions for charging and discharging of Li ion battery. Therefore, layered structures with high stability have always been of interest to

battery researchers. In this respect few well known layered structure like MoSe₂, WSe₂, MoS₂, WS₂ etc has been studied for their thermodynamical behaviour to intercalation with Li, Na and Mg ions. The intercalation of alkali ions like Li, Na and Mg has also been studied in various phases of V₂O₅ using static *ab-initio* DFT techniques[38,79]. The intercalated structures are found to form some metastable phases upon intercalations. Multivalent ions inserted within these structures encounter suboptimal coordination environments and expanded transition states, which facilitate easier ion diffusion. The calculated activation energy barrier using nudged elastic band(NEB) method for divalent Mg ion undergoes an activation energy barrier in the range of 0.2 to 0.8 eV in various phases[79]. This barrier reduces to 0.11–0.16 eV for Li diffusion in α -V₂O₅.

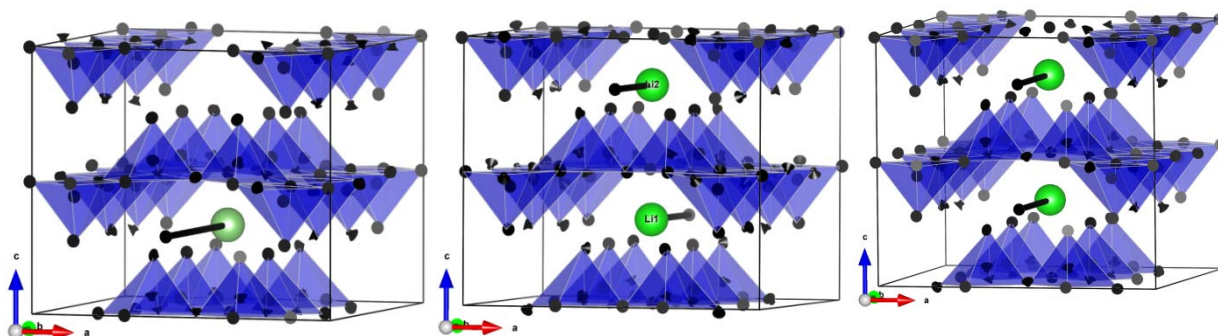


FIG 4.12 The calculated eigenvector of unstable phonon modes in (a) $\text{Li}_{0.08}\text{V}_2\text{O}_5$ and (b, c) $\text{Li}_{0.16}\text{V}_2\text{O}_5$ obtained from density functional perturbation theory approach.

In order to investigate the actual dynamics of alkali ions in V₂O₅ layers, the *ab-initio* molecular dynamics calculations are performed[36]. Moreover, the phonon frequencies and corresponding eigenvectors in the intercalated V₂O₅ are calculated using lattice dynamics to see the role of vibrational dynamics to onset the Li diffusion in the compound. For this purpose, a supercell $1 \times 3 \times 2$ of the ambient α -V₂O₅ containing 84 atoms is intercalated with one and two Li atoms giving rise to $\text{Li}_{0.08}\text{V}_2\text{O}_5$ and $\text{Li}_{0.16}\text{V}_2\text{O}_5$

configurations, respectively. The Brillion zone centre phonon frequencies for these two structures are calculated using density functional perturbation approach. These calculations show that there are one and two unstable phonon frequencies in $\text{Li}_{0.08}\text{V}_2\text{O}_5$ and $\text{Li}_{0.16}\text{V}_2\text{O}_5$ configurations, respectively. The eigenvectors of these phonon modes are shown in Fig 4.12. This unstable mode in $\text{Li}_{0.08}\text{V}_2\text{O}_5$ has large amplitude of Li atom along b -axis of unit cell. The large magnitude arises from the open channels along b -axis among the layers of V_2O_5 structure. On the other hand, in case of $\text{Li}_{0.16}\text{V}_2\text{O}_5$, calculations give two unstable phonon frequencies. The eigenvector corresponding to these frequencies give the movement along the b -axis of the unit cell. However, there are two possibilities of Li atoms movements along b -axis. In one phonon mode both the atoms can move opposite to each other (Fig 4.12) and in the other, both the Li atoms move in the same direction along b -axis. This implies that if Li atom diffusion may have initiated through Li ion movement along b -axis between the layers of V_2O_5 .

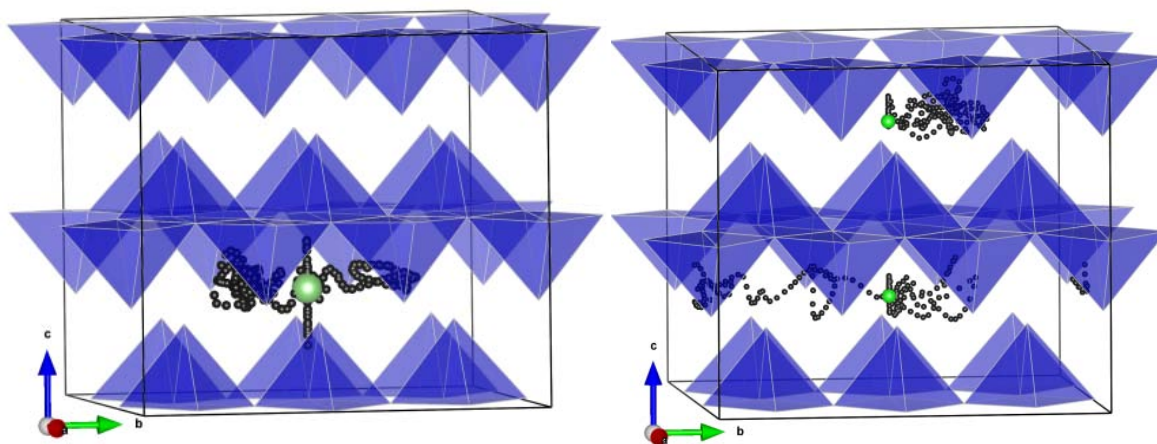


FIG 4.13 The calculated trajectories of Li in (a) $\text{Li}_{0.08}\text{V}_2\text{O}_5$ and (b) $\text{Li}_{0.16}\text{V}_2\text{O}_5$ obtained from *ab-initio* MD simulations at 1000K.

The *ab-initio* molecular dynamics simulations are further performed upto 8 ps at 1000 K. The trajectories of Li in $\text{Li}_{0.08}\text{V}_2\text{O}_5$ and $\text{Li}_{0.16}\text{V}_2\text{O}_5$ as obtained from these

simulations are displayed in Fig 4.13. The calculated trajectories show the net diffusion of Li along b -axis in both the configurations. The movement along other directions are not significant and they only make the diffusion path (along b -axis) curved which arises from the frustration in coordination of Li during the diffusion. On the overall, both the unstable phonon modes and the actual diffusion pathways from MD simulations shows diffusion of intercalated Li along the b -axis of the structure. Therefore, the diffusion of Li is followed the same path as guided by the eigenvector of unstable phonon modes in $\text{Li}_x\text{V}_2\text{O}_5$. This shows that the lattice dynamics methods may provide initial screening for diffusion pathways for Li ion migration as well as to choose better ionic conductors.

4.4 Conclusions

The experimental X-ray diffraction and inelastic neutron scattering studies along with extensive *ab-initio* lattice dynamical calculations shed light on the microscopic origin of anomalous lattice thermal expansion behaviour of V_2O_5 . The temperature dependent X-ray diffraction measurements from 12K to 853K do not show any evidence of structural phase transition or decomposition of $\alpha\text{-V}_2\text{O}_5$, which clarify the previous ambiguity existing in the literature. The inelastic neutron scattering measurements performed up to 673 K corroborate the result of the X-ray diffraction measurements. The van-der Waals dispersion and Hubbard interactions are found to play an important role in structure and dynamics of layered V_2O_5 . These interactions highly affect the phonon spectra and other thermodynamical properties of V_2O_5 . The anisotropic thermal expansion calculated under quasi-harmonic approximation agrees well with temperature dependent X-ray diffraction results and clarifies the ambiguity in reported dilatometer measurements. The compound is found to show negative thermal expansion and negative

linear compressibility along a -axis at low temperature. The anisotropic thermal expansion and anisotropic linear compressibility arises from the anisotropy in Grüneisen parameters and elastic constants. Free energy calculations show two first ordered phase transition at high pressure and temperature i.e. from α - to β - and then to a δ -phase. A combined *ab-initio* molecular dynamical simulations and lattice dynamics shows that the vibrational dynamics of Li may initiate the diffusion of Li along the b -axis in $\text{Li}_x\text{V}_2\text{O}_5$.

References

- [1] C. Wei, W. He, X. Zhang, J. Shen, and J. Ma, *New Journal of Chemistry* **40**, 2984 (2016).
- [2] J. B. Goodenough and K.-S. Park, *Journal of the American Chemical Society* **135**, 1167 (2013).
- [3] J.-M. Tarascon, *Philosophical Transactions of the Royal Society of London A: Mathematical, Physical and Engineering Sciences* **368**, 3227 (2010).
- [4] R. Schmich, R. Wagner, G. Hörpel, T. Placke, and M. Winter, *Nature Energy* **3**, 267 (2018).
- [5] I. E. Wachs, *Dalton Transactions* **42**, 11762 (2013).
- [6] N. B. Aetukuri *et al.*, *Nature Physics* **9**, 661 (2013).
- [7] J. Zhu *et al.*, *Nano Letters* **13**, 5408 (2013).
- [8] M. Sathiya, A. S. Prakash, K. Ramesha, J. M. Tarascon, and A. K. Shukla, *Journal of the American Chemical Society* **133**, 16291 (2011).
- [9] D. Yu, C. Chen, S. Xie, Y. Liu, K. Park, X. Zhou, Q. Zhang, J. Li, and G. Cao, *Energy & Environmental Science* **4**, 858 (2011).
- [10] Q. Liu *et al.*, *Nature Communications* **6** (2015).
- [11] Q. Wei, J. Liu, W. Feng, J. Sheng, X. Tian, L. He, Q. An, and L. Mai, *Journal of Materials Chemistry A* **3**, 8070 (2015).
- [12] Q. An, Q. Wei, P. Zhang, J. Sheng, K. M. Hercule, F. Lv, Q. Wang, X. Wei, and L. Mai, *Small* **11**, 2654 (2015).
- [13] M. Rao, *Research Journal of Recent Sciences* **2**, 67 (2013).
- [14] A. Talledo and C. G. Granqvist, *Journal of Applied Physics* **77**, 4655 (1995).
- [15] G. Micocci, A. Serra, A. Tepore, S. Capone, R. Rella, and P. Siciliano, *Journal of Vacuum Science & Technology A* **15**, 34 (1997).
- [16] G. Gu *et al.*, *Nat Mater* **2**, 316 (2003).
- [17] R. Enjalbert and J. Galy, *Acta Crystallographica Section C* **42**, 1467 (1986).
- [18] B. W. King and L. L. Suber, *Journal of the American Ceramic Society* **38**, 306 (1955).
- [19] I. Corvin and L. Cartz, *Journal of the American Ceramic Society* **48**, 328 (1965).
- [20] R. J. D. Tilley and B. G. Hyde, *Journal of Physics and Chemistry of Solids* **31**, 1613 (1970).
- [21] V. Thangadurai, S. Narayanan, and D. Pinzaru, *Chemical Society Reviews* **43**, 4714 (2014).
- [22] P. Balog, D. Orosel, Z. Cancarevic, C. Schön, and M. Jansen, *Journal of Alloys and Compounds* **429**, 87 (2007).
- [23] J. M. Gallardo-Amores, N. Biskup, U. Amador, K. Persson, G. Ceder, E. Morán, and M. E. Arroyo y de Dompablo, *Chemistry of Materials* **19**, 5262 (2007).
- [24] J. M. Cocciantelli, P. Gravereau, J. P. Doumerc, M. Pouchard, and P. Hagemuller, *Journal of Solid State Chemistry* **93**, 497 (1991).
- [25] Y. Repelin, E. Husson, L. Abello, and G. Lucazeau, *Spectrochimica Acta Part A: Molecular Spectroscopy* **41**, 993 (1985).
- [26] H. Poelman, L. Fiermans, J. Vennik, and G. Dalmai, *Solid State Communications* **84**, 811 (1992).
- [27] P. Clauws, J. Broeckx, and J. Vennik, *physica status solidi (b)* **131**, 459 (1985).
- [28] P. Clauws and J. Vennik, *Physica Status Solidi (b)* **76**, 707 (1976).
- [29] L. Abello, E. Husson, Y. Repelin, and G. Lucazeau, *Spectrochimica Acta Part A: Molecular Spectroscopy* **39**, 641 (1983).

- [30] B. Bootz, H. Finkenrath, G. Franz, and N. Uhle, *Solid State Communications* **13**, 1477 (1973).
- [31] T. R. Gilson, O. F. Bizri, and N. Cheetham, *Journal of the Chemical Society, Dalton Transactions*, 291 (1973).
- [32] C. Bhandari and W. R. L. Lambrecht, *Physical Review B* **89**, 045109 (2014).
- [33] B. Zhou and D. He, *Journal of Raman Spectroscopy* **39**, 1475 (2008).
- [34] V. Brázdová, M. V. Ganduglia-Pirovano, and J. Sauer, *Physical Review B* **69**, 165420 (2004).
- [35] X. Yin, A. Fahmi, A. Endou, R. Miura, I. Gunji, R. Yamauchi, M. Kubo, A. Chatterjee, and A. Miyamoto, *Applied Surface Science* **130–132**, 539 (1998).
- [36] B. Singh et. al., (Unpublished).
- [37] B. Singh, M. K. Gupta, S. K. Mishra, R. Mittal, P. Sastry, S. Rols, and S. L. Chaplot, *Physical Chemistry Chemical Physics* **19**, 17967 (2017).
- [38] G. Sai Gautam, P. Canepa, A. Abdellahi, A. Urban, R. Malik, and G. Ceder, *Chemistry of Materials* **27**, 3733 (2015).
- [39] J. Rodriguez-Carvajal, in *satellite meeting on powder diffraction of the XV congress of the IUCr* (Toulouse, France:[sn], 1990).
- [40] A. Sjolander, *Arkiv für Fysik* **14**, 315 (1958).
- [41] G. Kresse and D. Joubert, *Physical Review B* **59**, 1758 (1999).
- [42] G. Kresse and J. Furthmüller, *Computational Materials Science* **6**, 15 (1996).
- [43] H. J. Monkhorst and J. D. Pack, *Physical Review B* **13**, 5188 (1976).
- [44] S. Grimme, *Journal of Computational Chemistry* **27**, 1787 (2006).
- [45] S. Dudarev, G. Botton, S. Savrasov, C. Humphreys, and A. Sutton, *Physical Review B* **57**, 1505 (1998).
- [46] K. Parlinski, PHONON Software (2003).
- [47] D. D. Richardson, *Journal of Physics C: Solid State Physics* **10**, 3235 (1977).
- [48] A. K. Geim and I. V. Grigorieva, *Nature* **499**, 419 (2013).
- [49] A. Pergament, G. Stefanovich, N. Kuldin, and A. Velichko, *ISRN Condensed Matter Physics* **2013** (2013).
- [50] C. Bhandari, W. R. L. Lambrecht, and M. van Schilfgaarde, *Physical Review B* **91**, 125116 (2015).
- [51] R. Baddour-Hadjean, M. B. Smirnov, K. S. Smirnov, V. Y. Kazimirov, J. M. Gallardo-Amores, U. Amador, M. E. Arroyo-de Dompablo, and J. P. Pereira-Ramos, *Inorganic Chemistry* **51**, 3194 (2012).
- [52] M. V. Ganduglia-Pirovano and J. Sauer, *The Journal of Physical Chemistry B* **109**, 374 (2005).
- [53] A. Chakrabarti, K. Hermann, R. Druzinic, M. Witko, F. Wagner, and M. Petersen, *Physical Review B* **59**, 10583 (1999).
- [54] G. Jakub, G. Robert, W. Małgorzata, and H. Jürgen, *Journal of Physics: Condensed Matter* **21**, 095008 (2009).
- [55] G. Kresse, S. Surnev, M. G. Ramsey, and F. P. Netzer, *Surface Science* **492**, 329 (2001).
- [56] M. V. Ganduglia-Pirovano and J. Sauer, *Physical Review B* **70**, 045422 (2004).
- [57] Z. R. Xiao and G. Y. Guo, *The Journal of Chemical Physics* **130**, 214704 (2009).
- [58] S. Laubach, P. C. Schmidt, Thi, F. J. Fernandez-Madrigal, Q.-H. Wu, W. Jaegermann, M. Klemm, and S. Horn, *Physical Chemistry Chemical Physics* **9**, 2564 (2007).
- [59] B. Kristian, R. C. Valentino, L. Kyuho, S. Elsebeth, T. Thonhauser, H. Per, and I. L. Bengt, *Reports on Progress in Physics* **78**, 066501 (2015).

- [60] E. Londero and E. Schröder, *Computer Physics Communications* **182**, 1805 (2011).
- [61] J. Carrasco, *The Journal of Physical Chemistry C* **118**, 19599 (2014).
- [62] T. Bučko, S. Lebègue, J. Hafner, and J. G. Ángyán, *Physical Review B* **87**, 064110 (2013).
- [63] T. Bučko, J. Hafner, S. Lebègue, and J. G. Ángyán, *The Journal of Physical Chemistry A* **114**, 11814 (2010).
- [64] V. L. Volkov, *Inorg. Mater* **24**, 1568 (1988).
- [65] K. Berland, V. R. Cooper, K. Lee, E. Schröder, T. Thonhauser, P. Hyldgaard, and B. I. Lundqvist, *Reports on Progress in Physics* **78**, 066501 (2015).
- [66] M. E. Arroyo y de Dompablo, J. M. Gallardo-Amores, U. Amador, and E. Morán, *Electrochemistry Communications* **9**, 1305 (2007).
- [67] Y. Le Page and P. Saxe, *Physical Review B* **65**, 104104 (2002).
- [68] J. F. Nye, *Physical properties of crystals: their representation by tensors and matrices* (Oxford university press, 1985).
- [69] I. P. Zibrov, V. P. Filonenko, S. G. Lyapin, and V. A. Sidorov, *High Pressure Research* **33**, 399 (2013).
- [70] I. Loa, A. Grzechnik, U. Schwarz, K. Syassen, M. Hanfland, and R. K. Kremer, *Journal of Alloys and Compounds* **317–318**, 103 (2001).
- [71] V. P. Filonenko, M. Sundberg, P.-E. Werner, and I. P. Zibrov, *Acta Crystallographica Section B* **60**, 375 (2004).
- [72] A. Grzechnik, *Chemistry of Materials* **10**, 2505 (1998).
- [73] M. B. Smirnov, V. Y. Kazimirov, R. Baddour-Hadjean, K. S. Smirnov, and J.-P. Pereira-Ramos, *Journal of Physics and Chemistry of Solids* **75**, 115 (2014).
- [74] S. Minomura and H. G. Drickamer, *Journal of Applied Physics* **34**, 3043 (1963).
- [75] T. Suzuki, S. Saito, and W. Arakawa, *Journal of Non-Crystalline Solids* **24**, 355 (1977).
- [76] V. P. Filonenko and I. P. Zibrov, *Inorganic Materials* **37**, 953.
- [77] K. Kusaba, E. Ohshima, Y. Syono, and T. Kikegawa, *Journal of Crystal Growth* **229**, 467 (2001).
- [78] A. Parija, Y. Liang, J. L. Andrews, L. R. De Jesus, D. Prendergast, and S. Banerjee, *Chemistry of Materials* **28**, 5611 (2016).
- [79] A. Mukherjee, N. Sa, P. J. Phillips, A. Burrell, J. Vaughey, and R. F. Klie, *Chemistry of Materials* **29**, 2218 (2017).

CHAPTER 5

Phonon Spectra and Anomalous Lattice Behaviour of $\text{ZnAu}_2(\text{CN})_4$

5.1 Introduction

The understanding of mechanisms responsible for various functional properties [1-7] of materials is very important to improve their performance. By intuition, material should contract (or expand) on application of hydrostatic pressure (or temperature), yet a small number of crystals show opposite behaviour in a few directions. This type of anomalous behaviour with pressure (or temperature) is called negative linear compressibility, NLC (or negative thermal expansion, NTE) behaviour[8]. Materials with a NLC and NTE could have interesting applications[8-10] in muscle systems, marine optical telecommunication and devices for high pressure-temperature surroundings.

Many oxides and fluorides framework compounds are found to exhibit NTE behaviour[11-13]. However, the discovery of large NTE in $\text{Zn}(\text{CN})_2$ [14] triggered a keen interest in cyanide compounds. Later on many other cyanides such as $\text{M}(\text{CN})_2$ ($\text{M}=\text{Zn}, \text{Ni}, \text{Cd}$), $\text{KMn}[\text{Ag}(\text{CN})_2]_3$, MCN ($\text{M}=\text{Ag}, \text{Au}, \text{Cu}$), $\text{M}_3\text{Co}(\text{CN})_6$ ($\text{M}=\text{H}, \text{Ag}, \text{Au}, \text{Cu}$) and $\text{MAuX}_2(\text{CN})_2$ ($\text{M}=\text{Ag}, \text{Au}, \text{Cu}$ & $\text{X}=\text{CN}, \text{Cl}, \text{Br}$) etc., are discovered in this category[3,4,15-17]. A few of them also shows the property of negative linear or area compressibility. The reason for their anomalous lattice response as a function of temperature and pressure is observed due to their low density open framework structure and a large diversity in bonding. These compounds have small value of bulk modulus and highly anisotropic elastic properties.

5.1.1 Structural Details

The metal cyanide compound, $\text{ZnAu}_2(\text{CN})_4$, exhibit exceptionally large NTE and NLC simultaneously[3,6]. The compound has four polymorphs, each consist of $\text{Zn}(\text{CN})_4$ polyhedral units connected via Au atoms. Because of the long $\text{Au}(\text{CN})_2$ bridging unit, the structure is filled by two to five additional interpenetrated network. At ambient conditions of temperature and pressures, this compound crystallizes in hexagonal structure with $P6_222$ space group. This polymorph, also called α -polymorph, is studied in the present chapter. This polymorph is topologically similar to β -quartz and form helical chains oriented perpendicular to the c crystal axis giving rise to the honeycomb-like nature of its hexagonal pores. The honeycomb structure of $\text{ZnAu}_2(\text{CN})_4$ (Fig 5.1) is believed to be responsible for its anomalous lattice behavior.

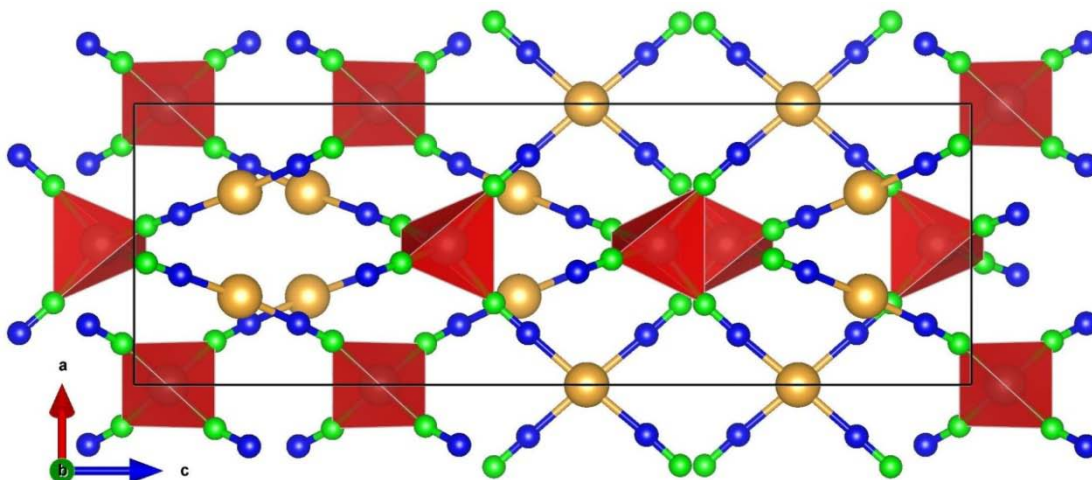


FIG 5.1 Crystal structure of the ambient pressure phase of $\text{ZnAu}_2(\text{CN})_4$. Zn atoms are at the centre of tetrahedral units (red colour). Key: N, green sphere; C, blue sphere; Au yellow sphere; Zn, red sphere.

The temperature dependence of the unit cell parameters of $\text{ZnAu}_2(\text{CN})_4$ indicates[3,6] that the thermal expansion is anisotropic and negative along the hexagonal

c-axes($\alpha_a \sim 36.9 \times 10^{-6} \text{ K}^{-1}$, $\alpha_c \sim -57.6 \times 10^{-6} \text{ K}^{-1}$). The NLC along the c-axes at ambient pressure is reported[3] to be -42 TPa^{-1} . The compound has a large positive linear compressibility (PLC) in a-b plane (-52 TPa^{-1}) which compensates the NLC along the c-axes. The compound also exhibits pressure driven structural phase transition at $\sim 1.8 \text{ GPa}$ [3]. The unit cell of the high-pressure phase is a $2 \times 2 \times 2$ supercell of the ambient pressure phase. The supercell implies that the transition may be driven by softening of an L-point phonon mode at the Brillouin zone boundary. This phase also shows NLC behavior along the c-axes but with a lower magnitude in comparison to that of the ambient pressure phase.

5.1.2 Motivations and Objectives of Research

The underlying mechanism governing the large NLC and NTE along the hexagonal c-axis has not been studied. Understanding this will be very helpful in designing new materials with enhanced NLC and NTE properties. Moreover, the high pressure phase transition is suspected to be derived by the softening of L-point phonon mode; however, detailed pressure dependent phonon dispersion is required to identify the corresponding phonon modes. Aim of this chapter is to understand the physics behind the rare and interesting combination of NTE and NLC in $\text{ZnAu}_2(\text{CN})_4$, and its possible relation with the high-pressure transition; as well as to quantitatively explain these features. The anharmonic phonons are expected to play a dominant role in giving rise to NTE and high pressure phase transitions. A detailed *ab-initio* density functional theory (DFT) calculations and temperature-dependent inelastic-neutron-scattering measurements of the phonon spectrum are studied[18].

5.2 Experimental and Computational Details

Inelastic neutron scattering measurements on about 1 cc of polycrystalline sample of $\text{ZnAu}_2(\text{CN})_4$ were carried out on the direct-geometry cold-neutron time-of-flight time-focusing spectrometer IN6 at the Institut Laue Langevin (ILL, Grenoble, France). Data were collected at 150, 225, 300 and 400 K, in the neutron energy gain setup and high-resolution mode, using an incident wavelength of 5.12 Å (3.12meV).

TABLE 5.1 *The calculated and measured[3] structure and elastic properties of the ambient pressure phase of $\text{ZnAu}_2(\text{CN})_4$.*

		Expt (x,y,z) (T=100 K)	Calc(x,y,z) (T=0 K)
$l(\text{Å})$	a, b, c	8.3967, 8.3967, 20.9219	8.2096, 8.2096, 21.4616
C1	(x, y, z) $u^2(\text{Å}^2)$	(0.4020, 0.2187, 0.5289) 0.0131	(0.4025, 0.2189, 0.5294) 0.0122 (100 K)
C2	(x, y, z) $u^2(\text{Å}^2)$	(0.2149, 0.3985, 0.3881) 0.0175	(0.2128, 0.3894, 0.3879) 0.0124 (100 K)
N1	(x, y, z) $u^2(\text{Å}^2)$	(0.4455, 0.1532, 0.5697) 0.0131	(0.4481, 0.1570, 0.5704) 0.0133 (100 K)
N2	(x, y, z) $u^2(\text{Å}^2)$	(0.7123, 0.1491, 0.6820) 0.0130	(0.7145, 0.1467, 0.6808) 0.0132 (100 K)
Zn	(x, y, z) $u^2(\text{Å}^2)$	(0.5, 0, 0.6260) 0.0085	(0.5, 0, 0.6261) 0.0081 (100 K)
Au	(x, y, z) $u^2(\text{Å}^2)$	(0.3164, 0.3169, 0.459) 0.0107	(0.3143, 0.3133, 0.4593) 0.0103 (100 K)
	$K_a(\text{TPa}^{-1})$	52 (6)	62.5
	$K_c(\text{TPa}^{-1})$	-42(5)	-51.7
	B(GPa)	16.7(16)	13.6

There are 66 atoms in the unit cell of $\text{ZnAu}_2(\text{CN})_4$ in ambient phase, which gives 198 modes. The PHONON software[19] is used to calculate phonon frequencies in the entire Brillouin zone, as a subsequent step to DFT total energy calculations using the VASP[20-22] software. An energy cut-off of 860 eV was used for plane wave's expansion. The Monkhorst Pack method is used for k point generation[23] with a $4 \times 4 \times 2$ k-point mesh was used. The exchange-correlation contributions were approximated using

the PBE functional[24,25]. The convergence breakdown criteria for the total energy and ionic loops were set to 10^{-8} eV and 10^{-5} eV \AA^{-1} , respectively. Initially the optimization of the crystal structure is performed with and without including the van-der Waals interactions. The calculations show that inclusion of van-der Waals interaction produces the structure close to the experimental [3]values (Table 5.1). The van-der Waals interaction were included using optB88-vdW[26,27] functional.

5.3 Results and Discussions

5.3.1 Experimental and Calculated Phonon Spectra

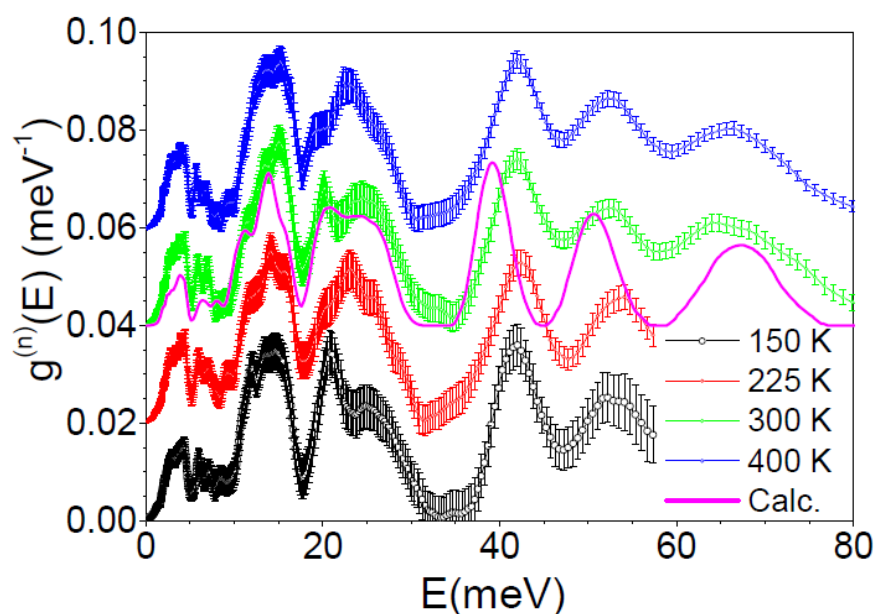


FIG 5.2 The temperature-dependent measured spectra of the ambient pressure phase of $\text{ZnAu}_2(\text{CN})_4$ along with the calculated neutron-weighted phonon spectrum.

The inelastic neutron scattering measurements are performed at various temperatures ranging from 150 K to 400 K as shown in Fig 5.2. The spectra show sharp peaks at about 4, 7, 12, 22, 25, 42, 50 and 70 meV. Modes between 20-30 meV are subject

to a significant change in energy as a function of temperature, indicating the anharmonic nature of these modes. The measured spectra at 150 K and 225 K are shown only up to 55 meV due to the effect of the Bose-Einstein population factor affecting higher energy phonons when cooling down. The energy of the C-N stretching mode is about 280 meV, which is not captured in the present measurements, using a cold neutron spectrometer. Since thermal expansion and other thermodynamical properties are driven by low energy modes, the measured spectral range is quite appropriate.

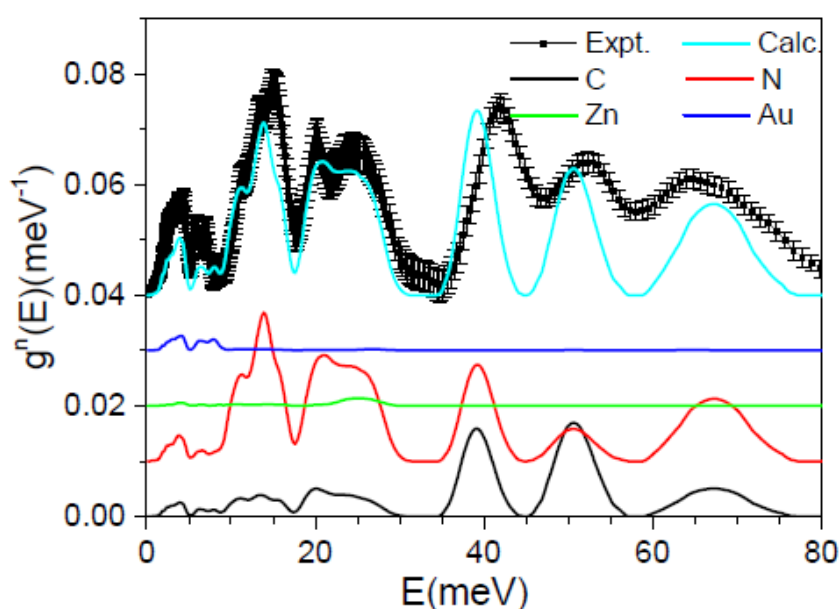


FIG 5.3 The calculated neutron weighted partial and total phonon spectra compared with measured inelastic spectra at $T=300$ K, in the ambient pressure phase of $\text{ZnAu}_2(\text{CN})_4$.

The computed partial and total neutron weighted phonon densities of states of various atoms in this compound are shown in Fig 5.3. The calculated phonon density of states reproduces well the experimental spectrum (Fig 5.3). These calculations reflect the atomic dynamics of individual atoms and their effect on properties of the compound. Vibrations of C and N atoms contribute to the entire spectral range, up to 280 meV, whereas Zn and Au atoms contribute up to 80meV. However, the lower energy spectra

below 20meV are largely dominated by heavier Au atoms. It is noted that Zn and Au do not contribute significantly to the total neutron-weighted density of states due to poor neutron cross-section of these atoms (Fig 5.3). This indicates that dynamics of C and N atoms contribute the most to the measured neutron spectrum. The low energy part below 30 meV has a major contribution from N atom; however, both C and N contribute almost equally within the range 30-80 meV.

5.3.2 Anisotropic Thermal Expansion Behaviour

The anisotropic thermal expansion behaviour can be understood by calculating the mode Grüneisen parameters and elastic compliance of the material as given in Eq. (1.30). The anisotropic Grüneisen parameters (Fig 5.4) are calculated by anisotropic pressure dependence of phonon frequencies. When the stress is applied, the maximum changes in the phonon spectra are observed above 20meV. Interestingly, modes in the range 20-30meV and above 60 meV behave differently than modes in the range 30 –60meV. The Grüneisen parameters show large negative values below 20 meV. The calculated elastic compliance tensor is given in Table 5.2.

TABLE 5.2 *The calculated elastic properties of the ambient pressure phase of $ZnAu_2(CN)_4$ as a function of pressure.*

Compliance	0 GPa	1 GPa	1.5GPa	2GPa
s_{11} (TPa ⁻¹)	131.8	120.5	109.9	106.0
s_{33} (TPa ⁻¹)	62.5	31.8	23.7	19.5
s_{44} (TPa ⁻¹)	80.7	83.6	82.9	71.1
s_{12} (TPa ⁻¹)	-12.2	-35.8	-42.4	-49.0
s_{13} (TPa ⁻¹)	-57.1	-32.7	-24.31	-19.6
K_a (TPa ⁻¹)	62.5	52.1	43.2	37.4
K_c (TPa ⁻¹)	-51.7	-33.5	-24.9	-19.7
B (GPa)	13.6	14.16	16.25	18.2

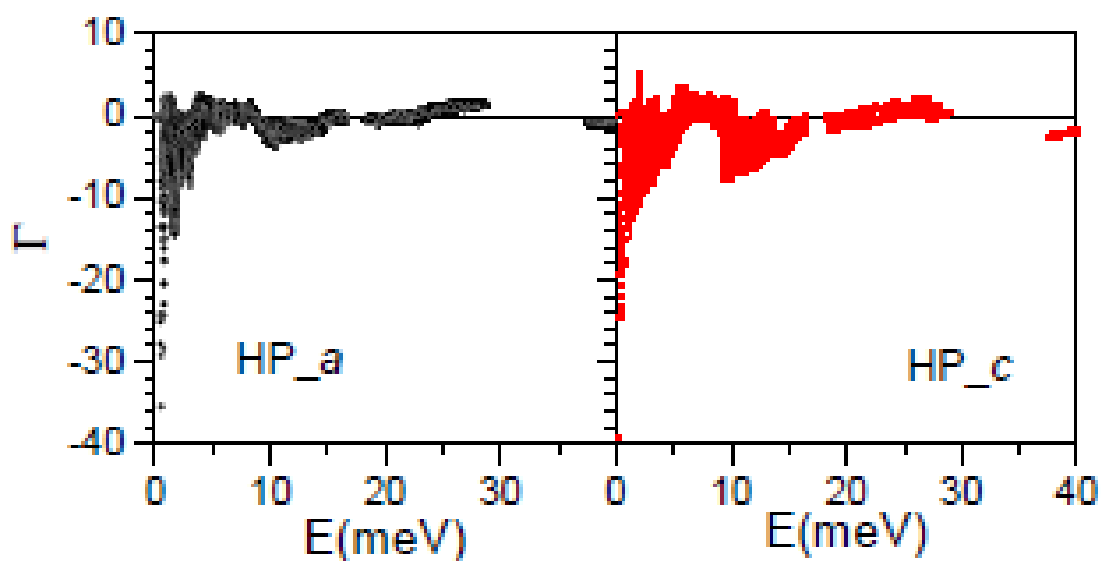


FIG 5.4 The calculated Grüneisen parameters of $\text{ZnAu}_2(\text{CN})_4$, Γ_a and Γ_c , averaged over the entire Brillouin zone on application of anisotropic pressure along a - (HP_a) and c -axes (HP_c), respectively.

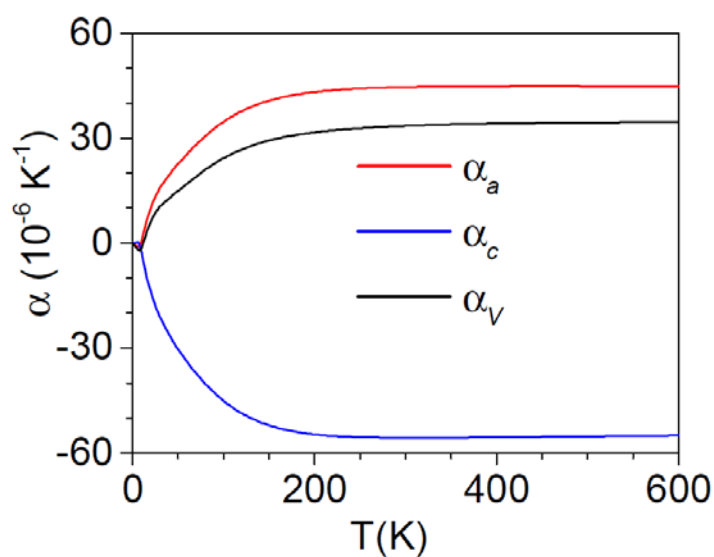


FIG 5.5 The calculated linear and volume thermal expansion as a function of temperature in the ambient pressure phase of $\text{ZnAu}_2(\text{CN})_4$.

The thermal expansion behaviour of a compound arises from anharmonic atomic vibrations. The calculated linear thermal expansion coefficients at 300K are $44 \times 10^{-6} \text{ K}^{-1}$

and $-55 \times 10^{-6} \text{ K}^{-1}$ along the a - and c -axes, respectively (Fig 5.5). The net volume thermal expansion coefficient is $33 \times 10^{-6} \text{ K}^{-1}$ (Fig 5.5). The comparison between the experimentally measured [3,6] fractional change in lattice parameters and volume with the calculated results as a function of temperature are shown in Fig 5.6(a). The calculated linear expansion along the a -axes is found to be in a good agreement with the measurements; however, along the c -axes the calculations are slightly underestimated. The computed linear thermal expansion coefficient as a function of phonon energy at $T=300 \text{ K}$ are shown in Fig 5.6(b).

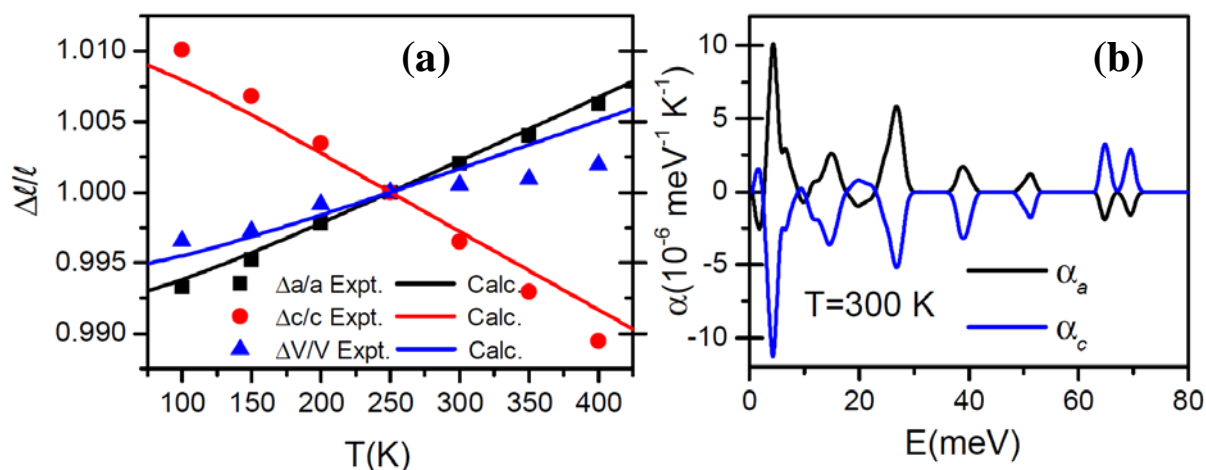


FIG 5.6 (a) The calculated and measured [6] fractional change in lattice parameters and volume as a function of temperature, in the ambient pressure phase of $\text{ZnAu}_2(\text{CN})_4$, and (b) the calculated contribution of various phonons of energy E to the linear thermal expansion along the a - and c -axes at 300 K.

It is interesting to see that modes which are contributing to the positive expansion in the a - b plane contribute to negative expansion along the c -axes. This unusual behaviour is attributed to large negative value of s_{13} (Table 5.2) and hence related with NLC behaviour of the compound. It suggests that any change in c -axes would lead to change in the a -axes in opposite way. Hence, as temperature increases, the c -axes decreases and the

a -axes expands. It is interesting to note that, although the anisotropic Grüneisen parameters are negative for compression along all the directions (Fig 5.4), the combination of NLC and Grüneisen parameter leads to NTE (Fig 5.6(a)) only along the hexagonal c -axis.

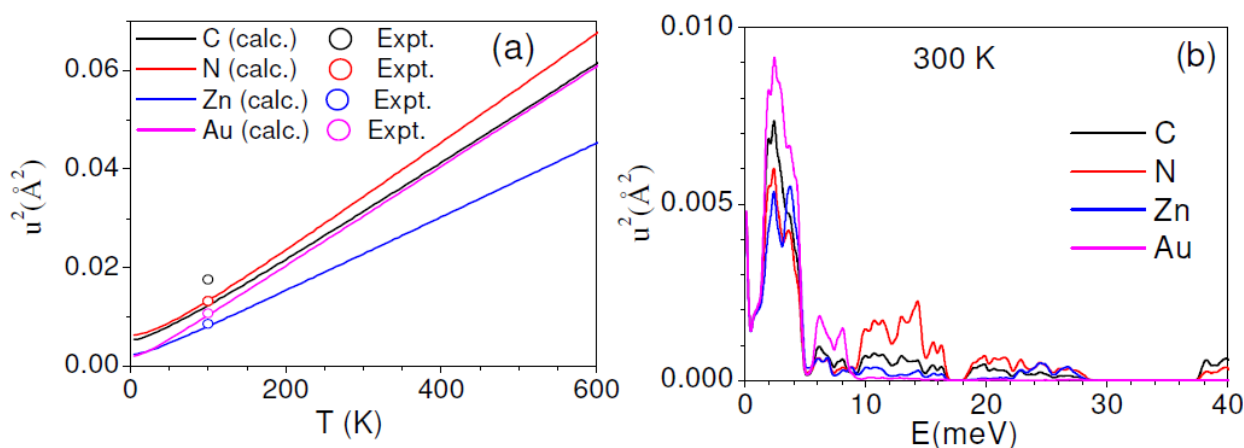


FIG 5.7 (a) The calculated and experimental[3] mean square displacement of various atoms in the ambient pressure phase of $\text{ZnAu}_2(\text{CN})_4$. (b) The calculated mean square displacement of various atoms as a function of phonon energy in the ambient pressure phase of $\text{ZnAu}_2(\text{CN})_4$ at 300K.

The calculated mean square displacements (u^2) of various atoms as a function of temperature are shown in Fig 5.7(a). Usually, lighter atoms have larger mean square displacement (u^2). However, the calculation shows that the u^2 value for Au atoms, which is the heaviest atom in the compound, is comparable with that of the lightest element, C. This suggests that the bonding of Au atom with their neighbouring atoms is highly flexible and provides enough flexibility to the structure for distortions required for NTE and NLC mechanism. Further, the contribution to mean square displacement from phonons of energy E at 300 K are calculated (Fig 5.7(b)). The mean square displacement of all the four atoms due to phonon of energy below 5meV is very large and dominated by

Au atoms. The large amplitude of Au vibration will lead to bending of -Zn-NC-Au-CN- Zn- chain and reduce the 'c' dimension.

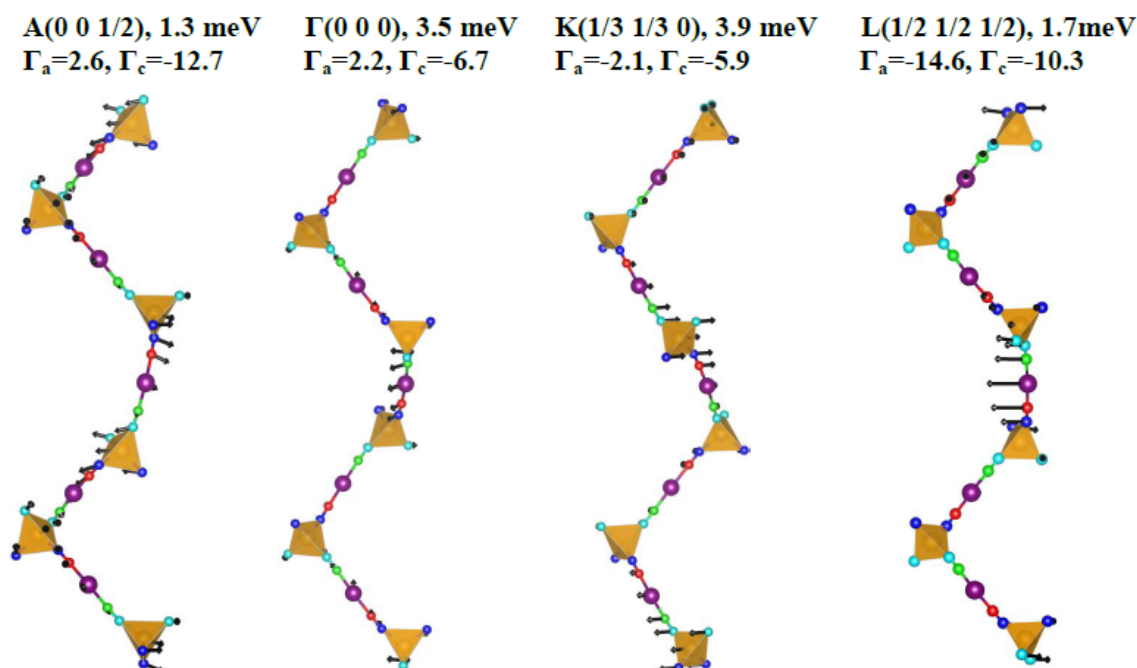


FIG 5.8 The calculated eigenvectors of selected phonon modes in the Brillouin zone in the ambient pressure phase of $ZnAu_2(CN)_4$. The *c*-axis is along the chain direction, while *a*- and *b*-axes are in the horizontal plane. Zn atoms are at the centre of tetrahedral units (yellow colour). Key: C1, red sphere; C2, green sphere; N1, blue sphere; N2, cyan sphere; Au purple sphere; Zn, yellow sphere.

Since NTE behavior is largely determined by low energy phonon modes, and also NLC is governed by the elastic constants which are related to the low energy acoustic phonon modes, it seems then that the low energy modes dominated by dynamics of Au atoms play a major role in these anomalous behaviours. A few phonon modes, that contribute to anomalous thermal expansion behaviour of $ZnAu_2(CN)_4$, are identified. The displacement pattern of such modes at high symmetry points of the Brillouin zone are

shown in Fig 5.8. The modes can be better visualized by the animations[18]. The A-point mode of 1.3meV($\Gamma_a=2.6$, $\Gamma_c=-12.7$) involves out-of-phase transverse vibrations of -Zn-NC-Au-CN-Zn- chains in the a - b plane. It is found that modes at the Γ -point (3.5 meV, $\Gamma_a=2.2$, $\Gamma_c=-6.7$) and the K-point (3.9 meV, $\Gamma_a= -2.1$, $\Gamma_c=-5.9$) involve out-of-phase translation motion and bending of -Zn-NC-Au-CN-Zn- chains. All these modes basically involve the transverse vibrations of -Zn-NC-Au-CN-Zn- chains and contribute to negative thermal expansion along c -axis and positive expansion in a - b plane.

Analysis of the displacement pattern of these modes shows that all these modes involve perpendicular displacement of Au, C and N atoms to the -Zn-NC-Au-CN-Zn- linkage. The magnitude of this displacement is largest for Au in these modes. These kinds of anharmonic modes bend the -Zn-NC-Au-CN-Zn- linkage and contract the c -axes as well as expand the a - b plane.

5.3.3 High Pressure Phase Transition

The compound $\text{ZnAu}_2(\text{CN})_4$ is known to undergo a high pressure structural transition at about 1.8 GPa[3]. The structure of the high-pressure phase (space group $P6_422$) is related to the $2 \times 2 \times 2$ super cell of the parent structure (space group $P6_222$). The high pressure phase transition is reported to be displacive in nature[3]. The two phases are found to be related by rotations of the Zn- centred coordination tetrahedra[3]. The supercell implied that the transition may be associated with a soft phonon mode at the $L(1/2 \ 1/2 \ 1/2)$ point in the Brillion zone of the parent structure (space group $P6_222$).

TABLE 5.3 The calculated and experimental [3] structure of high pressure phase of $ZnAu_2(CN)_4$. For easy comparison, the ambient phase structure in a $2 \times 2 \times 2$ supercell is presented. The distortion vector (i.e. difference between ambient and high-pressure phases) at 4 GPa is also presented.

	Expt. (x,y,z) (P=3.6GPa)	Calc. (High Pressure Phase at 4.0 GPa)	Calc.(Ambient Pressure Phase at 4.0GPa)	u_x	u_y	u_z	$ u $ (Å)
a (Å)	14.485	14.1744	14.1674	Distortion in fractional coordinates			Distortion amplitude
b (Å)	14.485	14.1744	14.1674				
c (Å)	45.796	46.6747	46.9919				
C1	0.0720,0.8660,0.3579	0.0754,0.8733,0.3594	0.0785,0.9056,0.3592	-0.003	-0.032	0.000	0.438
C2	0.6130,0.1780,0.6885	0.6131,0.1839,0.6897	0.5944,0.1729,0.6925	0.019	0.011	-0.003	0.266
C3	0.3380,0.9270,0.9023	0.3303,0.9201,0.9030	0.2943,0.9090,0.9029	0.036	0.011	0.000	0.453
C4	0.4140,0.0750,0.9775	0.4364,0.0869,0.9753	0.4056,0.0785,0.9741	0.031	0.009	0.001	0.394
C5	0.9090,0.7720,0.4308	0.9002,0.7603,0.4298	0.9090,0.7943,0.4304	-0.009	-0.034	-0.001	0.433
C6	0.0700,0.1450,0.1926	0.0680,0.1512,0.1926	0.0944,0.1729,0.1925	-0.026	-0.022	0.000	0.345
C7	0.4240,0.8230,0.4350	0.4216,0.8301,0.4343	0.4090,0.7943,0.4304	0.013	0.036	0.004	0.482
C8	0.1470,0.0630,0.2662	0.1654,0.0867,0.2659	0.2059,0.1147,0.2638	-0.040	-0.028	0.002	0.517
C9	0.3700,0.0960,0.5960	0.3684,0.1024,0.5954	0.3853,0.0910,0.5971	-0.017	0.011	-0.002	0.358
C10	0.5830,0.9100,0.3615	0.5879,0.9210,0.3617	0.5785,0.9056,0.3592	0.009	0.015	0.003	0.225
C11	0.2230,0.6300,0.2617	0.2369,0.6391,0.2601	0.2057,0.6147,0.2638	0.031	0.024	-0.004	0.438
C12	0.2760,0.9180,0.5261	0.2931,0.9236,0.5253	0.3271,0.9216,0.5259	-0.034	0.002	-0.001	0.499
C13	0.6630,0.0760,0.2659	0.6757,0.0946,0.2663	0.7057,0.1147,0.2638	-0.030	-0.020	0.003	0.394
C14	0.7230,0.1210,0.7611	0.7327,0.1294,0.7603	0.7057,0.1147,0.7638	0.027	0.015	-0.004	0.369
C15	0.0940,0.6690,0.1910	0.1069,0.6806,0.1896	0.0944,0.6729,0.1925	0.013	0.008	-0.003	0.206
C16	0.5840,0.1660,0.1937	0.5741,0.1615,0.1946	0.5944,0.1729,0.1925	-0.020	-0.011	0.002	0.268
N1	0.2540,0.6110,0.2825	0.2619,0.6137,0.2813	0.2379,0.5971,0.2848	0.024	0.017	-0.004	0.344
N2	0.2850,0.8740,0.8839	0.2861,0.8695,0.8826	0.2621,0.8592,0.8818	0.024	0.010	0.001	0.298
N3	0.1346,0.7200,0.8251	0.1302,0.7251,0.8284	0.1308,0.6957,0.8281	-0.001	0.029	0.000	0.421
N4	0.3960,0.1430,0.6177	0.4034,0.1537,0.6163	0.4029,0.1408,0.6182	0.001	0.013	-0.002	0.201
N5	0.1860,0.6350,0.5070	0.1972,0.6380,0.5070	0.1957,0.6308,0.5052	0.002	0.007	0.002	0.127
N6	0.3640,0.7900,0.4536	0.3713,0.7916,0.4551	0.3592,0.7621,0.4515	0.012	0.030	0.004	0.402
N7	0.4430,0.3080,0.6704	0.4571,0.3202,0.6702	0.4351,0.3043,0.6719	0.022	0.016	-0.002	0.289
N8	0.8641,0.0381,0.8408	0.8666,0.0495,0.8381	0.8692,0.0649,0.8385	-0.003	-0.015	0.000	0.203
N9	0.2090,0.0680,0.2824	0.2056,0.0779,0.2868	0.2379,0.0971,0.2848	-0.032	-0.019	0.002	0.409
N10	0.7450,0.0750,0.7770	0.7537,0.1001,0.7815	0.7379,0.0971,0.7848	0.016	0.003	-0.003	0.259
N11	0.8790,0.1130,0.3368	0.8720,0.0883,0.3390	0.8692,0.0649,0.3385	0.003	0.023	0.000	0.314
N12	0.6920,0.6440,0.5085	0.6871,0.6264,0.5031	0.6957,0.6308,0.5052	-0.009	-0.004	-0.002	0.144
N13	0.3790,0.5810,0.3356	0.3762,0.5712,0.3363	0.3692,0.5649,0.3385	0.007	0.006	-0.002	0.146
N14	0.7190,0.0710,0.2825	0.7189,0.0866,0.2868	0.7379,0.0971,0.2848	-0.019	-0.011	0.002	0.251
N15	0.8380,0.7410,0.4464	0.8491,0.7396,0.4508	0.8592,0.7621,0.4515	-0.010	-0.023	-0.001	0.279
N16	0.3510,0.0690,0.3441	0.3606,0.0654,0.3411	0.3692,0.0649,0.3385	-0.009	0.001	0.003	0.174
Zn1	0.2394,0.7534,0.4788	0.2450,0.7524,0.4789	0.2500,0.7500,0.4786	-0.005	0.002	0.000	0.093
Zn2	0.2555,0.5071,0.3097	0.2555,0.5099,0.3098	0.2500,0.5000,0.3119	0.006	0.010	-0.002	0.159
Zn3	0.7544,0.7524,0.4780	0.7485,0.7495,0.4774	0.7500,0.7500,0.4786	-0.002	-0.001	-0.001	0.060
Zn4	0.2420,0.9958,0.3140	0.2459,0.9977,0.3130	0.2500,0.0000,0.3119	-0.004	-0.002	0.001	0.072
Au1	0.1135,0.1130,0.2299	0.1079,0.1114,0.2295	0.1491,0.1433,0.2281	-0.041	-0.032	0.001	0.534

Au2	0.3275,0.0110,0.5605	0.3232,0.0123,0.5603	0.3567,0.0058,0.5615	-0.034	0.007	-0.001	0.531
Au3	0.1684,0.6569,0.2252	0.1786,0.6677,0.2246	0.1491,0.6433,0.2281	0.030	0.024	-0.004	0.422
Au4	0.3872,0.0057,0.9393	0.3931,0.0051,0.9387	0.3509,0.9943,0.9385	0.042	0.011	0.000	0.538
Au5	0.6268,0.1287,0.2306	0.6148,0.1192,0.2308	0.6491,0.1433,0.2281	-0.034	-0.024	0.003	0.450
Au6	0.5069,0.8765,0.3988	0.5055,0.8844,0.3981	0.4943,0.8509,0.3948	0.011	0.034	0.003	0.447
Au7	0.9892,0.8103,0.3941	0.9886,0.8107,0.3945	0.9943,0.8509,0.3948	-0.006	-0.040	0.000	0.535
Au8	0.6779,0.1651,0.7255	0.6796,0.1643,0.7248	0.6491,0.1433,0.7281	0.031	0.021	-0.003	0.414

The pressure dependence of crystal structure in both the phases (Table 5.3) shows a good agreement between the calculated and measured structure of the high-pressure phase at ~ 4 GPa. The enthalpy calculation as a function of pressure has been done to investigate the phase transition. The difference in enthalpy (ΔH) of the ambient and high-pressure phase as a function of pressure is shown in Fig 5.9(a). It can be seen that the enthalpy difference below 1.5 GPa is within the numerical accuracy of the calculation; however, ΔH is significantly large above 1.5 GPa and increases with increase in pressure. The calculation therefore indicates a phase transition at about 1.5 GPa.

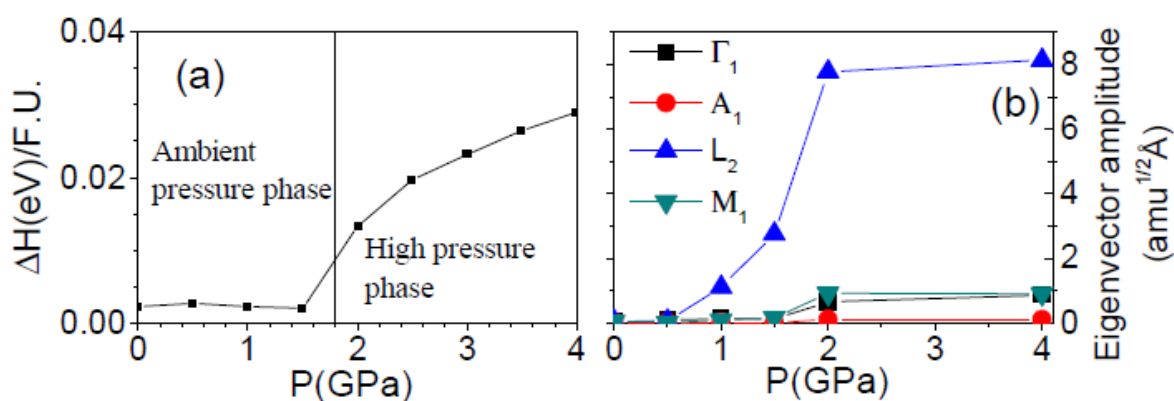


FIG 5.9 (a) The calculated difference in enthalpy between the ambient and high-pressure phases, as a function of pressure. (b) The calculated distortion in terms of the amplitude of eigenvector of phonon modes as a function of pressure in the ambient pressure phase of $\text{ZnAu}_2(\text{CN})_4$. The symbols represent the points at which calculations are performed.

In order to understand the nature of the phase transition, the group theoretical analysis of phonons at the zone centre and various high symmetry points in Brillouin zone has been performed. The classification of phonon modes at various high symmetry points is given as:

$$\Gamma(0\ 0\ 0) = 16\Gamma_1 + 16\Gamma_2 + 17\Gamma_3 + 17\Gamma_4 + 32\Gamma_5 + 34\Gamma_6$$

$$L(1/2\ 1/2\ 1/2) = 50L_1 + 50L_2 + 49L_3 + 49L_4$$

$$M(1/2\ 0\ 0) = 50M_1 + 50M_2 + 49M_3 + 49M_4$$

$$A(0\ 0\ 1/2) = 32A_1 + 32A_2 + 34A_3 + 34A_4 + 16A_5 + 17A_6$$

Here the Γ_5 , Γ_6 , A_5 and A_6 modes are double degenerate modes.

The amplitude mode analysis [28], indicates that the distortion induced by Γ_1 , A_1 , L_2 and M_1 phonon modes in the ambient pressure phase would lead to the high pressure phase transition. The calculations of the structural distortion between the ambient and high-pressure phase structure as a function of pressure are performed. This pressure dependent distortion is written in terms of distortions corresponding to the Γ_1 , A_1 , L_2 and M_1 points in the Brillouin zone (Fig 5.9(b)). The distortion picks up above 1.5 GPa and saturates above 2 GPa. It is observed that the magnitude of the distortion due to the A_1 point phonon is insignificant.

From the *ab-initio* lattice dynamics calculation, the specific phonon modes are identified that correspond to the distortions noted above. Table 5.4 shows that a linear combination of the distortions corresponding to the Γ_1 , L_2 and M_1 points in the Brillouin zone with appropriate weight factors can describe the observed distortion vector at 4 GPa as given in Table 5.3. It is found that the L_2 -point phonon mode (1.7 meV at 0 GPa) is the primary distortion mode driving the high-pressure phase transition; however, there is also a significant contribution from Γ_1 (4.0 meV at 0 GPa) and M_1 (2.3 meV at 0 GPa) point modes. The displacement pattern of the L -point mode of 1.7 meV shows twisting and

bending motion of -Zn-NC-Au-CN-Zn- chain (Fig 5.8 and animation[18]). All these modes show a large transverse motion of -Zn-NC-Au-CN-Zn- linkage, where Au has maximum amplitude of vibration (Fig 5.8). The difference in the structure of the ambient and the high-pressure phase at 4GPa is largely attributed to Au, C and N dynamics. It seems that the large vibrational amplitude of Au atoms along with connected CN units may create the distortion and lower the symmetry of the structure.

TABLE 5.4 A linear combination of the distortions corresponding to the Γ_1 , L_2 and M_1 points in the Brillouin zone with appropriate weight factors is used to generate the observed distortion vector at 4 GPa as given in Table 5.3.

	$0.9*\Gamma_1(0\ 0\ 0)$			$8.1*L_2(1/2\ 1/2\ 1/2)$			$0.9*M_1(1/2\ 0\ 0)$			$0.9*\Gamma_1+8.1*L_2+0.9*M_1$			Distortion vector at 4GPa			
	dx	dy	dz	dx	dy	dz	dx	dy	dz	dx	dy	dz	ux	uy	uz	u
C1	0.002	-0.001	0.000	-0.004	-0.029	0.000	-0.001	-0.002	0.000	-0.003	-0.032	0.000	-0.003	-0.032	0.000	0.438
C2	0.001	0.003	0.000	0.019	0.011	-0.002	-0.002	-0.003	0.000	0.018	0.010	-0.003	0.019	0.011	-0.003	0.266
C3	0.003	0.001	0.000	0.032	0.011	-0.001	0.001	-0.001	0.001	0.036	0.011	0.000	0.036	0.011	0.000	0.453
C4	-0.001	0.002	0.000	0.034	0.005	0.000	-0.002	0.001	0.001	0.032	0.008	0.001	0.031	0.009	0.001	0.394
C5	0.001	0.003	0.000	-0.011	-0.037	-0.002	0.001	0.000	0.001	-0.009	-0.034	-0.001	-0.009	-0.034	-0.001	0.433
C6	0.001	0.003	0.000	-0.029	-0.025	0.000	0.002	0.001	0.000	-0.026	-0.021	0.000	-0.026	-0.022	0.000	0.345
C7	0.001	0.003	0.000	0.010	0.033	0.004	0.002	0.000	0.000	0.013	0.036	0.004	0.013	0.036	0.004	0.482
C8	-0.003	-0.002	0.000	-0.037	-0.027	0.002	0.000	0.000	0.001	-0.041	-0.028	0.002	-0.040	-0.028	0.002	0.517
C9	0.002	-0.001	0.000	-0.020	0.011	-0.001	0.002	0.001	-0.001	-0.016	0.011	-0.002	-0.017	0.011	-0.002	0.358
C10	0.002	-0.001	0.000	0.007	0.015	0.002	0.001	0.002	0.000	0.010	0.016	0.002	0.009	0.015	0.003	0.225
C11	-0.003	-0.002	0.000	0.033	0.024	-0.004	0.000	0.002	0.000	0.031	0.024	-0.004	0.031	0.024	-0.004	0.438
C12	-0.003	-0.002	0.000	-0.029	0.005	0.000	-0.003	-0.001	-0.001	-0.034	0.002	-0.001	-0.034	0.002	-0.001	0.499
C13	-0.003	-0.002	0.000	-0.029	-0.018	0.003	0.001	-0.001	0.000	-0.030	-0.021	0.003	-0.030	-0.020	0.003	0.394
C14	-0.003	-0.002	0.000	0.029	0.018	-0.003	0.001	-0.001	0.000	0.027	0.015	-0.004	0.027	0.015	-0.004	0.369
C15	0.001	0.003	0.000	0.015	0.007	-0.002	-0.002	-0.002	0.000	0.013	0.008	-0.003	0.013	0.008	-0.003	0.206
C16	0.001	0.003	0.000	-0.019	-0.011	0.002	-0.002	-0.003	0.000	-0.020	-0.011	0.002	-0.020	-0.011	0.002	0.268
N1	-0.004	-0.004	0.000	0.027	0.017	-0.003	0.001	0.003	0.000	0.024	0.017	-0.003	0.024	0.017	-0.004	0.344
N2	0.004	0.000	0.000	0.018	0.011	-0.001	0.002	-0.001	0.001	0.024	0.010	0.001	0.024	0.010	0.001	0.298
N3	0.001	0.003	0.000	-0.003	0.023	-0.001	0.002	0.004	0.001	-0.001	0.030	0.000	-0.001	0.029	0.000	0.421
N4	0.004	0.000	0.000	-0.007	0.011	-0.001	0.003	0.001	-0.001	0.001	0.013	-0.002	0.001	0.013	-0.002	0.201
N5	0.003	0.001	0.000	0.002	0.007	0.002	-0.002	-0.001	0.000	0.002	0.007	0.002	0.002	0.007	0.002	0.127
N6	0.000	0.004	0.000	0.010	0.027	0.003	0.002	-0.001	0.000	0.012	0.030	0.003	0.012	0.030	0.004	0.402
N7	-0.002	-0.003	0.000	0.026	0.023	-0.001	-0.002	-0.004	-0.001	0.022	0.016	-0.002	0.022	0.016	-0.002	0.289
N8	-0.001	0.002	0.000	-0.002	-0.019	-0.001	0.001	0.002	0.000	-0.002	-0.015	-0.001	-0.003	-0.015	0.000	0.203
N9	-0.004	-0.004	0.000	-0.028	-0.016	0.002	-0.001	0.000	0.001	-0.033	-0.020	0.002	-0.032	-0.019	0.002	0.409

N10	-0.004	-0.004	0.000	0.017	0.007	-0.002	0.002	0.000	0.000	0.015	0.004	-0.003	0.016	0.003	-0.003	0.259
N11	-0.001	0.002	0.000	0.002	0.019	0.001	0.001	0.002	0.000	0.002	0.023	0.001	0.003	0.023	0.000	0.314
N12	0.003	0.001	0.000	-0.008	-0.007	-0.002	-0.003	0.001	0.000	-0.008	-0.004	-0.002	-0.009	-0.004	-0.002	0.144
N13	-0.001	0.002	0.000	0.007	0.006	-0.002	0.001	-0.001	0.000	0.007	0.006	-0.003	0.007	0.006	-0.002	0.146
N14	-0.004	-0.004	0.000	-0.017	-0.007	0.002	0.002	0.000	0.000	-0.019	-0.011	0.002	-0.019	-0.011	0.002	0.251
N15	0.000	0.004	0.000	-0.011	-0.028	-0.002	0.001	0.001	0.001	-0.010	-0.023	-0.001	-0.010	-0.023	-0.001	0.279
N16	-0.001	0.002	0.000	-0.007	0.002	0.002	-0.001	-0.003	0.000	-0.009	0.000	0.003	-0.009	0.001	0.003	0.174
Zn1	0.000	0.000	-0.001	-0.005	0.004	0.001	0.000	-0.002	0.000	-0.005	0.002	0.000	-0.005	0.002	0.000	0.093
Zn2	0.000	0.000	-0.001	0.004	0.009	-0.001	0.002	0.001	0.000	0.006	0.010	-0.002	0.006	0.010	-0.002	0.159
Zn3	0.000	0.000	-0.001	-0.002	-0.002	-0.001	0.000	0.002	0.000	-0.001	-0.001	-0.001	-0.002	-0.001	-0.001	0.060
Zn4	0.000	0.000	-0.001	-0.002	-0.001	0.001	-0.002	-0.002	0.000	-0.004	-0.002	0.001	-0.004	-0.002	0.001	0.072
Au1	-0.001	0.000	0.000	-0.041	-0.033	0.001	0.001	0.001	0.001	-0.041	-0.032	0.001	-0.041	-0.032	0.001	0.534
Au2	0.000	-0.002	0.000	-0.033	0.009	-0.001	-0.001	0.000	-0.001	-0.034	0.007	-0.002	-0.034	0.007	-0.001	0.531
Au3	-0.001	0.000	0.000	0.032	0.024	-0.003	-0.001	0.001	0.000	0.030	0.025	-0.003	0.030	0.024	-0.004	0.422
Au4	0.001	0.002	0.000	0.042	0.009	-0.001	0.000	0.000	0.001	0.043	0.011	0.000	0.042	0.011	0.000	0.538
Au5	-0.001	0.000	0.000	-0.033	-0.023	0.003	-0.001	-0.002	0.000	-0.035	-0.024	0.003	-0.034	-0.024	0.003	0.450
Au6	0.002	0.001	0.000	0.008	0.032	0.003	0.001	0.001	0.000	0.011	0.034	0.003	0.011	0.034	0.003	0.447
Au7	0.002	0.001	0.000	-0.007	-0.041	-0.001	0.000	-0.001	0.001	-0.006	-0.040	0.000	-0.006	-0.040	0.000	0.535
Au8	-0.001	0.000	0.000	0.033	0.023	-0.003	-0.001	-0.002	0.000	0.031	0.021	-0.004	0.031	0.021	-0.003	0.414

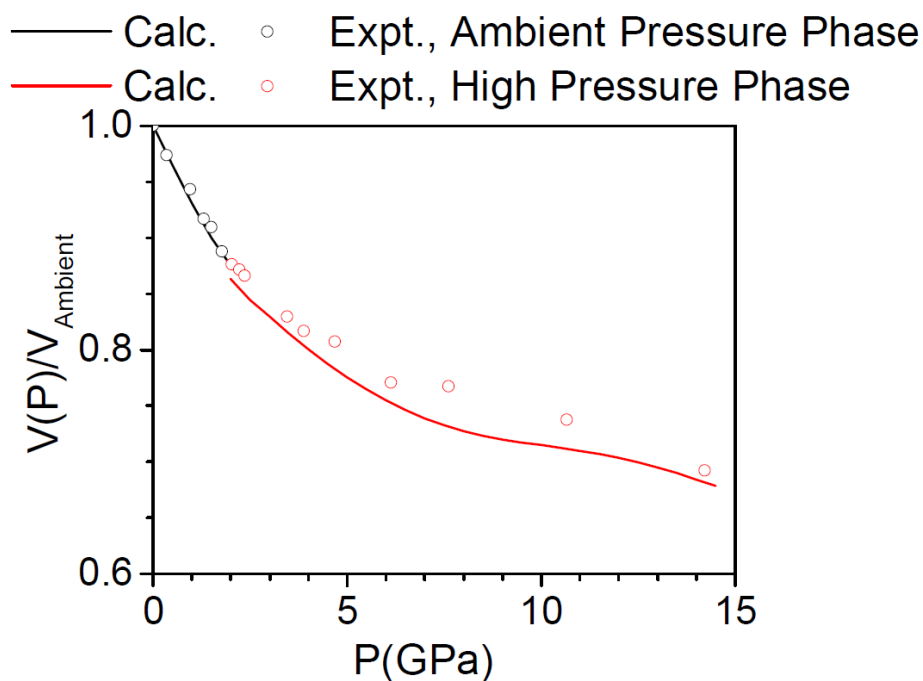


FIG 5.10 The calculated and experimental unit cell volumes of the ambient and high-pressure phases as a function of pressure. The calculated volumes of ambient and high-pressure phases have been normalized with respect to the volume of the ambient phase volume at zero pressure.

In order to confirm the nature of the phase transition, the pressure dependence of the volume is calculated. A small volume drop (~1.2%) at the transition pressure (Fig 5.10), suggest that the transition is of a weak first-order nature, and is in a good agreement with the experimental data[3].

TABLE 5.5 *The calculated elastic constants in the ambient pressure phase of $ZnAu_2(CN)_4$ as a function of pressure*

P(GPa)	Elastic Constants (in GPa)					
	C ₁₁	C ₃₃	C ₄₄	C ₆₆	C ₁₂	C ₁₃
0	36.6	126.8	12.1	3.2	29.7	60.6
1.0	31.6	151.5	12	3.2	25.2	58.4
1.5	31.6	161	12.1	3.2	25	57.9
2.0	31.7	166.4	14.1	3.2	25.3	57.3
3.0	33.4	177.2	13.4	3.1	27.3	57.4
4.0	36	187.6	8.9	3	30.3	58.6

TABLE 5.6 *The calculated Born stability criteria in the ambient pressure phase of $ZnAu_2(CN)_4$ as a function of pressure. For an elastically stable hexagonal crystal all the four Born criteria (elastic constants equations) must be positive.*

P (GPa)	Born Stability Criteria		
	(C ₄₄ -P)	(C ₆₆ -P)	(C ₃₃ -P)(C ₁₁ +C ₁₂) -2(C ₁₃ +P) ²
0	12.1	3.2	1062
1.0	11	2.2	1492
2.0	12.1	1.2	2338
3.0	10.4	0.1	3278
4.0	4.9	-1	4335

The calculated elastic constants in the ambient pressure phase of $ZnAu_2(CN)_4$ are given in Table 5.5 as a function of pressure. In Table 5.6, the calculated various Born stability criteria in the ambient pressure phase of $ZnAu_2(CN)_4$ as a function of pressure are

calculated. It is found that one of the Born stability criteria ($C_{66}-P>0$, which is equivalent to $C_{11}-C_{12}-2P>0$) are violated above 3 GPa., *i.e.*, the system becomes elastically unstable. It seems that although the phase transition is primarily driven by an L-point soft phonon mode, which usually leads to a second order transition with a $2\times 2\times 2$ supercell, in the present case the structure is close to an elastic instability that leads to a weakly first-order transition.

5.3.4 Negative Linear Compressibility

The pressure-dependent calculations of the structures in both the phases are performed. The calculated and measured lattice parameter changes with pressure have been compared in Fig 5.11. It is found that on compression to 1.8 GPa, the *a*-axes contracts by about 10% whereas the *c*-axes expands by about 8%. The NLC behaviour as observed along the *c*-axes from the experimental high pressure measurements[3] is reproduced by the calculations. The elastic constants as a function of pressure show that the elastic compressibilities along various crystallographic axes are highly anisotropic. This give rise to large positive and negative values of along the *a*- and *c*-axes respectively ($K_a= 62.7\text{TPa}^{-1}$, $K_c=-52.1\text{TPa}^{-1}$), which is in close agreement with the experimental values[3]. The origin of NLC can be understood by looking at the elastic compliance matrix (Table 5.2). The elastic compliance along the *a*-axes (s_{11}) and also the *c*-axes (s_{33}) are positive, and the shear compressibility s_{13} is large negative and comparable with s_{33} . This indicates that the *a*-axes will contract, but the *c*-axes is elongated with increasing pressure. Another shear compliance component s_{12} is also significantly negative. Interestingly this indicates that the effect of compression along the *a*-axes will also elongate the *b*-axes but with a reduced magnitude in comparison to the *c*-axes elongation.

As pressure increases, the magnitude of s_{13} decreases while that of s_{12} increases. This unusual behavior of elastic compliance is attributed to the double helical structure of $\text{ZnAu}_2(\text{CN})_4$, which gives rise to a very flexible structure in a - b plane.

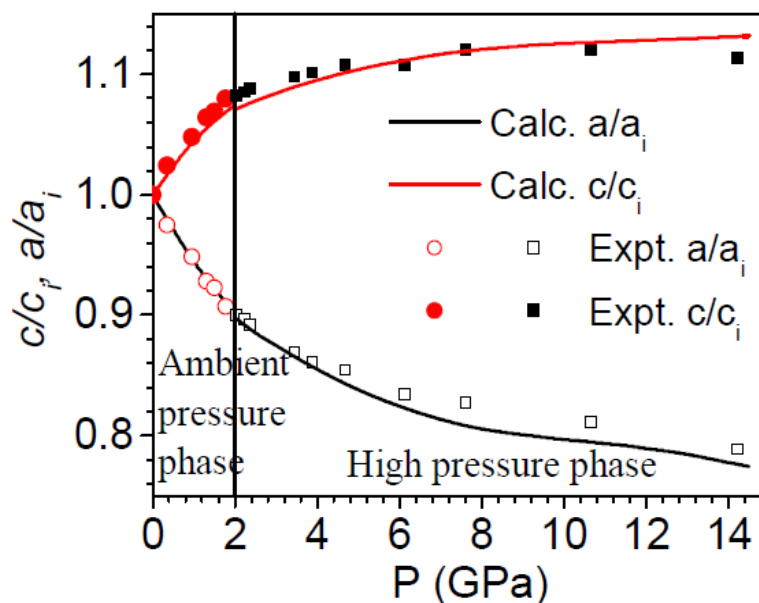


FIG 5.11 The calculated and measured[3] change in lattice parameters with pressure in the ambient and high pressure phases of $\text{ZnAu}_2(\text{CN})_4$. The high-pressure structural unit cell is a $2 \times 2 \times 2$ supercell of the ambient pressure phase. $a_i = a_0(2a_0)$ and $c_i = c_0(2c_0)$ are for the ambient (high) pressure phase. a_0 and c_0 are the lattice constants of ambient pressure phase at 0 GPa.

5.4 Conclusions

The inelastic neutron scattering experiments and *ab-initio* calculations are used to gain deeper insights into the structure and dynamics of $\text{ZnAu}_2(\text{CN})_4$ as a function of temperature and pressure. The calculations of the structure, phonon spectrum, anisotropic thermal expansion and anisotropic compressibility are in excellent agreement with experimental data. The specific soft phonon features that correlate very well with the

anomalous thermal expansion and compressibility exhibited by $\text{ZnAu}_2(\text{CN})_4$ has been identified. The large anisotropy in the elastic compliance matrix, which is attributed to the flexible network and Au bridging, are responsible for the NLC behaviour. It has been found that NLC could be another factor in materials which leads to NTE. The large negative shear elastic compliance (s_{13} and s_{12}) and small tensile elastic compliance (s_{33}) are indeed the major factors controlling the NTE behaviour in this compound. The known high-pressure transition at about 2 GPa occurs due to softening of an L-point phonon mode and its coupling with a zone-centre phonon and an M-point phonon. Further, the ambient pressure phase is found to be close to an elastic instability as revealed from violation of the Born stability criteria, which results in the phase transition being of a weakly first order nature.

References

- [1] F. Bridges, T. Keiber, P. Juhas, S. J. L. Billinge, L. Sutton, J. Wilde, and G. R. Kowach, *Physical Review Letters*, **112**, 045505 (2014).
- [2] A. L. Goodwin, M. Calleja, M. J. Conterio, M. T. Dove, J. S. O. Evans, D. A. Keen, L. Peters, and M. G. Tucker, *Science* **319**, 794 (2008).
- [3] A. B. Cairns *et al.*, *Nature Materials* **12**, 212 (2013).
- [4] A. L. Goodwin, D. A. Keen, and M. G. Tucker, *Proceedings of the National Academy of Sciences* **105**, 18708 (2008).
- [5] J. C. Michael, L. G. Andrew, G. T. Matthew, A. K. David, T. D. Martin, P. Lars, and S. O. E. John, *Journal of Physics: Condensed Matter* **20**, 255225 (2008).
- [6] A. L. Goodwin, B. J. Kennedy, and C. J. Kepert, *Journal of the American Chemical Society* **131**, 6334 (2009).
- [7] A. L. Goodwin, D. A. Keen, M. G. Tucker, M. T. Dove, L. Peters, and J. S. O. Evans, *Journal of the American Chemical Society* **130**, 9660 (2008).
- [8] A. B. Cairns and A. L. Goodwin, *Physical Chemistry Chemical Physics* **17**, 20449 (2015).
- [9] N. C. Burtch, J. Heinen, T. D. Bennett, D. Dubbeldam, and M. D. Allendorf, *Advanced Materials* (2017).
- [10] S. M. Mirvakili and I. W. Hunter, *Advanced Materials* **29** (2017).
- [11] K. Takenaka, *Science and Technology of Advanced Materials* **13**, 013001 (2012).
- [12] W. Miller, C. Smith, D. Mackenzie, and K. Evans, *Journal of materials science* **44**, 5441 (2009).
- [13] R. Mittal, M. K. Gupta, and S. L. Chaplot, *Progress in Materials Science* **92**, 360 (2018).
- [14] D. Williams, D. Partin, F. Lincoln, J. Kouvetakis, and M. O'Keeffe, *Journal of Solid State Chemistry* **134**, 164 (1997).
- [15] A. K. David, T. D. Martin, S. O. E. John, L. G. Andrew, P. Lars, and G. T. Matthew, *Journal of Physics: Condensed Matter* **22**, 404202 (2010).
- [16] A. F. Sapnik, X. Liu, H. L. B. Boström, C. S. Coates, A. R. Overy, E. M. Reynolds, A. Tkatchenko, and A. L. Goodwin, *Journal of Solid State Chemistry* **258**, 298 (2018).
- [17] J. S. Ovens and D. B. Leznoff, *Inorganic Chemistry* **56**, 7332 (2017).
- [18] M. K. Gupta, B. Singh, R. Mittal, M. Zbiri, A. B. Cairns, A. L. Goodwin, H. Schober, and S. L. Chaplot, *Physical Review B* **96**, 214303 (2017).
- [19] K. Parlinski, *PHONON*, 2003.
- [20] G. Kresse and J. Furthmüller, *Physical Review B* **54**, 11169 (1996).
- [21] G. Kresse and J. Furthmüller, *Computational Materials Science* **6**, 15 (1996).
- [22] G. Kresse and D. Joubert, *Physical Review B* **59**, 1758 (1999).
- [23] M. Zhang, H. Xu, E. K. H. Salje, and P. J. Heaney, *Physics and Chemistry of Minerals* **30**, 457 (2003).
- [24] J. P. Perdew, K. Burke, and M. Ernzerhof, *Physical Review Letters* **77**, 3865 (1996).
- [25] J. P. Perdew, K. Burke, and M. Ernzerhof, *Physical Review Letters* **78**, 1396 (1997).

- [26] K. Jiří, R. B. David, and M. Angelos, *Journal of Physics: Condensed Matter* **22**, 022201 (2010).
- [27] J. Klimeš, D. R. Bowler, and A. Michaelides, *Physical Review B* **83**, 195131 (2011).
- [28] <http://www.cryst.ehu.es/>.

CHAPTER 6

Computational Discovery of Anomalous Lattice Behaviour in Metal Cyanide Framework, AgC_8N_5

6.1 Introduction

The understanding of atomic level mechanisms responsible for various functional properties [1-8] of materials is very important to improve their performance and for design and discovery of new materials. It is increasingly recognized that theory and computation play a key role in materials discovery [9-11]. In the recent years, there has been an astonishing increase in the availability and power of computers along with development of robust and efficient computer codes for the prediction of materials properties. This has enabled the material scientists to computationally screen the hundreds of thousands of experimentally determined crystal structures, stored in available databases, for identifying interesting properties[12].

By intuition, material should contract (or expand) on application of hydrostatic pressure (or temperature), yet a small number of crystals show opposite behaviour in a few directions. This type of anomalous behaviour with pressure (or temperature) is called negative linear compressibility (or negative thermal expansion) behavior[13]. Materials with a negative linear compressibility (NLC) and negative thermal expansion (NTE) could have interesting technological applications[13-15] in body muscle systems(as actuators), in marine optical telecommunication, components of aviation, sensors, and devices working in high pressure- temperature surroundings.

6.1.1 Structural Details

The compound AgC_8N_5 crystallizes in a body centred orthorhombic structure (*Ibca*) with a rather large unit cell containing 336 atoms. The crystal structure (Fig 6.1) of AgC_8N_5 contains the C_8N_5 planar ligands and AgN_4 tetrahedral units. Both, the planar and polyhedral units are distorted. The planar sheets of C_8N_5 are vertically placed along *c*-axis with small tilting in the *a-b* plane. These sheets are well separated along *b*-axis (distance $\approx 3 \text{ \AA}$) in *a-b* plane. Therefore, these sheets must be weakly interacting through weak dispersion interaction to make the stable structure.

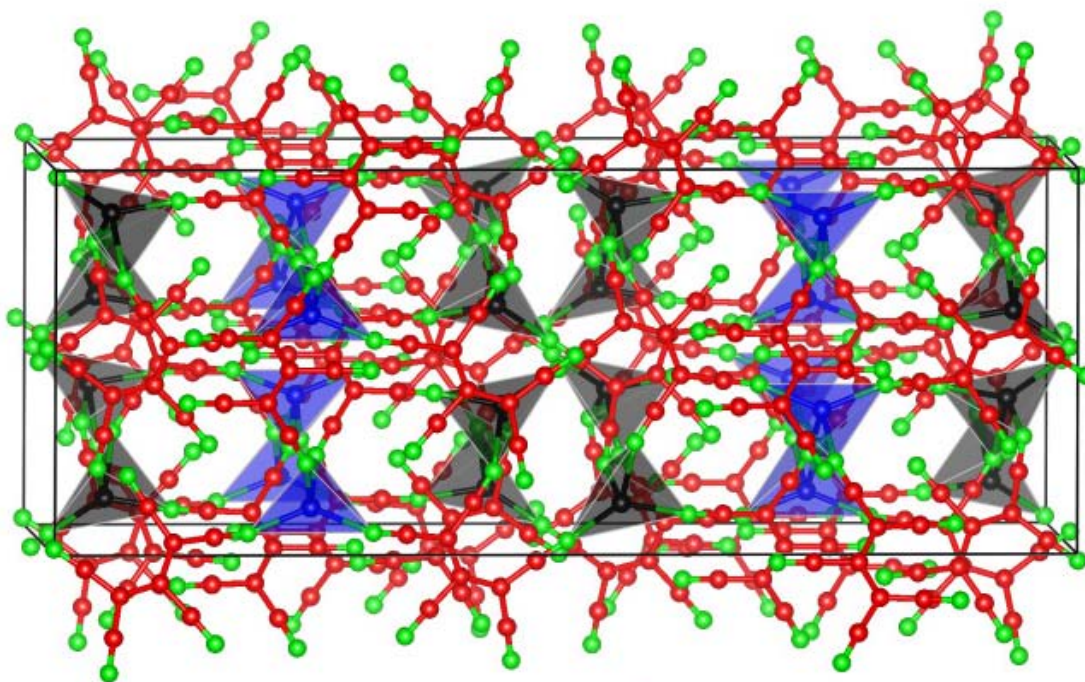


FIG 6.1 The crystal structure of AgC_8N_5 containing two types of AgN_4 (Poly-1: Black, and Poly-2: Blue) tetrahedra connected through C (Red) and N (Green) atoms.

6.1.2 Motivations and Objectives of Research

So far, few studies have been performed to realize the origin of NLC and NTE in crystalline solids[13,16]. This type of behaviour is predicted in open framework structure

with high unit cell volume per atom and low density (Table 6.1). Many cyanide based metal organic flexible framework structure [4,5,17-19] like $\text{ZnAu}_2(\text{CN})_4$, $\text{M}_3\text{Co}(\text{CN})_6$, $\text{MAuX}_2(\text{CN})_2$ where $\text{M}=\text{H}, \text{Au}, \text{Ag}, \text{Cu}$ and $\text{X}=\text{CN}, \text{Cl}, \text{Br}$ etc. show anomalous NLC and NTE behaviour. It seems that the occurrence of NLC is closely related to the NTE behaviour in these compounds[2]. Moreover, there is a very strong link between NLC, NTE and geometry of the material[3,4,8,20].

On the basis of current understanding of the mechanisms responsible for NLC, different approaches to design and fabricate new structures with NLC and NTE behaviour are being studied[21,22]. High-pressure and high-temperature X-ray and neutron diffraction techniques are used to experimentally determine the anisotropic linear compressibility and linear thermal expansion coefficients of crystalline materials[3-5,7,8,13,20,23]. However, *ab-initio* quantum mechanical calculations are well established to understand the microscopic mechanism governing these phenomena [2,16,24-26]. The compressibilities and expansion coefficients as calculated using *ab-initio* DFT and phonon calculations are found to reproduce fairly well the experimental values. These calculations, from the analysis of eigen vectors, provide the insight about the anharmonic phonon modes responsible for anomalous lattice behaviour in the material[2,24,25].

The metal organic framework compound, AgC_8N_5 has comparatively lower density[27] (Table 6.1) than its family compounds[20,25] like AgCN and AgC_4N_3 . As per our knowledge, there are no temperature/pressure dependent experimental or theoretical studies reported on this compound regarding its anomalous lattice behavior. This motivated us to study the anomalous lattice behaviour of AgC_8N_5 using *ab-initio* density functional theory calculations[28].

TABLE 6.1 The experimental unit cell volume per atom, density and linear thermal expansion coefficients (α_l) at 300 K of metal cyanides from literature. The values of α_l ($l=a, b, c$) for AgC_8N_5 are obtained from our *ab-initio* calculations.

Compound	V/atom (\AA^3)	Density (g/cm^3)	$\alpha_l \times 10^{-6} \text{ K}^{-1}$		
			α_a	α_b	α_c
AgCN[29]	13.6	4.07	66	66	-24
AgC ₄ N ₃ [20]	15.5	2.63	-48	200	-54
AgC ₈ N ₅	16.3	2.00	105	32	-98
Ag ₃ Co(CN) ₆ [3]	19.1	2.93	132	132	-130
ZnAu ₂ (CN) ₄ [4]	19.3	4.37	37	37	-58
KMnAg ₃ (CN) ₆ [23]	19.8	2.83	61	61	-60

6.2 Computational Details

The VASP simulation package [30,31] is used for the structure optimization and total energy calculations. All the calculations are performed using the projected augmented wave (PAW) formalism[32] of the Kohn-Sham density functional theory within generalized gradient approximation[33,34] (GGA) for exchange correlation following the parameterization by Perdew, Becke and Ernzerhof. The kinetic energy cutoff of 900 eV is adapted for plane wave pseudo-potential. A k-point sampling with a grid of $2 \times 2 \times 1$, generated automatically using the Monkhorst-Pack method[35], is used for structure optimizations. The above parameters were found to be sufficient to obtain a total energy convergence of less than 0.1 meV for the fully relaxed (lattice constants & atomic positions) geometries. The total energy is minimized with respect to structural parameters. The compound AgC_8N_5 crystallizes in a body centred orthorhombic structure (*Ibca*) with a rather large unit cell containing 336 atoms. The calculation of zone centre phonon modes in conventional unit cell of 336 atoms has been performed using linear response density functional perturbation theory (DFPT).

Ab-initio molecular dynamical simulations are performed in Parrinello-Rahman[36,37] (NPT) dynamics with a Langevin thermostat[38] to obtain the thermal expansion behavior of the compound. Newton's equations of motion are integrated using Verlet's algorithm with a time step of 1 fs. A unit cell of 336 atoms subject to the periodic boundary conditions is used. Temperature dependence is obtained by averaging every 500 steps of the ramp run to get single data point. The temperature stability is maintained with a friction coefficient of 10 ps^{-1} for all atoms. A mass of 20 *amu* and a friction coefficient of 10 ps^{-1} were used for the extra degree of freedom coupled with the lattice degrees of freedom.

TABLE 6.2 *The comparison of calculated and experimental lattice parameters in AgC_8N_5 .*

Optimization Scheme	a (Å)	b (Å)	c (Å)	V (Å ³)
DFT-GGA (0K)	12.46	15.91	32.27	6392
DFT-GGA+ vdW (0K)	12.26	13.25	32.61	5297
Experimental (300K)	12.43	13.62	32.30	5466

6.3 Results and Discussions

The structure optimizations done without considering these weak interactions is found to highly overestimate (Table 6.2) the *b*-lattice parameters. However, when van der Waals interactions are considered between these planar sheets the calculated structure is found to match with the experimental structure[27], within the limitations of GGA (Table 6.2). It seems van der Waals interactions play a very important role in governing the structure stability of AgC_8N_5 . The weak dispersion interactions acting in *a-b* plane (especially along *b*-axis) make the structure flexible in *a-b* plane as compared to that

along *c*-axis. The structure with presence of van der Waals dispersion interactions is considered for all further calculations.

6.3.1 Elastic Properties and Born Stability Criteria

The elastic constants of AgC₈N₅ are derived from the strain-stress relationships obtained from finite distortions of the equilibrium lattice. For small deformations we remain in the elastic domain of the solid and a quadratic dependence of the total energy with respect to the strain is expected (Hooke's law). Three tensile and three shear strains are manually applied to the crystal structure of AgC₈N₅ and corresponding stress components of final relaxed structure are calculated. The ratio of stress and corresponding strains are used to calculate the elastic constant matrix. The number of components of elastic constant tensor is related to the symmetry of the crystal phase. Nine different components (in GPa units), obtained for the present structure are given below:

$$\begin{pmatrix} 20.6 & 12.8 & 25.3 & 0 & 0 & 0 \\ 12.8 & 15.1 & 13.9 & 0 & 0 & 0 \\ 25.3 & 13.9 & 64.0 & 0 & 0 & 0 \\ 0 & 0 & 0 & 2.3 & 0 & 0 \\ 0 & 0 & 0 & 0 & 4.9 & 0 \\ 0 & 0 & 0 & 0 & 0 & 4.9 \end{pmatrix}$$

For a crystalline solid, to be stable in any conditions, all the phonon frequencies must be positive and the Born elastic stability criteria must be fulfilled. The Born stability criteria demand the elastic constant matrix to be positive definite which give rise to following simplified expressions for orthorhombic structures[39]

$$C_{11} > 0, C_{11}C_{22} > C_{12}^2, C_{44} > 0, C_{55} > 0, C_{66} > 0$$

$$C_{11}C_{22}C_{33} + 2C_{12}C_{13}C_{23} - C_{11}C_{23}^2 - C_{22}C_{13}^2 - C_{33}C_{12}^2 > 0$$

The above stability criteria are found to be satisfied at ambient pressure. Thus, the structure is elastically and dynamically stable at ambient pressure conditions. The elastic

constants are used to get the Bulk modulus and elastic compliance matrix, $S=C^{-1}$ (in 10^{-3} GPa $^{-1}$ units) as:

$$\begin{pmatrix} 162.95 & -99.12 & -42.81 & 0 & 0 & 0 \\ -99.12 & 143.22 & 7.97 & 0 & 0 & 0 \\ -42.81 & 7.97 & 30.81 & 0 & 0 & 0 \\ 0 & 0 & 0 & 435.16 & 0 & 0 \\ 0 & 0 & 0 & 0 & 202.80 & 0 \\ 0 & 0 & 0 & 0 & 0 & 203.79 \end{pmatrix}$$

For negative compressibility along the crystallographic axes[40], in an orthorhombic crystal, the following inequalities should hold

$$X_a=S_{11} + S_{12} + S_{13}<0, X_b=S_{12} + S_{22} + S_{23}<0 \ \& \ X_c=S_{13} + S_{23} + S_{33}<0$$

Where X_i ($i=a, b, c$) are the compressibilities of crystal along various crystallographic axes. It is observed that only the last inequality holds, implying that compound exhibits negative linear compressibility along the c-axis.

6.3.2 High Pressure Behaviour

To quantify NLC behaviour of AgC_8N_5 , the crystal structure is relaxed under application of isotropic pressures and corresponding lattice parameters are calculated. The calculated lattice parameters as a function of pressure are shown in Fig 6.2. It is observed that the lattice parameters ‘a’ and ‘b’ decrease with increasing pressure and show normal behavior. The ‘b’ lattice parameter shows a larger decrease as compared to ‘a’ lattice parameter. This arises from the soft nature of van der Waals dispersion interaction acting among the planar sheets of C_8N_5 along b-axis. However, the ‘c’ lattice parameter shows an increase with increasing pressure. This confirms the negative linear compressibility along the c-axis.

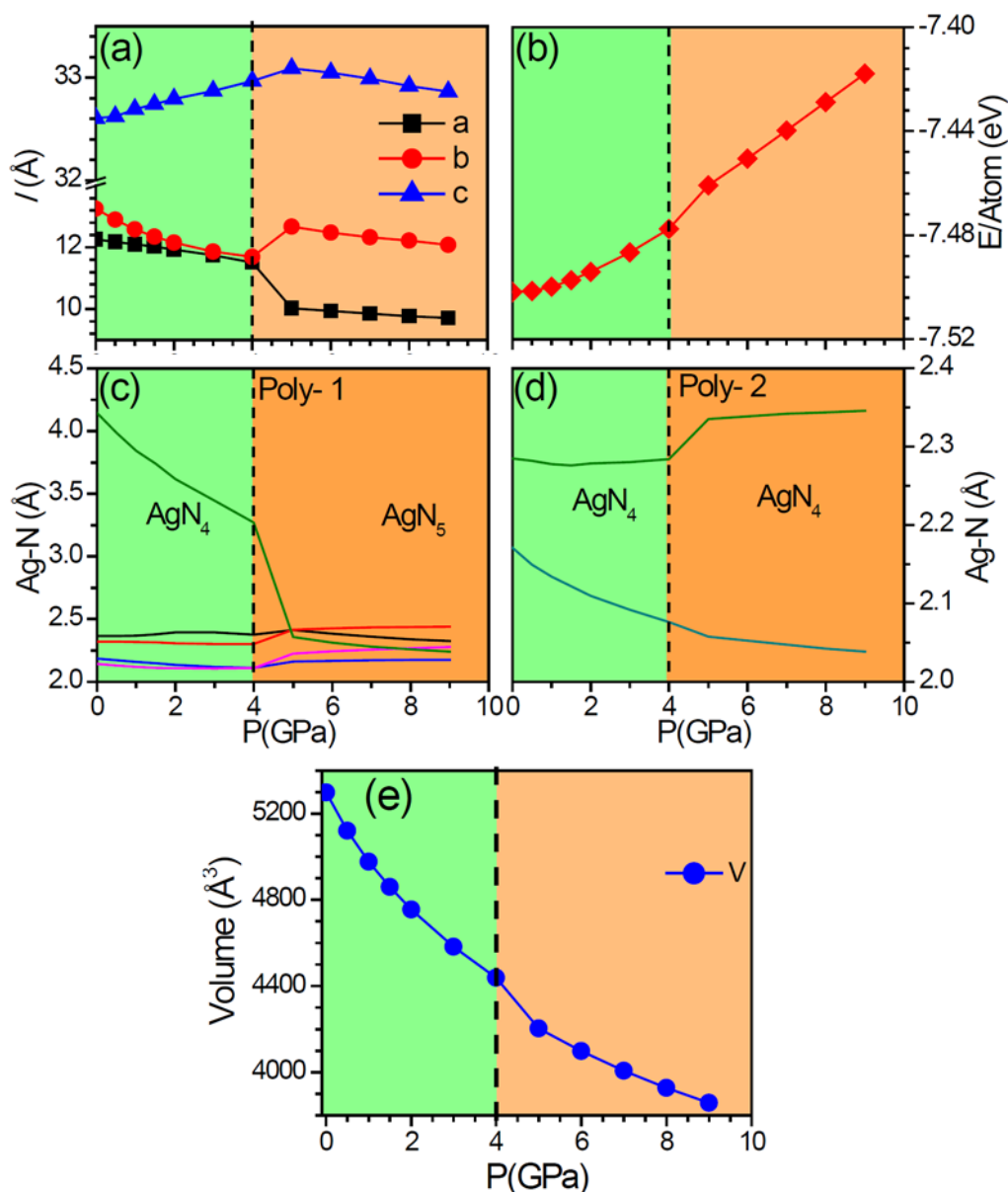


FIG 6.2 The calculated pressure dependence of lattice parameters (l), unit cell volume, bond lengths and total energy/atom for AgC_8N_5 .

Overall volume is found to decrease with increase in pressure. Bulk modulus is calculated from the pressure dependence of unit cell volume. The PV equation of state is fitted with the well-known Birch–Murnaghan (2nd ordered) isothermal equation of state to get the value of bulk modulus. The calculated bulk modulus using this approach has the value of 14.5GPa. This is consistent with that calculated from the elastic compliance

(14.48 GPa) matrix. At ambient pressure, the calculated linear compressibilities are found to have the values of $X_a=21.0 \times 10^{-3}$, $X_b=52.1 \times 10^{-3}$ and $X_c=-4.0 \times 10^{-3} \text{ GPa}^{-1}$.

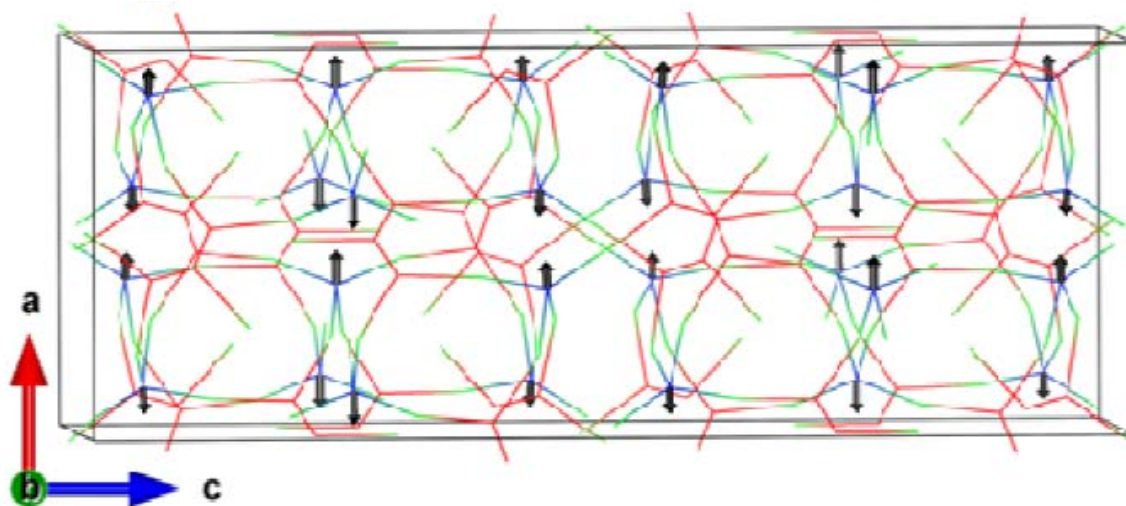


FIG 6.3 The calculated displacement pattern giving rise to negative linear compressibility along c -axis of AgC_8N_5 . The arrow represents the displacement vector for Ag as obtained from the difference in atomic coordinates of all the atoms corresponding to ambient pressure and 4 GPa structure.

We observe that atomic coordinates of Ag atoms show major change on application of pressure. The displacement corresponding to this change is indicated as vectors in Fig 6.3. The displacement vector shows that the Ag atoms displace along the a -axis of the crystal. Further we found significant displacement of $\text{C}\equiv\text{N}$ unit, as a single rigid unit, attached to the corresponding Ag atoms. We found that $\text{C}\equiv\text{N}$ units only connected to Ag atoms are displaced in the a - b plane. Therefore, a hinging movement of rigid $\text{C}\equiv\text{N}$ units occurs about Ag atoms. On application of pressure, this gives rise to an expansion of the framework along c -axis and contraction in a - b plane.

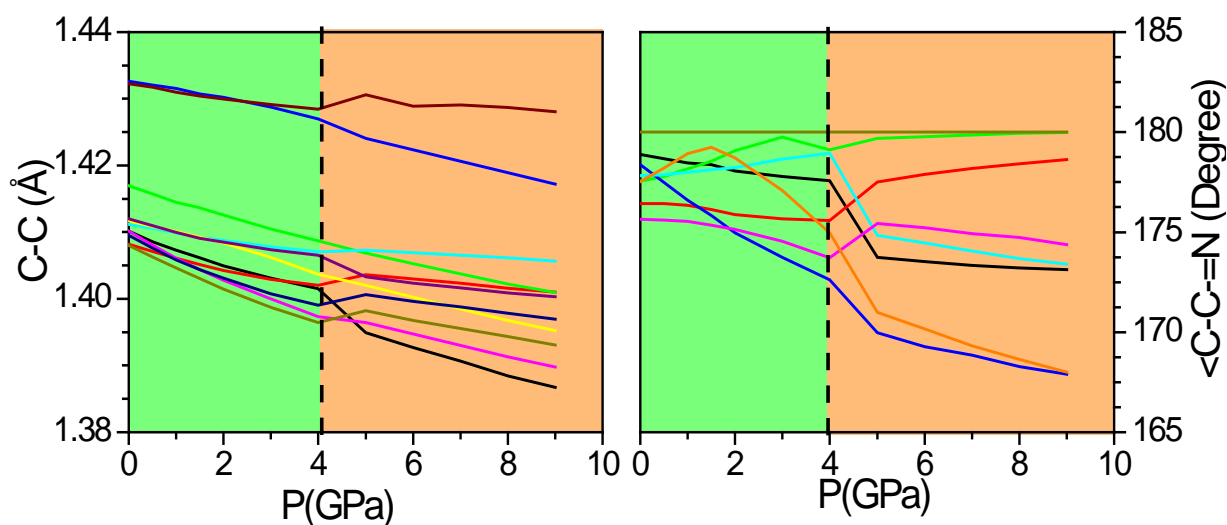


FIG 6.4 The calculated pressure dependence of bond length (C-C) and bond angles (\angle C-C=N) of hard building block (C_8N_5) planer unit in AgC_8N_5 .

As pressure increases above 4GPa, the structure undergoes an unusual change. Around this pressure there are sudden jumps in lattice parameters, total energy and bond lengths of the compound (Fig 6.2). A sudden decrease in volume (Fig 6.2 (e)) gives a signature of some high pressure phase transition which could also be amorphization or decomposition. However, detailed high-pressure diffraction would be needed to identify the resultant structure of the new phase. We found an anomalous change in the Ag atomic coordinate at this pressure. There are two different types of AgN_4 polyhedral units (Poly-1 and Poly-2) corresponding to the two different types of Wyckoff sites of Ag atoms present in this compound. Fig 6.2(c) and 6.2(d) show the pressure dependence of Ag-N bond lengths in the two polyhedral units. Poly-1 has four different values of Ag-N bonds lengths, while poly-2 has only two different bond lengths. The bonds which lie in the a - b plane of the crystal show very little pressure dependence. These bonds are strained very little with increase in pressure due to movement of Ag atoms in the a - b plane. However, large strain is developed in these bonds above 4.0 GPa, which results in the abrupt

changes in these bonds at the phase transition (or dissociation/amorphization). Above 4.0 GPa, AgN_4 tetrahedra (Fig 6.2(c)) change the coordination and convert to AgN_5 .

The calculated structure as a function of pressure shows that the $\text{C}\equiv\text{N}$ bond remains unchanged with a value of about 1.16 Å. Moreover, various C-C bonds (Fig 6.4) in $-\text{C}_8\text{N}_5-$ planar units do not show any significant changes (less than 1-2 %) with increase in pressure. The Ag-N bonds of AgN_4 tetrahedral units show (Fig 6.2) a variation of 5-6 %. This change would be due to the flexible nature of Ag-N bonds. There are significant changes (up to 6% of original bond angle) in the C-C \equiv N bond angle (Fig 6.4) present on the periphery of C_8N_5 structural units. To understand these structural changes and the mechanism for negative and positive linear compressibility along c- axis and in the a-b plane respectively, we have calculated the difference in atomic coordinates of all the atoms corresponding to ambient pressure structure and 4GPa structure.

6.3.3 Total and Partial Phonon Density of States

The primitive unit cell of AgC_8N_5 contains 168 atoms and has 504 phonon modes of vibrations. The calculation of complete phonon spectra in the entire Brillouin zone is computationally expensive for such a large system. We have calculated the zone centre phonon spectra in conventional unit cell with 336 atoms using linear response density functional perturbation theory (DFPT). These 1008 phonons at the zone- centre of the conventional unit cell correspond to 504 phonons each at the zone- centre and the (111) zone- boundary point of the Brillouin zone of the body centred orthorhombic structure. Leaving 3 acoustic branches, we have calculated the phonon spectrum for 1005 phonon modes. The calculated partial density of states of C, N and Ag atoms show that these atoms contribute in different energy regions (Fig 6.5) of the spectra. The very high energy

peaks around 270 meV in the spectra of C and N is related to the vibrational stretching modes associated with very strong $C\equiv N$ bonds.

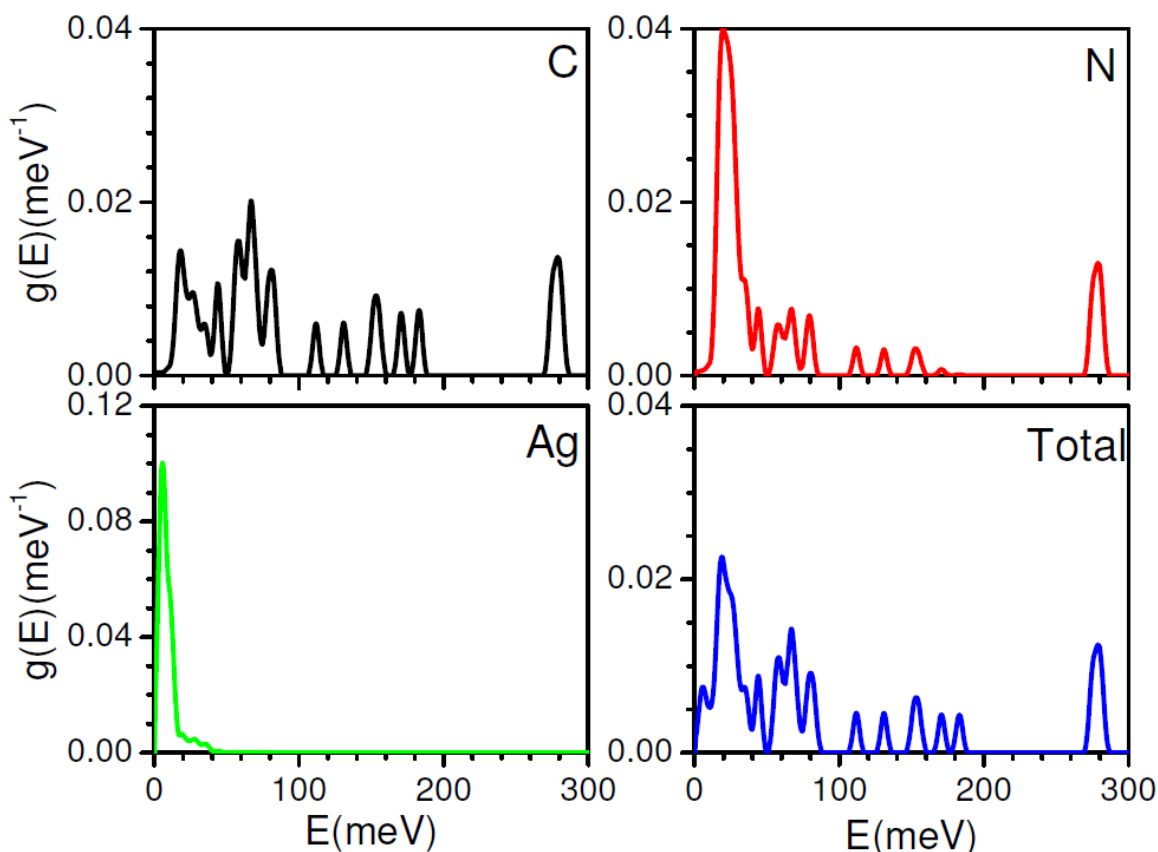


FIG 6.5 The calculated total and partial phonon density of states for various atoms of AgC_8N_5 .

The spectra in the 100-200meV range is highly contributed by C atoms and is related to stretching vibrations of strong C-C bonds in the $-C_8N_5$ -planar structural units. The lower energy modes in spectra of C and N atoms are associated with bending vibrations of constructing $-C_8N_5$ -units. It is interesting to note that the Ag atoms only contribute to the vibrational spectra in very low energy upto 40 meV. Hence, the vibrational modes associated with Ag atoms would be populated at low temperatures and would give rise to interesting structural and dynamical properties. This also confirms, on

application of pressure, the dominant role of Ag in giving rise to NLC and phase transition in AgC_8N_5 .

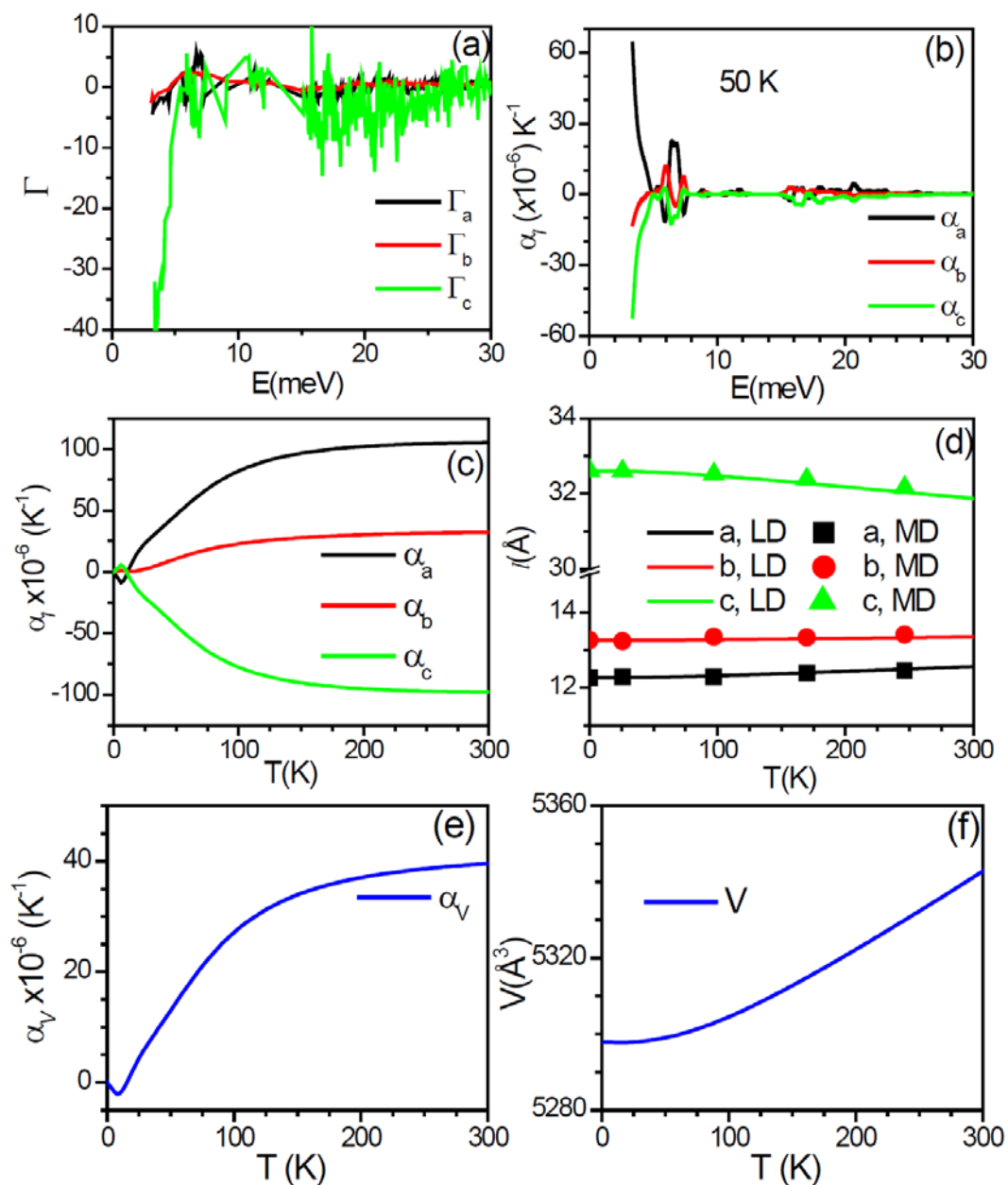


FIG 6.6 (a) The calculated energy dependence of anisotropic Grüneisen parameters, Γ for AgC_8N_5 . (b) The contribution of phonon mode of energy E to the linear thermal expansion coefficients. (c,e) The calculated temperature dependence of linear and volume thermal expansion coefficients respectively (d, f) The calculated temperature dependence of lattice parameters and unit cell volume respectively.

6.3.4 Anisotropic Thermal Expansion Behaviour

The stress dependence of phonon energies is used for the calculation of anisotropic Grüneisen parameters of AgC_8N_5 . An anisotropic stress of 5 kbar is implemented by changing only one of the lattice constants and keeping the others fixed. The calculated mode Grüneisen parameters as a function of phonon energy along different crystal directions are shown in Fig 6.6(a). The Grüneisen parameters along a and b axes show normal positive behavior. However, the Grüneisen parameters along c -axis have large negative values. The calculated anisotropic Grüneisen parameters and elastic compliance matrix are used to calculate the anisotropic thermal expansion coefficient. The calculated temperature dependence of anisotropic thermal expansion coefficients and lattice parameters are shown in Fig 6.6 (c,d). Negative thermal expansion is found along c -axis while positive along a and b axes. The change with temperature along a -axis is more pronounced than that along b -axis. This is contrary to the calculated behavior as a function of pressure. The volume shows normal positive thermal expansion behaviour. The quantitative thermal expansion behavior is obtained from the calculated temperature dependence of linear thermal expansion coefficients (Fig 6.6).

At 300K, the values of linear and volume thermal expansion coefficient are found to be $\alpha_a=105.4\times 10^{-6} \text{ K}^{-1}$, $\alpha_b=32.3\times 10^{-6} \text{ K}^{-1}$, $\alpha_c=-98.1\times 10^{-6} \text{ K}^{-1}$ and $\alpha_v=39.6\times 10^{-6} \text{ K}^{-1}$ respectively. These values are comparable to those reported for the highly anomalous thermal expansion cyanides[3,7,20] like AgC_4N_3 , $\text{Ag}_3\text{Co}(\text{CN})_6$, $\text{ZnAu}_2(\text{CN})_4$ etc. The quasi-harmonic approximations has been proven very good for studying the NTE materials like[2,16,25,26] LiAlSiO_4 , V_2O_5 , MCN ($\text{M}=\text{Ag}$, Au , Cu), ZrW_2O_8 , $\text{Ag}_3\text{Co}(\text{CN})_6$, and $\text{ZnAu}_2(\text{CN})_4$. The available data in the literature show[3-5,7,20] that the compounds exhibiting NLC along a certain crystallographic axis also show the NTE along

the same axis. However, the reverse is not always true[2,25,41-44]. Therefore, it seems that NLC drives NTE, although there is no specific thermodynamic relation connecting NLC and NTE.

Thermal expansion behavior is a consequence of anharmonicity of crystal potential energy. The anharmonicity of phonons arises due to implicit as well as explicit contributions. The implicit anharmonicity arises from the volume dependence of bond lengths and is implemented via quasiharmonic lattice dynamics (LD) calculations. On the other hand, the explicit anharmonicity arises from the temperature dependent thermal amplitudes of atoms. Both the explicit and the implicit parts are implemented in molecular dynamics simulations. The explicit contribution is found to give significant contribution in a few compounds[26,45-47]. Therefore, we have calculated the temperature dependence of lattice parameters using *ab-initio* molecular dynamical (MD) simulations (Fig 6.6 (c)). These calculations reproduce the anomalous thermal expansion behavior as calculated from the quasi-harmonic lattice dynamics (LD). The very good agreement between LD and MD results for thermal expansion behavior suggest that the contribution from the explicit part is insignificant in this compound.

6.3.5 Mechanism of Negative Thermal Expansion

In order to understand the mechanism of anomalous thermal expansion behavior in AgC_8N_5 , we have calculated the contribution of individual phonon modes to the linear thermal expansion coefficients (Fig 6.6(b)). It is observed that the low energy phonon modes around 5 meV are responsible for the observed negative thermal expansion along *c*-axis and positive thermal expansion along *a*- and *b*-axis. These modes show highly anisotropic Grüneisen parameters (Fig 6.6 (a)). The calculated phonon spectra show

(Fig 6.5) that the low energy phonon modes have large contributions from Ag atoms in comparison to C and N atoms.

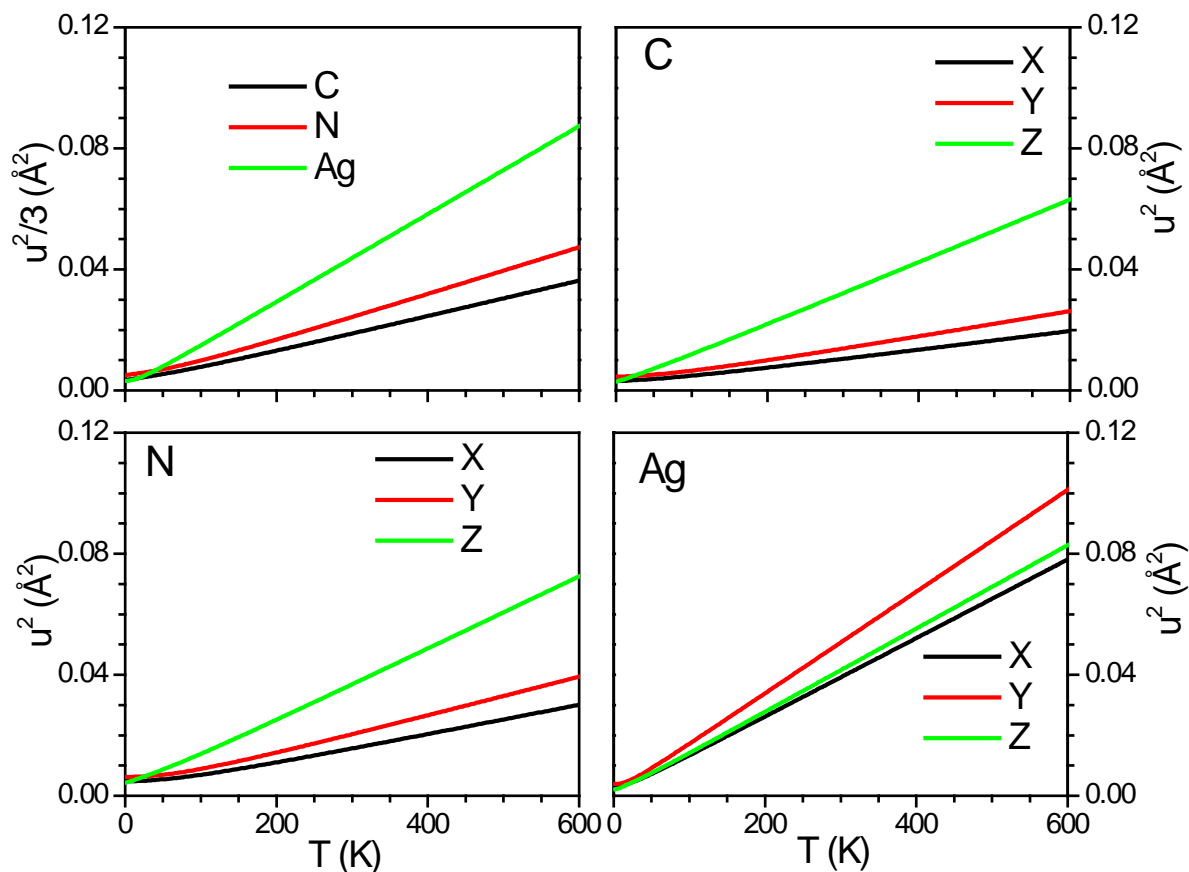


FIG 6.7 The calculated total and anisotropic mean square displacements for various atoms as a function of temperature for AgC₈N₅.

The calculated MSD of various atoms as a function of temperature are shown in Fig 6.7. Ag atom has higher total MSD values than C and N atoms. The anisotropic MSD shows that the C and N atoms have easier movement along *c*-axis in comparison to that in *a-b* plane, and it further enhances with rise in temperature. However, Ag atoms show almost isotropic MSD as a function of temperature. The contribution to the anisotropic and total mean square displacements due to phonons of energy *E* for various atoms has been calculated (Fig 6.8). It is clear from the plot that the phonon modes in the energy

range 3-8 meV involve the dominant Ag dynamics in the a - b plane while the dynamics of C and N atoms are negligible in these modes.

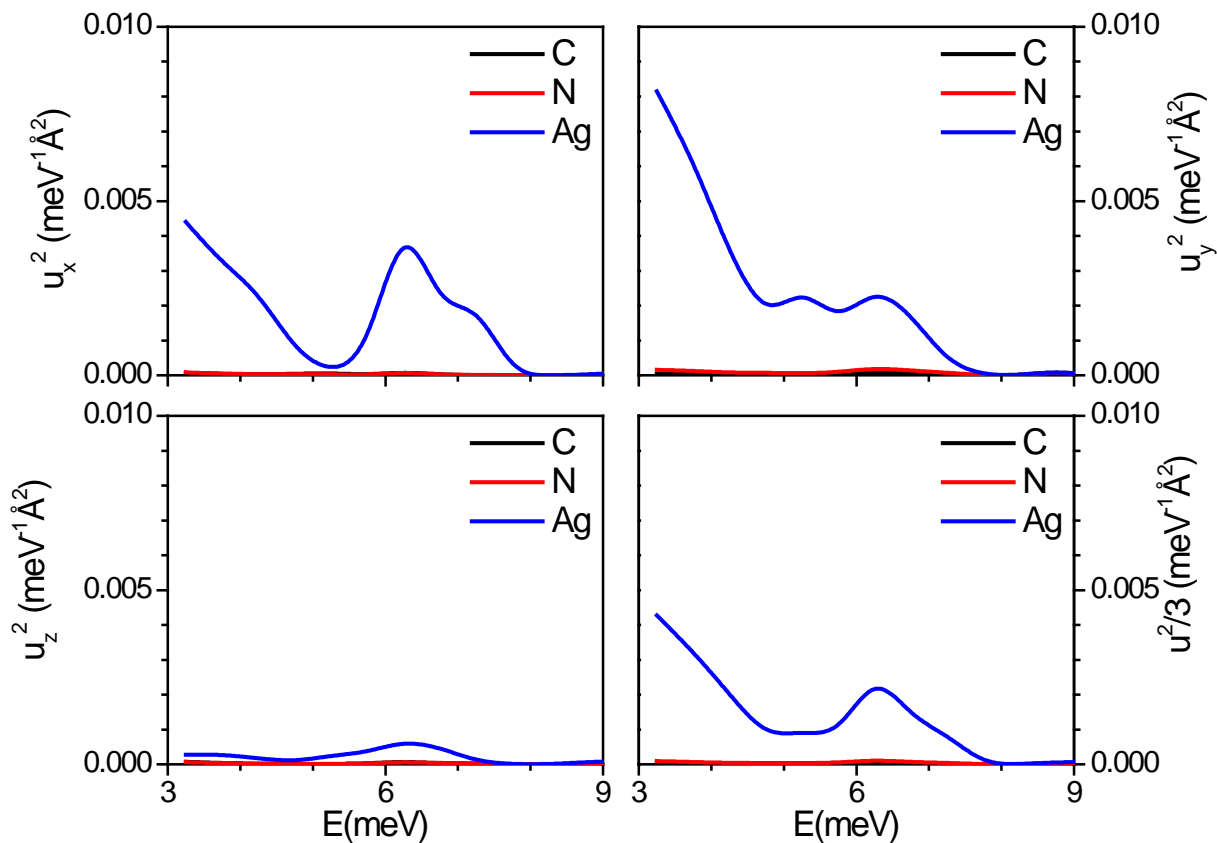


FIG 6.8 The calculated anisotropic and total mean square displacements for various atoms as a function of phonon energy for AgC_8N_5 .

The contribution of phonons of low energies to mean square displacements (MSD) of Ag is highly anisotropic with large values in a - b plane (Fig 6.8), while N/C has almost negligible contributions which confirm the criticality of Ag motion to negative thermal expansion along c -axis of AgC_8N_5 . The displacement patterns of two modes with energy 3.34 meV and 5.32 meV are shown in Fig 6.9. The low energy phonon modes have dominant contributions from the Ag atoms. These two modes (assuming them as Einstein modes with one degree of freedom each) gives the linear thermal expansion of $\alpha_a=4.3 \times 10^{-6} \text{K}^{-1}$, $\alpha_b=-1.0 \times 10^{-6} \text{K}^{-1}$, $\alpha_c=-3.1 \times 10^{-6} \text{K}^{-1}$ and $\alpha_a=0.3 \times 10^{-6} \text{K}^{-1}$, $\alpha_b=0.4 \times 10^{-6} \text{K}^{-1}$, $\alpha_c=-0.2 \times 10^{-6}$

K^{-1} at 300K respectively. The mode at 3.34 meV involves the rotation of Ag atoms around the connecting $-\text{C}_8\text{N}_5-$ structural units in the a - b plane. On the other hand, the mode at 5.32 meV involves displacement of Ag atoms along b -axis. The motion of Ag produces effect of a closing hinge exactly opposite to that observed on application of pressure. This gives rise to contraction along the c -axis and expansion along a and b -axis.

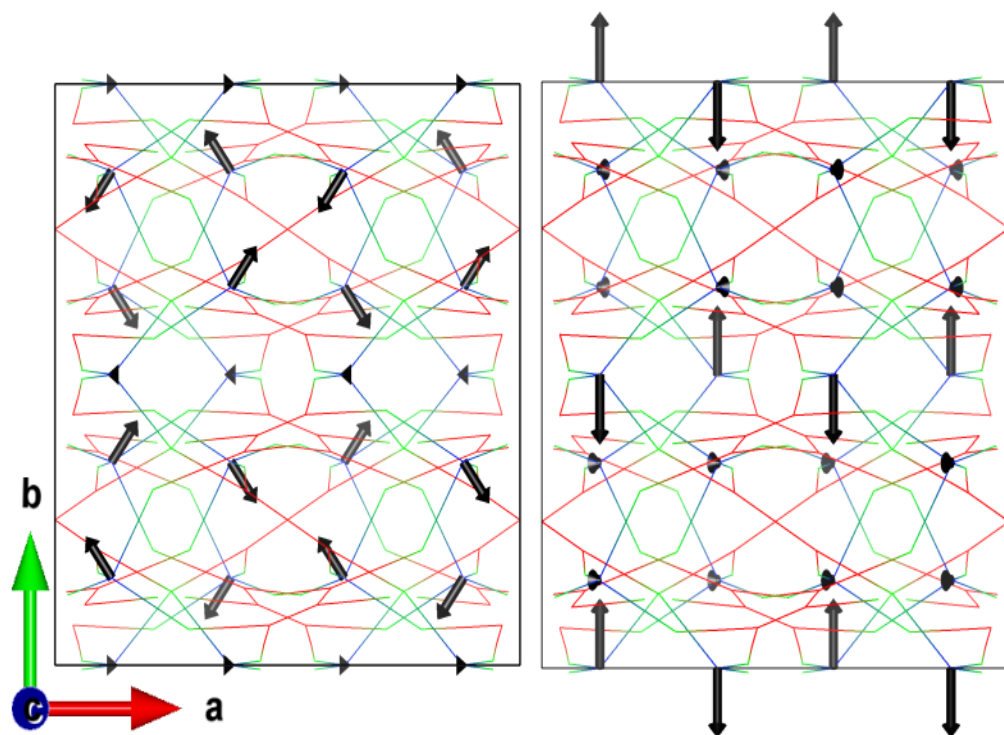


FIG 6.9 The displacement pattern of optic phonon modes projected in a - b plane of AgC_8N_5 . The arrow represents the displacement vector for Ag atoms. The displacement vectors for C and N atoms are negligible and are not shown for clarity.

6.4 Conclusions

In conclusion, our *ab-initio* DFT calculations reveal large anomalous lattice behaviour in AgC_8N_5 , which is a metal organic framework material with very low crystal density. Extensive calculations as a function of pressure reveal negative linear

compressibility along the c -axis. Moreover, the pressure dependent phonon calculations performed using linear response density functional perturbation theory methods show anomalous thermal expansion behaviour in this compound. The temperature dependence of lattice parameters with (MD) and without (LD) explicit anharmonic effects agrees very well. The NLC and NTE along c -axis of the structure are governed by the dominant dynamics of Ag atoms in a - b plane which give rise to hinge-like mechanism. The compound AgC_8N_5 may be very useful for strong armour applications due to its anomalous lattice behaviour.

References

- [1] F. Bridges, T. Keiber, P. Juhas, S. J. L. Billinge, L. Sutton, J. Wilde, and G. R. Kowach, *Physical Review Letters* **112**, 045505 (2014).
- [2] M. K. Gupta, B. Singh, R. Mittal, M. Zbiri, A. B. Cairns, A. L. Goodwin, H. Schober, and S. L. Chaplot, *Physical Review B* **96**, 214303 (2017).
- [3] A. L. Goodwin, M. Calleja, M. J. Conterio, M. T. Dove, J. S. O. Evans, D. A. Keen, L. Peters, and M. G. Tucker, *Science* **319**, 794 (2008).
- [4] A. B. Cairns *et al.*, *Nature Materials* **12**, 212 (2013).
- [5] A. L. Goodwin, D. A. Keen, and M. G. Tucker, *Proceedings of the National Academy of Sciences* **105**, 18708 (2008).
- [6] J. C. Michael, L. G. Andrew, G. T. Matthew, A. K. David, T. D. Martin, P. Lars, and S. O. E. John, *Journal of Physics: Condensed Matter* **20**, 255225 (2008).
- [7] A. L. Goodwin, B. J. Kennedy, and C. J. Kepert, *Journal of the American Chemical Society* **131**, 6334 (2009).
- [8] A. L. Goodwin, D. A. Keen, M. G. Tucker, M. T. Dove, L. Peters, and J. S. O. Evans, *Journal of the American Chemical Society* **130**, 9660 (2008).
- [9] L.-Q. Chen, L.-D. Chen, S. V. Kalinin, G. Klimeck, S. K. Kumar, J. Neugebauer, and I. Terasaki, *npj Computational Materials* **1**, 15007 (2015).
- [10] D. P. Tabor *et al.*, *Nature Reviews Materials* **3**, 5 (2018).
- [11] M. Asta, *JOM* **66**, 364 (2014).
- [12] S. Curtarolo, G. L. W. Hart, M. B. Nardelli, N. Mingo, S. Sanvito, and O. Levy, *Nature Materials* **12**, 191 (2013).
- [13] A. B. Cairns and A. L. Goodwin, *Physical Chemistry Chemical Physics* **17**, 20449 (2015).
- [14] N. C. Burtch, J. Heinen, T. D. Bennett, D. Dubbeldam, and M. D. Allendorf, *Advanced Materials* (2017).
- [15] S. M. Mirvakili and I. W. Hunter, *Advanced Materials* **29** (2017).
- [16] R. Mittal, M. K. Gupta, and S. L. Chaplot, *Progress in Materials Science* **92**, 360 (2018).
- [17] A. K. David, T. D. Martin, S. O. E. John, L. G. Andrew, P. Lars, and G. T. Matthew, *Journal of Physics: Condensed Matter* **22**, 404202 (2010).
- [18] A. F. Sapanik, X. Liu, H. L. B. Boström, C. S. Coates, A. R. Overy, E. M. Reynolds, A. Tkatchenko, and A. L. Goodwin, *Journal of Solid State Chemistry* **258**, 298 (2018).
- [19] J. S. Ovens and D. B. Leznoff, *Inorganic Chemistry* **56**, 7332 (2017).
- [20] S. A. Hodgson, J. Adamson, S. J. Hunt, M. J. Cliffe, A. B. Cairns, A. L. Thompson, M. G. Tucker, N. P. Funnell, and A. L. Goodwin, *Chemical Communications* **50**, 5264 (2014).
- [21] A. Ghaedizadeh, J. Shen, X. Ren, and Y. M. Xie, *Materials & Design* **131**, 343 (2017).
- [22] K. K. Dudek, D. Attard, R. Caruana-Gauci, K. W. Wojciechowski, and J. N. Grima, *Smart Materials and Structures* **25**, 025009 (2016).

- [23] A. B. Cairns, A. L. Thompson, M. G. Tucker, J. Haines, and A. L. Goodwin, *Journal of the American Chemical Society* **134**, 4454 (2012).
- [24] B. Singh, M. K. Gupta, S. K. Mishra, R. Mittal, P. U. Sastry, S. Rols, and S. L. Chaplot, *Physical Chemistry Chemical Physics* **19**, 17967 (2017).
- [25] M. K. Gupta, B. Singh, R. Mittal, S. Rols, and S. L. Chaplot, *Physical Review B* **93**, 134307 (2016).
- [26] M. K. Gupta, R. Mittal, and S. L. Chaplot, *Physical Review B* **88**, 014303 (2013).
- [27] L. Jäger, C. Wagner, and W. Hanke, *Journal of Molecular Structure* **525**, 107 (2000).
- [28] B. Singh, M. K. Gupta, R. Mittal, and S. L. Chaplot, *The Journal of Physical Chemistry C* (2018).
- [29] S. J. Hibble, G. B. Wood, E. J. Bilbé, A. H. Pohl, M. G. Tucker, A. C. Hannon, and A. M. Chippindale, *Zeitschrift für Kristallographie Crystalline Materials* **225**, 457 (2010).
- [30] G. Kresse and J. Furthmüller, *Computational Materials Science* **6**, 15 (1996).
- [31] G. Kresse and J. Furthmüller, *Physical Review B* **54**, 11169 (1996).
- [32] P. E. Blöchl, *Physical Review B* **50**, 17953 (1994).
- [33] K. Burke, J. Perdew, and M. Ernzerhof, *Physical Review Letters* **78**, 1396 (1997).
- [34] J. P. Perdew, K. Burke, and M. Ernzerhof, *Physical Review Letters* **77**, 3865 (1996).
- [35] H. J. Monkhorst and J. D. Pack, *Physical Review B* **13**, 5188 (1976).
- [36] M. Parrinello and A. Rahman, *Physical Review Letters* **45**, 1196 (1980).
- [37] M. Parrinello and A. Rahman, *Journal of Applied Physics* **52**, 7182 (1981).
- [38] M. P. Allen and D. J. Tildesley, *Computer Simulation of Liquids* (Oxford university press, 2017).
- [39] F. Mouhat and F.-X. Coudert, *Physical Review B* **90**, 224104 (2014).
- [40] C. N. Weng, K. T. Wang, and T. Chen, *Advanced Materials Research* **33-37**, 807 (2008).
- [41] Y. Chen, S. Manna, B. Narayanan, Z. Wang, I. E. Reimanis, and C. V. Ciobanu, *Scripta Materialia* **122**, 64 (2016).
- [42] S. K. Mishra *et al.*, *Journal of Physics: Condensed Matter* **28**, 045402 (2016).
- [43] A. B. Cairns, M. J. Cliffe, J. A. Paddison, D. Daisenberger, M. G. Tucker, F.-X. Coudert, and A. L. Goodwin, *Nature Chemistry* **8**, 442 (2016).
- [44] K. W. Chapman and P. J. Chupas, *Journal of the American Chemical Society* **129**, 10090 (2007).
- [45] P. Lazar, T. Bučko, and J. Hafner, *Physical Review B* **92**, 224302 (2015).
- [46] G. Ernst, C. Broholm, G. R. Kowach, and A. P. Ramirez, *Nature* **396**, 147 (1998).
- [47] S. L. Chaplot, R. Mittal, and N. Choudhury, *Thermodynamic Properties of Solids: Experiments and Modeling* (John Wiley & Sons, 2010).

CHAPTER 7

Negative Thermal Expansion in Polyhedral Framework Connected via Terminal Atoms

7.1 Introduction

The magnitude and anisotropy of negative thermal expansion (NTE) of a compound depends upon its structural framework and bonding. The compounds ZrW_2O_8 [1-4], ScF_3 [5-9] and $Cd(CN)_2$ [10] are a few well known materials which show isotropic negative thermal expansion behaviour. The compounds like $LiAlSiO_4$ [11], $Ag_3Co(CN)_6$ [12], $KMn[Ag(CN)_2]_3$ [13], $ZnAu_2(CN)_4$ [14,15], and MCN ($M=Ag, Au, Cu$) [16] show anisotropic thermal expansion, where one of the direction shows NTE behaviour. Most of these compounds consist of polyhedral units, and NTE arises due to cooperative rotation and deformation of these polyhedral units collapsing open spaces in the lattice [17]. In this chapter, the mechanism of NTE behaviour in $MZrF_6$ ($M=Mg, Ca, Sr$) and Ih phase of ice are studied [18,19]. The polyhedral units, in both compounds, are connected via terminal atoms, which give flexibility of polyhedral rotations and deformations. In case of $MZrF_6$, the bonding of terminal Fluorine atom is quite strong (covalent) with Zr atom of corresponding polyhedral units (ZrF_6) and comparatively weak (with partial ionic character) with M (Mg, Ca, Sr) atoms [20]. On the other hand, the bonding of terminal hydrogen or deuterium to the central atom (oxygen) of polyhedral unit (trigonal planar) is very strong (covalent bond) within one polyhedral and very weak (hydrogen bond) within the other polyhedral unit [21]. Therefore, it is interesting to study the mechanism of NTE behaviour in these structurally and bindingly different classes of compounds.

7.2 Metal Fluorides, $MZrF_6$ (M=Mg, Ca, Sr)

For application of a NTE material, it has to be stable under conditions of use and amenable to the fabrication of composite or bulk component. The main drawback of metal organic framework (MOF) including cyanide bridges framework NTE materials is that they are not easy to process into ceramic bodies. They are highly hygroscopic in nature, which reduces their coefficient of NTE; hence are not suitable for ambient environment applications. The discovery of large NTE in fluoride based compounds opens the way to overcome this problem to certain extent.

Most of the fluorides with ReO_3 structure show NTE behaviour in their high temperature cubic phase, while at low temperature the compounds transform to a lower symmetry (rhombohedral) structure. It has been observed that in the lower symmetry phase, NTE is either reduced or absent. This might be due to phonon softening along R-M direction in the Brillouin zone which is observed in the cubic phase and absent in the low temperature phase. A large NTE behaviour has been reported in cubic ScF_3 . This compound is found to remain in the cubic phase down to 0.4 K [22]. It has been shown [9] that at low temperature and high pressure of about 0.2 GPa, the compound shows structural transition. The structural phase transition kills NTE behaviour in this compound. The much large electro-negativity of F in M--F as compared to that of O in M--O leads to highly ionic character of bonding in these compounds and enhances their flexibility [23]. The difference in the nature of bonding also significantly changes the thermo-physical properties in these compounds.

$M^{II}Zr^{IV}F_6$ (M=Ca, Mg, etc), which resemble ReO_3 structure, are found to show a wide diversity in thermal expansion behaviour, i.e. from large negative expansion to large positive expansion [20,24-26]. The studies show that in $MZrF_6$ series the thermal

expansion can be tuned by choosing appropriate metal cation. MgZrF_6 has almost zero thermal expansion[25]. Based on temperature dependent synchrotron X-ray total scattering diffraction, the authors [26] proposed that flexibility of M--F atomic linkages in MZrF_6 governs the thermal expansions in these fluorides. The more flexible linkage favors the negative expansion, while stiffer linkage leads to positive expansion behaviour. Similar prediction has been reported [23] in M_2O oxides based on *first-principles* density functional theory calculations. The first observation of NTE behaviour in this series is made by Hancock et al [20] on CaZrF_6 and CaHfF_6 . The authors found that CaZrF_6 and CaHfF_6 have much larger negative thermal expansion (NTE) than in ZrW_2O_8 and other corner-shared framework structures. The NTE behavior is comparable with metal cyanides and metal-organic framework compounds. These ceramic compounds are transparent over a wide wavelength range and can be handled in air, which is not the case for cyanides. The coefficient of NTE in CaZrF_6 is strongly temperature dependent. The compound is relatively soft with bulk modulus of 37 GPa, and exhibits disorder at pressure about 400 MPa. The NTE coefficient in CaZrF_6 is greater in magnitude than ScF_3 and comparable to metal cyanides [10,12,27], and CaZrF_6 is not hygroscopic.

The large diversity in thermal expansion behaviour observed by Hu. et. al. [26] among fluoride compounds provides an opportunity to analyse the thermal expansion behaviour in terms of the bonding and local distortion as degree of freedom. However, there is lack of microscopic understanding of the diversity of thermal expansion behaviour in this series of compounds. In view of this, *first-principles* lattice dynamical studies of metal fluorides (CaZrF_6 , MgZrF_6 and SrZrF_6) are performed to analyse the factors which control the thermal expansion coefficient of these compounds. The focus of study[18] is to understand the diversity in thermal expansion behaviour in these compounds in terms of atomic dynamics.

7.2.1 Computational Details

The $A^{II}B^{IV}F_6$ in cubic phase (space group 225, $Fm-3m$) has eight atoms in the primitive unit cell. The VASP [28,29] code along with PHONON software [30] is used to calculate the phonon frequencies in entire Brillouin zone. The Hellman-Feynman forces on the atoms in a $2 \times 2 \times 2$ super cell of the conventional face-centred cubic cell have been calculated using DFT. The forces are calculated by displacing the symmetrically inequivalent atoms along $(\pm x, \pm y, \pm z)$ directions in the supercell. The $2 \times 2 \times 2$ super cell was found to be sufficient for convergence of phonon frequencies in the entire Brillouin zone. The energy cut off is 580 eV and $8 \times 8 \times 8$ k point mesh has been used to obtain total energy convergence of the order of meV, which is sufficient to obtain the required accuracy in phonon energies. The Monkhorst Pack method is used for k point generation[31]. The exchange-correlation contributions were included within PBE generalized gradient approximation (GGA)[32]. The convergence criteria for the total energy and ionic forces were set to 10^{-8} eV and 10^{-3} eV \AA^{-1} , respectively.

TABLE 7.1 *The comparison of calculated lattice parameter and bulk modulus of $MZrF_6$ ($M=Ca, Mg$ and Sr) with previously reported [20,24] experimental and calculated values.*

Compound	a(\AA) Present Calc. (T=0 K)	a(\AA) Expt.	a(\AA) Previous Calc.	B(GPa) Present Calc.	B(GPa) Expt.	B(GPa) Previous Calc.
CaZrF ₆	8.600	8.5128 (10 K) [20]	8.780 [20] 8.426 [33]	57.8	36 (298K) [20]	51.7 [20]
MgZrF ₆	8.058	7.940 (100 K) [24]	-	75.8	48.2 (298 K) [24]	-
SrZrF ₆	8.945	-	-	49.5	-	-

The lattice parameter and bulk modulus of $MZrF_6$ ($M= Ca, Mg, Sr$) as obtained from the *ab-initio* calculations are shown in Table 7.1. The calculated values are compared with available measurements [20,24] and previous calculations [20,24]. To best of our knowledge, there are no previous measurements and calculations available for $SrZrF_6$. A fair agreement in lattice parameters between the calculations and measurements of $CaZrF_6$ and $MgZrF_6$ compounds are obtained. The calculated values are slightly overestimated as expected in GGA calculations. The bulk modulus for these two compounds as calculated at 0 K appear to be overestimated as compared with the measurements performed at 298 K. Interestingly, these compounds are also known to exhibit strong pressure dependence of the bulk modulus [20,24]. However, the calculated bulk modulus is in fairly good agreement with previous calculation in $CaZrF_6$ [20].

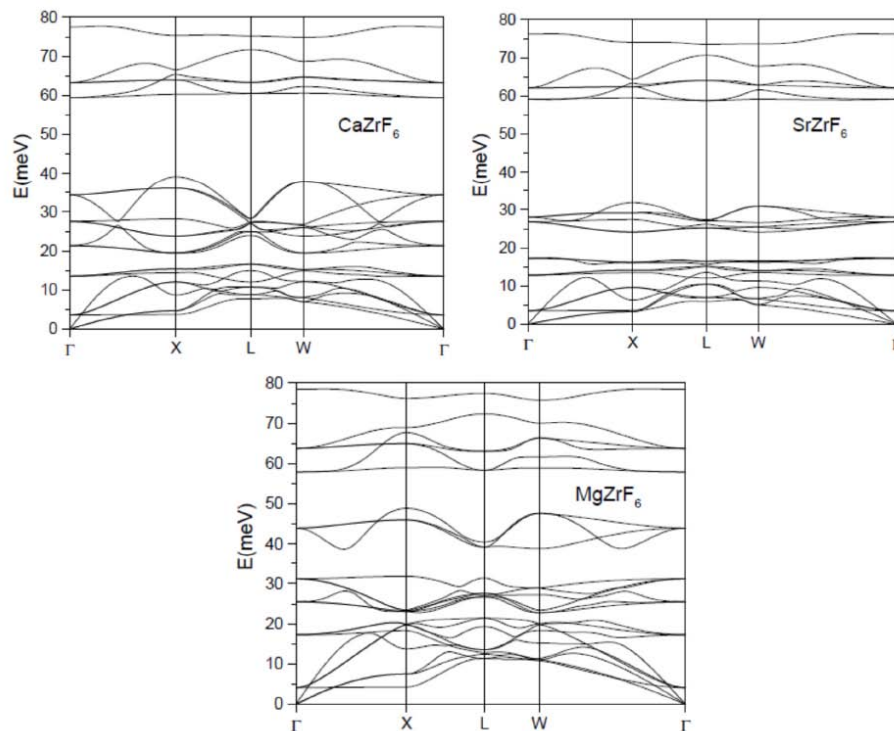


FIG 7.1 Calculated phonon dispersion relation of $MZrF_6$ ($M=Ca, Mg$ and Sr). The high symmetry points in the cubic Brillouin zone are defined as $\Gamma(0\ 0\ 0)$, $X(1\ 0\ 0)$, $L(1/2\ 1/2\ 1/2)$, $W(1/2\ 1\ 0)$.

7.2.2 Phonon Spectra

The phonon dispersion relation along various high symmetry directions for CaZrF_6 , MgZrF_6 and SrZrF_6 are shown in Fig 7.1. The calculated phonon dispersion relation shows large dispersion of low energy phonons below 30 meV in MgZrF_6 , while the dispersion is least in SrZrF_6 . The maximum phonon energy in all the three compounds is around 80 meV. The longitudinal and transverse acoustic branches along Γ -X line show large slope in MgZrF_6 and least in SrZrF_6 . This indicates that MgZrF_6 is the hardest material among the three fluorides. Several dispersion branches in SrZrF_6 form a narrow band around 25-30 meV; however, in CaZrF_6 and MgZrF_6 compounds these dispersion branches show much larger dispersion in a wide energy range.

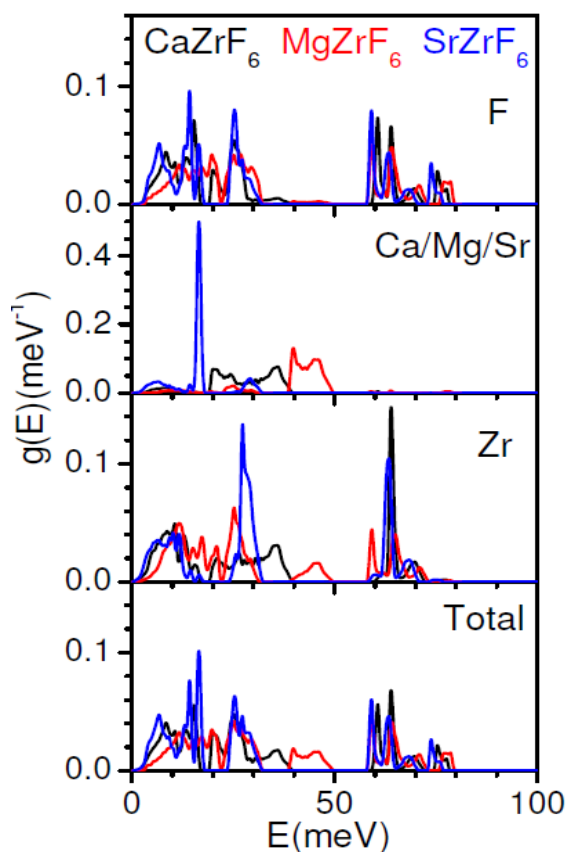


FIG 7.2 Calculated partial phonon density of states of various atoms and the total phonon density of states in MZrF_6 ($M=\text{Ca}$, Mg and Sr).

In Fig 7.2, the calculated partial atomic and the total density of states are displayed. The first peak in the partial density of states of fluorine atom in MgZrF_6 is at about 12 meV, while, in CaZrF_6 and SrZrF_6 the peak is at about 8 meV. The shift in the fluorine density of states peak in MgZrF_6 is attributed to difference in strength of Zr-F bonds in these compounds. The metal atom (M=Ca, Mg, Sr) contribution in phonon density of states is extended up to 40, 50 and 30 meV for Ca, Mg and Sr compound, respectively. Interestingly, in SrZrF_6 the Sr density of states shows huge localized density of states at about 18 meV. The zirconium atom shows contribution in the entire spectrum of density of states in all the three compounds. The lowest peak in the partial density of state due to Zr is at about 10 meV in both CaZrF_6 and SrZrF_6 , while it is at about 12 meV in MgZrF_6 . This may be again due to difference in the strength of Zr-F bond among these compounds. The total density of states is the weighted sum of atomic density of states, which also shows that the lowest peak in the density of state is at about 8 meV in both CaZrF_6 and SrZrF_6 and 12 meV in MgZrF_6 . The total density of state shows band gap at 35-57 meV, 50-57 meV and 40-57 meV in the Ca, Mg and Sr compounds, respectively. The individual contribution of atoms is important to understand the NTE behaviour, as one will see in the next section that NTE in these fluorides is dominated by the fluorine atom dynamics.

7.2.3 Thermal Expansion Behaviour

The thermal expansion behaviour in all the three fluorides has been computed in the quasiharmonic approximation[34]. The pressure dependence of phonon frequencies has been used to calculate the mode Grüneisen parameters, which are further used to compute the thermal expansion coefficient. The calculated Grüneisen parameters of the

three fluorides are shown in Fig 7.3. The calculated Grüneisen parameter (Fig 7.3(a)) for all the individual phonons in the Brillouin zone as a function of phonon energy (E) indicates a large variation of the Grüneisen parameters of modes around the same energy in the whole Brillouin zone. In Fig 7.3(b), the Grüneisen parameters as averaged over all the phonons in the Brillouin zone around energy E are shown. The modes below 10 meV show negative Grüneisen parameters. For CaZrF_6 , the maximum negative value of the averaged Grüneisen parameters in Fig 7.3(b) is -26 for phonons of about 5 meV energy. However, for MgZrF_6 and SrZrF_6 , the maximum negative value is -18 and -12 respectively at about 5 meV (Fig 7.3(b)). It seems that the phonon modes of energy around 5 meV have a major role to contract the lattice in all the three compounds. However, the value of coefficient of NTE would also depend on the density of states of ~ 5 meV phonons in these compounds.

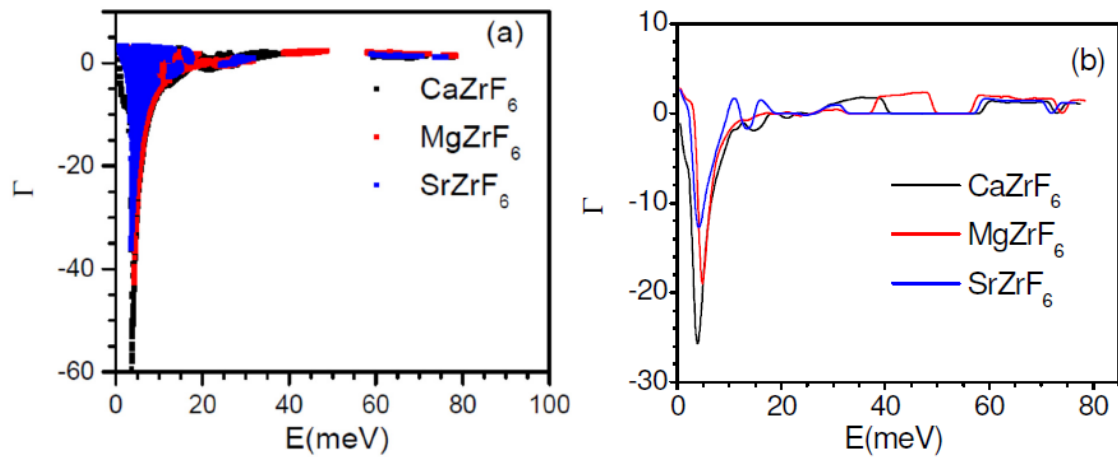


FIG 7.3 Calculated Grüneisen parameter as a function of phonon energy (E) of MZrF_6 ($M=\text{Ca}$, Mg and Sr); (a) plotted for individual phonons, and (b) averaged for all phonons around energy E in the entire Brillouin zone.

The calculated Grüneisen parameters and specific heat contribution from each mode are used to compute the volume thermal expansion coefficient (Fig 7.4). As discussed

above, the large negative Grüneisen parameters of low energy modes around 5 meV result in NTE behaviour in all the three compounds. The compound CaZrF_6 shows largest negative volume thermal expansion coefficient at $\sim 100\text{K}$ and NTE remains upto a very large range of temperature. SrZrF_6 also shows similar behaviour but the magnitude of NTE coefficient is less in comparison to that in CaZrF_6 . However, MgZrF_6 shows NTE behaviour only upto 300 K, and at high temperatures the coefficient of thermal expansion has a very small positive value ($\sim 10^{-7} \text{K}^{-1}$). The difference in behaviour as observed in MgZrF_6 in comparison to that in CaZrF_6 and SrZrF_6 may be due to significant difference in the phonon spectra (Figs 7.1 and 7.2). To understand this the contribution of phonon energy E averaged over Brillouin zone (BZ) to the volume thermal expansion is calculated (Fig 7.5) at 300K.

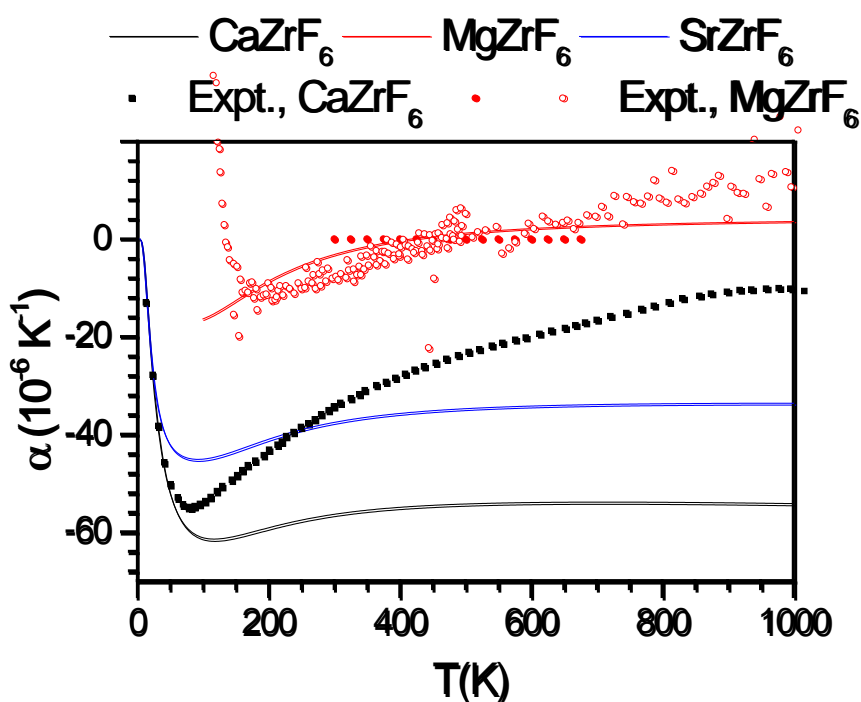


FIG 7.4 The calculated and experimental volume thermal expansion coefficient in the cubic phase of MZrF_6 ($M=\text{Ca}$, Mg and Sr) as a function of temperature. The cubic phase of MgZrF_6 is known to be stable only above $\sim 100 \text{K}$ [24]. The open circles[24], solid circles[25] and solid squares[20] correspond to experimental data, respectively.

The value of volume thermal expansion coefficient depends on sum of the product of specific heat and Grüneisen parameters. It seems that larger the negative value of Grüneisen parameters larger would be the negative coefficient of thermal expansion. For MgZrF_6 and SrZrF_6 the maximum negative value of averaged Γ of phonons at about 5 meV is -18 and -12 respectively (Fig 7.3(b)). However, the contribution of these 5 meV modes to negative thermal expansion coefficient at 300 K (Fig 7.5) is about -4×10^{-6} and -12×10^{-6} for Mg and Sr compounds respectively. This is not an anomaly but this is due to the difference in phonon density of states at 5 meV. At 5 meV, the phonon spectrum of MgZrF_6 (Fig 7.2) has a lower density of states in comparison to that of SrZrF_6 . Hence, the specific heat contribution from 5 meV phonons would be less in MgZrF_6 .

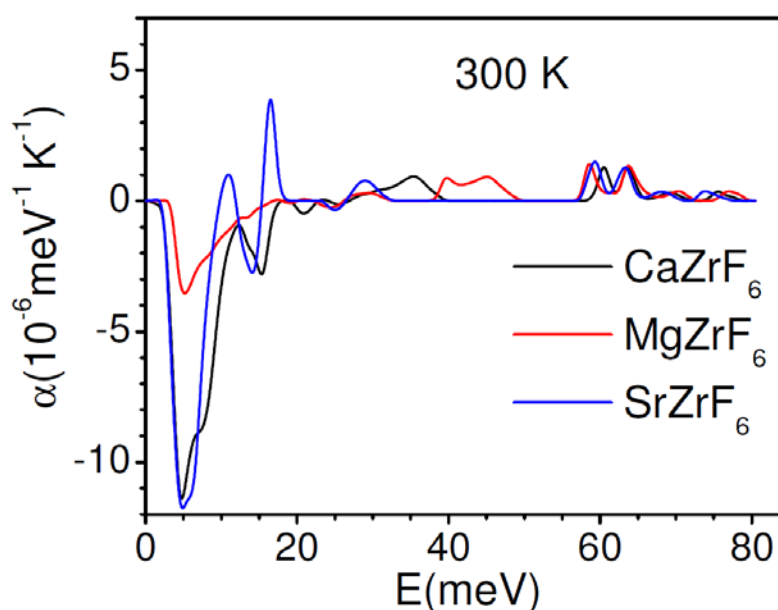


FIG 7.5 The contribution to the calculated volume thermal expansion coefficient of MZrF_6 ($M = \text{Ca}, \text{Mg}$ and Sr) from phonons of energy E averaged over the BZ at 300K.

The comparison of calculated fractional volume change with available experimental values in CaZrF_6 [20] and MgZrF_6 [24,25] is shown in Fig 7.6. The experimental data of SrZrF_6 are not available. The thermal expansion behaviour of

MgZrF₆ shows very good agreement with the available experimental data [24,25]. However, in case of CaZrF₆, the experiment [20] shows good agreement with calculation only upto 200 K and at high temperature it deviates significantly. This discrepancy might be attributed to the temperature dependent anharmonicity of phonons, which is not taken care by quasiharmonic approximation. In order to understand this, the anharmonicity of a few phonon modes in these compounds is investigated (see Sec. 7.2.4).

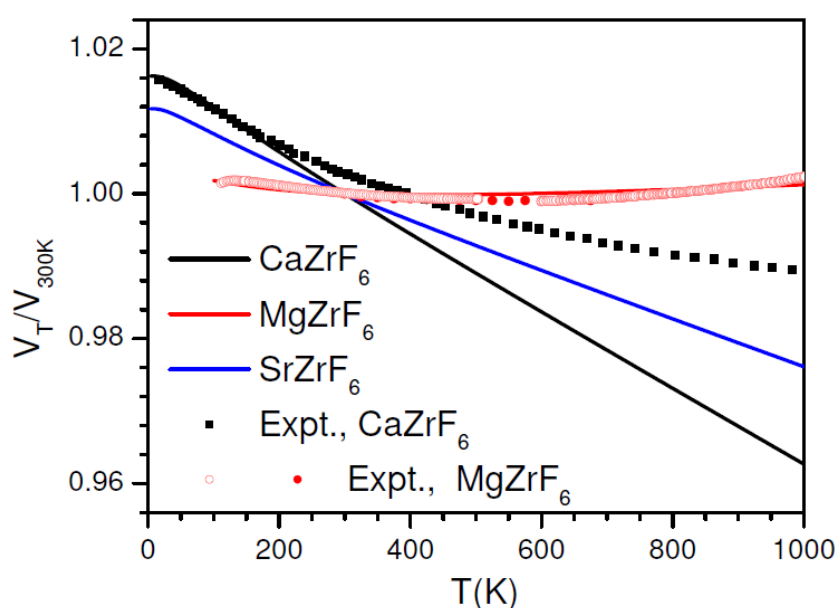


FIG 7.6 The calculated (solid line) and experimental (symbols) [20,24,25] fractional change in volume with respect to the volume at 300 K in the cubic phase of MZrF₆ (M=Ca, Mg and Sr) as a function of temperature. The cubic phase of MgZrF₆ is known to be stable only above ~100 K [24]. The open circles, solid circles and solid squares correspond to experimental data from Refs[24], [25] and [20] respectively.

Thermal expansion in these compounds is argued to be related with large thermal amplitude of the linkage atom (F) between the ZrF₆ and MF₆ polyhedra. The Zr-F-M bonds lie along (100) direction of the cubic cell. Hence, the anisotropic mean-squared displacements of various atoms are calculated as contributed from phonons in entire

Brillouin zone in these compounds (Fig 7.7(a) and (b)). The F-atom serves as the linkage atom between the two polyhedra, and therefore has larger mean-squared displacement than Zr/M atoms. Among the three compounds, the fluorine atom in SrZrF₆ compound shows the largest mean square displacement, which suggests that the nature of bonding in SrZrF₆ is softer in comparison to the other two compounds. Although the largest value of the mean squared displacement of F atoms is in SrZrF₆, it is found that CaZrF₆ shows the maximum NTE behaviour. This behaviour may be related to the anisotropy in the mean squared displacement.

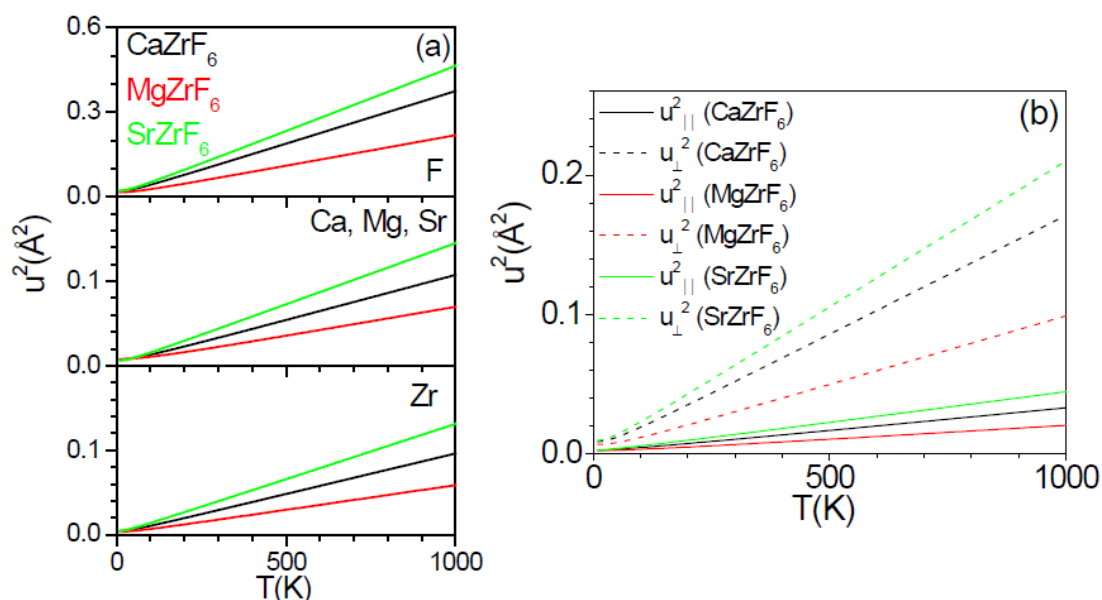


FIG 7.7(a) The calculated mean squared displacement of various atoms in $MZrF_6$ ($M=Ca, Mg$ and Sr) as a function of temperature. (b) The calculated anisotropic mean squared displacement of fluorine atoms, along ($u_{||}^2$) and perpendicular (u_{\perp}^2) to the Zr-F bond, in $MZrF_6$ ($M=Ca, Mg$ and Sr) compounds as a function of temperature.

The mean-squared displacement is larger along the perpendicular (u_{\perp}^2) to the Zr-F bond than along the bond ($u_{||}^2$) in all the three compounds (Fig 7.7(b)). It should be noted that the ratio of anisotropic mean square displacements ($u_{\perp}^2/u_{||}^2$) of F atoms is 4.7, 4.4 and

4.2 at 200 K in Ca, Sr and Mg compounds respectively (Fig 7.7(b)). The large amplitude of the vibrations perpendicular to the Zr-F bond may correspond to librational motion of ZrF_6 polyhedra. The anisotropy of fluorine vibrations could drive the rotational dynamics of ZrF_6 polyhedra, which in turn could result in NTE behaviour in these compounds. This may explain the trend of thermal expansion behaviour in these fluorides.

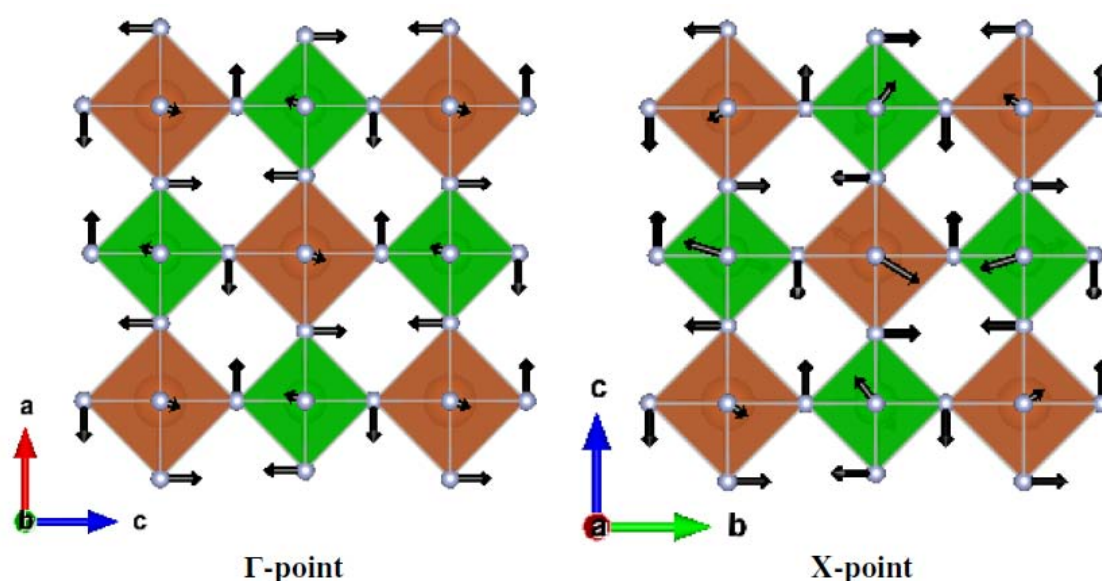


FIG 7.8 The displacement pattern of typical phonon modes having large negative Grüneisen parameter at $\Gamma(0\ 0\ 0)$ and $X(1\ 0\ 0)$ points in the Brillouin zone. The energy of the $\Gamma(0\ 0\ 0)$ point mode is 3.6, 3.87 and 3.31 meV and that of the X point mode is 3.66, 3.95 and 3.51 meV for $CaZrF_6$, $MgZrF_6$ and $SrZrF_6$ respectively. The orange and green octahedral units correspond to MF_6 and ZrF_6 respectively.

In Fig 7.8, the displacement pattern of typical phonon modes are displayed that have large mode Grüneisen parameter $\bar{\alpha}$ at Γ and X points respectively. Both the modes show anti-phase rotation of ZrF_6 and Ca/Mg/Sr F_6 units. The Grüneisen parameter of the Γ -point optic mode is -50, -45 and -36, and for X point mode the values are -61, -47 and -35, for Ca, Mg and Sr compounds respectively. It seems that the rotational dynamics of

the polyhedra, as described from the Γ and X point phonon modes, lead to the maximum NTE in CaZrF_6 , which is consistent with the experiment [20,24,25]. The same dynamics gives the least NTE in SrZrF_6 compound. However, present calculations (Fig 7.4 and 7.6) show a larger NTE in SrZrF_6 than in MgZrF_6 ; so in SrZrF_6 something more than the rotational dynamics of Γ and X point phonon modes is adding to the NTE. Indeed, as already discussed above, the phonon density of states (Fig 7.2) is smaller at low energies around 5 meV in MgZrF_6 than in the other compounds, and therefore the net contribution to the thermal expansion is also smaller in MgZrF_6 as calculated in Fig 7.5.

7.2.4 Anharmonicity of Phonon Modes

The phonon frequencies are usually expected to soften with increase of temperature. However, in a few systems some of the phonons harden [2]. The change in phonon frequency with temperature arises from two contributions, one due to the change in volume, called the implicit anharmonicity; and the other is due to anharmonic vibrations of atoms corresponding to a given phonon as well as phonon-phonon interaction, called the explicit anharmonicity. The potential energy of a few phonons at high symmetry points in the BZ are calculated to estimate the explicit anharmonicity.

The lowest energy optical phonon branch in all the three fluorides contributes to the negative thermal expansion behaviour. Interestingly this branch along Γ -X direction is nearly dispersion-less. The lowest energy optic mode at the zone centre involves (Fig 7.8) out-of-phase rotational motion of ZrF_6 and CaF_6 units, which lead to contraction in the cell dimension by utilizing the open space among these polyhedral units. Sanson et al [33] has reported the temperature dependence of a few high energy zone centre modes. Interestingly they have observed large anharmonic behaviour of these modes. In order to

see the effect of vibrational amplitude of such phonon modes, their potential energy profile are calculated (Fig 7.9).

TABLE 7.2 The calculated anharmonicity parameters in the potential of certain phonon modes. The values of the parameters ‘ $a_{4,j}$ ’ are extracted from fitting of $V(\theta_j) = a_{0,j} + a_{2,j}\theta_j^2 + a_{3,j}\theta_j^3 + a_{4,j}\theta_j^4$ to the potential energy profile of the mode with fixed value of ‘ $a_{2,j}$ ’ as determined from the harmonic phonon energies. The calculated Grüneisen parameter $\Gamma(E)$ of the respective mode is also given.

Wave-vector	E (meV)	$\Gamma(E)$	$a_{2,j}$ (10^{-3} eV/ $\text{Å}^2 \cdot \text{amu}$)	$a_{3,j}$ (10^{-3} eV/ $\text{Å}^3 \cdot \text{amu}^{3/2}$)	$a_{4,j}$ (10^{-3} eV/ $\text{Å}^4 \cdot \text{amu}^2$)
CaZrF ₆					
$\Gamma(A_g)$	77.8	1.1	723.65	77.6	2.78
$\Gamma(F_{2g})$	27.6	-0.2	90.82	0.17	0.95
$\Gamma(F_{1g})$	3.6	-62.7	1.55	0.0	0.44
X	3.7	-58.4	1.62	0.0	0.53
MgZrF ₆					
$\Gamma(F_{1g})$	3.9	-48.5	1.77	0.0	0.47
X	4.0	-44.8	1.93	0.0	0.61
SrZrF ₆					
$\Gamma(F_{1g})$	3.5	-35.0	1.48	0.0	0.41
X	3.6	-34.2	1.57	0.0	0.40

The crystal potential energy is then fitted to the expression $V(\theta_j) = a_{0,j} + a_{2,j}\theta_j^2 + a_{3,j}\theta_j^3 + a_{4,j}\theta_j^4$ (where θ_j is the normal coordinate of the j^{th} phonon mode and $a_{2,j}$, $a_{3,j}$, and $a_{4,j}$ are the coefficients of the harmonic and third and fourth order anharmonic terms, respectively). Table 7.2 show the calculated anharmonic coefficients (cubic and quartic anharmonicity) of a few selected phonons in all the three fluorides. It is found that in CaZrF₆, as mentioned in Ref. [33], the A_g mode has dominant contribution of cubic anharmonicity, while F_{3g} mode has contribution only from the quartic

anharmonicity. It is also observe that both the lowest energy optic mode at Γ -point and X point in the Brillouin zone show significant quartic anharmonicity (Fig 7.9). A significant reduction of NTE due to quartic potential of relevant vibrational modes has been demonstrated in ScF_3 by Li et al. [7]. Similar effect may be expected in the present compounds, which would improve the agreement between the calculation and the experiments at high temperatures.

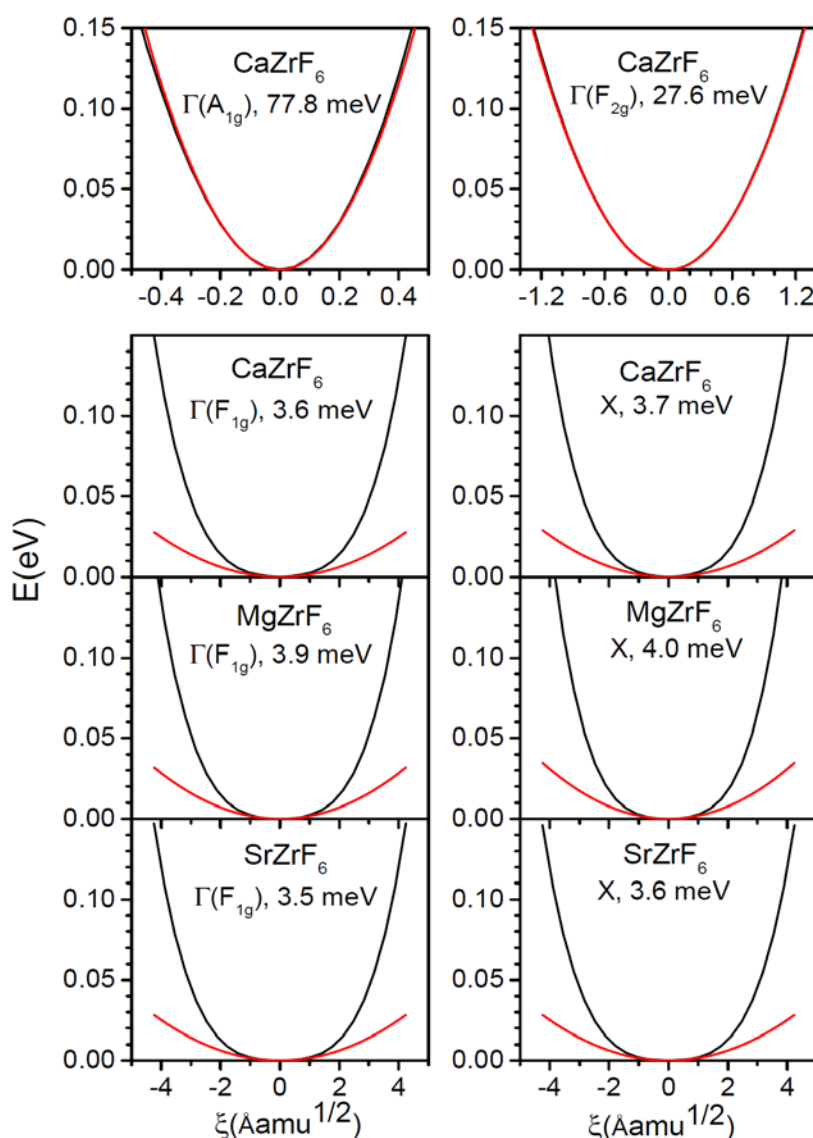


FIG 7.9 The calculated potential energy profile (black lines) of specific phonon modes at $\Gamma(0\ 0\ 0)$ and $X(1\ 0\ 0)$ points in the BZ. The red line shows the harmonic profile of respective phonon modes. The corresponding phonon energy of each mode is also given.

7.3 H₂O and D₂O Ice *Ih*

Understanding the behaviour of ice over a broad range of thermodynamic conditions is of great importance in the field of Earth and planetary sciences as well as in fundamental physics and chemistry [21,35-54]. Ice is known to exhibit polymorphic structures, depending on the environmental conditions[35]. It exists even in outer space, in comet clouds and interstellar grains [41-43]. The known phase diagram of ice is extremely rich. The hydrogen bonds in ice are weak enough to be bent, stretched, or shortened substantially under pressure, which explains various crystalline structures that have been identified so far.

Ice has many anomalous properties and perhaps a most complex phase diagram. Ordinary ice (*Ih*) crystallizes in an open structure which provides ample possibilities for rearrangements with pressure and temperature. The region of stability of ice *Ih* has been extensively studied [21,35,46,47] both by experiments as well as theories. Among all the known crystalline ice phases, ice (*Ih phase*) exhibits anomalous thermal expansion[21,46] behaviour. It exhibits negative thermal expansion (NTE) at temperatures below ~ 60 K. As temperature increases above 60 K, it shows a large positive thermal expansion coefficient. The understanding of the mechanism of the anomalous thermal expansion involves an understanding of the underlying dynamics of hydrogen-bonded water molecules in ice and their behaviour on compression. Here the focus of study is on one of the peculiarities, namely, the anomalous expansion behaviour with temperature in ice *Ih*. The thermodynamic stability of various phases of ice including the role of vibrational anharmonicity [36,47,52,53,55-66] have been studied by various groups. *Koza et al* [48-50] reported extensive neutron and X-ray scattering experiments dedicated to the study of the dynamics of some high-density crystalline and amorphous ice structures.

Spectroscopic studies have been reported using dielectric, infrared (IR), Raman and neutron measurements [54,67-70]. Strassle *et al*[47] have measured the pressure dependence of low energy phonon dispersion in deuterated ice (D₂O) to understand the pressure induced amorphization and NTE behaviour. The measurements along the high symmetry directions in the Brillouin zone show softening of low energy modes of about 5-7 meV. The phonon density of states of H₂O and D₂O ice in *Ih* phase [71] has been measured at 15 K. Edgar *et al*[53] theoretically studied the significance of phonon anharmonicity on the stability of hexagonal ice over the stability of cubic phase. The isotope effect of H and O on ice volumes has been studied by various authors [37,38,72,73]. The effect at low temperature has been related to low-energy phonons linked to the hydrogen bonding network. Others studies on ice addressed the proton hopping/disorder and diffusion in ice using dielectric and quasielastic neutron scattering method[54,74].

Since the mechanism of the anomalous thermal expansion involves anharmonic phonons over the entire Brillouin zone, it is necessary to study the complete phonon spectrum. Similarly, there is a need to investigate the anharmonicity and phonon eigenvectors across the entire Brillouin zone by *ab-initio* density functional theory. The pressure dependence of the phonon spectrum are calculated using extensive *ab-initio* lattice dynamics calculations of H₂O and D₂O ice in the *Ih* phase. The results bring out the nature of specific anharmonic soft phonon modes that show anomalous behaviour as a function of pressure and temperature, which leads to the anomalous thermal expansion behaviour of ice. Therefore, an explanation of the physical mechanism behind the anomalous thermal expansion in ice *Ih* is provided[19].

7.3.1 Computational Details

The phonon calculations of H₂O and D₂O are performed in *Ih* phase using the *ab-initio* DFT as implemented in the VASP software [28,75]. The compounds are known to exhibit H/D disorder, hence the calculations are performed in order equivalent structure *Ih* phase which is a $\sqrt{3} \times \sqrt{3} \times 1$ supercell (space group P6₃cm) of the actual unit cell[76]. The required force constants were computed within the Hellman-Feynman framework, on various atoms in different configurations of a supercell with ($\pm x$, $\pm y$, $\pm z$) atomic displacement patterns. A supercell of ($2 \times 2 \times 2$) dimension of order equivalent cell, which consist of 96 H₂O molecule has been used in the computations. An energy cut-off of 900 eV was used for plane wave expansion. The Monkhorst Pack method is used for k point generation[68] with a $4 \times 4 \times 4$ k-point mesh was used. The valence electronic configurations of H and O, as used in calculations for pseudo-potential generation are $1s^1$ and s^2p^4 respectively. The convergence breakdown criteria for the total energy and ionic loops were set to 10^{-8} eV and 10^{-4} eV \AA^{-1} , respectively. Further, to obtain the phonon frequencies in the entire Brillouin zone, PHONON software[77] is used as a subsequent step to DFT total energy calculations. The calculation of D₂O compound has been carried out using the same pseudo potential as used in H₂O compound. The structure is optimized with all the vdW functional available in VASP. It is found that the vdW functional by Dion et al[78] , namely, the DRSSL with revPBE functional, gives the closest structure and dynamical properties of ice *Ih*. Hence, this functional is used for all subsequent calculations. Here our interest is primarily to reproduce the observed anomalous thermal expansion, and thereby to identify the physical mechanism behind it, which is achieved quite well by this functional.

7.3.2 Total and Partial Phonon Density of States

The calculated neutron-weighted phonon density of states compared with the measurements is shown in Fig 7.10. The calculation agrees fairly well with the measurements at low temperature at 10 K. However, the peaks at 28 and 38 meV in the experimental data are slightly overestimated and underestimated respectively in the calculated spectra. The negative expansion behaviour occurs below 60 K and the contributions of high energy modes is not very significant at such low temperatures, which gives us confidence to understand the anomalous behaviour of H₂O and D₂O in the *Ih* phase with the current computational formalism.

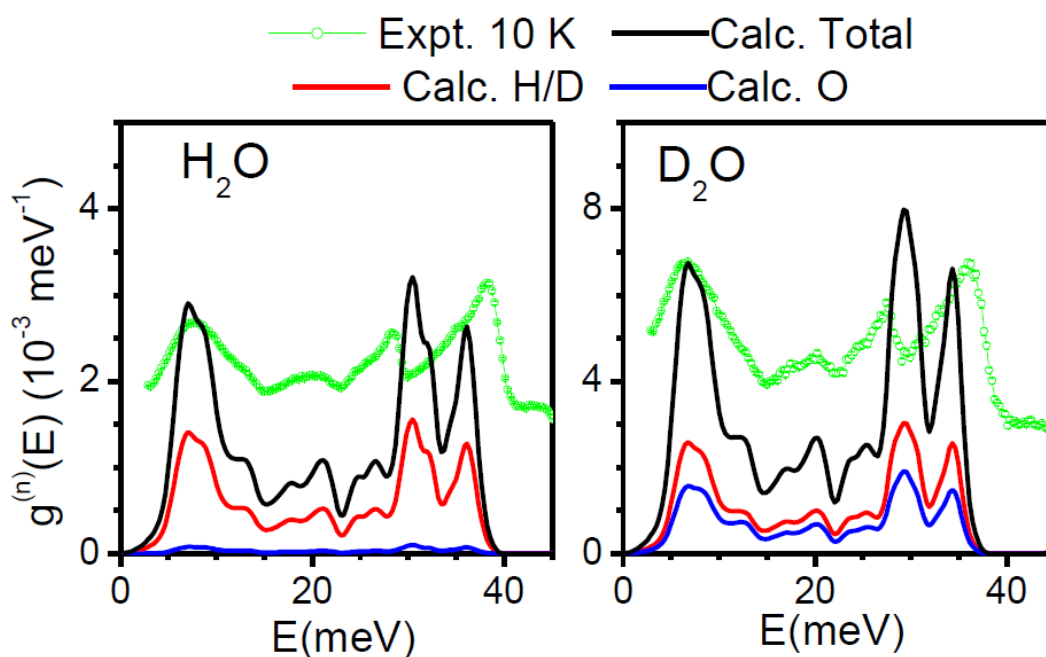


FIG 7.10 The low energy part of experimental phonon spectra, in the *Ih* phase of H₂O and D₂O ice, as a function of temperature. The calculated neutron weighted phonon spectra as well as partial phonon contributions of H/D and O atoms are also shown. The inelastic neutron scattering measurements are performed by Dr. M. K. Gupta using the MERLIN spectrometer at ISIS Facility, Rutherford Appleton Laboratory, UK.

An examination of the calculated phonon eigenvectors shows that the modes below 40 meV are essentially the translational modes of H₂O/D₂O molecules. To see the individual atomic contribution to the phonon frequency, the phonon density of states contributed from individual atoms (Fig 7.11) is calculated. The calculated neutron cross-section weighted partial phonon density of states shows (Fig. 7.10) that at low energies, the experimental neutron spectrum in H₂O ice is dominated by H atoms due to the large incoherent cross section of H. However, in the experimental neutron spectra of D₂O ice, both the D and O atoms have comparable contributions.

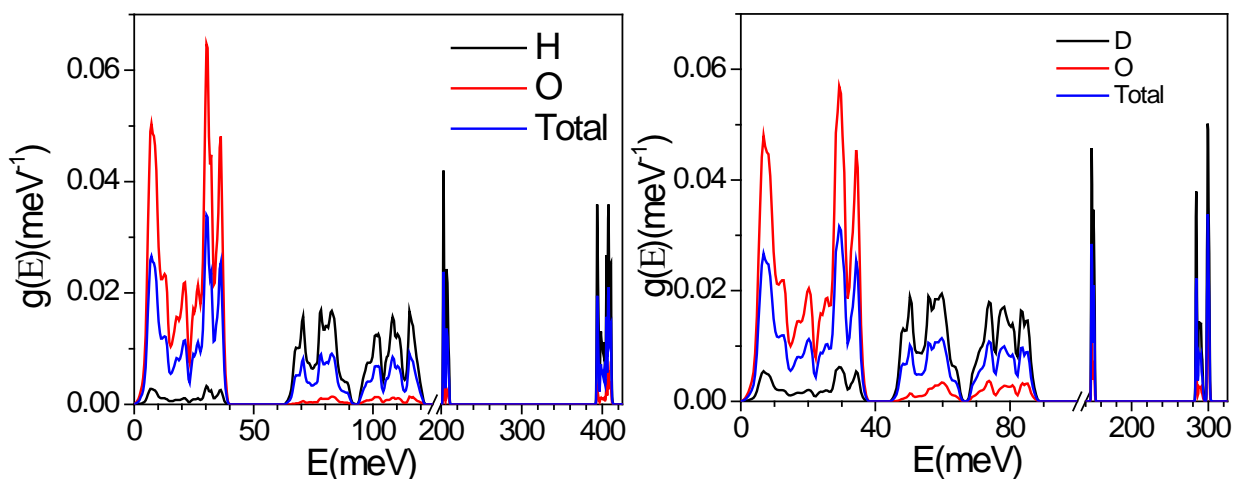


FIG 7.11 The calculated total and partial phonon density of states in the *Ih* phase of H₂O and D₂O ice.

7.3.3 Grünesen Parameters and Thermal Expansion

In order to calculate the thermal expansion behaviour, we need to have Grünesen parameters as derived from pressure dependence of phonon frequencies. The pressure dependence of phonon dispersion relation along various high symmetry direction is calculated. We obtained the softening of low energy modes below 12 meV on

compression from the calculations. Further we have also calculated the phonon frequencies on anisotropic compression along a and c -axis. Table 7.3 shows the calculated Grüneisen parameters (Γ_a , Γ_c and Γ_v) of a few selected phonon modes of about 6 meV. The anisotropic compression along c -axis shows (Fig 7.12) that phonon modes below 2 meV have positive Grüneisen parameters (Γ_c).

TABLE 7.3 The calculated anisotropic Grüneisen parameter of a few phonons having large Grüneisen parameters in the BZ of an ordered analogue (space group $P6_3cm$) of ice Ih. E and Γ are the energy and Grüneisen parameter respectively. The wave-vectors are $\Gamma(0\ 0\ 0)$, $A(0\ 0\ 0.5)$, $K(.33\ 0.33\ 0)$, $H(.33\ 0.33\ 0.5)$, $M(0.5\ 0.5\ 0)$ and $L(0.5\ 0.5\ 0.5)$.

Wave-vector	E(meV)	Γ_a	Γ_c	Γ_v
H₂O/D₂O				
Γ	5.6/5.3	-2.0/-2.0	-5.3/-5.2	-3.1/-3.0
A	4.5/4.2	-0.9/-0.9	-3.7/-3.6	-1.9/-1.8
A	6.8/6.5	-3.0/-3.1	-2.9/-2.8	-3.0/-3.0
K	4.7/4.5	-4.0/-3.9	-3.0/-2.7	-3.7/-3.5
K	5.2/4.9	-2.9/-2.9	-1.6/-1.4	-2.5/-2.4
K	7.1/6.8	-0.5/-0.5	-0.7/0.7	-0.6/0.6
H	7.3/6.9	-1.6/-1.5	-1.5/-1.5	-1.6/-1.5
H	7.7/7.4	-1.6/-1.7	-1.6/-1.7	-1.6/-1.7
M	5.3/5.0	-3.9/-4.0	-2.1/-2.2	-3.4/-3.4
M	6.1/5.8	-0.5/-0.5	-0.2/-0.2	-0.4/-0.4
L	7.5/7.2	-1.6/-1.5	-1.6/-1.7	-1.6/-1.6
L	7.8/7.5	-1.6/-1.6	-1.4/-1.4	-1.5/-1.5

Since lowering of the phonon frequency would enhance the entropy, these phonon modes (<12 meV) act to reduce the volume of the system. However, the energy of other higher-energy modes increases on compression which would decrease the entropy. These modes will not favor volume contraction and instead work to expand the lattice. The competition between these two regimes of phonon modes and their population govern the overall thermal expansion behaviour. The calculated thermal expansion coefficients are

shown in Fig 7.13. At low temperature (<60 K) only the low energy modes are populated significantly. The other high-energy modes are not sufficiently populated to compete with these low energy modes. Hence D₂O/H₂O ice Ih shows negative thermal expansion behaviour at low temperature (Fig 7.13). Further, at high temperature above 60 K the high energy modes above 12 meV start populating significantly and dominate, which leads to positive expansion behaviour.

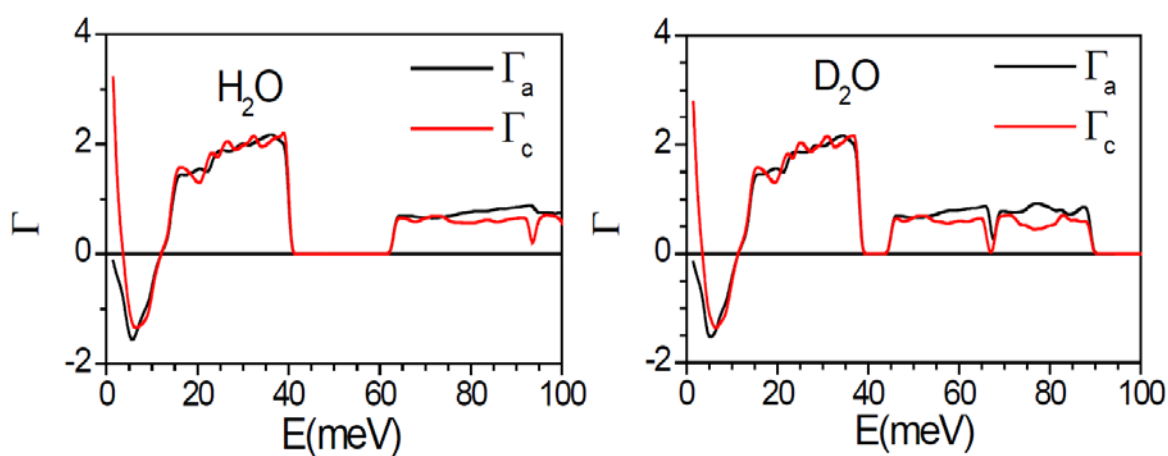


FIG 7.12 The calculated anisotropic Grüneisen parameters in the Ih phase of H₂O and D₂O ice.

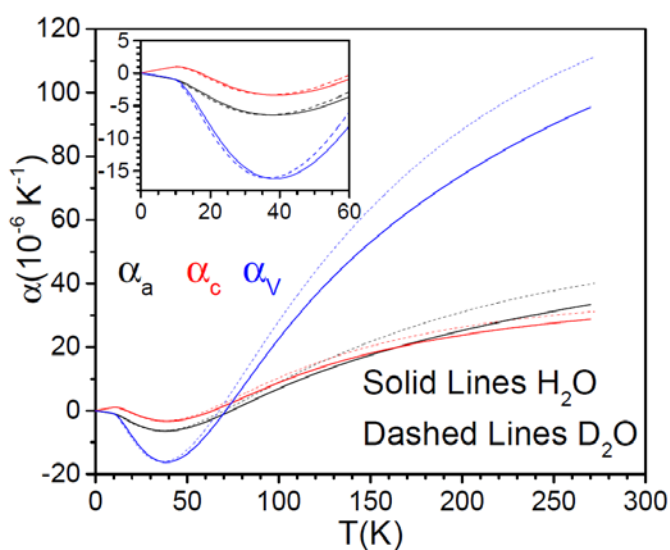


FIG 7.13 The calculated linear and volume thermal expansion coefficients the Ih phase of H₂O and D₂O ice.

TABLE 7.4 The calculated elastic properties of the *Ih* phase of H_2O ice as a function of pressure.

Compliance	0 kbar	10 kbar	20 kbar	25 kbar
s_{11} (10^{-4} kbar $^{-1}$)	77.6	86.2	105.3	122.0
s_{33} (10^{-4} kbar $^{-1}$)	60.6	62.3	67.8	71.8
s_{44} (10^{-4} kbar $^{-1}$)	249.1	291.0	371.7	443.0
s_{12} (10^{-4} kbar $^{-1}$)	-34.3	-44.1	-61.0	-75.0
s_{13} (10^{-4} kbar $^{-1}$)	-18.5	-22.6	-27.6	-30.8
K_a (10^{-4} kbar $^{-1}$)	24.8	19.5	16.7	14.2
K_c (10^{-4} kbar $^{-1}$)	23.6	17.1	12.6	10.2
K (10^{-4} kbar $^{-1}$)	73.2	56.1	46.0	38.6
B (kbar)	137	178	217	259

Since the hexagonal structure of the *Ih* phase is anisotropic, we have also calculated the anisotropic linear thermal expansion (Fig 7.13). The behaviour of linear expansion coefficients (α_a and α_c) are related to anisotropic Grüneisen parameter (Γ_a and Γ_c) as well as elastic compliance matrix. The elastic compliance tensor (Table 7.4), which is the inverse of the elastic constant tensor (Table 7.5), shows that compressibilities along *a* and *c*-axis are very similar. The anisotropic Grüneisen parameter (Γ_a and Γ_c) behaviour is also very similar (Fig 7.12). Hence, only the negative magnitude of the Grüneisen parameter will give rise to negative expansion behaviour at low temperature.

TABLE 7.5 The calculated and experimental[79] elastic constants of H_2O ice *Ih* in kbar units. The calculations are performed in ordered analogue of H_2O ice *Ih*.

Elastic Constants	Calculation at 0 K	Experiment[79]at 237.5K
C_{11}	195	145
C_{12}	103	74
C_{13}	86	60
C_{33}	217	156
C_{44}	42	32
C_{66}	46	36
B	137	92

The experimental measurements[21,46] of thermal expansion behaviour show that magnitude of NTE below 40 K in D₂O ice is slightly more in comparison to H₂O ice, while at high temperature the magnitude of positive thermal expansion behaviour in D₂O ice is larger than that in H₂O ice (Fig 7.13 and 7.14). This can be understood from the calculated partial and total phonon spectrum. The negative thermal expansion is contributed by low energy phonon modes below 12 meV. The partial and total phonon spectrum looks very similar (Fig 7.11) in both the cases [80]. However due to mass effect the lowest peak at about 7 meV in density of states in H₂O is shifted to slightly lower energies at about 6.5 meV.

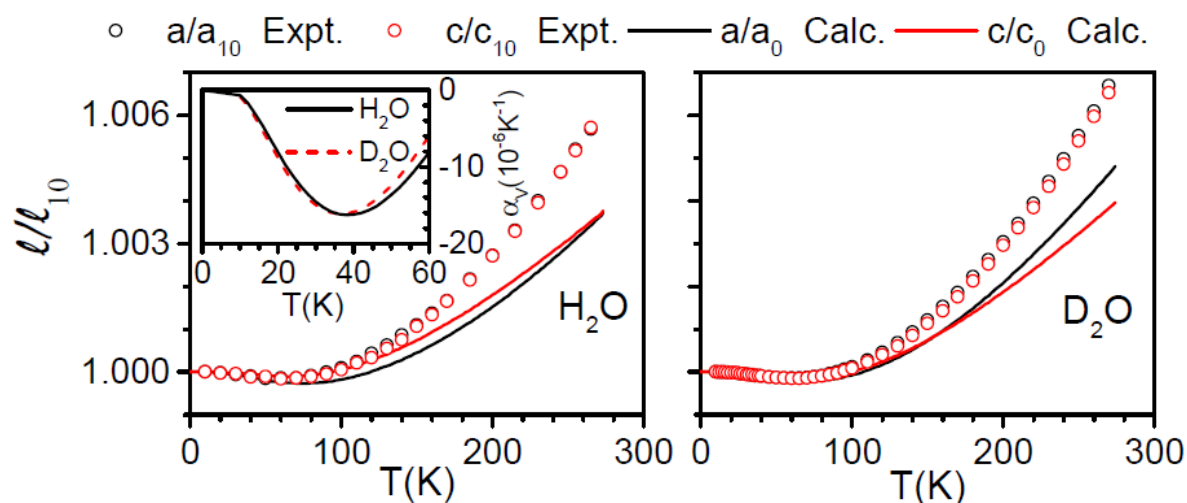


FIG 7.14 The calculated and measured [46] lattice parameter change (l/l_{10} ; $l= a, c$) of ice with temperature. Inset in the left panel shows the calculated volume thermal expansion coefficient (α_v) of H₂O and D₂O ice up to 60K.

The nature of Grüneisen parameters show a negative sign below 12 meV and afterward it is positive. The NTE could indeed arise from negative compliance tensor components or negative Grüneisen parameters. In the present case, we find that the

Grüneisen parameters are almost isotropic, $\Gamma_a = \Gamma_b \approx \Gamma_c$ and therefore, we can simply rewrite the eq. (1.30) using elastic compliance tensor values as:

$$\alpha_a(T) \propto \sum_{q,j} C_v(q,j,T) [0.00248\Gamma_a(E_{q,j})] \quad (7.1)$$

$$\text{and } \alpha_c(T) \propto \sum_{q,j} C_v(q,j,T) [0.00236\Gamma_a(E_{q,j})] \quad (7.2)$$

This clearly shows that the thermal expansion coefficients as a function of temperature essentially follow the Grüneisen parameters and the phonon population, since the compliance tensor terms add up to a positive number. Hence, the expansion behaviour along both the a and c -axis shows negative expansion behaviour at low temperature (<60 K) and after that it shows positive expansion behaviour.

The calculated fractional change in the lattice parameters with temperature shows excellent agreement with the available measurements[46] at temperature below 100 K (Fig 7.14). At temperature around 200 K, the calculated thermal expansion behaviour is underestimated in comparison to the experimental data. We note that the experimental bulk modulus value of H₂O Ice in Ih phase is known to show large variation from 10.5 GPa to 8.3 GPa on increase of temperature from 60 K to 270 K. The increase in the compressibility or the elastic compliance tensor would lead to increase in the thermal expansion. Our *ab-initio* calculations are performed using quasi-harmonic approximation (QHA) at 0 K. For thermal expansion calculation, we used the elastic compliance tensor as calculated from DFT at 0 K. Which means that some of the elastic compliance component would increase significantly with temperature and would be responsible for increase in positive expansion behaviour at high temperature. The present formalism of calculation of thermal expansion behaviour does not account for this effect, hence may lead to underestimation of calculated volume thermal expansion at higher temperature. This essentially reflects the limitation of QHA in the present case [81]. The magnitude of

positive expansion in D₂O (Fig 7.14) is larger than that in H₂O, which is due to the fact that high energy phonon modes which contribute to positive expansion are shifted towards lower energy side due to heavy mass of D, hence they are excited at lower temperature and add to the extra positive expansion in comparison to H₂O.

7.3.4 Mechanism of Negative Thermal Expansion

The nature of dynamics of phonon modes which contributes to NTE behaviour in the compound can be understood by calculating the mean square displacement of various atom as a function of phonon energy (Fig 7.15). It can be seen that the magnitude of mean square displacements of both the atoms (H/D and O) are equal for the modes upto 40 meV. This suggest that phonon dynamics at low energy involves translational motion of the H₂O as a rigid body and not any librations or internal modes of H₂O/D₂O. Hence internal dynamics of H₂O/D₂O does not play any role in NTE behaviour.

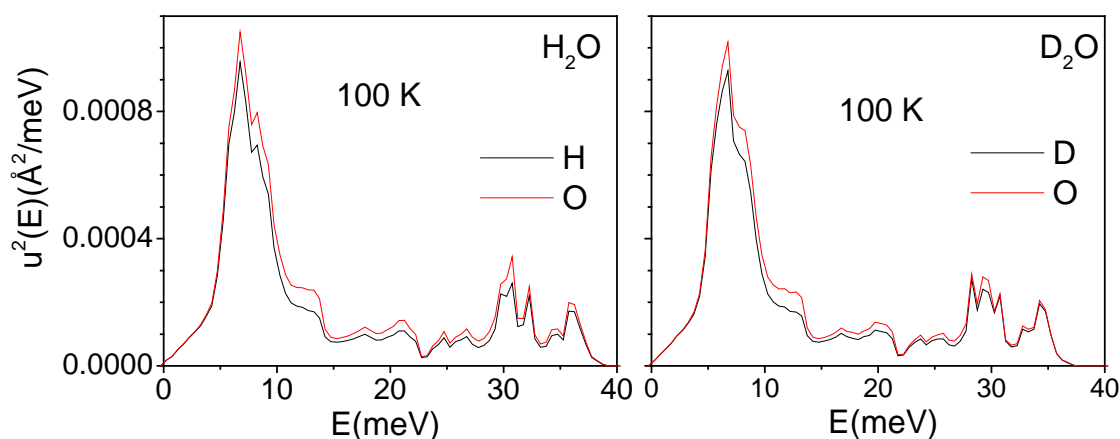


Fig 7.15 The calculated mean square displacement as a function of phonon energy averaged over Brillouin zone.

As discussed above low energy phonon modes below 12 meV contribute to negative expansion in both the *Ih* phase of ice D₂O and H₂O. Table 7.3 show the

Grüneisen parameters of a few selected phonon modes relevant to NTE behaviour in the compound. However, the nature of the dynamics, .i.e., the atomic motion pattern for such modes is not known. The atomic displacement pattern of one representative phonon mode which contributes to NTE is plotted (Fig 7.16).

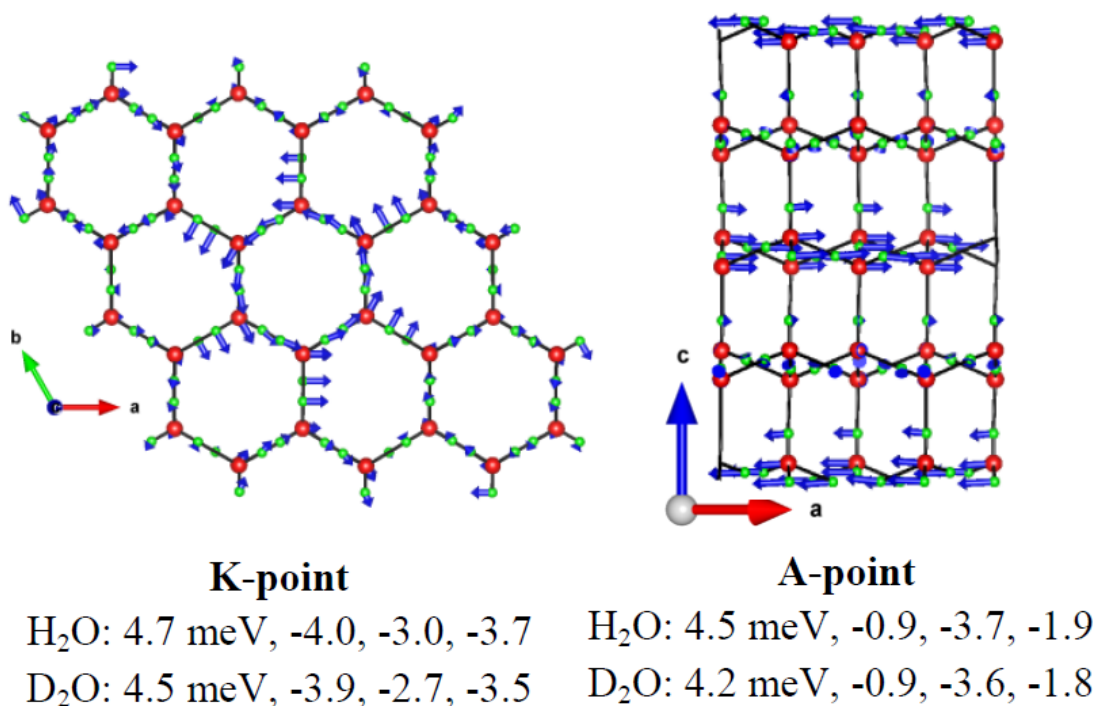


FIG 7.16 The atomic displacement pattern of selected phonon modes of H₂O/D₂O in Ih phase of ice. The number below the figure gives the phonon energies, Γ_a , Γ_c and Γ_v respectively. Key- H/D: Green and O: Red.

The displacement pattern of the K-point phonon mode of 4.7 meV energy is shown in Fig 7.16; this manifests itself as a rotational motion of the hexagonal rings and a distortion of the ring structure, which acts to reduce the area of the rings and thereby give rise to NTE in the *a-b* plane. The hexagonal rings, arranged into sheets, are stacked along the *c*-direction. These cooperative rotation of the hexagonal rings in one plane influences, due to polyhedral connectivity of the H bonds, the interplanar separation.

Another mode (Fig 7.16) of similar energy ~4.5 meV at the A-point involves transverse vibrations of the hexagonal layers, which further contributes to NTE along the *c*-axis. These calculations show that it is the rotational dynamics of the hexagonal rings that leads to NTE in these ice. Animations of a few selected modes are given in supplementary material [80].

7.3.5 High Pressure Stability of *Ih* Phase of Ice

Ice shows large number of phase transition with pressure as well as temperature. These phase transition are expected to be related to phonon instabilities and elastic instabilities with pressure and temperature. The temperature and pressure dependence measurement of phonon modes can be used to find the soft phonon modes, which could lead to phase transition.

TABLE 7.6 *The calculated Born stability criteria in the *Ih* phase of H₂O ice as a function of pressure. For elastically stable hexagonal crystal all three Born criteria (elastic constants equations) must be positive.*

P (kbar)	Born Stability Criteria		
	(C ₄₄ -P) (kbar)	(C ₆₆ -P) (kbar)	(C ₃₃ -P)(C ₁₁ +C ₁₂)-2(C ₁₃ +P) ² (kbar ²)
0	40.0	45	51439
10	24.5	28.5	52883
20	7	10	42821
25	-2.5	0.2	33335

The pressure dependence of various Born stability criteria (Table 7.6) are calculated. It is interesting to see that with increase in pressure the Born stability criteria related to C₄₄ and C₆₆ elastic constant are found to be violated at about 2.5 GPa. These

elastic constants are related with long-wavelength transverse acoustic phonons along (100) and (110) directions in the compounds. As mentioned above, the negative thermal expansion in these compounds are attributed to transverse acoustic phonons and same phonon softening at high pressure would lead to elastic instability.

7.4 Conclusions

The extensive investigations of the phonon dynamics in three isostructural ReO_3 -type compounds are performed. The large volume anharmonicity of low energy modes in CaZrF_6 and SrZrF_6 is found to be responsible for NTE in these compounds. In MgZrF_6 , at high temperature, the thermal expansion coefficient becomes much smaller, since some of the high energy phonon modes contribute to positive expansion behaviour and kill the NTE. The anisotropy in the mean squared displacement ($u_{\perp}^2/u_{\parallel}^2$) correlates well with the thermal expansion behaviour in these compounds. Larger the ratio, higher is the NTE coefficient. The potential energy profile of a few phonon modes are calculated in all the three fluorides and obtained the high order anharmonic coefficients. Further, it is found that in CaZrF_6 , A_g mode shows cubic anharmonicity, while F_{3g} mode has quartic anharmonicity, which is consistent with previous [33] Raman measurements.

The quantitative study of the anisotropic and anomalous thermal expansion in H_2O and D_2O ice in the *Ih* phase is performed. This has also enabled to understand the quantitative difference in thermal expansion behaviour of the H_2O and D_2O ice. The *ab-initio* density functional theory provided the nature of specific anharmonic phonons, namely, the librational motion of the hexagonal rings of the ice molecules and the transverse vibrations of the hexagonal layers that lead to the observed behaviour in ice.

References

- [1] M. K. Gupta, R. Mittal, and S. L. Chaplot, *Physical Review B* **88**, 014303 (2013).
- [2] G. Ernst, C. Broholm, G. Kowach, and A. Ramirez, *Nature* **396**, 147 (1998).
- [3] C. Perottoni and J. Da Jornada, *Science* **280**, 886 (1998).
- [4] T. Mary, J. Evans, T. Vogt, and A. Sleight, *Science* **272**, 90 (1996).
- [5] L. Hu *et al.*, *Journal of the American Chemical Society* **138**, 8320 (2016).
- [6] P. Lazar, T. Bučko, and J. Hafner, *Physical Review B* **92**, 224302 (2015).
- [7] C. W. Li, X. Tang, J. A. Munoz, J. B. Keith, S. J. Tracy, D. L. Abernathy, and B. Fultz, *Physical review letters* **107**, 195504 (2011).
- [8] B. K. Greve, K. L. Martin, P. L. Lee, P. J. Chupas, K. W. Chapman, and A. P. Wilkinson, *Journal of the American Chemical Society* **132**, 15496 (2010).
- [9] S. U. Handunkanda, E. B. Curry, V. Voronov, A. H. Said, G. G. Guzmán-Verri, R. T. Brierley, P. B. Littlewood, and J. N. Hancock, *Physical Review B* **92**, 134101 (2015).
- [10] V. E. Fairbank, A. L. Thompson, R. I. Cooper, and A. L. Goodwin, *Physical Review B* **86**, 104113 (2012).
- [11] B. Singh *et al.*, *Journal of Applied Physics* **121**, 085106 (2017).
- [12] A. L. Goodwin, M. Calleja, M. J. Conterio, M. T. Dove, J. S. Evans, D. A. Keen, L. Peters, and M. G. Tucker, *Science* **319**, 794 (2008).
- [13] K. Kamali, C. Ravi, T. Ravindran, R. Sarguna, T. Sairam, and G. Kaur, *The Journal of Physical Chemistry C* **117**, 25704 (2013).
- [14] A. Goodwin, *Journal of American Chemical Society* **131**, 6334 (2009).
- [15] M. K. Gupta, B. Singh, R. Mittal, M. Zbiri, A. B. Cairns, A. L. Goodwin, H. Schober, and S. L. Chaplot, *Physical Review B* **96**, 214303 (2017).
- [16] M. K. Gupta, B. Singh, R. Mittal, S. Rols, and S. L. Chaplot, *Physical Review B* **93**, 134307 (2016).
- [17] R. Mittal, M. K. Gupta, and S. L. Chaplot, *Progress in Materials Science* **92**, 360 (2018).
- [18] M. K. Gupta, B. Singh, R. Mittal, and S. L. Chaplot, *Physical Review B* **98**, 014301 (2018).
- [19] M. K. Gupta, R. Mittal, Baltej Singh, S. K. Mishra, D. T. Adroja, A. D. Fortes and S. L. Chaplot, *Physical Review B* **98**, 104301 (2018).
- [20] J. C. Hancock *et al.*, *Chemistry of Materials* **27**, 3912 (2015).
- [21] K. Rottger, A. Endriss, J. Ihringer, S. Doyle, and W. F. Kuhs, *Acta Crystallographica Section B* **50**, 644 (1994).
- [22] C. P. Romao, C. R. Morelock, M. B. Johnson, J. W. Zwanziger, A. P. Wilkinson, and M. A. White, *Journal of Materials Science* **50**, 3409 (2015).
- [23] M. K. Gupta, R. Mittal, S. L. Chaplot, and S. Rols, *Journal of Applied Physics* **115**, 093507 (2014).
- [24] B. R. Hester, J. C. Hancock, S. H. Lapidus, and A. P. Wilkinson, *Chemistry of Materials* **29**, 823 (2017).

- [25] J. Xu, L. Hu, Y. Song, F. Han, Y. Qiao, J. Deng, J. Chen, and X. Xing, *Journal of the American Ceramic Society* (2017).
- [26] Y. X. Wang, Q. Wu, X. R. Chen, and H. Y. Geng, *Scientific Reports* **6**, 32419 (2016).
- [27] A. B. Cairns *et al.*, *Nature materials* **12**, 212 (2013).
- [28] G. Kresse and D. Joubert, *Physical Review B* **59**, 1758 (1999).
- [29] G. Kresse and J. Furthmüller, *Physical Review B* **54**, 11169 (1996).
- [30] K. Parlinski, *Phonon Software* (2003).
- [31] H. J. Monkhorst and J. D. Pack, *Physical Review B* **13**, 5188 (1976).
- [32] J. P. Perdew, K. Burke, and M. Ernzerhof, *Physical Review Letters* **77**, 3865 (1996).
- [33] A. Sanson, M. Giarola, G. Mariotto, L. Hu, J. Chen, and X. Xing, *Materials Chemistry and Physics* **180**, 213 (2016).
- [34] G. Venkataraman, L. A. Feldkamp, and V. C. Sahni, *Dynamics of perfect crystals* (MIT Press, Cambridge, 1975).
- [35] V. F. Petrenko and R. W. Whitworth, *Physics of Ice* (OUP Oxford, 1999).
- [36] E. A. Engel, Y. Li, and R. J. Needs, *Physical Review B* **97**, 054312 (2018).
- [37] B. Pamuk, P. B. Allen, and M. V. Fernández-Serra, *Physical Review B* **92**, 134105 (2015).
- [38] B. Pamuk, J. M. Soler, R. Ramírez, C. P. Herrero, P. W. Stephens, P. B. Allen, and M. V. Fernández-Serra, *Physical Review Letters* **108**, 193003 (2012).
- [39] K. Kobayashi, M. Koshino, and K. Suenaga, *Physical Review Letters* **106**, 206101 (2011).
- [40] N. H. Fletcher, *The Chemical Physics of Ice*, by NH Fletcher, Cambridge, UK: Cambridge University Press, 2009 (2009).
- [41] C. G. Salzmann, P. G. Radaelli, A. Hallbrucker, E. Mayer, and J. L. Finney, *Science* **311**, 1758 (2006).
- [42] E. B. Moore and V. Molinero, *Nature* **479**, 506 (2011).
- [43] O. Mishima and H. E. Stanley, *Nature* **396**, 329 (1998).
- [44] L. E. Bove, S. Klotz, J. Philippe, and A. M. Saitta, *Physical Review Letters* **106**, 125701 (2011).
- [45] C. Fang, W.-F. Li, R. S. Koster, J. Klimes, A. van Blaaderen, and M. A. van Huis, *Physical Chemistry Chemical Physics* **17**, 365 (2015).
- [46] A. D. Fortes, *Acta Crystallographica Section B*, **74**, 196-216 (2018).
- [47] T. Strässle, A. M. Saitta, S. Klotz, and M. Braden, *Physical Review Letters* **93**, 225901 (2004).
- [48] M. M. Koza, *Physical Review B* **78**, 064303 (2008).
- [49] M. M. Koza, B. Geil, K. Winkel, C. Köhler, F. Czeschka, M. Scheuermann, H. Schober, and T. Hansen, *Physical Review Letters* **94**, 125506 (2005).
- [50] M. M. Koza, H. Schober, S. F. Parker, and J. Peters, *Physical Review B* **77**, 104306 (2008).
- [51] P. Gallo *et al.*, *Chemical Reviews* **116**, 7463 (2016).

- [52] E. A. Engel, B. Monserrat, and R. J. Needs, *The Journal of Chemical Physics* **143**, 244708 (2015).
- [53] E. A. Engel, B. Monserrat, and R. J. Needs, *Physical Review X* **5**, 021033 (2015).
- [54] F. Yen and T. Gao, *The Journal of Physical Chemistry Letters* **6**, 2822 (2015).
- [55] P. Zhang, L. Tian, Z. P. Zhang, G. Shao, and J. C. Li, *The Journal of Chemical Physics* **137**, 044504 (2012).
- [56] L. Tian, A. I. Kolesnikov, and J. Li, *The Journal of Chemical Physics* **137**, 204507 (2012).
- [57] P. Demontis, R. LeSar, and M. L. Klein, *Physical Review Letters* **60**, 2284 (1988).
- [58] M. Benoit, M. Bernasconi, P. Focher, and M. Parrinello, *Physical Review Letters* **76**, 2934 (1996).
- [59] R. LeSar, R. Najafabadi, and D. J. Srolovitz, *Physical Review Letter* **63**, 624 (1989)
- [60] A. Polian and M. Grimsditch, *Physical Review Letters* **52**, 1312 (1984).
- [61] C. Bellin, B. Barbiellini, S. Klotz, T. Buslaps, G. Rousse, T. Strässle, and A. Shukla, *Physical Review B* **83**, 094117 (2011).
- [62] T. Strässle, A. Caviezel, B. Padmanabhan, V. Y. Pomjakushin, and S. Klotz, *Physical Review B* **82**, 094103 (2010).
- [63] S. Klotz, L. E. Bove, T. Strässle, T. C. Hansen, and A. M. Saitta, *Nature Materials* **8**, 405 (2009).
- [64] T. Strässle, S. Klotz, G. Hamel, M. M. Koza, and H. Schober, *Physical Review Letters* **99**, 175501 (2007).
- [65] R. J. Nelmes, J. S. Loveday, T. Strässle, C. L. Bull, M. Guthrie, G. Hamel, and S. Klotz, *Nature Physics* **2**, 414 (2006).
- [66] S. Th, S. Klotz, J. S. Loveday, and M. Braden, *Journal of Physics: Condensed Matter* **17**, S3029 (2005).
- [67] B. Minceva-Sukarova, W. F. Sherman, and G. R. Wilkinson, *Journal of Physics C: Solid State Physics* **17**, 5833 (1984).
- [68] M. Zhang, H. Xu, E. K. H. Salje, and P. J. Heaney, *Physics and Chemistry of Minerals* **30**, 457 (2003).
- [69] T. Shigenari and K. Abe, *The Journal of Chemical Physics* **136**, 174504 (2012).
- [70] F. Perakis, S. Widmer, and P. Hamm, *The Journal of Chemical Physics* **134**, 204505 (2011).
- [71] J. Li, *The Journal of Chemical Physics* **105**, 6733 (1996).
- [72] B. I. Pamuk, P. B. Allen, and M.-V. Fernández-Serra, *The Journal of Physical Chemistry B* (2018).
- [73] É. D. Murray and G. Galli, *Physical Review Letters* **108**, 105502 (2012).
- [74] I. Presiado, J. Lal, E. Mamontov, A. I. Kolesnikov, and D. Huppert, *The Journal of Physical Chemistry C* **115**, 10245 (2011).
- [75] G. Kresse and J. Furthmüller, *Computational Materials Science* **6**, 15 (1996).
- [76] J. D. Bernal and R. H. Fowler, *The Journal of Chemical Physics* **1**, 515 (1933).
- [77] P. Software and K. Parlinski, PHONON Software, 2003.
- [78] M. Dion, H. Rydberg, E. Schröder, D. C. Langreth, and B. I. Lundqvist, *Physical Review Letters* **92**, 246401 (2004).

- [79] R. Gagnon, H. Kiefte, M. Clouter, and E. Whalley, *The Journal of Chemical Physics* **89**, 4522 (1988).
- [80] A. W. Sleight, *Annual Review of Materials Science* **28**, 29 (1998).
- [81] L. Monacelli, I. Errea, M. Calandra, and F. Mauri, *ArXiv preprint ArXiv:1804.06793* (2018).

CHAPTER 8

Summary and Future Research Plans

8.1 Summary

The research work presented in the thesis mainly deals with understanding of ionic diffusion and anomalous lattice behaviour in framework compounds. This research work involves the study the vibrational dynamics in battery materials and low density metal organic/inorganic framework compounds. The author has extensively investigated the role of lattice vibrations (phonons) in giving rise to negative thermal expansion, negative linear compressibility, ionic diffusion and phase transitions in crystalline solids. The inclusion of vibrational entropy of a system enables to accurately calculate the free energy of the system, which is very important to calculate the phase stability and temperature-pressure phase diagram. The study of phonons in these compounds provides atomistic mechanisms responsible for ionic diffusion and their anomalous lattice behaviour.

For this purpose, a combination of experimental tools, like, inelastic neutron scattering and X-ray diffraction along with state-of-the-art computational methodologies, like, density functional theory (DFT), lattice dynamics (LD), classical molecular dynamics (MD) as well as *ab-initio* MD are used. In order to validate the theoretical calculations, the measurements of phonon density of states from polycrystalline samples are performed using time-of-flight spectrometers. The Li atom, due to its small atomic number and low scattering cross section, acts as a poor scatterer of X-ray and neutron, which makes it difficult to study the dynamics of Li. Computational tools, like, DFT and MD simulations, provide a very good alternative to study the atomic scale behaviour of Li atom. The computational studies have been used to compute and analyze various features

in the solids, like, the phonon dispersion curves, the polarization vector of the phonons, phonon density of states, elastic constants, equation of state, thermal expansion, diffusion coefficients and activation energy barriers for ionic diffusion. Moreover, the variations of phonon frequencies with pressure are calculated to investigate soft phonon modes that may be responsible for high pressure phase transitions. The outcome of various studies performed in the thesis can be summarised as:

- (1) The temperature dependent inelastic neutron scattering measurements, density functional theory, and molecular dynamics simulations are used to investigate the mechanism of large anisotropy in Li ion conduction and thermal expansion behavior in solid electrolyte, LiAlSiO_4 . The low-energy phonons involving rotational degrees of freedom as well as a distortion of polyhedral units are found to be responsible for the negative thermal expansion behavior. The disordering of Li along the hexagonal c -axis gives rise to high temperature phase transition. The softening of Li related vibrational modes with increase in temperature gives rise to superionic conduction of Li, which is found to occur by intra-channel correlated jumps along c -axis. The negative thermal expansion along c -axis along with the positive expansion in a - b plane is found to enhance Li ionic conductivity along the c -axis. The introduction of defects in the crystal, namely, Li interstitial, Li vacancy and O vacancy, are found to increase the ionic conductivity and hence might reduce the temperature of superionic phase transition in this material. These results show a potential capability of this compound to be used as solid electrolyte in Li-ion batteries.
- (2) A combination of temperature dependent inelastic neutron scattering and *ab-initio* DFT simulations has provided the pressure-temperature phase diagram, thermal expansion behaviour along with Li diffusion in cathode material, LiAlO_2 . Three dimensional diffusion pathways are obtained and presence of defects in the crystal

reduces the temperature of diffusion. The application of pressure leads to structural changes in γ -phase through tetrahedral to octahedral coordination change around Li/Al atoms. The vibrational entropy is found to play an important role in phase stability and transitions among various phases. Moreover, the phonon mode responsible for δ to γ -phase transition on heating involves breaking of two Al-O bonds of AlO_6 octahedra to convert to corresponding tetrahedra.

- (3) The experimental X-ray diffraction and inelastic neutron scattering studies along with extensive *ab-initio* LD calculations shed light on the microscopic origin of anomalous lattice behavior of V_2O_5 . The compound is found to show NTE and NLC along a -axis at low temperatures and pressures, respectively. The NTE and NLC arise from the anisotropy in Grüneisen parameters and elastic constants. Free energy calculations show two first ordered phase transition at high pressure and temperature, i.e., from α to β and then to δ -phase. The diffusion pathways for alkali intercalated V_2O_5 , as obtained from the MD simulations, are predicted to follow the eigenvectors of soft phonon modes obtained in the intercalated structure. The diffusion happens in the a - b plane of the structure.
- (4) The inelastic neutron scattering experiments and *ab-initio* calculations are used to gain deeper insights into the structure and dynamics of $\text{ZnAu}_2(\text{CN})_4$ as a function of temperature and pressure. The large anisotropy in the elastic compliance matrix, which is attributed to the flexible network and Au bridging, are responsible for the NLC and NTE behaviour in this compound. The softening of an L-point phonon mode coupled with a zone-centre phonon and an M-point phonon gives rise to high-pressure transition at about 2 GPa which is of a weakly first order nature.
- (5) It is increasingly recognized that theory and computation play a key role in materials discovery. *Ab-initio* DFT calculations are applied to reveal large anomalous lattice

behaviour in metal organic framework material, AgC_8N_5 . The presence of NLC and NTE behavior along the hexagonal c -axis of crystal are found to be governed by the dominant dynamics of Ag atoms in a - b plane, which give rise to hinge-like mechanism for NLC and NTE.

- (6) The mechanism of NTE behaviour in terminally connected polyhedral networks like MZrF_6 ($M=\text{Mg, Ca, Sr}$) and I_h -phase of ice are studied using *ab-initio* lattice dynamics. The NTE in MZrF_6 is governed by phonons involving ZrF_6 polyhedral librational motion, which leads to large transverse amplitude of the vibration of the fluorine atom in the Zr-F-Zr bond. The compounds with larger anisotropy in the thermal amplitude of the fluorine atoms show larger NTE behaviour.
- (7) In the case of in H_2O and D_2O ice I_h , the NTE below 60 K in the hexagonal a - b plane is due to anharmonic librational motion of the hexagonal rings of the ice molecules, and the NTE along the hexagonal c -axis originates from the transverse vibrations of the hexagonal layers.

The atomic vibrations are found to govern important functional properties of materials. The changes of atomic vibrations that may be achieved via designing, doping and intercalating the compounds may enhance these functionalities. The studies of phase diagram of materials presented in the thesis are important for determining the temperature-pressure range suitable for their applications. The thermal expansion is an issue for micro-batteries because batteries heat up during operation which may produce cracking or loose connection. Materials with low thermal expansion over wide temperature range may be very useful, e.g., LiAlSiO_4 electrolyte (which has almost zero thermal expansion from 200 to 400K).

8.2 Future Research Plans

The research work performed during the course of this thesis has given a valuable experience in the field of phonons and related physical properties of materials. This experience can be utilized to design and discover new materials with enhanced negative linear compressibility and negative thermal expansion. The typical phonon modes governing ionic diffusion in the crystal lattice are studied within the quasi-harmonic approximation and this work can be extended to calculate the actual anharmonicity through calculation of temperature dependent phonon dispersion curves using *ab-initio* molecular dynamics simulations.

Recently it has been shown that the presence of guest molecules in the compounds exhibiting NTE behaviour affects the thermal expansion behaviour of compounds. We plan to do *ab-initio* calculations to understand the phenomenon. Further, high throughput material simulations are planned which will involve the scanning of available low density metal organic framework compounds using *ab-initio* density functional calculations. The high pressure density functional studies on these compounds will provide their anisotropic compressibility which will help in determining the usage of these materials. The studies can further be used to investigate the mechanism of anisotropic compressibility in the compounds.

The quasielastic neutron scattering experiments can be done to understand the diffusion of lithium and sodium in various compounds. By combining the inelastic and quasielastic neutron measurements with *first-principles* phonon calculations and temperature-dependent molecular dynamics simulations, we expect to gain deeper insights of the mechanism of ionic conductivity and anomalous thermal expansion and their relationship to phonons in these compounds.

Moreover, the calculation of configurational entropy in structure with disorder plays an important role in accurate determination of free energy of the system which can be used to find the ground state structure. This kind of work will be highly useful for determining the phase diagrams of battery electrode materials during charging and discharging (intercalation/deintercalation) processes. These calculations can further be extended to calculate the role of configurational disorder in giving rise to anomalous lattice response of the functional material.